ISSN en trámite

instituto de astronomía

unam

revista mexicana de astronomía y astrofísica

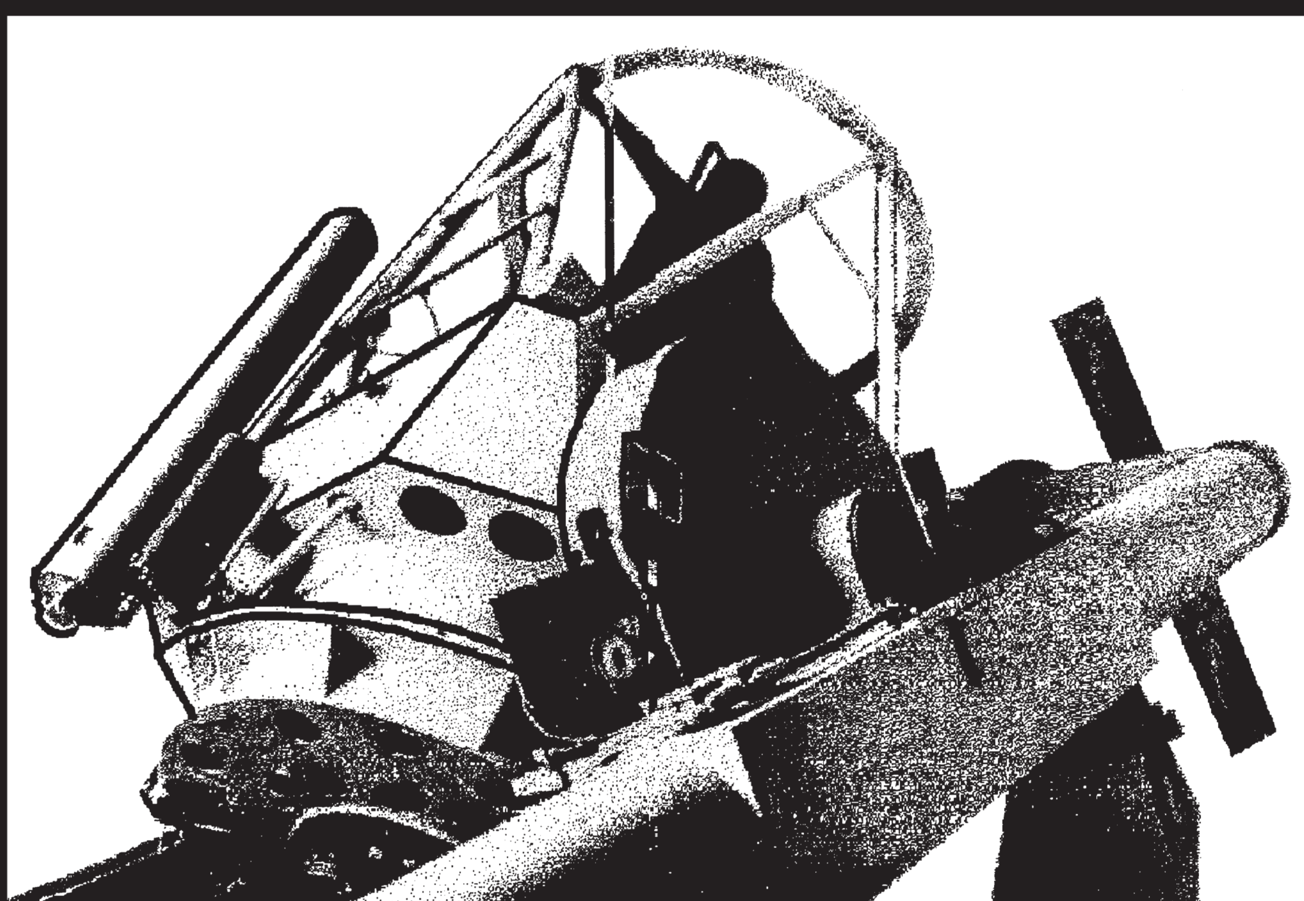

volumen 55
número 1
octubre 2019

volumen 55, número 1, abril 2019

revista mexicana de astronomía y astrofísica

Instituto de Astronomía
Universidad Nacional Autónoma de México

revista mexicana de astronomía y astrofísica

ISSN en trámite

URL de DOI: https://doi.org/10.22201/ia.01851101p.2019.55.01

rmaa@astro.unam.mx

http://www.astroscu.unam.mx/RMxAA/

La *RMxAA* aparece indexada en Current Contents, Science Citation Index, Astronomy and Astrophysics Abstracts, Physics Briefs, Publicaciones Científicas en América Latina, Astronomy and Astrophysics Monthly Index, PERIODICA, RedALyC, Latindex y SciELO.

Revista Mexicana de Astronomía y Astrofísica, volumen 55, número 1, abril 2019, es una publicación semestral, editada y distribuida por el Instituto de Astronomía, UNAM, Circuito Exterior, Ciudad Universitaria, 04510, Alcaldía Coyoacán, Ciudad de México, Teléfono: 5556223906, Correo Electrónico: rmaa@astro.unam.mx, ISSN en trámite. Editora responsable: Christine Patricia Allen Armiño. Distribución: Bienes y Servicios del Instituto de Astronomía, UNAM. Impresa por Grupo Edición, S.A. de C.V., Xochicalco 619, Colonia Letrán Valle, 03650, Alcaldía Benito Juárez, Ciudad de México. Fecha de impresión: 27 de marzo de 2019. Número de ejemplares impresos: 500 en papel Couché de 100 gramos los interiores y en cartulina Couché de 250 gramos los forros. Precio de la publicación: gratuito.

CONTENTS

Revista Mexicana de Astronomía y Astrofísica, **55**, 3–9 (2019)

ENTRAINMENT FACTOR OF INDIVIDUAL GLITCH FRACTIONAL MOMENT OF INERTIA

I. O. Eya[1,3], J. O. Urama[2,3], and A. E. Chukwude[1,2,3]

Received May 21 2018; accepted September 4 2018

ABSTRACT

The superfluid in the inner crust of a neutron star is assumed to be the reservoir of momentum released in a pulsar glitch. Recently, due to crustal entrainment, it appears debatable whether the magnitude of the inner crust is sufficient to contain the superfluid responsible for large glitches. This paper calculates the fractional moment of inertia (FMI)(i.e. the ratio of the inner crust superfluid moment of inertia to that of the coupled components) associated with individual glitches. It is shown that the effective moment of inertia associated with the transferred momentum is that of the entrained neutrons. The FMI for glitches in three pulsars, which exhibit the signature of exhausting their momentum reservoir, were calculated and scaled with the entrainment factor. Some of the glitches require an inner crust superfluid with moment of inertia larger than the current suggested values of 7-10% of the stellar moment of inertia.

RESUMEN

Se asume que la corteza interna de las estrellas neutrón es el reservorio del impulso liberado durante las discontinuidades del pulsor. Debido al arrastre de la corteza, se debate si el tamaño de la corteza interna es suficiente para retener al superfluido responsable de las grandes discontinuidades. Calculamos el FMI (el momento de inercia fraccional, es decir, el cociente entre el momento de inercia del superfluido de la corteza interna y el de las componentes acopladas), asociado a cada discontinuidad. Mostramos que el momento de inercia efectivo asociado al impulso transferido es el de los neutrones arrastrados. Se calcula el FMI para las discontinuidades en tres pulsores que muestran señales de haber ya agotado su reservorio de impulso, y se escala con el factor de arrastre. Algunas de las discontinuidades requieren superfluidos en la corteza interna con momentos de inercia mayores que los que actualmente se consideran, 7-10% del momento de inercia estelar.

Key Words: methods: statistical — pulsars: general — stars: neutron

1. INTRODUCTION

Pulsars are spinning magnetized neutron stars (Gold 1968). The spin rates of these objects are highly stable due to the huge moment of inertia they possess ($\approx 10^{45}$ g cm^2). In spite of this, the spin rate of some pulsars is occasionally perturbed during events known as glitches. Pulsar glitches are impulsive increases in the pulsar spin frequency, $\Delta\nu$ (Radhakrishnan & Manchester 1969; Wang et al. 2000; Espinoza et al. 2011; Yu et al. 2013). These events are sometimes associated with changes in the pulsar spin-down rate, $\Delta\dot{\nu}$ (Lyne et al. 1993). In most of the pulsars, glitch events are believed to involve superfluid neutrons in the inner crust of the neutron star (Baym et al. 1969; Anderson & Itoh 1975; Alpar et al. 1984). Firstly, this is due to the long time it takes a pulsar to recover to a steady spin frequency after a glitch (days to months) and, secondly, due to the recovery phase, which is exponential in nature for most pulsars. Recently, studies of the interior of neutron stars containing superfluids have gained observational support by the cooling of young neu-

[1]Department of Science Laboratory Technology, University of Nigeria, Nsukka, Nigeria.
[2]Department of Physics and Astronomy, University of Nigeria, Nsukka, Nigeria.
[3]Astronomy and Astrophysics Research Lab, Faculty of Physical Sciences, University of Nigeria, Nsukka, Nigeria.

tron stars (Page et al. 2011; Shternin et al. 2011). So there is no doubt that neutron stars contain a superfluid component.

Pulsar glitch models involving a superfluid component view the neutron star as a system in which its components rotate differentially. The main components are: the solid crust, the interior superfluid neutrons (inner crust and outer core), and the core (Takatsuka & Tamagaki 1989). In this model, the solid crust and the core are coupled electromagnetically. The inner crust superfluid component viewed as a momentum reservoir, rotates via an array of quantized vortices whose areal density is proportional to the fluid velocity. These vortices are pinned in the ion lattice of the inner crust, leading to partial decoupling of the inner crust superfluid component from the other components (Anderson & Itoh 1975; Alpar et al. 1984). As the coupled components spin down electromagnetically, the inner crust superfluid maintains its own velocity. In this situation, the superfluid at a higher velocity stores angular momentum, which is occasionally released in glitches. For the superfluid to spin down, the vortex areal density must decrease. This could happen either by reduction of the vortex number, or by outward migration of vortices. Such processes are prevented by the pinning force on the vortices. As long as the vortices remain in their pinned position, the superfluid angular momentum is conserved.

Meanwhile, as the solid crust lags behind the superfluid component, the rotation lag (i.e. the magnitude of the velocity difference between the two components) increases with time. The lag is not sustainable over the pulsar life time. At a critical lag, unclear mechanisms unpin some of the vortices (or all of them). The vortices migrate outward transferring their momentum to the crust; the superfluid spins-down and the crust spins-up (Anderson & Itoh 1975; Alpar et al. 1984). The magnitude of the crustal spin-up, $\Delta\nu$, is the glitch spin-up size. Large glitches, such as that of the Vela pulsar, are characterised by $\Delta\nu > 10^{-6}$ Hz. Such a glitch size is one of the reasons why scholars believed that there is an angular momentum reservoir somewhere in the neutron star interior.

A glitch model involving angular momentum transfer has been standard for discussing pulsar glitches for decades. This is partly due to its ability to explain post glitch features such as exponential recoveries and long recovery times (Baym et al. 1969; Alpar et al. 1984), and mainly due to the agreement between the theoretical prediction of neutron star crustal thickness and the pulsar glitch size (Ravenhall & Pethick 1994; Link et al. 1999). Recently, most aspects of the Vela pulsar glitches have been fully described based on this model (Haskell et al. 2012). Plausibly, the angular momentum transfer model is becoming the most widely accepted theory. In the work of Link et al. (1999), the moment of inertia of the superfluid component involved in the Vela glitches is just about 1.4% of the stellar moment of inertia. This amount of superfluid can conveniently reside in the inner crust of the star. In view of the inner crust superfluid involvement in pulsar glitches, the regularity of the glitches of the Vela pulsar and of PSR J0357 − 6910, is seen as a consequence of recycling a reservoir that is exhausted at each event (Andersson et al. 2012).

However, following the recent involvement of crustal entrainment in pulsar glitch size (Andersson et al. 2012; Chamel 2013), angular momentum transfer models are under a serious challenge. Basically, entrainment increases the inertia of superfluid neutrons, thereby reducing the mobility of the fluid (Chamel 2005; Chamel & Carter 2006; Chamel 2012). For this reason, the superfluid confined in the inner crust is not sufficient to produce Vela-like glitches; unless glitching pulsars are low mass neutron stars ($\leq 1.0\ M_{\odot}$), or the core fluid is involved in the glitch (Andersson et al. 2012). Consequently, in Link et al. (1999) the inner crust superfluid moment of inertia is underestimated by a factor of 4.3 (Andersson et al. 2012; Chamel 2013), which is the likely value of the entrainment factor. Physically, this means that the moment of inertia of the superfluid contained in the inner crust should be above 6% of the stellar moment of inertia for it to produce the observed glitches (i.e. $4.3 \times 1.4\%$).

On the other hand, recent works (Piekarewicz et al. 2014; Steiner et al. 2015) have argued that the inner crust superfluid could sufficiently produce the observed glitches. The argument is based on exploring the uncertainties of the equation-of-state (EoS) of the nuclear matter, which models the structure of the neutron star. With this approach, Piekarewicz et al. (2014) obtained a crust thick enough to contain a fluid with up to 7% of the stellar moment of inertia, given a neutron star mass $< 1.6\ M_{\odot}$. Similarly, for a neutron star mass of $1.4\ M_{\odot}$, Steiner et al. (2015) obtained a thicker crust with up to 10% of the stellar moment of inertia. Large crustal thickness implies large stellar radius and small stellar mass. In this framework, there is a limit for how much one can extend the crust irrespective of the magnitude of the uncertainty of the EoS, else one would approach a white dwarf.

In the previous analyses, the approach has been to calculate the fractional moment of inertia (FMI) (i.e. the ratio of inner crust superfluid moment of inertia to that of the coupled components) of the neutron star components participating in the glitch based on the average glitch size of a given pulsar. The result is then compared with the theoretical magnitude of neutron star crustal thickness. However fair this approach is, it hides the intrinsic size of the inner crust fluid. Efforts should be channelled towards calculating the FMI based on individual glitches, as this will show the possible range of crustal thickness. This paper treats each glitch as a unique event, and calculates the FMI for each glitch in three pulsars that exhibit strong linear transfer of angular momentum with time. The linearity of glitches in these pulsars is believed to be a consequence of a reservoir that is exhausted at each event, thereby making each glitch independent of others. In such a situation, the FMI for each glitch is a measure of a distinct momentum reservoir. The result shows that some glitches exceed the initial inner crust moment of inertia as constrained in Link et al. (1999) even without the entrainment factor. In addition, if the entrainment factor stands at 4.3, the present neutron star crustal thickness ($\approx 10\%$) is not sufficient to produce some glitches.

2. ROTATION LAG AND FRACTIONAL MOMENT OF INERTIA

For a spinning neutron star, the standard rotation lag between the momentum reservoir[4] and the observable solid crust, which leads to accumulation of transferable momentum, is

$$\omega(t) = \Omega_{res} - \Omega_c(t), \tag{1}$$

where $\Omega_{res} = 2\pi\nu_{res}$ is the reservoir's angular frequency, $\Omega_c = 2\pi\nu_c$ the angular frequency of the solid crust and any other component coupled to it. The stellar moment of inertia is

$$I = I_{res} + I_c, \tag{2}$$

where I_{res} and I_c are the moments of inertia of the momentum reservoir and that of the coupled components, respectively. In this model, I_c makes up at least 90% of the neutron star moment of inertia (Link et al. 1999, and references therein), implying $I_c \approx I$.

In a glitching pulsar, at a time-interval (t_i) preceding a glitch, the reservoir accumulates transferable momentum due to the rotation lag, which can be quantified by

$$L_i = I_{res}\omega(t), \tag{3}$$

at a rate of

$$\dot{L}_i = -I_{res}\dot{\Omega}_{ic}(t), \tag{4}$$

where $\dot{\Omega}_{ic}(t) = 2\pi\dot{\nu}_{ic}$ is the spin-down rate of the crust at a time-interval preceding the glitch. Here, it is assumed that the momentum accumulated over a period t_i, results in a spin-up of the crust $\Delta\Omega_{ic}$. A measure of $\Delta\Omega_c$ is an indirect way of estimating the transferred momentum. In this, for a given glitch, the transferred momentum is

$$L_i = I_c\Delta\Omega_{ic}(t), \tag{5}$$

at a rate of

$$\dot{L}_i = I_c\frac{\Delta\Omega_{ic}(t)}{t_i}. \tag{6}$$

In this framework, if the rate of accumulation of angular momentum by the reservoir is directly proportional to the rate angular momentum is transferred, the cumulative glitch spin-up sizes ($\Sigma\Delta\Omega_{ic}$) should be linear over time if the momentum reservoir is exhausted at each glitch. Such pulsars of linear transfer of angular momentum over time are shown in Figure 1. This kind of behaviour has been reported in PSRs J0835 − 4510 (Vela pulsar) (Link et al. 1999; Marshall et al. 2004; Eya & Urama 2014), J0537 − 6910 (Middleditch et al. 2006), and J1420 − 6048 (Eya et al. 2017). Hence, equations (4) and (6) give the individual glitch FMI

$$\frac{I_{res}}{I_c} = -\frac{1}{\dot{\Omega}_{ic}(t)}\frac{\Delta\Omega_{ic}}{t_i}(t). \tag{7}$$

Such an expression for the FMI has been obtained earlier (Eya et al. 2017). The magnitude of FMI gives an insight on the magnitude of the momentum reservoir.

3. ENTRAINMENT FACTOR AND THE MAGNITUDE OF FMI/GLITCH SIZE

It is known that a superfluid flows with zero viscosity. The superfluid neutrons in the inner crust of a neutron star also flow with zero viscosity, but they are still entrained by the crust (Pethick et al. 2010). The entrainment is non-dissipative, it occurs due to the elastic scattering of free neutrons by the crustal lattice (Chamel 2013). The magnitude of the entrainment in the inner crust is quantified by either the density of conduction neutrons in the crust or by the effective mass of the neutron (Andersson et al.

[4] The superfluid confined in the inner crust.

2012; Chamel 2013). In this paper, the interest is on how the entrainment factor constrains the observed glitch sizes.

For a sphere spinning down, such as pulsars, the loss in rotational energy is

$$\dot{E} = I\Omega_c\dot{\Omega}_c. \tag{8}$$

This loss in rotational energy results in the observed radiation from the pulsar, which can be approximated to that of a dipole radiator in a vacuum,

$$\dot{E} = -\frac{B^2R^6\Omega^4}{6c^3}\sin\alpha^2, \tag{9}$$

where B is the magnetic field strength, R is the stellar radius, and c is the speed of light. Comparing equations (8) and (9) (with $\Omega \equiv \Omega_c$) leads to

$$I\dot{\Omega}_c = -K\Omega_c^3. \tag{10}$$

Equation (10) is the standard spin-down law of pulsars, where $K = 6^{-1}B^2R^6\ c^{-3}\sin^2\alpha$ is assumed to be constant. For the two components model and owing to the pinned vortices,

$$I_c\dot{\Omega}_c + I_{res}\dot{\Omega}_{res} = -K\Omega_c^3. \tag{11}$$

As entrainment is non-dissipative, $I_{res}\dot{\Omega}_{res}$ is not expected to affect the spin down of the pulsar. In the frame of perfect pinning and expressing entrainment in terms of the coefficient, e_n, (Andersson et al. 2012, and references therein),

$$I_{res}\dot{\Omega}_{res} = -\frac{e_nI_{res}\dot{\Omega}_c}{(1-e_n)}. \tag{12}$$

Therefore, the effective torque on the pulsar is

$$I_{ef}\dot{\Omega}_c = -K\Omega^3, \tag{13}$$

where $I_{ef} = I_c - (\frac{e_n}{1-e_n})I_{res}$ is the effective moment of inertia of the pulsar due to entrainment, and $(\frac{e_n}{1-e_n}) = E_n$ is the entrainment factor. If the entrainment coefficient is zero, the standard spin-down law is recovered.

Let us determine the effective moment of inertia associated with the glitch event. Based on the two component model, the total angular momentum of the system is

$$L_{tot} = I_{res}\Omega_{res} + I_c\Omega_c, \tag{14}$$

where $I_{res}\Omega_{res}$ is the angular momentum of the momentum reservoir (neutron superfluid), and $I_c\Omega_c$ is the observable angular momentum of the star. However, owing to entrainment, the angular momentum of the superfluid is a function of both the superfluid angular velocity and the angular velocity of the star, Ω_c, (Chamel 2013), which is expressed as (Chamel & Carter 2006; Chamel 2013)

$$L = I_{ss}\Omega_{res} + (I_{res} - I_{ss})\Omega_c, \tag{15}$$

where I_{ss} is the moment of inertia associated with the entrained neutrons. Hence, the total angular momentum of the system as a result of entrainment is[5]

$$L_{tot} = I_{ss}(\Omega_{res} - \Omega_c) + I\Omega_c. \tag{16}$$

The term in parentheses is the differential rotational lag, $\omega(t)$. The implication of this is that the effective moment of inertia associated with the transferred momentum is that of the entrained neutron, and I_{res} in equation (7) could be safely replaced with I_{ss}. From equation (16), the effective torque is $(I - I_{ss})\dot{\Omega}_c$ and with equation (13)[6] $I_{ss} = E_nI_{res}$. Hence incorporating the entrainment factor in the expression of FMI leads to

$$\frac{I_{res}}{I_c} = -\frac{1}{E_n}\frac{1}{\dot{\Omega}_{ic}(t)}\frac{\Delta\Omega_{ic}}{t_i}(t), \tag{17}$$

The interpretation of this result is quite simple; the observed glitch sizes should be less by a factor of $1/E_n$, or equivalently, the moment of inertia of the momentum reservoir should be enhanced by a factor of E_n for the observed glitch sizes. Though this argument is not new, it has not been extended to individual glitch FMI.

4. DATA AND RESULTS

The glitches for this analysis are taken from Espinoza et al. (2011), and updated with JBO glitch tables and references therein[7] to include more recent events, up to the time of this analysis. Three pulsars in which glitch spin-up sizes ($\Delta\nu$) are quite regular over time were selected for this analysis (Figure 1). Concentrating on such pulsars is a precaution to avoid glitches that may originate from any component other than the crustal superfluid, which is the basis for the regularity of the glitches. In addition, pulsars in which glitches follow this trend are believed to possess a reservoir that is exhausted at each glitch. In this view, each of the glitches is a unique event independent of others.

For nearly two decades, the constraint on crustal thickness estimated from glitch data was based on

[5] We use $I = I_c + I_{res}$.

[6] We use $I \approx I_c$.

[7] http://www.jb.man.ac.uk/pulsar/glitches.html, accessed on may 1, 2017.

comparing the moment of inertia of the inner crust superfluid obtained from a linear fit to glitch points in plots such as Figure 1. With the slope of the linear fits in Figure 1 and the mean spin down rate of the corresponding pulsar, the mean FMI for each of the pulsars are: 0.85% for PSR J0537 − 6910, 1.55% for PSR J0835 − 4510 and 1.29% for PSR J1420 − 6048. These values are in line with other analyses (Link et al. 1999; Andersson et al. 2012; Eya et al. 2017). A constraint of this kind is based on the average glitch sizes in a pulsar. This approach does not allow for the extreme values.

The FMIs for each glitch are shown in Table 1. The FMI corresponding to the first glitch in a given pulsar could not be calculated since the time interval preceding the glitch is not available. The distribution of FMIs is shown in the top panel of Figure 2, while the bottom panel shows the distribution of FMIs scaled with the entrainment factor (4.3). From the top panel, it is clear that an 1.4% crustal thickness moment of inertia could not accommodate the observed glitches, even without the entrainment factor. The relevant glitches are the glitches with FMIs at the right side of the 1.4% line. These glitches make up ≈ 52% of the total glitches in these pulsars. Interestingly, when the FMIs are scaled by the entrainment factor, ≈ 93% of the glitches require crustal thickness that are more than 1.4% of the stellar moment of inertia, as seen in the bottom panel of Figure 2. In addition, with the entrainment factor, ≈ 26% of the glitches require a crust beyond the possible 10% stellar moment of inertia proposed by Steiner et al. (2015).

5. DISCUSSION

The FMI in this analysis is a measure of distinct reservoir moment of inertia. The upper limit in the range of FMIs in a given pulsar gives an insight on the minimum size of the neutron star crustal thickness. Without the entrainment factor, the: 6th, 8th and 17th glitch in PSR J0537 − 6910; 5th, 7th, 10th, 12th, 13th, 14th, 16th and 18th glitch in the Vela pulsar require a crustal thickness that is above 2%, of the stellar moment of inertia. Only the glitches in PSR J1420 − 6048 are exempt from this anomaly. Owing to this, the earlier theoretical calculations of the neutron star crust (Ravenhall & Pethick 1994; Link et al. 1999) could not account for some of the glitches, even without entrainment factor. This effect is more severe with the entrainment factor, where some of the glitches will require a crust thickness that is above 10% of the stellar moment of inertia. The FMI could be as large as 90% and 24% for

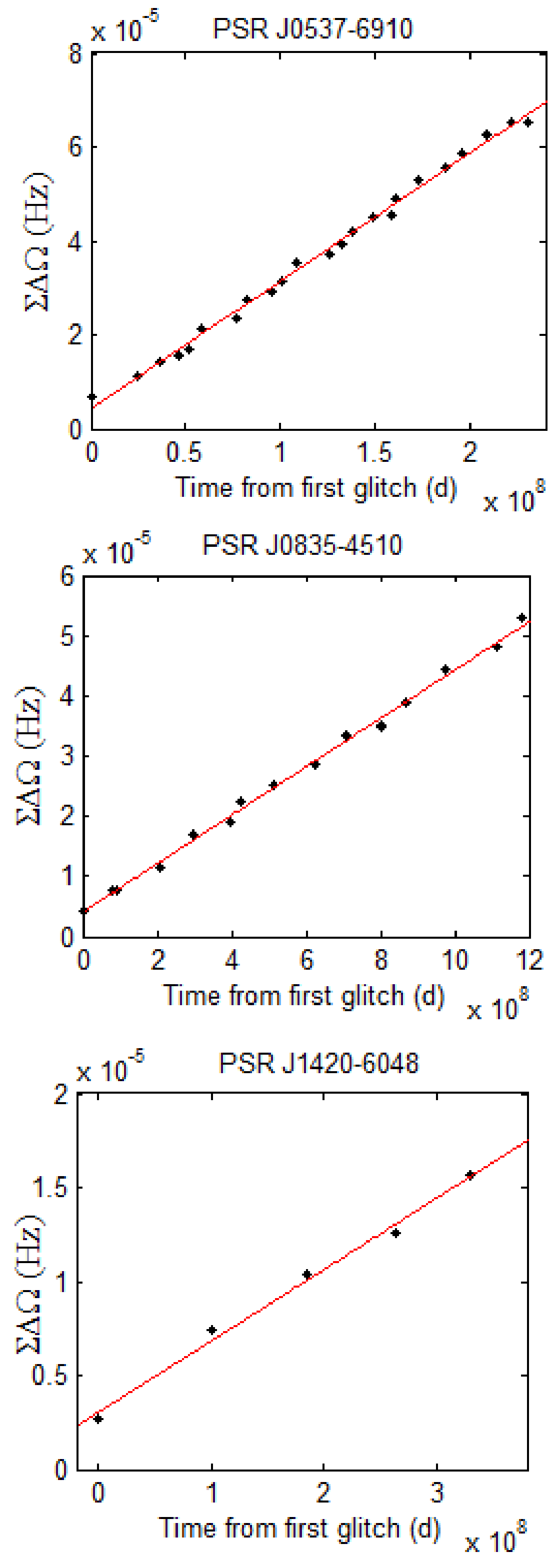

Fig. 1. Regularity of pulsar glitches. The straight line is a linear fit to the points.

TABLE 1

CHARACTERISTIC FMI IN THE PULSARS.

N_g	J0537-6910	J0835-4510	J1420-6048
1	—	—	—
2	0.763	1.851	1.660
3	1.067	0.080	1.241
4	0.724	1.448	0.959
5	0.964	2.605	1.685
6	2.182	0.792	—
7	0.595	5.570	—
8	21.267	1.244	—
9	0.418	1.184	—
10	1.156	2.395	—
11	1.449	0.627	—
12	0.301	5.116	—
13	1.165	2.241	—
14	1.234	2.145	—
15	1.025	1.093	—
16	0.057	2.812	—
17	6.804	1.095	—
18	0.944	2.225	—
19	0.612	0.001	—
20	1.089	—	—
21	0.990	—	—
22	0.492	—	—
23	0.067	—	—

Note: The FMIs are measured in percent (%), N_g denotes the glitch number.

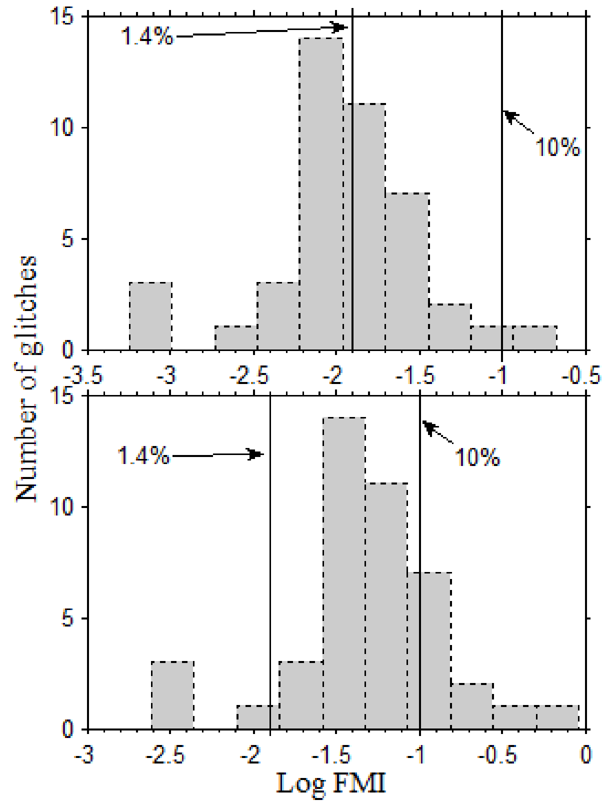

Fig. 2. Distribution of FMIs calculated from equation (7); bottom panel is the distribution of FMIs scaled with an entrainment factor as suggested by equation (17).

the 8th and 7th glitches in PSRs J0537 − 6910 and J0835 − 4510 respectively[8]. As at present, no EoS provides a neutron star crust that could contain a crustal fluid for such a reservoir. This result is quite disturbing if one recalls that these glitches are from pulsars which deplete their reservoir at each glitch. There is no evidence of radiative change in these pulsars during the glitch, which might have suggested that glitches are enhanced by magnetospheric activity. The 7-10% crustal thickness moment of inertia (Piekarewicz et al. 2014; Steiner et al. 2015) is an upper limit in the current theoretical calculation of the neutron star structure. The actual value could be lower, since the authors neglected superfluidity. In particular, for such a crustal thickness, the neutron star radius should be as large as $\approx 14.0 \pm 0.5$ km. Clearly this value is in contrast with the recent analysis of low mass X -ray binaries, with predicted small radii of $\approx 11.8 \pm 0.9$ km (Lattimer & Steiner 2014), or even smaller from the analysis of Guillot et al. (2013).

Finally, pulsar glitch models relying on an inner crust superfluid and nuclear matter EoS are under serious challenge unless the vortex unpinning trigger mechanism, which is still elusive, has the ability to squeeze angular momentum and liberate it at the onset of the glitch.

[8]i.e. multiplying the FMI by entrainment factor (4.3).

REFERENCES

Alpar, M. A., Pines, D., Anderson, P. W., & Shaham, J. 1984, ApJ, 276, 325
Anderson, P. W., & Itoh, N. 1975, Natur, 256, 25
Andersson, N., Glampedakis, K., Ho, W. C. G., & Espinoza, C. M. 2012, PhRvL, 109, 1103
Baym, G., Pethick, C., Pines, D., & Ruderman, M. 1969, Natur, 224, 872
Chamel, N. 2005, NuPh A, 747, 109
__________. 2012, PhRvC, 85, 5801

_________. 2013, PhRvL, 110, 1101
Chamel, N. & Carter, B. 2006, MNRAS, 368, 796
Eya, I. O. & Urama, J. O. 2014, International Journal of Astrophysics and Space Science, 2, 16
Eya, I. O., Urama, J. O., & Chukwude, A. E. 2017, ApJ, 840, 56
Espinoza, C. M., Lyne, A. G., Stappers, B. W., & Kramer M. 2011, MNRAS, 414, 1679
Gold, T. 1968, Natur, 218, 731
Guillot, S., Servillat, M., Webb, N. A., & Rutledge, R. E. 2013, ApJ, 772, 7
Haskell, B., Pizzochero, P. M., & Sidery, T. 2012, MNRAS, 420, 658
Lattimer, J. M., & Steiner A. W. 2014, ApJ, 784, 123
Link, B., Epstein, R. I., & Lattimer, J. M. 1999, PhRvL, 83, 3362
Lyne, A. G., Pritchard, R. S., & Graham-Smith, F. 1993, MNRAS, 265, 1003
Marshall, F. E., Gotthelf, E. V., Middleditch J., Wang Q. D., & Zhang W. 2004, ApJ, 603, 682
Middleditch, J., Marshall, F. E., Wang, Q. D., Gotthelf, E. V., & Zhang, W. 2006, ApJ, 652, 1531
Page, D., Prakash, M., Lattimer, J. M., & Steiner, A. W. 2011, PhRvL, 106, 1101
Pethick, C. J., Chamel, N., & Reddy, S. 2010, PThPS, 186, 9
Piekarewicz, J., Fattoyev, F. J., & Horowitz, C. J. 2014, PhRvC, 90, 5803
Radhakrishnan, V. & Manchester, R. N. 1969, Natur, 222, 228
Ravenhall, D. G. & Pethick, C. J. 1994, ApJ, 424, 846
Steiner, A. W., Gandolfi, S., Fattoyev, F. J., & Newton, W. G. 2015, PhRvC, 91, 5804
Shternin, P. S., Yakovlev, D. G., Heinke, C. O., Ho, W. C. G., & Patnaude, D. J. 2011, MNRAS, 412, L108
Takatsuka, T. & Tamagaki, R. 1989, PThPh, 82, 945
Wang, N., Manchester, R. N., & Pace, R. T. 2000, MNRAS, 317, 843
Yu, M., Manchester, R. N., Hobbs, G., et al. 2013, MNRAS 429, 688

Augustine Ejike Chukwude and Johnson Ozoemena Urama: Department of Physics and Astronomy, Faculty of Physical Sciences, University of Nigeria, Nsukka, Nigeria (augustine.chukwude, johnson.urama@unn.edu.ng).
Innocent Okwudili Eya: Department of Science Laboratory Technology, Faculty of Physical Sciences, University of Nigeria, Nsukka, Nigeria (innocent.eya@unn.edu.ng).

Revista Mexicana de Astronomía y Astrofísica, **55**, 11–16 (2019)

A SOLAR MID-INFRARED TELESCOPE

J. E. Mendoza-Torres[1], J. S. Palacios-Fonseca[2], M. Velázquez-de-la-Rosa[1], P. Rodríguez-Montero[1], A. De-Roa-Campoy[3], E. Valadez-Campos[3], M. O. Arias-Estrada[1], J. Peña-Saint-Martín[4], B. Rodríguez-Pedroza[1], I. Gómez-Arista[3], M. Juárez-Gama[5], K. Gottschalk[6], and I. C. Medina-Carrillo[2]

Received January 19 2018; accepted October 9 2018

ABSTRACT

We developed a mid infrared (MIR) solar telescope, centered at 10μm. Various optical layouts were analyzed based on computer simulations and a Ritchey-Chretien 6-inches telescope was selected with a plate scale of $2.5''$/mm using a pyroelectric 4×16 pixels detector. The angular resolution is $36''$/pixel with a field of view of $9.6' \times 2.4'$. Two germanium filters are used, one at the aperture of the telescope and another near its focal plane. The detector was characterized with a laboratory black-body. The count values follow a linear relation with the black-body temperature. The control systems for both the telescope and the detector were developed. Proper mechanical supports were designed for the filters, detector and electronics. The system has been integrated and a user interface was developed. Preliminary observations have been made giving a signal-to-noise ratio of ≈ 1000.

RESUMEN

Desarrollamos un telescopio solar en el infrarrojo medio (MIR), centrado en 10μm. Estudiamos varios diseños ópticos, con base en simulaciones de computadora y seleccionamos un telescopio Ritchey-Chretien de 6 pulgadas con escala de placa de $2.5''$/mm, con un detector piroeléctrico de 4×16 pixeles. La resolución angular es de $36''$/pixel con un campo de visión de $9.6' \times 2.4'$. Se usan dos filtros de germanio, uno en la apertura del telescopio y otro cerca del plano focal. El detector se caracterizó con un cuerpo negro de laboratorio. Los valores, en cuentas, siguen una relación lineal con la temperatura del cuerpo negro. Se hicieron los sistemas de control del telescopio y del detector. Se diseñaron soportes mecánicos para los filtros, el detector y la electrónica. El sistema se integró y se hizo una interfaz para el usuario. Las observaciones preliminares muestran que se obtiene una relación señal a ruido de ≈ 1000.

Key Words: telescopes — Sun: general — Sun: infrared

1. INTRODUCTION

The Sun has been observed for several decades in many frequencies of the electromagnetic spectrum. The first reported studies of the Sun in the mid infrared range (MIR) were made in the seventies (Ohki & Hudson 1975). Among the results obtained in those years, it can be mentioned that low fluxes were found at the spot areas (Hudson 1975), which locates the origin of this emission in the low atmosphere, near the photosphere. During the following decades no devoted solar instruments were regularly operating at MIR and few observations were reported. The first reported MIR flare was a M7.9 GOES class, observed on March 13, 2012 at 10μ (30 THz) by Kaufman et al. (2013), and after that other flares (M2.0 and X2.0) were observed by Kaufmann et al. (2015). Recently, Penn et al. (2016) reported a C7.0 GOES class flare observed at 8.6 and 4.9μm. These flares were simultaneously detected at other wavelengths and it seems that the association between the MIR and white light emission is common.

[1]Instituto Nacional de Astrofísica, Óptica y Electrónica, Puebla, México.

[2]Universidad Autónoma de Nayarit, Nayarit, México.

[3]Facultad de Ciencias de la Electrónica, Benemérita Universidad Autónoma de Puebla, Puebla, México.

[4]Instituto de Astronomía, Universidad Nacional Autónoma de México, México.

[5]Facultad de Físico-Matemáticas, Benemérita Universidad Autónoma de Puebla, Puebla, México.

[6]Peace-Corps México, Querétaro, Qro., México.

Until just a few years ago, the flux of solar flares was considered to reach a maximum at microwave frequencies, around 5-10 GHz, and to decrease toward higher frequencies. About a decade ago, flares were seen at 212 and 405 GHz (sub-THz range) noting that the flux grew with frequency (Kaufman et al. 2013). Various mechanisms have been proposed to explain this behavior. It could be due, for instance, to particles different from those responsible of the microwave emission, such as relativistic positrons generating synchrotron emission. However, the origin of this new spectral component of the solar flare emission is still under debate (Fleishman & Kontar 2010). In such flares also MIR has been detected, showing a time evolution similar to that at the sub-THz emission (Kaufmann et al. 2015).

The few MIR flares above described are the only ones reported. The MIR emission is considered to be of thermal origin. However, the similarity of the MIR time profiles with sub-THz profiles and other wavelength profiles (such as hard X-ray) indicates possible non-thermal emission.

Even though there are few observations at the MIR and sub-THz ranges, they provided interesting information about flares and showed that they are more complex than thought a few years ago. These frequence ranges can still give results for a better understanding of the solar activity, and of the Sun in general. To gain better insight into the emission mechanisms involved in the flare phenomena, requires more observations, in particular at the MIR wavelength range.

Astronomical observations at MIR wavelengths are limited by the high opacity of the Earth's atmosphere. In addition, the opacity is highly variable over several time-scales. In the observations, opacity fluctuations lead to variations that overplot the solar emission. As a result, flares and flux fluctuations of solar origin are more difficult to distinguish. Nevertheless, during winter, the opacity at high altitudes in central Mexico is low, and quite stable for time intervals longer than one hour (Pérez-León 2013). Solar flares last from a few minutes to about an hour. Therefore, at these sites, it is feasible to obtain more stable observations and to detect flares and, possibly, solar flux variations.

2. CHARACTERISTICS OF THE MIR TELESCOPE

We performed simulations of various telescope optical layouts with mirrors and lenses and analized the spot diagrams obtained. In some layouts with parabolic mirrors, the spots lie inside the Airy

Fig. 1. The Solar Infrared Telescope with the housings for the germanium and Mylar filters at the aperture. The Mylar filter is used for visible light observations.

disk, so that the spatial resolution is determined by the diffraction limit; however, they produce a coma distortion. Hyperbolic surfaces have a better performance. Hence, we selected a Ritchey-Chretien 6-inch telescope, whose plate scale is about $2.5''$/mm.

Various detectors were also analyzed, among them microbolometers and pyroelectric ones. A Melexis $16{\times}4$ pixels non-cooled pyroelectric array detector was used at the focal plane of the telescope (Figure 1). The field of view for the whole detector is of $9.6' \times 2.4'$ with a resolution of $36''$/pixel. This means that the field covered by the detector has a length, at the sides of the 16 pixels, of about 1/3 of the solar diameter.

Two germanium windows were used, the first with a diameter of 75 mm and a thickness of 5 mm. Mounted in a holder case this window has an apperture of 72 mm diameter. The second germanium window has a diameter of 12.5 mm and a thickness of 1 mm. The transmittance of the first window is 45% between 2μm and 25μm. For the second window, the transmittance is 95% between 8 and 12μm (Thorlabs, Inc., 2017, `www.thorlabs.com`). The sur-

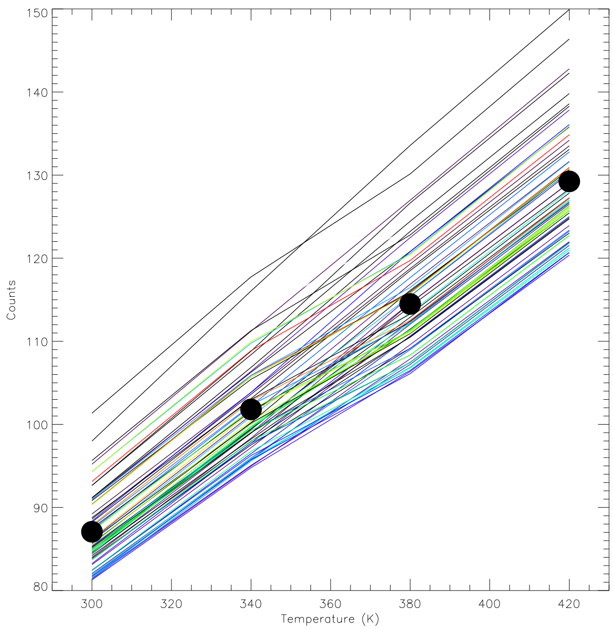

Fig. 2. The color lines represent counts versus temperature of the laboratory black-body for the 64 pixels of the detector. The circles are the 64 values averaged for each temperature. The color figure can be viewed online.

face of both sides of the first window is natural germanium. The second window has an anti-reflective coating on both sides to improve its transmission in the MIR. The combined transmittance of the two windows, operating in cascade, is about 42% for the spectral range from 8 to 12μm.

The control for the detector was developed using the Cypress PSoC (Programmable System-on-Chip) electronic interface board. The user interface software was written aiming to have an overall view of the observational information, such as time coordinates, detector data and images, in a single computer interface. The values given at the output of the electronics, displayed in the interface and recorded in the data files, are referred to as counts.

The control system of the telescope was developed based on the mounting control made by the Orion company. Various observational regimes were developed in the control software. They include, a scanning of the Sun at different NS and EW disk locations, a tracking of a given region of the Sun, and sky scans.

The mechanical supports for the filters and for the electronics of the detector have been constructed so that the detector and part of its electronics can be located inside an ocular tube near the focal plane of the telescope.

3. CALIBRATIONS

Measurements of the response of the detector pixels to a laboratory black-body were made. The counts given by each pixel of the detector for four black body temperatures were measured at the laboratory. For a given temperature, the black-body was scanned, in X-Y directions, by the detector, and the measuremententes were recorded. The maximum amplitude for each pixel was identified. This was done at the four temperatures of the black body.

For the 64 pixels of the detector the maximum amplitudes follow a linear relation with the black-body temperature (Figure 2). The maximum amplitudes recorded for each pixel allow us to know the detector flat-field response at each temperature.

The ratiation energy received at intervals of area da, frequency $d\nu$, solid angle $d\Omega$, during a time interval dt is given by

$$E \;=\; I_\nu \cos\theta \; da \; d\nu \; dt \; d\Omega \,, \tag{1}$$

where I_ν is the specific radiation intensity and θ is the angle between the normal to da and the direction of the incident radiation.

The laboratory black body was observed in a frequency band $\Delta\nu_{bb} = 1.25 \times 10^{13}$ Hz, an integration time $\tau = 1$ s, a solid angle $\Omega_{bb} = 6.93\times10^{-2}$ str, with an area per pixel of the detector $A_{det} = 4.0\times10^{-8}$ m^2 and with $\theta = 0°$. In terms of these parameters the received energy is

$$E_{bb} \;=\; I_\nu \; A_{det} \; \Delta\nu_{bb} \; \tau \; \Omega_{bb} \,. \tag{2}$$

In this case, I_ν is the specific intensity for a given temperature of the laboratory black body at the frequency ν . The counts obtained for the four laboratory black-body temperatures (300, 340, 380 and 420 K) are plotted in Figure 2. The averaged values, for each temperature are represented with circles.

The specific intensity is estimated for each black-body temperature using the Planck equation. Then, the energy is computed using equation 2 and the parameters of the laboratory black body observations, given above. The resulting energies are: 1.14×10^{-7}, 2.03×10^{-7}, 3.19×10^{-7} and 4.62×10^{-7} J. A two degree polynomial fitted to these energies and the corresponding average value in counts (for each temperature) results in

$$E = 1.57\times10^{-7} - 6.47\times10^{-9}\times C + 6.85\times10^{-11}\times C^2 \,, \tag{3}$$

where C is an observed value in counts, and E the corresponding energy in Joules.

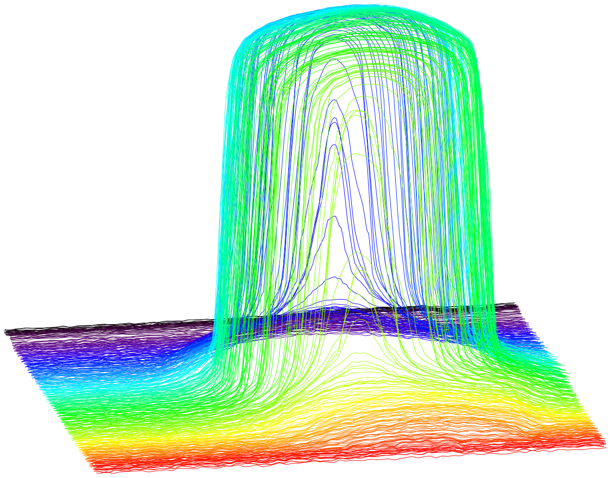

Fig. 3. Scans of the Sun taken with the solar telescope at different X, Y locations across the solar disk. The color figure can be viewed online.

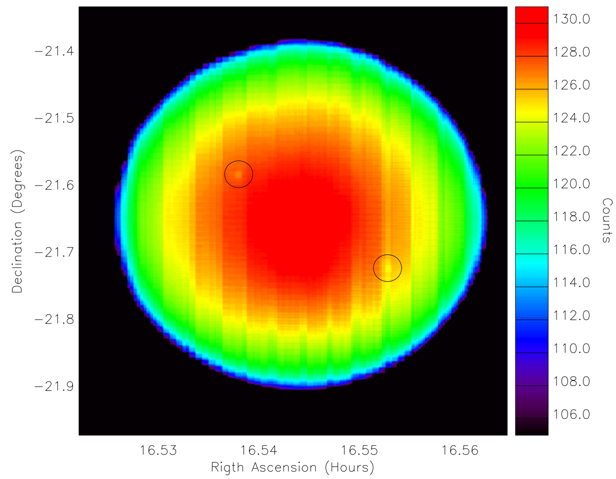

Fig. 4. Image made using the data of scans such as those of Figure 3. Two active regions are seen, one on the upper-left quadrant, denoted by the upper circle, and another active region on the lower-right quadrant of the disk, denoted by the lower circle. The color figure can be viewed online.

For the center of the quiet Sun a value of 130.5 counts was recorded. The corresponding energy, computed with the fitted polynomial (equation 3), is $E_s = 4.79 \times 10^{-7}$ J. To estimate the specific intensity that corresponds to this energy, we now use the parameters for the Sun observations, which are the aperture during the observations $A_{ap} = 4.07 \times 10^{-3}$ m^2, the solid angle covered by a detector pixel at the telescope focal plane $\Omega_s = 2.39 \times 10^{-8}$ str, the frequency band $\Delta\nu_s = 1.25 \times 10^{13}$ Hz, and the time integration $\tau = 1$ s. These values are substituted in equation 2, but now for E_s. The resulting specific intensity, considering an attenutation of 0.42 by the two germanium windows, is $1.143{\times}10^{-9}$ J Hz^{-1} s^{-1} m^{-2} str^{-1}, which corresponds, according to the black-body Planck equation, to a temperature of 4825 K. Since the field of view of a detector pixel pointing to the disk center is fully covered, then this corresponds to the brightness temperature. This value is similar to the numbers reported in other works for similar wavelengths. For example, Shimabukuro & Stacey (1968) give 5036 K at 11.1μm and 5160 K at 8.63μm. From these values, one may expect a brightness temperature of about 5100 at 10μm. However, Trottet et al. (2015) applied a model of the quiet Sun to estimate the brightness temperature, obtaining 4700 K. Also, using two flare atmospheric models, they obtained brightness temperatures of 4900 and 5000 K prior to the beginning of the flare. Our value is similar to those obtained in other works.

4. OBSERVATIONS

Figure 3 shows curves obtained by scanning the solar disk at different EW locations on the Sun. An image obtained by scans like these is shown in Figure 4, where two active regions (AR) are seen, one on the upper-left quadrant and another on the lower-right quadrant of the solar disk. In Figure 5 a solar scan shows the quiet Sun and also the AR seen on the upper-left quadrant of Figure 4. A decrease of the amplitude at the location of this AR is seen. This decrease is about 0.008 of the quiet Sun amplitude. By computing the standard deviation around the disk center, it was found that the signal to noise ratio is ≈ 1000. Then, the sensitivity is of 4.8 K.

The Trottet et al. (2015) estimations of the excess brightness temperature during the maximum of the flare they observed at 10μm are 200 and 300 K, respectively, for the two flare models, which correspond to 0.041 and 0.060 of the quiet Sun brightness temperature. The amplitude we are able to detect, at 1σ, is 0.001 of the quiet Sun. Hence, we could detect a flare as that observed by Trottet et al. (2015), and also as that observed by Penn et al. (2016), whose maximum amplitudes at 8.6 and 4.9μm, relative to the quiet Sun, are 0.032 and 0.023, respectively.

One of the purposes of developing a portable telescope is to temporarily install it at high altitude sites, where the atmospheric opacity is low, to conduct observation campaigns. Also, to use it in expe-

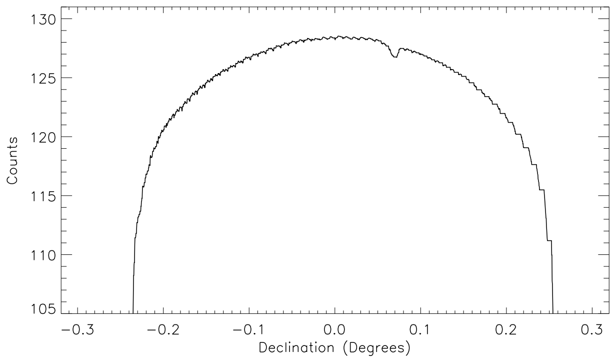

Fig. 5. North-South scan of the Sun across the active region seen on the upper-left quadrant of the disk (Figure 4).

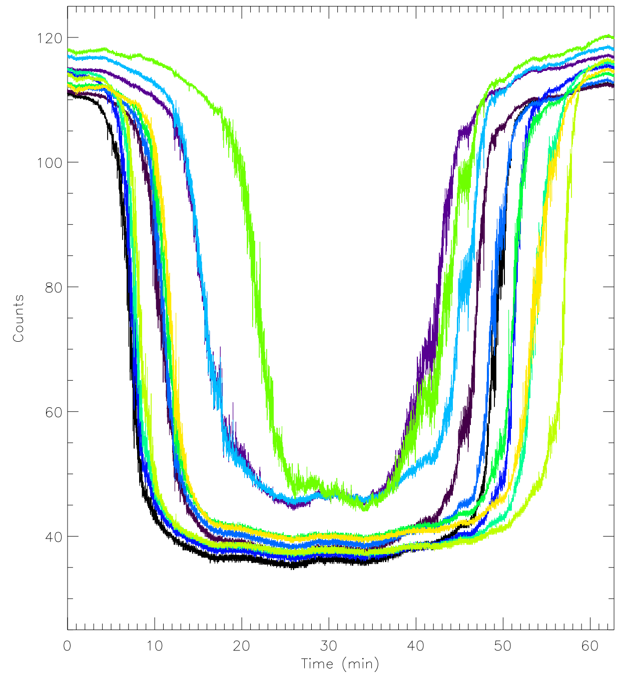

Fig. 6. Time curves of the amplitude recorded at various pixels during the 21 August 2017 eclipse. The time is given in minutes from T_{loc}=13:19:55, local time, which is T_{loc} =T_{UTC}-5. It may be seen that at some pixels the amplitude drops to lower values while at others it remains near the level previous to the eclipse. The color figure can be viewed online.

ditions for solar eclipse observations. We observed the August 21, 2017 solar eclipse. In Figure 6, the time curves obtained for various pixels during the eclipse are shown. It may be seen that the amplitude decreased to a low value, where it remained during the eclipse time, and then again increased to the level previous to the eclipse. Further studies of the solar limb could be done based on solar eclipse data, since the spatial resolution can be improved and complemented with data of scans of the quiet Sun. With the present sensitivity we are able to detect flares, as those above described. It can be better at sites with low atmospheric opacity. We are also developing a camera to estimate the atmospheric opacity at the same wavelength.

5. CONCLUSIONS

A mid infrared solar telescope centered at 10μm was developed with a 6-inches Ritchey-Cretien optical system by using a 4×16 pixels pyroelectric detector at its focal plane. Under the conditions of the preliminary observations here reported, we reached a sensitivity of about ≈ 1000 of the quiet Sun. The spatial resolution was of $36''$.

We acknowledge the technical team of UNAM at Tonantzintla observatory for their help during two observation campaigns.

REFERENCES

Fleishman, G. D. & Kontar, E. 2010, ApJ, 709, L127
Hudson, H. S. 1975, SoPh, 45, 69
Kaufman, P., Raulin, J-P., Giménez de Castro, C. G., et al. 2004, ApJ, 603, L121
Kaufmann, P., Abrantes, A., Bortolucci, E. C., et al. 2012, SPIE 8442, Space Telescopes and Instrmentation 2012: Optical, Infrared and Millimeter Wave
Kaufmann, P., White, S. M., Freeland, S. L., et al. 2013, ApJ, 768, 134
Kaufmann, P., White, S. M., Marcon, R., et al. 2015, JGRA, 120, 4155
Melo, A. M., Kaufmann, P., Kudaka, A. S. et al. 2006, PASP, 118, 1558
Ohki, K. & Hudson, H. S. 1975, SoPh, 43, 405
Penn, M., Krucker, S., Hudson, H., et al. 2016, ApJ, 819, L30
Pérez-León, J. E. 2013, PhD Thesis, IA UNAM, México
Shimabukuro, F. I. & Stacey, J. M. 1968, ApJ, 152, 777
Trottet, G., Raulin, J.-P., Mackinnon, A., et al. 2015, SoPh, 290, 2809

M. O. Arias-Estrada, J. E. Mendoza-Torres, P. Rodríguez-Montero, B. Rodríguez-Pedroza, and M. Velázquez-de-la-Rosa: Instituto Nacional de Astrofísica, Óptica y Electrónica, Calle Luis Enrique Erro No.1, Sta. María Tonantzintla, Puebla, CP 72840, México (ariasmo, mend, ponciano@inaoep.mx, bere_1103@hotmail.com, miyang@inaoep.mx).

A. De-Roa-Campoy, I. Gómez-Arista, and E. Valadez-Campos: Facultad de Ciencias de la Electrónica, Benemérita Universidad Autónoma de Puebla, Av. San Claudioy 18 Sur, Puebla, Pue., CP 72570, México (deroa.201005111@gmail.com, ivan.goar@gmail.com, e_valadez89@outlook.com).

K. Gottschalk: Peace Corps México, Avenida Universidad 202, Centro, Santiago de Querétaro, Qro., CP 76000, México (kgottsch2001@yahoo.com).

M. Juárez-Gama: Facultad de Ciencias Físico-Matemáticas, Benemérita Universidad Autónoma de Puebla, Av. San Claudio y 18 Sur, Puebla, Pue., CP 72570, México (mariana.gama60@gmail.com).

I. C. Medina-Carrillo and J. S. Palacios-Fonseca: Universidad Autónoma de Nayarit, Ciudad de la Cultura “Amado Nervo”, Tepic, Nayarit, CP 63155, México (isabel.medina@uan.edu.mx, espectroku@hotmail.com).

J. Peña-Saint-Martín: Instituto de Astronomía, Universidad Nacional Autónoma de México, Circuito de la Investigación Científica s/n, CU, Coyoacán, Ciudad de México, CP 04510, México (jhpena@astro.unam.mx).

Revista Mexicana de Astronomía y Astrofísica, **55**, 17–19 (2019)

EXACT SOLUTION FOR FLAT SCALE-INVARIANT COSMOLOGY

J. F. Jesus[1,2]

Received August 30 2018; accepted October 9 2018

ABSTRACT

An exact solution for the spatially flat scale-invariant cosmology, recently proposed by Maeder (2017a) is deduced. No deviation from the numerical solution was detected. The exact solution yields transparency for the dynamical equations, and faster cosmological constraints may be performed.

RESUMEN

Se obiene una solución exacta para la cosmología espacialmente plana de escala invariante propuesta recientemente por Maeder. No se encuentran diferencias respecto a la solución numérica. La solución exacta le da transparencia a las ecuaciones dinámicas y permite obtener límites cosmológicos más rápidamente.

Key Words: cosmology: theory — dark energy — dark matter

1. INTRODUCTION

Recently, Maeder (2017a) proposed that the accelerating expansion of the Universe (Riess et al. 1998; Permultter et al. 1999) may be explained by the scale invariance of the empty space. It was argued that in empty space there is no preferred scale of length or time. He applied the theoretical framework developed for a scale-invariant theory of gravitation (Weyl 1923; Eddington 1923; Dirac 1973; Canuto et al. 1977) and found, as a result, that the effects of scale invariance are smaller when there is a greater quantity of matter present in the Universe.

This model has some interesting consequences. The cosmological constant, for example, is replaced by a variable term involving the scale-invariant scale factor. There is no need for a cosmological constant nor for dark energy in this context. The scale-invariant effects over the CMB temperature $T_{CMB}(z)$ were analysed by Maeder (2017b), where he found that if galactic corrections are applied, scale invariance may not be discarded. By analysing the Milky Way rotation curve in the context of scale invariant model, Maeder (2017c) argued that the flat rotation curves may be seen as an age effect and indicated that no dark matter was needed in this theoretical context.

This paper is focused on finding exact solutions of his equation of cosmological dynamics. Exact solutions provide transparency for the cosmological equations, may provide insights and can be used for a faster determination of cosmological constraints.

In § 2 the equations of the scale-invariant cosmology are briefly discussed. In § 3, the exact solution for the spatially flat scale-invariant cosmology is deduced and compared with the numerical results by Maeder (2017a). In § 4, the conclusions are presented.

2. SCALE-INVARIANT COSMOLOGY

Maeder (2017a) shows that the general relativity (GR) metric is related to the scale-invariant one by $ds' = \lambda(x^\mu)ds$, where λ is the scale factor which connects both line elements. By applying this theory to the empty space, he finds that λ relates to the Einstein's cosmological constant, Λ_E, by

$$\lambda = \sqrt{\frac{3}{\Lambda_E}}\frac{1}{ct}\,, \tag{1}$$

where c is the speed of light, which will be assumed to be unity elsewhere.

By applying the Robertson-Walker metric to a Universe filled with pressureless matter, he finds for the scale-invariant cosmology:

$$\dot{R}^2Rt - 2\dot{R}R^2 + kRt - Ct^2 = 0\,, \tag{2}$$

where R is the scale factor, time is expressed in units of $t_0 = 1$, k is the curvature constant, which can be 0,

[1]Universidade Estadual Paulista (UNESP), Campus Experimental de Itapeva, Brazil.

[2]Universidade Estadual Paulista (UNESP), Faculdade de Engenharia, Guaratinguetá, Departamento de Física e Química, Brazil.

-1 or $+1$ for a spatially flat, open or closed Universe, respectively, $C = \frac{8\pi G\rho_m R^3\lambda}{3}$ and ρ_m is the density of pressureless matter. The density parameters are defined in the usual form, $\Omega_m \equiv \frac{\rho}{\rho_c}$, where $\rho_c = \frac{3H^2}{8\pi G}$, $\Omega_k = -\frac{k}{R^2H^2}$, but Ω_Λ is now replaced by Ω_λ:

$$\Omega_\lambda \equiv \frac{2}{Ht}\,, \tag{3}$$

such that the normalization condition:

$$\Omega_m + \Omega_k + \Omega_\lambda = 1\,, \tag{4}$$

is valid.

Our focus here is to find exact solutions of (2). As nonflat exact solutions could not be found, we aim to solve the case where $k = 0$.

3. FLAT SCALE-INVARIANT COSMOLOGY

For the spatially flat Universe, the equation for scale-invariant Universe evolution (2) reads:

$$\dot{R}^2Rt - 2\dot{R}R^2 - Ct^2 = 0\,, \tag{5}$$

where the time is expressed in units of $t_0 = 1$, and it is assumed that $R_0 = 1$. By evaluating (5) today, the relation for the Hubble constant $H_0 = \frac{\dot{R}_0}{R_0}$ is $H_0^2 - 2H_0 = C$. This yields $H_0 = 1 \pm \sqrt{1+C}$ and we choose the positive sign since the Universe is expanding ($H_0 > 0$).

In order to solve (5), we replace $R(t)$ by $R(t) = tv(t)$, so:

$$\dot{R} = v + t\dot{v}\,, \tag{6}$$

and (5) may be written as:

$$\dot{v}^2 = \frac{v^3 + c}{vt^2} \Rightarrow \dot{v} = \pm\sqrt{\frac{v^3+c}{vt^2}}\,. \tag{7}$$

So, we have to choose a sign for $\dot{v}$ in order to integrate the separable equation (7). From (6), we have:

$$\dot{v} = \frac{R}{t^2}(Ht - 1)\,. \tag{8}$$

In such a way that we have $\dot{v}_0 = H_0 - 1 = \sqrt{1+C}$. So, we choose the positive sign in (7) in order to integrate it from the present time. The result is:

$$\sqrt{v^3 + C} + v^{3/2} = c_1 t^{3/2}\,, \tag{9}$$

where c_1 is an integration constant. From (9), we find

$$c_1 = 1 + \sqrt{1+C} = H_0\,. \tag{10}$$

We want to solve (9) for $v(t)$ in order to write $R(t)$. We write $v^{3/2} = c_1t^{3/2} - \sqrt{v^3+C}$ and square both sides. The result is:

$$v = \left[\left(\frac{c_1^2t^3 - C}{2c_1t^{3/2}}\right)^2\right]^{1/3}\,. \tag{11}$$

Before writing the power as $2/3$ in (11), there was an ambiguity sign inside the parentheses after we squared the expression (9). We must choose the sign which is in agreement with the initial condition (10). By choosing the negative sign inside the parentheses, we find $c_1 = -1 \pm \sqrt{1+C}$, which are both in disagreement with (10). By choosing the positive sign, we find $c_1 = 1 \pm \sqrt{1+C}$, where there is a solution in agreement with (10), so we choose the positive sign and:

$$v = \left(\frac{c_1^2t^3 - C}{2c_1t^{3/2}}\right)^{2/3}\,. \tag{12}$$

Now:

$$R = tv = \left[\frac{(2H_0 + C)t^3 - C}{2H_0}\right]^{2/3}\,, \tag{13}$$

where we have replaced the value of c_1. As explained by Maeder (2017a) and shown in equations (3)-(4), in a flat scale invariant cosmology, Ω_m can be written today as:

$$\Omega_m + \frac{2}{H_0t_0} = 1\,; \tag{14}$$

then $H_0 = \frac{2}{1-\Omega_m}$ in units of t_0 and $C = \frac{4\Omega_m}{(1-\Omega_m)^2}$. So, by writing (13) in terms of Ω_m:

$$R = \left[\frac{t^3 - \Omega_m}{1 - \Omega_m}\right]^{2/3}\,. \tag{15}$$

In Figure 1 we show some evolutions of the scale factor for different values of the density parameter, based on equation (15). It may be compared with Figure 2 of (Maeder 2017a), where the solutions were numerically obtained. No difference may be found between the exact and the numerical results.

As can be seen in Figure 1 and equation (15), with time in units of t_0 there is an initial time, t_{in}, where $R = 0$. From (15), this time is:

$$t_{in} = t_0\Omega_m^{1/3}\,. \tag{16}$$

From this we may write for the total age of the Universe, $\tau_0 = t_0 - t_{in}$:

$$\tau_0 = (1 - \Omega_m^{1/3})t_0 = \frac{2}{H_0}\frac{1 - \Omega_m^{1/3}}{1 - \Omega_m}\,. \tag{17}$$

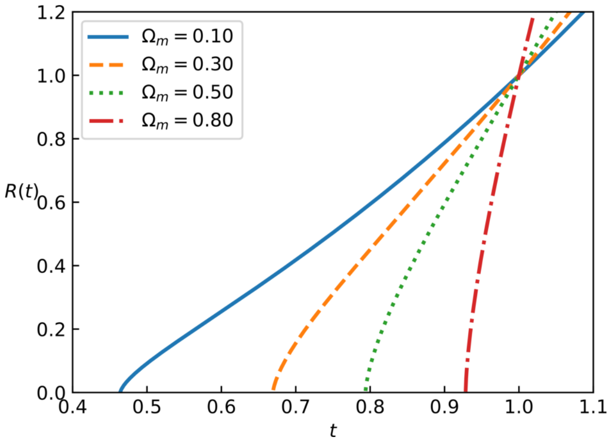

Fig. 1. Scale factor $R(t)$ for some values of the matter density parameter in the flat scale-invariant cosmology. The color figure can be viewed online.

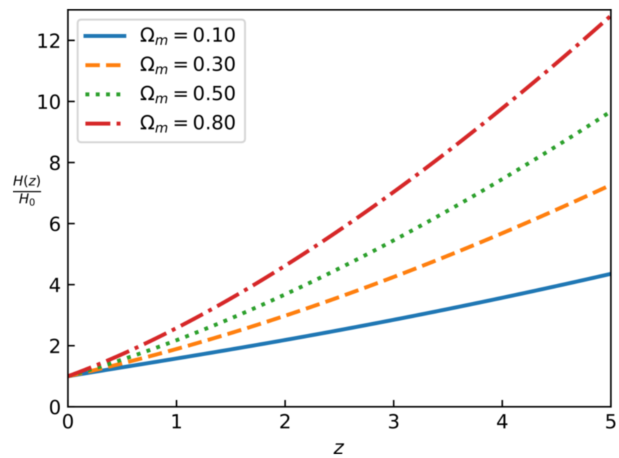

Fig. 2. Hubble parameter $H(z)$ for some values of the matter density parameter in the flat scale-invariant cosmology. The color figure can be viewed online.

By solving (15) for time, we may write for the age at redshift z, $\tau(z) = t(z) - t_{in}$:

$$\tau(z) = \frac{2}{H_0(1-\Omega_m)}\left\{[\Omega_m + (1-\Omega_m)(1+z)^{-3/2}] - \Omega_m^{1/3}\right\}. \tag{18}$$

Calculating $H = \frac{\dot{R}}{R}$ from (15), we find:

$$H(t) = \frac{2t^2}{t^3 - \Omega_m}\,. \tag{19}$$

We solve equation (15) for time, then replace in (19) to find:

$$\begin{aligned} H &= \frac{2[\Omega_m + (1-\Omega_m)R^{3/2}]^{2/3}}{(1-\Omega_m)R^{3/2}} \\ &= H_0[\Omega_m R^{-9/4} + (1-\Omega_m)R^{-3/4}]^{2/3}, \end{aligned} \tag{20}$$

or, in terms of redshift z:

$$H = H_0[\Omega_m(1+z)^{9/4} + (1-\Omega_m)(1+z)^{3/4}]^{2/3}. \tag{21}$$

In Figure 2 is plotted $H(z)$ for some values of the matter density parameter from equation (21).

From equations (15), (18) and (21) the results of Tables 1 and 2 of Maeder (2017a) can be recovered. No difference between analytical and numerical results could be found.

4. CONCLUSION

An interesting theory of scale-invariant cosmology was recently proposed. While the original focus was on the numerics, here we focus on finding an exact solution, at least for the spatially flat case. We show that our exact solution does not deviate from the original numerical solution. Physical insights about the dynamical equations may now be developed and cosmological constraints can be obtained faster.

JFJ is supported by Fundação de Amparo à Pesquisa do Estado de São Paulo - FAPESP (Process no. 2017/05859-0).

REFERENCES

Canuto, V., Adams, P. J., Hsieh, S. H., & Tsiang, E. 1977, PhRvD, 16, 1643
Dirac, P. A. M. 1973, RSPSA, 333, 403
Eddington, A. S. 1923, The Mathematical Theory of Relativity (1st ed,; Cambridge: MA: CUP)
Maeder, A. 2017a, ApJ, 834, 194
__________. 2017b, ApJ, 847, 65
__________. 2017c, ApJ, 849, 158
Perlmutter, S., et al. 1999, ApJ, 517, 565
Riess, A. G., et al. 1998, ApJ, 116, 1009
Weyl, H. 1923, Raum, Zeit, Materie. Vorlesungen über allgemeine Relativitätstheorie (Berlin: Springer)

J. F. Jesus: Universidade Estadual Paulista (UNESP), Campus Experimental de Itapeva, R. Geraldo Alckmin, 519, 18409-010, Itapeva, SP, Brazil (jfjesus@itapeva.unesp.br).

Revista Mexicana de Astronomía y Astrofísica, **55**, 21–30 (2019)

EXTENSIVE PHOTOMETRY OF V1838 AQL DURING THE 2013 SUPEROUTBURST

J. Echevarría[1], E. de Miguel[2], J. V. Hernández Santisteban[3], R. Michel[4], R. Costero[1], L. J. Sánchez[1], A. Ruelas-Mayorga[1], J. Olivares[5], D. González-Buitrago[6], J. L. Jones[7], A. Oskanen[8], W. Goff[9], J. Ulowetz[10], G. Bolt[11], R. Sabo[12], F.-J Hambsch[13], D. Slauson[14], and W. Stein[15]

Received August 8 2018; accepted October 24 2018

ABSTRACT

We present an in-depth photometric study of the 2013 superoutburst of the recently discovered cataclysmic variable V1838 Aql and subsequent photometry near its quiescent state. A careful examination of the development of the superhumps is presented. Our best determination of the orbital period is $P_{\rm orb} = 0.05698(9)$ days, based on the periodicity of early superhumps. Comparing the superhump periods at stages A and B with the early superhump value we derive a period excess of $\epsilon = 0.024(2)$ and a mass ratio of $q = 0.10(1)$. We suggest that V1838 Aql is approaching the orbital period minimum and thus has a low-mass star as a donor instead of a substellar object.

RESUMEN

Presentamos un estudio fotométrico detallado de la super-erupción de V1838 Aql, una variable cataclísmica recientemente descubierta, desde el máximo en 2013 hasta su regreso al mínimo. Examinamos en detalle la evolución de las superjorobas (*superhumps*). Determinamos el período orbital $P_{\rm orb} = 0.05698(9)$ días a partir de la periodicidad de las superjorobas tempranas. Comparando los períodos de las superjorobas en las etapas A y B con el valor del período orbital, derivamos un valor del cambio en el período orbital de $\epsilon = 0.024(2)$ y un cociente de masa para el sistema de $q = 0.10(1)$. Sugerimos que V1838 Aql se está acercando al mínimo período orbital, por lo que la secundaria sería una estrella de baja masa y no un objeto sub-estelar.

Key Words: techniques: photometric — stars: novae, cataclysmic variables — stars: dwarf novae — stars: individual: V1838 Aql

1. INTRODUCTION

Cataclysmic variables (CVs) are close binary systems in which a white dwarf (WD) accretes from a low-mass star via Roche-lobe overflow, often creating an accretion disc (for a review see Warner 1995). A large fraction of CVs belong to the subclass of dwarf novae (DNe). They undergo recurrent outbursts with typical amplitudes of $\approx 2 - 6$ mag in the optical, which are commonly accepted to be caused by a thermal-viscous instability in the disc (Osaki 1974). In addition, SU UMa-type DNe (the subclass of DNe systems with short orbital periods, $P_{\rm orb} < 2.5$ hr) exhibit occasional eruptions that are less frequent, longer lasting, and slightly brighter (by $\approx 0.5 - 1.0$ mag) than the normal out-

[1]Instituto de Astronomía, Universidad Nacional Autónoma de México, México.
[2]Departamento de Ciencias Integradas, Universidad de Huelva, Huelva, Spain.
[3]Anton Pannekoek Institute for Astronomy, University of Amsterdam, Amsterdam, The Netherlands.
[4]Instituto de Astronomía, Universidad Nacional Autónoma de México, Ensenada, Baja California, México.
[5]Laboratoire d'astrophysique de Bordeaux, Univ. Bordeaux, Pessac, France.
[6]Departament of Physics and Astronomy, University of California, Irvine, CA, USA.
[7]CBA-Oregon, Jack Jones Observatory, Aurora, OR, USA.
[8]CBA-Finland, Hankasalmi Observatory, Muurame, Finland.
[9]CBA-California, Sutter Creek, CA, USA.
[10]CBA-Illinois, Northbrook Meadow Observatory, Northbrook, IL, USA.
[11]CBA-Australia, Craigie, Western Australia, Australia.
[12]CBA-Montana, Bozeman, MT, USA.
[13]CBA-Mol, Andromeda Observatory, Mol, Belgium.
[14]CBA-Iowa, Owl Ridge Observatory, IA, USA.
[15]CBA-Las Cruces, Las Cruces, NM, USA.

bursts. The key feature during these so-called superoutbursts is the presence of superhumps a modulation in the light curve with an underlying periodicity, $P_{\rm sh}$, a few percent longer than the orbital period. They are thought to arise from a precessing non-axisymmetric disc (Vogt 1982), with the eccentricity being produced by the tidal instability developed at the radius of the 3:1 resonance (Whitehurst 1988). The analysis of the timing and evolution of such light oscillations provides estimates of the system's parameters using empirical (Patterson et al. 2005) and theoretical (Kato & Osaki 2013) relationships between the superhump/orbital period excess, $\epsilon \equiv (P_{\rm sh} - P_{\rm orb})/P_{\rm orb}$, and the binary mass ratio $q \equiv M_2/M_1$. Several $\epsilon(q)$ relations have been proposed by these authors based on different stages of the superhumps, although Otulakowska-Hypka et al. (2016) show that the scatter in the ϵ-q diagram is considerable for very short orbital periods. This is due to a lack of objects with dynamically confirmed small values of q (Patterson 2011; Kato & Osaki 2013).

Among the SU UMa–type systems, there is a large group that accumulates around the minimum of the orbital period distribution of CVs ($P_{\rm orb} \approx 78$ min) (Paczynski & Sienkiewicz 1981; Gänsicke et al. 2009; Knigge et al. 2011). These are binaries with extremely low mass-transfer rates, named WZ Sge-type objects, which are characterised by rare (commonly detected every $\approx$ 10 years), and large amplitude superoutbursts of duration of ≈ 30 days, caused by an instability in low viscosity accretion discs with $\alpha \approx 0.01 - 0.001$ (Smak 1993; Osaki 1994). Some of them are systems currently evolving towards longer periods and are collectively known as period bouncers (e.g. Littlefair, Dhillon & Martin 2003). These binaries are expected to harbour a substellar secondary companion (Howell et al. 1997), i.e. brown dwarfs (e.g. Littlefair et al. 2006; Harrison 2016; Hernández Santisteban et al. 2016; Neustroev et al. 2017).

Worth noting is that WZ Sge-type objects are characterised not only by a long superoutburst recurrence time in comparison to typical SU UMa stars, but also by the presence of early superhumps (double-wave modulation) during the first few days of the eruption, with a periodicity ($P_{\rm esh}$) essentially equal to the orbital period of the binary (details in O'Donoghue et al. 1991; Kato 2015). The advent of all-sky surveys (e.g. Breedt et al. 2014) and worldwide citizen-telescope networks has contributed to the discovery of a large population of faint DNe. Among these discoveries, the elusive population of short-period systems, in particular period bouncers, has been found and investigated (Patterson 2011; Coppejans et al. 2016; Otulakowska-Hypka et al. 2016).

The discovery of a new transient, initially proposed as possible nova, was reported by Itagaki on 2013 May 31. Henden[16] pointed out that the colour indices of the object and the un-reddened field suggested a DN rather than a nova. As pointed out by Hurst[17], Kojima reported a pre-discovery image on 2013 May 30.721 UT, when the magnitude was at about 9.8 mag (un-filtered). A CBET report of this new DNe in Aquila, can be found in Itagaki (2013).

Although a preliminary analysis of the behaviour of V1838 Aql (originally designated as PNV J19150199+0719471) was published by Kato et al. (2014), we present here a full analysis of the superhump behaviour based on our extensive data.

In § 2 we present the observations and their reduction methods. The photometric data and the period analysis are presented in § 3, while in § 4 we address the discussion of our results. We present our conclusions in § 5.

2. OBSERVATIONS AND REDUCTION

Photometric observations in the V band were obtained in 2013 during the nights of June 3, 4, 5, 6, 17, 18, 28 and September 2 and 25 at the 0.84 m telescope of the Observatorio Astronómico Nacional at San Pedro Mártir (SPM). We used the Blue-ESOPO CCD detector[18] on a 2×2 binning configuration. The exposure time of the SPM observations varied between 10 and 30 s. In addition, time-series photometry of the superoutburst was obtained from 10 observatories of the Center for Backyard Astrophysics (CBA) –a network of small ($0.2 - 0.4$ m) telescopes that covers a wide range in terrestrial longitude. Skillman & Patterson (1993) and de Miguel et al. (2016) describe the methods and observing stations of the CBA network. These observations amounted to 162 separate time-series during 58 nights from June 1 to August 2, 2013, and the typical exposure time ranged from 20 to 120 seconds, depending on the brightness of V1838 Aql. Nearly half of these observations were obtained in V light, while the rest (mainly during the post-outburst regime) were unfiltered. We did not attempt any absolute calibration of the data during the eruption, but the magnitude scale is expected to resemble

[16]http://ooruri.kusastro.kyoto-u.ac.jp/mailarchive/vsnet-alert/15772).

[17]www.theastronomer.org/tacirc/2013/e2919.txt.

[18]http://www.astrossp.unam.mx/indexspm.html.

closely V magnitudes with a zero-point uncertainty of ≈ 0.05 mag. Further observations in the R band using the 2.1 m telescope at SPM during 2018, July 18 were conducted. Unfortunately, the weather was unstable and we only managed to obtain differential photometry over three orbital cycles. In the following, we report times and refer to specific dates in a truncated form defined as HJD $- 2,456,000$.

3. PHOTOMETRY AND PERIOD ANALYSIS

3.1. *Photometric Observations*

Most of our photometric observations come from the CBA network, with additional V-band observations obtained with the 0.84 m telescope at SPM at some critical stages of the outburst and during the late decline.[19] We observed the typical pattern seen in SU UMa stars during superoutburst: a plateau phase –lasting $\approx$ 25 days, from HJD 444 to 469– where the mean brightness varied smoothly from 10.5 to 13.0 mag, followed by a rapid decline ($\approx$ 3 mag in 2 days) at the end of the main eruption. The subsequent fading towards quiescence occurred at a rather low rate ($\approx$ 0.035 mag d^{-1}), and even 3.5 years after the end of the eruption, the system was found to be $\approx$ 0.5 mag above the pre-eruption quiescent brightness. However, based on the observations obtained with the NTT telescope (La Palma, Spain), we confirmed that the object had reached the pre-outburst level by June 2017. These observations and the general spectral distribution at quiescence have no further relevance here and will be discussed in a future publication.

3.2. *Full Analysis of the Different Stages of the Superhump*

Our primary tool for studying periodic signals was the Period 04 package (Lenz & Breger 2005). First, we subtracted the mean and (linear) trend from each individual light curve and formed nightly-spliced light curves. Then, after combining light curves from adjacent nights, a search for periodic signals was done. This approach allows us to improve the frequency resolution, but it has to be implemented with caution, since variations in the amplitude and/or the period of the modulation –both effects known to afflict erupting DNe– can distort the outcome of the frequency analysis.

A general view of the superhump transitions can be looked up by identifying the different stages of the superhumps: early superhumps, Stages A, B and C as well as the post-outburst stage (see Kato et al. 2009, 2014, for this terminology in our general discussion). Thus, we looked at the time variations of the superhump period and its amplitude by examining the variation in time with respect to a well-defined feature of the superhump signal.

[19] All CBA and SPM data are available on request.

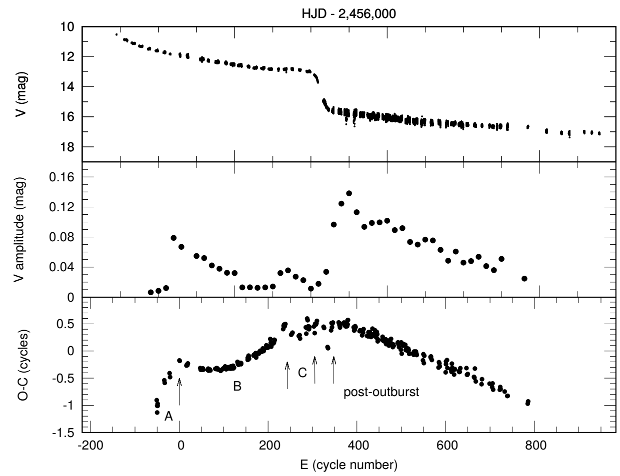

Fig. 1. Photometric behaviour of V1838 Aql during its superoutburst in 2013. Top frame: global light curve of the observational campaign. Middle frame: amplitude variations of the superhumps along the superoutburst (see text). Bottom frame: O–C diagram for the superhump maxima in the HJD 449.6–498.6 day interval with respect to the ephemeris given in equation (1). The arrows indicate the (approximate) location of transitions between different regimes of superhump period variations (see text).

After this general analysis, a detailed explanation of these stages was made. First, we derived the timings of superhump maxima. A total of 310 times of superhump maxima was identified in the light curves in the interval HJD 449.6–498.6 days. These maxima are shown in Table 1. The early stage of the eruption was not considered, since the signal there was of very low amplitude and individual maxima were not well defined. A linear regression to these timings provides the following test ephemeris:

$$T_{\max}(\mathrm{HJD}) = 2,456,452.8035(23) + 0.058191(6)\,E\,. \tag{1}$$

The top panel of Figure 1 displays the general photometric behaviour of the system during our campaign. Next, on the middle panel of Figure 1 is presented the variation of the amplitude of the superhump modulation, defined as the semi-amplitude of the sine wave that best fits the nightly photometric data.

TABLE 1

TIMES OF SUPERHUMP MAXIMA OF V1838 Aql DURING THE 2013 SUPEROUTBURST.[a]

E[b]	T_max[c]	O-C[d]	E[b]	T_max[c]	O-C[d]	E[b]	T_max[c]	O-C[d]	E[b]	T_max[c]	O-C[d]
-51	449.7831	-0.906	116	459.5372	-0.283	189	463.8032	0.028	345	472.9088	0.506
-50	449.8282	-1.131	116	459.5365	-0.295	190	463.8598	-0.001	346	472.9681	0.524
-50	449.8354	-1.007	117	459.5944	-0.301	190	463.8607	0.016	359	473.7247	0.527
-49	449.8934	-1.011	117	459.5939	-0.309	195	464.1540	0.056	360	473.7820	0.511
-49	449.8956	-0.972	118	459.6513	-0.322	196	464.2150	0.104	361	473.8381	0.474
-34	450.7936	-0.541	120	459.7703	-0.278	197	464.2728	0.097	362	473.8938	0.431
-33	450.8491	-0.586	121	459.8289	-0.271	198	464.3288	0.060	363	473.9561	0.502
-22	451.4995	-0.410	122	459.8842	-0.320	199	464.3889	0.092	371	474.4228	0.523
-21	451.5535	-0.481	123	459.9432	-0.307	200	464.4455	0.065	372	474.4782	0.475
0	452.7934	-0.174	131	460.4149	-0.200	205	464.7456	0.222	373	474.5387	0.514
1	452.8512	-0.181	132	460.4708	-0.239	206	464.7997	0.151	374	474.5940	0.464
16	453.7190	-0.268	132	460.4718	-0.223	207	464.8537	0.080	375	474.6515	0.453
17	453.7782	-0.250	133	460.5281	-0.254	212	465.1482	0.141	376	474.7119	0.490
18	453.8358	-0.261	133	460.5286	-0.247	213	465.2072	0.154	377	474.7702	0.492
19	453.8959	-0.228	134	460.5883	-0.220	214	465.2684	0.205	377	474.7705	0.497
47	455.5203	-0.313	134	460.5883	-0.220	215	465.3263	0.201	377	474.7706	0.500
48	455.5766	-0.345	135	460.6459	-0.231	234	466.4437	0.403	378	474.8263	0.456
49	455.6356	-0.331	136	460.7049	-0.218	235	466.5055	0.465	378	474.8280	0.486
50	455.6938	-0.331	137	460.7625	-0.227	236	466.5650	0.488	379	474.8868	0.497
51	455.7512	-0.345	138	460.8201	-0.237	237	466.6212	0.453	379	474.8862	0.486
52	455.8099	-0.336	139	460.8780	-0.243	239	466.7401	0.497	379	474.8909	0.566
53	455.8690	-0.321	139	460.8787	-0.230	252	467.4850	0.298	380	474.9493	0.570
54	455.9259	-0.342	139	460.8792	-0.221	253	467.5438	0.309	393	475.6979	0.435
64	456.5073	-0.351	154	461.7554	-0.164	254	467.6029	0.324	394	475.7561	0.435
65	456.5671	-0.323	154	461.7576	-0.126	255	467.6619	0.338	394	475.7527	0.376
66	456.6232	-0.361	155	461.8140	-0.158	269	468.4730	0.277	395	475.8151	0.449
69	456.7989	-0.341	156	461.8764	-0.085	271	468.5903	0.292	395	475.8118	0.392
70	456.8561	-0.358	156	461.8756	-0.098	272	468.6448	0.229	395	475.8140	0.430
81	457.4979	-0.328	157	461.9311	-0.144	285	469.4134	0.436	396	475.8725	0.436
82	457.5560	-0.330	167	462.5166	-0.083	286	469.4648	0.320	396	475.8737	0.456
83	457.6146	-0.323	168	462.5755	-0.070	287	469.5288	0.420	397	475.9309	0.439
84	457.6733	-0.314	169	462.6334	-0.076	288	469.5973	0.598	406	476.4504	0.366
85	457.7303	-0.335	170	462.6916	-0.075	289	469.6537	0.567	407	476.5093	0.380
86	457.7893	-0.320	171	462.7489	-0.090	290	469.7051	0.451	411	476.7418	0.374
87	457.8469	-0.332	171	462.7500	-0.072	291	469.7620	0.428	412	476.7950	0.288
88	457.9044	-0.343	171	462.7514	-0.047	292	469.8186	0.400	413	476.8565	0.345
92	458.1365	-0.354	172	462.8101	-0.039	292	469.8215	0.450	414	476.9143	0.338
93	458.1941	-0.365	172	462.8074	-0.086	293	469.8789	0.437	415	476.9763	0.404
97	458.4284	-0.338	172	462.8078	-0.078	303	470.4617	0.452	423	477.4346	0.280
99	458.5459	-0.318	173	462.8644	-0.106	305	470.5709	0.329	425	477.5504	0.270
102	458.7208	-0.313	173	462.8635	-0.122	306	470.6391	0.501	426	477.6130	0.346
103	458.7807	-0.283	178	463.1596	-0.033	308	470.7548	0.489	427	477.6698	0.321
104	458.8372	-0.313	179	463.2169	-0.049	309	470.8143	0.510	429	477.7832	0.270
105	458.8942	-0.333	180	463.2767	-0.021	310	470.8750	0.554	429	477.7877	0.348
106	458.9522	-0.336	181	463.3344	-0.030	325	471.7415	0.446	430	477.8417	0.275
110	459.1872	-0.298	182	463.3946	0.005	326	471.7985	0.424	430	477.8434	0.305
111	459.2441	-0.321	184	463.5105	-0.003	334	472.2435	0.072	431	477.9022	0.315
112	459.3025	-0.316	185	463.5680	-0.015	335	472.3005	0.051	432	477.9570	0.257
113	459.3617	-0.300	186	463.6273	0.003	342	472.7271	0.381	435	478.1406	0.412
115	459.4778	-0.305	187	463.6863	0.019	343	472.7931	0.516	436	478.1927	0.308
115	459.4767	-0.323	188	463.7462	0.047	344	472.8467	0.437	437	478.2500	0.293

TABLE 1. CONTINUED

E[b]	T_max[c]	O-C[d]	E[b]	T_max[c]	O-C[d]	E[b]	T_max[c]	O-C[d]	E[b]	T_max[c]	O-C[d]
438	478.3092	0.310	482	480.8586	0.120	535	483.9315	-0.073	631	489.4996	-0.386
440	478.4235	0.273	483	480.9154	0.097	549	484.7405	-0.170	632	489.5580	-0.382
441	478.4880	0.381	492	481.4423	0.151	550	484.8051	-0.060	633	489.6199	-0.318
442	478.5401	0.277	493	481.5009	0.159	551	484.8538	-0.222	647	490.4349	-0.313
443	478.6004	0.313	494	481.5564	0.112	552	484.9199	-0.087	648	490.4859	-0.437
444	478.6549	0.251	495	481.6122	0.071	566	485.7333	-0.109	649	490.5440	-0.438
445	478.7189	0.351	499	481.8423	0.026	567	485.7904	-0.128	650	490.6030	-0.424
446	478.7747	0.309	500	481.9082	0.158	567	485.7921	-0.098	664	491.4146	-0.476
447	478.8253	0.179	501	481.9544	-0.048	569	485.9045	-0.166	665	491.4719	-0.493
447	478.8274	0.215	504	482.1375	0.098	584	486.7694	-0.303	666	491.5400	-0.322
457	479.4087	0.204	505	482.1974	0.127	585	486.8333	-0.206	668	491.6425	-0.560
458	479.4702	0.262	509	482.4295	0.116	586	486.8901	-0.229	681	492.3960	-0.611
460	479.5823	0.188	510	482.4819	0.017	587	486.9451	-0.285	682	492.4595	-0.520
461	479.6400	0.180	511	482.5406	0.025	600	487.6953	-0.392	699	493.4440	-0.602
464	479.8154	0.194	512	482.6006	0.056	601	487.7651	-0.193	705	493.7895	-0.665
465	479.8748	0.214	515	482.7719	-0.000	601	487.7622	-0.243	706	493.8516	-0.597
466	479.9279	0.127	516	482.8296	-0.008	603	487.8830	-0.167	707	493.9032	-0.711
470	480.1643	0.188	516	482.8326	0.042	604	487.9327	-0.312	722	494.7758	-0.715
471	480.2222	0.185	517	482.8892	0.015	612	488.3968	-0.337	723	494.8371	-0.662
472	480.2755	0.100	518	482.9433	-0.054	613	488.4523	-0.383	724	494.8931	-0.700
474	480.3975	0.197	526	483.4092	-0.047	614	488.5193	-0.231	733	495.4140	-0.747
475	480.4534	0.157	527	483.4678	-0.040	615	488.5730	-0.308	739	495.7585	-0.828
476	480.5116	0.157	528	483.5244	-0.068	618	488.7454	-0.347	740	495.8167	-0.828
477	480.5736	0.224	529	483.5860	-0.010	619	488.7985	-0.434	785	498.4271	-0.968
478	480.6261	0.125	532	483.7593	-0.032	620	488.8621	-0.341	786	498.4876	-0.929
480	480.7420	0.117	533	483.8188	-0.010	621	488.9207	-0.333			
481	480.7976	0.072	534	483.8748	-0.047	630	489.4422	-0.372			

[a]Individual errors in these timings are not explicitly included here.
[b]E (cycle number).
[c]Superhump maxima expressed as HJD - 2,456,000.
[d]O - C value (in cycles) according to the ephemeris.
T_max (HJD) = 2,456,452.8035 + 0.058191 E.

The O–C residuals of the times of maximum light relative to the ephemeris given by equation 1 are shown in the lower panel of Figure 1. The resulting O–C diagram is complex, but it displays a number of features that are usually observed in other SU UMa-type systems (Kato 2015). Among the most relevant features visible in this diagram we point out the following:

1. During the first four days of the outburst a weak modulation (early superhumps) with a period $P_{\rm esh} \approx 0.057$ d was visible in the light curve.

2. The onset of fully-grown (Stage A superhumps) took place in a short time-scale (≈ 2 d) and involved an increase in the amplitude of the modulations. Their (mean) period, $P_{\rm sh(A)} \approx 0.059$ d, was longer than $P_{\rm esh}$.

3. Once the superhump modulation reached full amplitude, the system entered Stage B where the amplitude of the superhump decreased slowly, and the mean period became shorter ($P_{\rm sh(B)} \approx 0.058$ d). The upward curvature of the residuals during this stage (days HJD 449–466) signifies that the period of the superhumps was not constant, but increased over time. From a quadratic fit of the residuals in this interval, we find an increase rate of $dP_{\rm sh(B)}/dt = 5.8(4) \times 10^{-5}$.

4. Before the end of the main eruption, the amplitude of the superhumps was found to grow larger (≈ 0.10 mag). The system entered Stage C, extending from day HJD 466 to the end of the main plateau (around day HJD 470), where the period of the superhump remained essentially constant ($P_{\rm sh(C)} \approx 0.0582$ d).

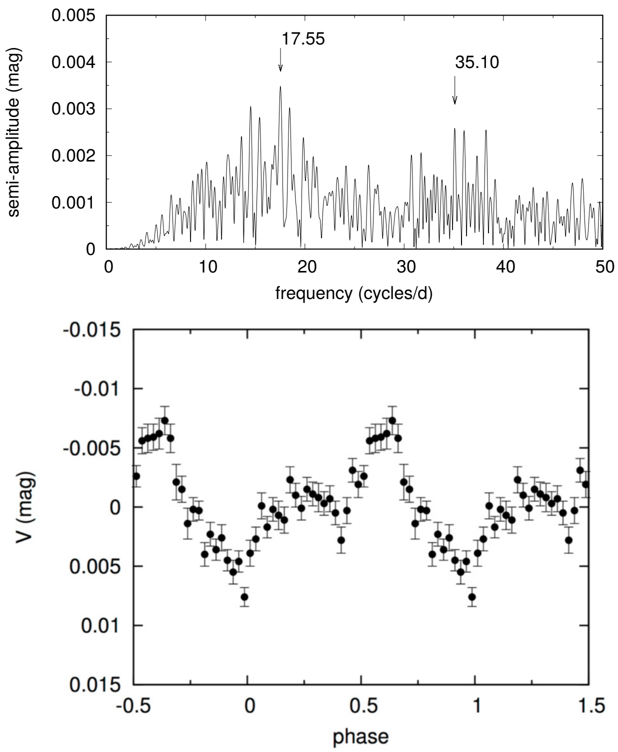

Fig. 2. Upper frame: Power spectrum during days HJD 445–448 (early superhumps), showing broad peaks centred at 17.55 cycles d^{-1} and its first harmonic. Lower frame: Waveform of the early superhumps obtained after folding the data with $P_{\rm esh}$ = 0.05698 d. The zero phase is arbitrary.

5. Worth noting is the increase of the amplitude variations as the system dropped by about 3 mag between Stage C and the post-outburst stage.

6. After the end of the main eruption (day $\geq$ HJD 473) the superhumps were still visible with a significantly larger amplitude $\approx$ 0.2 mag), and with a period which remained constant for at least the subsequent $\approx$ 25 days. The period of the post–outburst modulation was shorter than $P_{\rm sh}$.

A summary of the main periodicities along the eruption is given in Table 2, as found in the next subsections.

3.2.1. *Early Superhumps*

From the beginning of our campaign, a weak modulation of about 0.010 mag full amplitude was observed in the light curves. This signal persisted over days HJD 445–448. The power spectrum of the spliced light curve covering this 4-day segment is shown in the upper frame of Figure 2. It is dominated by two broad peaks centred at frequencies 35.10(3) and 17.55(3) cycles d^{-1}. These signals were weak, with amplitudes of 0.0036 and 0.0030 mag, respectively. Although they were barely detected above the noise, we interpret them as a likely manifestation of early superhumps (Kato et al. 2014).

This photometric feature is known to be typical of WZ Sge-type stars, and is not shown by any other type of dwarf nova. Although its physical origin is still under debate, there is increasing observational evidence that its period ($P_{\rm esh}$) is essentially equal to $P_{\rm orb}$ (Patterson et al. 1996; Kato 2015). A folded curve of the spliced light curve with $P_{\rm esh} = 0.05698(9)$ d is also shown in the lower frame of Figure 2, which shows the double-humped pattern characteristic of early superhumps. The value of $P_{\rm esh}$ obtained in this paper is slightly different from, but consistent with, the value of 0.05706(2) d reported in Kato et al. (2014).

3.2.2. *Common Superhumps*

The double-humped pattern of the early superhumps turned into single-peaked humps on day HJD 449. Over days HJD 449–451, the mean amplitude was around $\approx$ 0.007 mag and the period was $\approx$ 4% longer than the period found for early superhumps. The dominant signal occurred at 16.83(8) cycles d^{-1} corresponding to a period of 0.0594(3) d. Since the modulation was better defined in this 2-day interval, we were able to determine the times of maximum in the signal. We identified a total of 9 maxima in the HJD 449.6–451.6 day interval, and obtained a period of 0.05934(11) d (corresponding to a frequency of 16.85(3) cycles d^{-1}) from a linear regression. This value is fully consistent with the one found from the Fourier analysis. The modulation over this 2-day segment is interpreted as Stage-A superhumps. The period we find is close to, but slightly different from, the value of 0.05883(6) d reported in Kato et al. (2014).

Fully-grown, large-amplitude superhumps were finally observed on day HJD 452 (amplitude of 0.10 mag). As a representative example, we show in the upper frame of Figure 3 the light curve from day HJD 455. As the eruption proceeded, the mean amplitude of the superhumps decreased (as shown in the middle panel of Figure 3). The variation in amplitude was smooth in the HJD 452–466 day interval. We formed a spliced light curve in this interval, and obtained the power spectrum shown in the middle frame of Figure 3. The strongest signals occurred at f_1 = 17.128(3) and f_2 = 34.265(3) cycles d^{-1}.

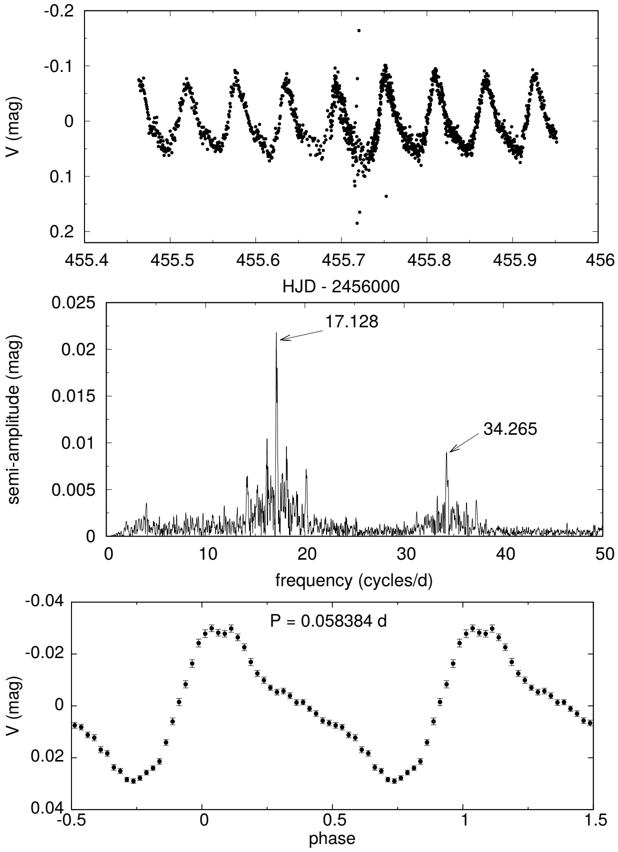

Fig. 3. Upper frame: A 12–hour spliced light curve obtained on day HJD 455, dominated by large-amplitude common superhumps. The zero level in the figure corresponds to $V \approx 12.1$ mag. Middle frame: Power spectrum during the common superhump era (days HJD 442–466), with main peaks centred at frequencies 17.128 and 34.265 cycles d^{-1}. Lower frame: Mean waveform of the common superhump obtained after folding the data on $P = 0.058384$ d. The zero phase is arbitrary.

They were interpreted as the frequency of Stage-B superhumps (period of $P_{\rm sh} = 0.058384(10)$ d) and its first harmonic, respectively. Other (weaker) peaks, not shown in Figure 3, were found at $f_3 = 51.381(6)$ and $f_4 = 68.403(6)$ cycles d^{-1}. The mean waveform of the superhump modulation during this interval is shown in the lower panel of Figure 3.

We note that after subtracting the superhump signal and its harmonics, the power spectrum of the residual light curve showed peaks at 17.20 and 17.28 cycles d^{-1}. But we do not give any physical significance to these detections, and interpret them as the result of period and amplitude variations of the superhump wave during the eruption.

The amplitude of the superhumps increased around day HJD 466, and decreased thereafter until the end of the main eruption (Stage C). The

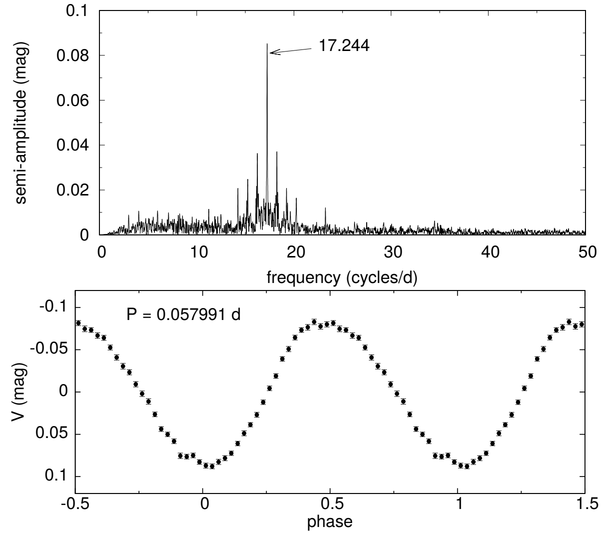

Fig. 4. Upper frame: Power spectrum after the main eruption (day HJD $\geq$ 473) showing a strong peak centred at 17.244(1) cycles d^{-1} (post–outburst superhump). Lower frame: Mean waveform of the post–outburst superhump, obtained after folding the data on $P = 0.057991$ d. The zero phase is arbitrary.

strongest signal in the power spectrum in the HJD 466–470 day interval occurred at 17.191(10) cycles d^{-1}, corresponding to a period of 0.05817(3) d, with additional peaks at higher harmonics.

3.2.3. *Post–Outburst Stage*

Once the main eruption was over, the light curve was still dominated by superhumps, but now with significantly larger amplitude ($\approx$ 0.15 mag) which decreased slowly (≈ 0.013 mag d^{-1}). This behaviour remained essentially unchanged for nearly 20 days of our observations after the main fading.

We formed a spliced light curve including all the observations from day HJD $\geq$ 473, and found a power spectrum (shown in the upper frame of Figure 4), with a peak at 17.244(1) cycles d^{-1}. This was interpreted as the frequency of the post-outburst superhump, and dominated the spectrum. Higher-order harmonics were also found, but their amplitude was very low ($<$ 0.0065 mag). This signifies that the waveform of the post-outburst superhump was nearly sinusoidal. The lower frame of Figure 4 shows that this was indeed the case.

3.3. *Photometry Near and at Minimum Light*

As detailed in § 2, we took two runs near minimum light covering around one orbital period each. The light curves are shown in the upper panel of Figure 5. When folded with the orbital period

TABLE 2

MEAN PHOTOMETRIC PERIODS AND FREQUENCIES OF THE SUPERHUMP MODULATION.*

Time interval (HJD–2456000)	Period (d)	Frequency (cycles d^{-1})	Comments
445–448	0.05698(9)	17.55(3)	early superhumps
449–451	0.0594(3)	16.83(8)	Stage A
452–466	0.058384(10)	17.128(3)	Stage B
466–470	0.05817(3)	17.191(10)	Stage C
473–498	0.05799(1)	17.244(1)	post outburst
449–498	0.0581910(1)	17.1847(3)	mean superhump period

*Values correspond to the 2013 superoutburst of V1838 Aql. The errors in parentheses correspond to the last significant figures.

(0.05698 d), the light curves seem to be out of phase. But this is not surprising: over the 23 days (nearly 400 orbital cycles) elapsed between both runs, an uncertainty of 0.0001 days in $P_{\rm orb}$ involves an uncertainty of 0.7 in phase. We carried out a period analysis of both nights using the Phase Dispersion Minimization (PDM) technique (Stellingwerf 1978) in the *Peranso* package (Paunzen & Vanmunster 2016). This technique is frequently used to detect variations of superhumps in SU UMa systems (e.g. Kato et al. 2014). The lower frame in Figure 5 shows the results of combining the two nights with the best period estimate (0.0576 d) determined from the PDM technique. Assuming that the observed light comes from the accretion disc, the zero point obtained in this case is HJD 2456537.6946 (time of inferior conjunction of the secondary). The period found using the PDM method yielded a value which is still close to the post-outburst state, but the sinusoidal shape is gone. There was only a small peak around phase 0.25. No double modulation with orbital period was found as would be expected in a bounce-back object. Further observations in the R band were obtained on 2018, July 18 covering three orbital cycles. Since the night was not photometric, we were unable to make absolute calibrations and only differential photometry is shown in Figure 6. No obvious orbital modulation was detected within the individual errors, which are rather large (≈ 0.03 mag).

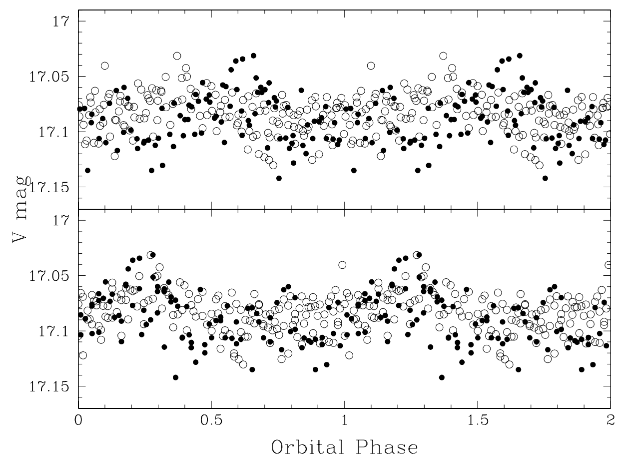

Fig. 5. Upper panel: V light curves obtained near minimum light in 2013. Open dots are from September 2 and filled dots from September 25. The size of the points corresponds to the mean individual errors. The orbital phases have been taken from the ephemeris obtained in this paper. Lower panel: The two nights folded with the ephemeris obtained by using the PDM technique (see more details in text).

4. DISCUSSION

The values derived for the superhump period in Stages A and B allowed us to estimate the mass ratio of the system through the known “superhump excess” $\epsilon - q$ relations (Patterson 1998, 2011; Kato & Osaki 2013). Considering the lack of a reliable determination of the orbital period from spectroscopic observations, we assume here that $P_{\rm orb}$ is equal to the period of early superhumps. We find $\epsilon_A = 0.042(5)$ and $\epsilon_B = 0.024(2)$. Thus, our estimates for the mass ratio are $q_A = 0.12(2)$ and $q_B = 0.10(1)$, respectively. Comparing these two values with the $\epsilon - q$ relation shown in Bakowska et al. (2017, Figure 19) we can see clearly that ϵ_B is well within the expected value, while ϵ_A is not. This is further supported by using the updated Stolz & Schoembs (1984) relation in Otulakowska-Hypka et al. (2016, equation 4), which for our assumed orbital period gives $\epsilon = 0.019(10)$. Although we are inclined to use the Stage B results, we point out that both values are suggestive of a

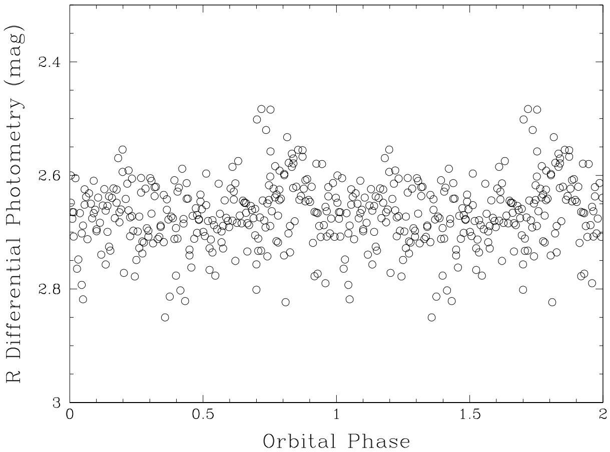

Fig. 6. Differential R light curve obtained at minimum light in July 18, 2018. The size of the individual errors ($\approx$ 0.03 mag) is rather large. The orbital phases have been taken from the ephemeris obtained in this paper. No obvious orbital modulation, within the errors, is detected at this level.

low-mass donor, although as pointed out in § 1 (e.g. Otulakowska-Hypka et al. 2016, see their Figure 7), empirical relations ϵ-q at low q values may carry large systematic uncertainties. For a typical white dwarf with mass $\approx 0.8 M_\odot$ (Zorotovic, Schreiber & Gänsicke 2011) and mass ratio $q \approx 0.1$, the mass of the secondary is very close to the substellar limit i.e. $0.072 M_\odot$ (Chabrier & Baraffe 2000). Further characterisation of systems like V1838 Aql will allow us to discern empirically where this limit lies for mass-losing donors.

It has been noted by many authors, both theoretically and observationally, that the CV orbital period distribution should present a sharp cut-off at about ≈ 80 min, usually termed as the minimum period (e.g. Rappaport et al. 1982; Ritter & Kolb 1998; Gänsicke et al. 2009). V1838 Aql has an orbital period of about 82 min, very close to the minimum period, which makes it difficult to discern whether it is approaching to, or receding from, this minimum orbital period. Before asserting its true nature, we could look at some observational features in those CVs systems around the minimum orbital period. Most of these systems possess WZ Sge-like features. Their optical spectra are mostly dominated by the white dwarf and accretion disc itself, with no visible features from the donor. Since the rate of accretion is an order of magnitude smaller than that for systems before reaching the minimum period ($\dot{m} \approx 10^{-11} M_\odot$ yr^{-1}), the accretion discs become very faint, and the broad absorption lines of the white dwarf become visible below ≈ 5000 Å) e.g. WZ Sge (Howell et al. 2008). However, the donor's observed properties should vary significantly for systems with the same orbital period but evolving towards or away from the period minimum. This is a consequence of the donor's temperature steep relationship as a function of orbital period (e.g. Knigge et al. 2011). From the superhump analysis presented here, we suspect that the system is approaching the period minimum and thus, the donor is probably a late-M dwarf with an observed effective temperature of ≈ 2400 K (Knigge et al. 2011).

The donor of V1838 Aql is therefore an ideal candidate for NIR time-resolved spectroscopy (e.g. SDSS J143317.78+101123.3, Hernández Santisteban et al. 2016), which would render a fully independent measurement of the orbital period and the mass ratio, to confirm or reject its substellar nature. This is particularly important since few low-q systems have been observed in outburst and for which a dynamical measurement of their components is feasible. (Figure 3 in Kato & Osaki 2013). Thus, V1838 Aql could be a system to calibrate the empirical superhump relations in this poorly-explored region of parameter space.

5. CONCLUSIONS

We have presented a long-term study of the 2013 superoutburst of V1838 Aql from its peak to quiescence. Our main results are as follows:

- The observed early superhumps suggest an orbital period of $P_{\rm orb} = 0.05698(9)$ d, which locates V1838 Aql close to the minimum of the orbital period distribution in CVs.
- From Stages A and B and early superhump periods, we found the mass ratio to be $q_A = 0.12(2)$ and $q_B = 0.10(1)$, respectively.
- Based on the obtained values of the mass ratio, we claim that the donor in V1838 Aql is a low-mass star rather than a substellar object, and that the system is approaching the period minimum.

Given the long interval between outbursts in low q systems, it is of paramount importance to confirm by dynamical methods the orbital parameters of such systems. This would indicate which systems may be used in order to calibrate the empirical superhump excess relations.

The authors are indebted to DGAPA (Universidad Nacional Autónoma de México) support, PAPIIT projects IN111713, IN122409, IN100617, IN102517, IN102617, IN108316 and IN114917. GT acknowledges CONACyT grant 166376. JE acknowledges support from a LKBF travel grant to visit the API at UvA. JVHS is supported by a Vidi grant awarded to N. Degenaar by the Netherlands Organization for Scientific Research (NWO) and acknowledges travel support from DGAPA/UNAM. E. de la F. wishes to thank CGCI-UdeG staff for mobility support. We thank the day and night-time support staff at the OAN-SPM for facilitating and helping obtain our observations.

REFERENCES

Bąkowska, K., Olech, A., Pospieszyński, R., et al. 2017, A&A, 603, 72
Breedt, E., Gänsicke, B. T., Drake, A. J., et al. 2014, MNRAS, 443, 3174
Chabrier, G. & Baraffe, I. 2000, ARA&A, 38, 337
Coppejans, D. L., Körding, E. G., Knigge, C., et al. 2016, MNRAS, 456, 4441
de Miguel, E., Patterson, J., Cejudo, D., et al. 2016, MNRAS, 457, 1447
Gänsicke, B. T., Dillon, M., Southworth, J., et al. 2009, MNRAS, 397, 2170
Harrison, T. E. 2016, ApJ, 816, 4
Hernández Santisteban, J. V., Knigge, C., Littlefair, S. P., et al. 2016, Natur, 533, 366
Howell, S. B., Rappaport, S., & Politano, M. 1997, MNRAS, 287, 929
Howell, S. B., Hoard, D. W., Brinkworth, C., et al. 2008, ApJ, 685, 418
Itagaki, K. et al. 2013, CBET, 3554, 1
Kato, T. 2015, PASJ, 67, 108
Kato, T., et al. 2009, PASJ, 61, 395
Kato, T. et al. 2014, PASJ, 66, 90
Kato, T. & Osaki, Y. 2013, PASJ, 65, 115
Knigge, C., Baraffe, I., & Patterson, J. 2011, ApJS, 194, 28
Lenz P., & Breger M. 2005, CoAst, 146, 53
Littlefair, S. P., Dhillon, V. S. & Martin, E. L. 2003, MNRAS, 340, 264
Littlefair, S. P., Dhillon, V. S., Marsh, T. R., et al. 2006, Sci, 314, 1578
Neustroev, V. V., Marsh, T. R., Zharikov, S. V., et al. 2017, MNRAS, 467, 597
O'Donoghue, D., Chen, A., Marang, F., Mittaz, J. P. D., Winkler, H. & Warner, B. 1991, MNRAS, 250, 363
Osaki, Y. 1974, PASJ, 26, 429
_________. 1994, ASIC, 417, 93
Otulakowska-Hypka, M., Olech, A., & Patterson, J. 2016, MNRAS, 460, 2526
Paczynski, B. & Sienkiewicz, R. 1981, ApJ, 248, 27
Patterson, J. 1998, PASP, 110, 1132
_________. 2011, MNRAS, 411, 2695
Patterson, J. et al. 1996, PASP, 108, 748
Patterson, J. et al. 2005, PASP, 117, 1204
Paunzen, E. & Vanmunster, T. 2016, AN, 337, 239
Rappaport, S., Joss, P. C., & Webbink, R. F. 1982, ApJ, 254, 616
Ritter, H. & Kolb, U. 1998, A&A, 129, 83
Skillman D. R. & Patterson J. 1993, ApJ, 417, 298
Smak, J. 1993, AcA, 43, 101
Stellingwerf, R. F. 1978, ApJ, 224, 953
Stolz, B. & Schoembs, R. 1984, A&A 132, 187
Vogt, N. 1982, ApJ, 252, 653
Warner, B. 1995, Cataclysmic Variable Stars (Cambridge, MA: CUP)
Whitehurst, R. 1988, MNRAS, 232, 35
Zorotovic, M., Schreiber, M. R., & Gänsicke, B. T., 2011, A&A, 536, A42

G. Bolt: CBA-Australia, 295 Camberwarra Drive, Craigie, Western Australia 6025, Australia.
R. Costero, C. Echevarría, A. Ruelas-Mayorga, and L. J. Sánchez: Instituto de Astronomía, Apartado Postal 70-264, México, CDMX, C.P. 04510 (jer@astro.unam.mx).
E. de Miguel: Departamento de Ciencias Integradas, Universidad de Huelva, E-21071 Huelva, Spain.
W. Goff: CBA-California, 13508 Monitor Lane, Sutter Creek, CA 95685, USA.
D. González-Buitrago: Departament of Physics and Astronomy 4129, Frederick Reines Hall, University of California, Irvine, CA 92697-4575, USA.
F.-J Hambsch: CBA-Mol, Andromeda Observatory, Oude Bleken 12, B-2400 Mol, Belgium.
J. V. Hernández Santisteban: Anton Pannekoek Institute for Astronomy, University of Amsterdam, Science Park 904, 1098XH Amsterdam, The Netherlands.
J. L. Jones: CBA-Oregon, Jack Jones Observatory, 22665 Bents Road NE, Aurora, OR, USA.
R. Michel: Instituto de Astronomía, Universidad Nacional Autónoma de México, Apartado Postal 877, Ensenada, Baja California, C.P. 22830, México.
J. Olivares: Laboratoire d'astrophysique de Bordeaux, Univ. Bordeaux, CNRS, B18N, allée Geoffroy Saint-Hilaire, 33615 Pessac, France.
A. Oskanen: CBA-Finland, Hankasalmi Observatory, Verkkoniementie 30, FI-40950 Muurame, Finland.
R. Sabo: CBA-Montana, 2336 Tailcrest Dr., Bozeman, MT 59718, USA.
D. Slauson: CBA-Iowa, Owl Ridge Observatory, 73 Summit Avenue NE, Swisher, IA 52338, USA.
W. Stein: CBA-Las Cruces, 6025 Calle Paraiso, Las Cruces, NM 88012, USA.
J. Ulowetz: CBA-Illinois, Northbrook Meadow Observatory, 855 Fair Lane, Northbrook, IL 60062, USA.

Revista Mexicana de Astronomía y Astrofísica, **55**, 31–38 (2019)

ASYMMETRIC SHAPES OF RADIO RECOMBINATION LINES FROM IONIZED STELLAR WINDS

R. Ignace

Department of Physics & Astronomy, East Tennessee State University, USA.

Received September 10 2018; accepted October 30 2018

ABSTRACT

Recombination line profile shapes are derived for ionized spherical stellar winds at radio wavelengths. It is assumed that the wind is optically thick owing to free-free opacity. Emission lines of arbitrary optical depth are obtained assuming that the free-free photosphere forms in the outer, constant expansion portion of the wind. Previous works have derived analytic results for isothermal winds when the line and continuum source functions are equal. Here, semi-analytic results are derived for unequal source functions to reveal that line shapes can be asymmetric about line center. A parameter study is presented and applications discussed.

RESUMEN

Se calcula la forma de los perfiles en radiofrecuencia de las líneas de recombinación para vientos estelares esféricos ionizados. Se supone que el viento es ópticamente grueso debido a la opacidad libre-libre. Se obtienen líneas de emisión para profundidades ópticas arbitrarias, suponiendo que la fotósfera libre-libre se forma en la parte externa del viento, la cual se expande de manera constante. En trabajos anteriores se habían obtenido resultados analíticos para vientos isotérmicos, en los que las funciones fuente para las líneas y el continuo se suponían iguales. En este artículo obtenemos resultados semi-analíticos cundo las funciones fuente no son iguales. Las líneas resultantes pueden mostrar formas asimétricas. Se presenta un estudio de los parámetros y se discuten algunas aplicaciones.

Key Words: line: profiles — radiative transfer — stars: early-type — stars: winds, outflows — radio lines: stars

1. INTRODUCTION

Radio astronomy has long proven to be an important window into the study of stellar astrophysics, and stellar outflows have been no exception (e.g., Dulk 1995; Güdel 2002; Kurt et al. 2002). For stellar winds a key driver has been the prospect of measuring wind mass-loss rates, $\dot{M}$, from the excess infrared (IR) and radio continuum emission relative to the stellar atmosphere (e.g., Panagia & Felli 1975; Wright & Barlow 1975). Numerous studies have focused on determining $\dot{M}$ values based on this approach (e.g., Abbott et al. 1980; Abbot, Bieging, & Churchwell 1981; Abbott et al. 1986; Bieging, Abbott, & Churchwell 1989; Leitherer, Chapman, & Koribalski 1995).

One of the main results from a consideration of free-free excesses formed in the wind is that the spectral energy distribution (SED) at long wavelengths will have a power-law slope with flux $f_\nu \propto \lambda^{-0.6}$. However, this outcome depends on several assumptions: isothermal, spherical symmetry, large optical depth, negligible contribution from the stellar atmosphere, and constant outflow speed. Cassinelli & Hartmann (1977) explored the effects of different power laws for the wind density and temperature distributions to relate the SED power-law slope to these influences. Schmid-Burgk (1982) showed that such SED slopes persist even for axisymmetric stellar envelopes, as long as the same power-law relations are adopted. The main difference is that flux levels are modified, which would have implications for inferring $\dot{M}$ values.

Of greater relevance in recent decades has been the abundance of evidence for clumping in massive star winds. In this regard the literature is voluminous, and there has even been a conference to focus on the topic (Hamann, Feldmeier, & Oskinova 2008). The line-driven winds of massive stars (Castor, Abbot, & Klein 1975; Friend & Abbott 1986; Pauldrach, Puls, & Kudritzski 1986) are known to be subject to an instability (e.g., Lucy & White 1980; Owocki, Castor, & Rybicki 1988). This instability produces shocks in the flow and is a natural culprit for stochastic wind clumping. The clumping is well-known to affect the long wavelength emission because of the density-square dependence of the free-free emissivity. In the presence of clumping, the radio emission is overly bright for a given value of $\dot{M}$ as compared to a smooth (i.e., unclumped) wind with the same mass loss. Neglecting the clumping leads to overestimates of $\dot{M}$, scaling as the square root of the clumping factor, or inverse to the square root of the volume filling factor of clumps. These factors will be defined precisely in the following section.

Clumping affects any density-square emissivity, including recombination lines. Clumping has been incorporated into several detailed complex numerical codes for modeling massive star atmospheres and their winds, such as CMFGEN (Hillier & Miller 1999) and PoWR (Hamann, Gräfener, & Liermann 2006). An important distinction for clumping is between "macroclumping" and "microclumping". The former leads to modifications of observables that can depend on the shape of the clump and is sometimes synonymous with a "porosity" treatment. The latter occurs when clumps are all optically thin, so that the radiative transfer does not depend on details of clump morphology. Consequently, microclumping can be handled in terms of a scale parameter, and in fact does not alter the SED slope relative to an unclumped wind (Nugis, Crowther, & Willis 1998). Ignace (2016a) considered the impact of macroclumping vs microclumping for ionized winds at long wavelengths.

This contribution is concerned with modeling a radio recombination line (RRL) profile shape that also includes continuum free-free opacity. The problem has been addressed many times before. Rodríguez (1982) derived the line profile shape for this case, with the interest of supplementing the use of the continuum to obtain $\dot{M}$ with line broadening formed in the same spatial locale to obtain the wind terminal speed v_∞. Hillier, Jones, & Hyland (1983) did so as well. Ignace (2009) repeated the derivation, and expanded the consideration to include line blends. All of these treatments assume that the source function for the line and continuum is the same, as given by the Planck function for an isothermal wind. Using a numerical radiative transfer calculation, Viner, Vallee, & Hughes (1979) showed that an asymmetric line shape can result when the line and continuum source functions are unequal. Here, this result is explored further through analytic derivations. § 2 introduces the model assumptions and presents a derivation for the line shape. Unlike most previous treatments, the derivation also allows for a power-law distribution of microclumping in the wind. § 3 provides for a parameter study for line profile shapes. § 4 discusses relevant applications for various astrophysical sources.

2. RADIO RECOMBINATION LINE MODELING

Various authors have addressed the relevance of non-LTE effects for interpreting observed RRLs. A discussion of progress on the topic can be found in Gordon & Sorochenko (2002). Relevant to wind-broadened emission lines, Viner et al. undertook a calculation of departure coefficients for studies of H II regions. As previously noted, they allowed for spherical outflow and found that line shapes can be asymmetric. Peters, Longmore, & Dullemond (2012) conducted a similar study for H II regions, and elaborated further on line asymmetry for an outflow. However, neither Viner et al. nor Peters et al. explored the possibility of analytic solutions for the radiative transfer. Here, the approach largely follows Ignace (2009), but relaxing the assumption that the line and continuum source functions are equal. The primary assumptions of the model are as follows:

i. The wind is spherically symmetric in time average.

ii. The wind is optically thick to free-free opacity. The line can be thin or thick.

iii. While the line and continuum source functions may not be equal, they are taken as constant with radius.

iv. Microclumping is included in the treatment, specifically as a power-law distribution[1] with radius. Clumping in massive star winds is both predicted and measured to vary with radius (e.g., Runacres & Owocki 2002; Blomme et al. 2002, 2003; Puls et al. 2006).

[1] The additional power-law distribution need not be attributed to clumping. It could be attributed to something else that modifies the density. However, it cannot be the velocity law, since that would lead to a different geometry for the isovelocity zones and would invalidate the derivation that follows. The inclusion of the additional power law follows the spirit of the approach in Cassinelli & Hartmann (1977).

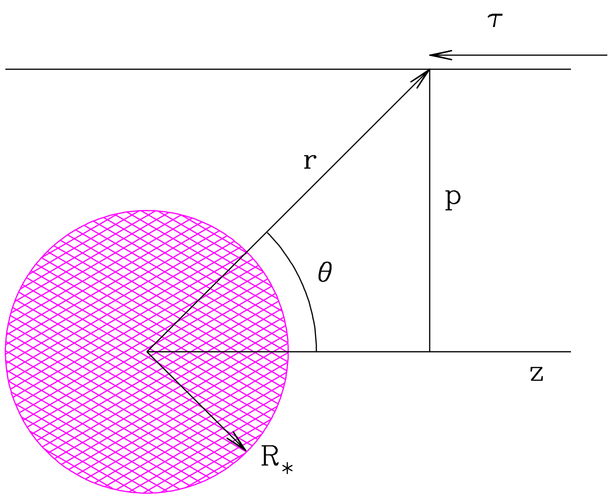

Fig. 1. Coordinate definitions used in the derivation for the line and continuum emission from a spherical ionized wind. See text for explanation. The color figure can be viewed online.

2.1. *Wind Parameters*

Spherical symmetry requires the wind to have a strictly radial wind velocity and density. Being optically thick to free-free opacity, only the large radius flow at constant expansion will be considered. The wind terminal speed is represented by v_∞. The wind also has a time-average mass-loss rate of $\dot{M}$, and the star has radius R_*.

Microclumping is represented as

$$\langle \rho^2 \rangle = D_{\rm cl}\, \langle \rho \rangle^2, \tag{1}$$

where $\langle x \rangle$ represents spatial averaging. On the right-hand side, the average density is given by the smooth wind relation for spherical symmetry, with

$$\langle \rho \rangle = \frac{\dot{M}}{4\pi\, R_*^2\, v_\infty} \left(\frac{R_*}{r}\right)^2 \equiv \rho_0 \left(\frac{R_*}{r}\right)^2. \tag{2}$$

For emissivity $j_\nu \propto \rho^2$, the emission is enhanced above the smooth wind by the clumping factor $D_{\rm cl}$. It is common to represent the clumping in the wind with a volume filling factor, $f_V = D_{\rm cl}^{-1}$. Both approaches are used in the literature (c.f., clumping factor: Hamann & Koesterke 1998 or Ignace, Quigley, & Cassinelli 2003; volume filling factor: Abbott et al. 1981 or Dessart et al. 2000).

For this study the clumping factor is allowed to vary with radius as a power law, with

$$D_{\rm cl} \propto r^{-m}. \tag{3}$$

The case of $m = 0$ is for clumping that is constant throughout the flow; $m > 0$ implies that clumping declines with radius; $m < 0$ is the opposite case. (Note that some care must be taken with use of the power law for clumping, since $D_{\rm c} \geq 1$.)

2.2. *Line and Continuum Opacities*

The free-free opacity, κ_ν, is given by

$$\kappa_\nu\, \rho = K_{\rm ff}\, n_{\rm i}\, n_{\rm e}, \tag{4}$$

where $n_{\rm i} = \rho/\mu_{\rm i} m_H$ is the number density of ions, with $\mu_{\rm i}$ the mean molecular weight per free ion; $n_{\rm e} = \rho/\mu_{\rm e} m_H$ is the number density of electrons, with $\mu_{\rm e}$ the mean molecular weight per free electron; m_H is the mass of hydrogen; and (Cox 2001)

$$K_{\rm ff} = 3.692 \times 10^8 \left(1 - e^{-h\nu/kT_C}\right) Z_{\rm i}^2 g_\nu T_C^{-1/2} \nu^{-3}. \tag{5}$$

In the preceding equation, h is Planck's constant, k is the Boltzmann constant, T_C is the temperature of the gas appropriate for the continuum emission, $Z_{\rm i}$ is the root mean square ion charge, ν is the frequency, and g_ν is the Gaunt factor.

Figure 1 shows the geometry for evaluating the optical depth τ along a ray. Cylindrical coordinates for the observer are (p, α, z), with the observer located at great distance along the $+z$-axis. Spherical observer coordinates are (r, θ, α), with $r^2 = p^2 + z^2$. The continuum optical depth along a ray of fixed impact parameter, p, is

$$\tau_C = \mathcal{T}_C(\lambda) \int \tilde{\rho}^2(\tilde{r})\, D_{\rm cl}(\tilde{r})\, d\tilde{z}, \tag{6}$$

where $\tilde{x}$ signifies a normalized parameter, in this case $\tilde{\rho} = \rho/\rho_0$ and lengths are relative to R_*, and the optical depth scaling is

$$\mathcal{T}_C = \frac{K_{\rm ff}\, R_*\, \rho_0^2}{\mu_{\rm i}\, \mu_{\rm e}\, m_H^2}. \tag{7}$$

At long wavelengths that are the focus of this paper, $\mathcal{T}_C \propto g_\nu\, \lambda^2$ for the Rayleigh-Jeans limit, and $g_\nu \propto \lambda^{0.1}$.

The line opacity is somewhat similar to that of the continuum in the sense that there is a dependence on the square of the density for recombination. Assuming that the wind speed is highly supersonic, the line optical depth can be approximated from Sobolev theory (Sobolev 1960). The line optical depth becomes

$$\tau_L = \frac{\kappa_L\, \rho\, \lambda}{(v_\infty/r)\,(1 - \mu^2)}, \tag{8}$$

where $\kappa_L\,\rho \propto D_{\rm cl}\,\rho^2\,F(T_L)$, for $F(T_L)$ a function of temperature appropriate for the line emission, and $\mu = \cos\theta$.

For the case of constant expansion of the wind at v_∞, the line-of-sight velocity shift due to the Doppler effect is $v_{\rm z} = -v_\infty\,\mu$. It is convenient to introduce a normalized velocity shift with

$$w_{\rm z} = v_{\rm z}/v_\infty = -\mu. \tag{9}$$

Also note that $p = r\sin\theta$. Then the line optical depth becomes

$$\tau_L = \mathcal{T}_L\,\tilde{p}^{-3-m}\,(\sin\theta)^{1+m}, \tag{10}$$

where the power-law dependence of $D_{\rm cl}$ with radius has been substituted into the expression, along with $\tilde{\rho}^2 = \tilde{r}^{-4}$, and $\mathcal{T}_L$ is the optical depth scaling for the line. Casting the line optical depth in terms of p and θ will prove useful for solving the radiative transfer problems in the following sections.

2.3. *Solution for the Case of $S_L = S_C$*

When the line and continuum source functions are the same, let $S_0 = S_L = S_C$. At wavelength λ, just outside the maximum velocity shift of the line, the flux of continuum emission is given by

$$f_C = \frac{2\pi R_*^2}{d^2}\int_0^\infty I_\nu\,\tilde{p}\,d\tilde{p}, \tag{11}$$

where I_ν is the emergent intensity as given by

$$I_\nu = S_0\left[1 - e^{-\tau_C(\tilde{p})}\right]. \tag{12}$$

When the wind is optically thick, such that the excess emission from the wind greatly exceeds the attentuated stellar emisison through the wind, the radiative transfer has a well-known solution when there is no clumping (Panagia & Felli 1975; Wright & Barlow 1975). When constant clumping is present ($m = 0$), the spectral energy distribution is unchanged, and the flux is simply enhanced above that of a smooth wind (Nugis et al. 1998).

Ignace (2009) also showed that an analytic solution can result with a power-law distribution in the clumping. The following integral relation will be found of general use in subsequent steps:

$$\int_0^\infty \left(1 - e^{-ax^\beta}\right)\,x\,dx = \frac{1}{\beta}\,\Gamma\left(\frac{2}{\beta}\right)\,a^{2/\beta}, \tag{13}$$

where Γ is the Gamma-function.

For the case at hand, the continuum optical depth is

$$\begin{aligned}\tau_C(\tilde{p}) &= \int_{-\infty}^{+\infty} \mathcal{T}_C\,\frac{d\tilde{z}}{\tilde{r}^{4+m}} &(14)\\ &= \mathcal{T}_C\,\tilde{p}^{-3-m}\int_0^\pi (\sin\theta)^{2+m}\,d\theta &(15)\\ &= \mathcal{T}_C\,\tilde{p}^{-3-m}\,G_{\rm m}(\pi), &(16)\end{aligned}$$

where the second line above uses a change of variable to θ, with $\tan\theta = p/z$, and

$$G_{\rm m}(\theta) = \int_0^\theta (\sin x)^{2+m}\,dx. \tag{17}$$

The flux of continuum emission becomes

$$\begin{aligned}f_C &= \frac{2\pi R_*^2}{d^2}\,S_0\left(\frac{1}{3+m}\right)\Gamma\left(\frac{2}{3+m}\right)\times\\ &\quad [G_{\rm m}(\pi)\,\mathcal{T}_C(\lambda)]^{2/(3+m)}\,. &(18)\end{aligned}$$

In the Rayleigh-Jeans limit, the continuum flux will have a power-law slope of $-2 + 4.2/(3+m)$, with S_0 scaling as λ^{-2} for the Planck function. When $m = 0$, the canonical slope of -0.6 results. Formally, the analytic solution of equation (18) requires that $m > -1$.

Within the line, the solution is really no more complicated. Again, Ignace (2009) showed that

$$\begin{aligned}f(w_{\rm z}) &= \frac{2\pi R_*^2}{d^2}\,S_0\int_0^\infty \{1 - \exp\,[-(\mathcal{T}_C G_{\rm m}(\pi) +\\ &\quad \mathcal{T}_L\sin\theta)\tilde{p}^{-3-m}]\}\;\tilde{p}\,d\tilde{p}. &(19)\end{aligned}$$

While the argument of the exponential now has two terms, the form of the integral is just like that of the pure continuum. The analytic result is

$$\begin{aligned}f(w_{\rm z}) &= \frac{2\pi R_*^2}{d^2}\,S_0\left(\frac{1}{3+m}\right)\Gamma\left(\frac{2}{3+m}\right)\times\\ &\quad [G_{\rm m}(\pi)\mathcal{T}_C(\lambda) + \mathcal{T}_L\sin\theta]^{2/(3+m)}\,. &(20)\end{aligned}$$

Note that $\sin\theta = \sqrt{1 - w_{\rm z}^2}$. When $m = 0$, the result of Rodríguez (1982) is recovered. The foremost outcome for equal line and continuum source functions is that regardless of the value of m, the line profile is always symmetric about line center. However, when the two source functions are not equal, the line shape will be asymmetric, as demonstrated in the next section.

2.4. *Solution for the Case of $S_L \neq S_C$*

In the previous section, a relatively complicated radiative transfer problem for line and continuum was found to have an analytic solution. The simplifications required to obtain that solution were spherical symmetry, time-independent flow, and the limit of constant wind expansion. Variation in the clumping factor could be included if the variation could be treated as a power law. Especially important was that both the free-free and line opacities scaled as the square of density.

The final key assumption was that the line and continuum source functions were equal. However, this assumption can be relaxed to allow for unequal source functions (yet still constant throughout the flow at large radius). In this case the solution for the emergent intensity is more complicated, and becomes

$$I_\nu(\tilde{p}, w_z) = S_C\left(e^{-\tau_W} - e^{-\tau_C}\right) e^{-\tau_L} + S_C\left(1 - e^{-\tau_W}\right) + S_L\left(1 - e^{-\tau_L}\right) e^{-\tau_W}. \qquad (21)$$

This expression has three terms. A ray at impact parameter $\tilde{p}$ intersects the conical isovelocity zone in the form of a ring. Considering just one point on this ring, corresponding to $\tilde{z}$ for a given velocity shift w_z, we have two path segments and one point to consider for the accumulation of sinks and sources that contribute to the emergent intensity. The first term in the expression is for the continuum emission up to the point of interest, and then its attenuation by the line opacity at the point. The second term is for the continuum emission from the point of interest to the observer. The third term is the contribution by the line emission, as attenuated by the foreground continuum opacity. Thus as before, τ_C is the total continuum optical depth along the ray, and we also have τ_W as the continuum optical depth from the observer to the point of interest where the line emissivity contributes to the emission.

When $S_L = S_C$, terms involving τ_W cancel out. With unequal source functions, the dependence on τ_W persists. The emergent intensity now becomes:

$$I_\nu(\tilde{p}) = S_C\left(1 - e^{-\tau_C - \tau_L}\right) - (S_L - S_C)\, e^{-\tau_W - \tau_L} + (S_L - S_C)\, e^{-\tau_W}. \qquad (22)$$

For this expression the first term closely mimics the result from the preceding section when $S_L = S_C$. Thus the other two terms in the arrangement of equation (22) represent modifications when the source functions are unequal.

The flux still has an analytic solution. However, an additional standard integral relation is required, of the form

$$\int_0^\infty x^{-\beta}\, e^{-ax}\, dx = \Gamma(1-\beta)\, a^{\beta-1}. \qquad (23)$$

This relation can be applied to the solution for the flux by allowing $x = \tilde{p}^{-3-m}$, for which $\tilde{p} = x^{-1/(3+m)}$. One also has $pdp = -(3+m)\, x^{-\beta}\, dx$ with $\beta = (5+m)/(3+m)$.

The flux in the continuum, outside the velocities of the line, is the same as in the preceding section. However, within the line, the flux now becomes

$$\begin{aligned}\frac{f(w_z)}{f_0} = &\left(\frac{1}{3+m}\right)\Gamma\left(\frac{2}{3+m}\right) \times \\ &\left[G_m(\pi)\mathcal{T}_C(\lambda) + \mathcal{T}_L(\sin\theta)^{1+m}\right]^{2/(3+m)} - \\ &\delta_{LC}\Gamma\left(\frac{-2}{3+m}\right) \times \\ &\left[G_m(\theta)\mathcal{T}_C(\lambda) + \mathcal{T}_L(\sin\theta)^{1+m}\right]^{2/(3+m)} + \\ &\delta_{LC}\,\Gamma\left(\frac{-2}{3+m}\right)\left[G_m(\theta)\mathcal{T}_C(\lambda)\right]^{2/(3+m)}, \end{aligned} \qquad (24)$$

where

$$\delta_{LC} = \frac{S_L}{S_C} - 1, \qquad (25)$$

and

$$f_0 = \frac{2\pi R_*^2}{d^2}\, S_C. \qquad (26)$$

It is frequently the case that line profile data are plotted as continuum normalized. The continuum-normalized emission line profile is given by

$$\begin{aligned}\frac{f(w_z)}{f_C} = &\left[1 + \frac{t_{LC}}{G_m(\pi)}(\sin\theta)^{1+m}\right] + \delta_{LC}\gamma_m \times \\ &\left\{\left[\frac{G_m(\theta)}{G_m(\pi)} + \frac{t_{LC}}{G_m(\pi)}(\sin\theta)^{1+m}\right]^{2/(3+m)} - \right. \\ &\left.\left[\frac{G_m(\theta)}{G_m(\pi)}\right]^{2/(3+m)}\right\}, \end{aligned} \qquad (27)$$

where

$$t_{LC}(\lambda) = \mathcal{T}_L/\mathcal{T}_C, \qquad (28)$$

and

$$\gamma_m = -(3+m)\,\frac{\Gamma[-2/(3+m)]}{\Gamma[+2/(3+m)]}, \qquad (29)$$

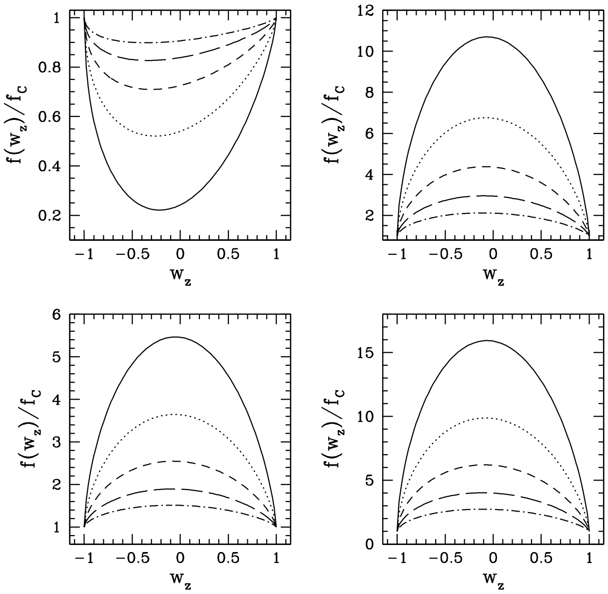

Fig. 2. Continuum normalized emission line profiles for the case of $m = -0.5$. The 4 panels are: upper left for $\delta_{LC} = -0.15$, lower left for $\delta_{LC} = +0.23$, upper right for $\delta_{LC} = +0.62$, and lower right for $\delta_{LC} = +1.0$. In each panel, the 5 line profiles are shown for $t_{LC} = 0.32$ (dot-dashed), 0.56 (long dashed), 1.0 (short dashed), 1.8 (dotted), and 3.2 (solid), from the weakest line to the strongest. Lines are plotted against normalized velocity shift. Note that each panel has a different scale.

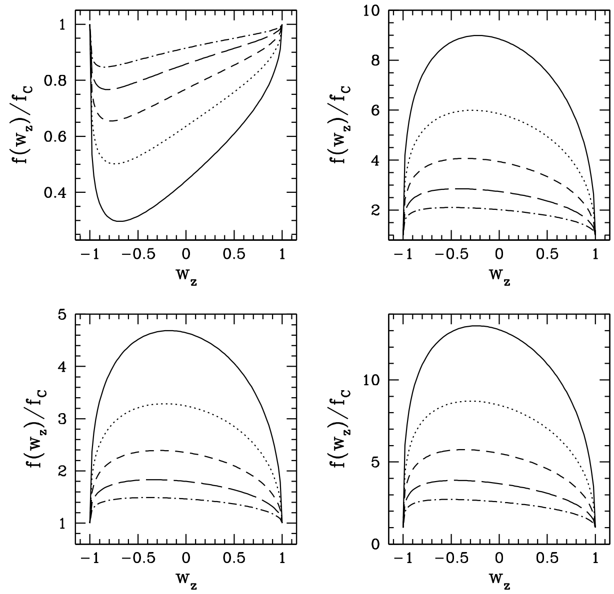

Fig. 3. As in Figure 2, except for $m = 0$.

where the negative anticipates that the Gamma function in the numerator is also negative.

Note the following special cases. Of course, where there is no line opacity, the radio SED will be a power law in wavelength with

$$f_\nu \propto B_\nu\, \mathcal{T}_c^{2/(3+m)} \propto g_\nu^{2/(3+m)}\, \lambda^{-2(1+m)/(3+m)}, \tag{30}$$

for $S_C = B_\nu(T_C)$. The opposite extreme occurs when the line opacity is significant, but the continuum is negligible. The emission line profile shape becomes

$$f(w_{\rm z}) \propto S_L\, (\mathcal{T}_L)^{2/(3+m)}\, \left(1 - w_{\rm z}^2\right)^{1/(3+m)} . \tag{31}$$

Note that the line shape is symmetric about line center in the limit of a strong line. Wavelength dependence pertinent to the specific line transition is implied through the factors S_L and $\mathcal{T}_L$.

Equation (27) is the main result of this study. The first term represents a symmetric component to the emission line profile. The subsequent two terms contribute generally to asymmetric influences to the line in the form of $G_{\rm m}(\theta)$. These influences depend on the clumping power-law exponent m, on the ratio of the source functions S_L/S_C, and on the ratio of optical depths $\mathcal{T}_L/\mathcal{T}_C$. Note that if $\delta_{LC} > 0$, the line is in emission, whereas for $\delta_{LC} < 0$, the line is in absorption. Illustrative examples are given in the following section.

3. RESULTS

Figures 2–4 provide illustrative results for line profile shapes. Figure 2 shows results for $m = -0.5$ (i.e., clumping that increases with radius); Figure 3 for $m = 0$ (i.e., clumping that is constant with radius); and Figure 4 for $m = +1$ (i.e., clumping that declines with radius). Each figure has 4 panels: upper left is for $\delta_{LC} = -0.15$, lower left is for $\delta_{LC} = +0.23$, upper right is for $\delta_{LC} = +0.62$, and lower right is for $\delta_{LC} = +1.0$ for Figures 2 and 3, but $\delta_{LC} = -0.1, 0.4, 0.9$, and 1.4 for Figure 4. Each panel has 5 line profiles, with $t_{LC} = 0.32, 0.56, 1.0, 1.8$, and 3.2, from the weakest line to the strongest. The profiles are continuum normalized and plotted against velocity shift, $w_{\rm z}$. Note that each panel has a different ordinate scale.

When $\delta_{LC} < 0$, the line profile is actually in absorption. For $m = +1$, the line shape takes the appearance of a weak P Cygni line shape, with blueshifted net absorption and redshifted net emission.

For $m = -0.5$, the line profiles are more symmetric about line center as compared to either $m = 0.0$

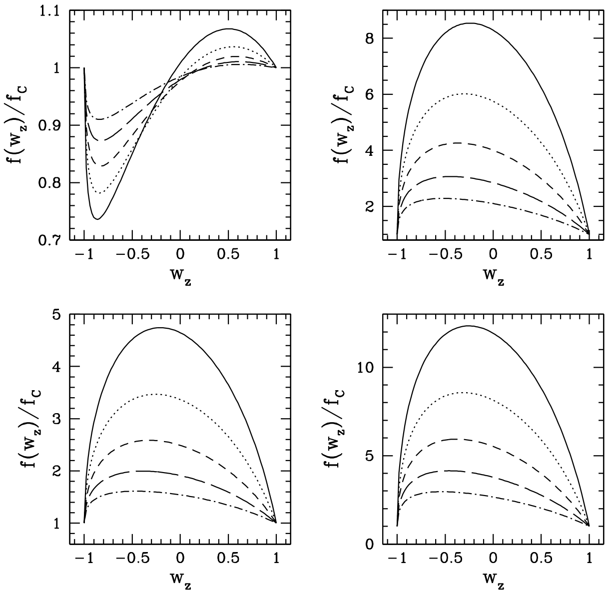

Fig. 4. As in Figure 2, except for $m = 1$ and with $\delta_{LC} = -0.1, 0.4, 0.9$, and 1.4.

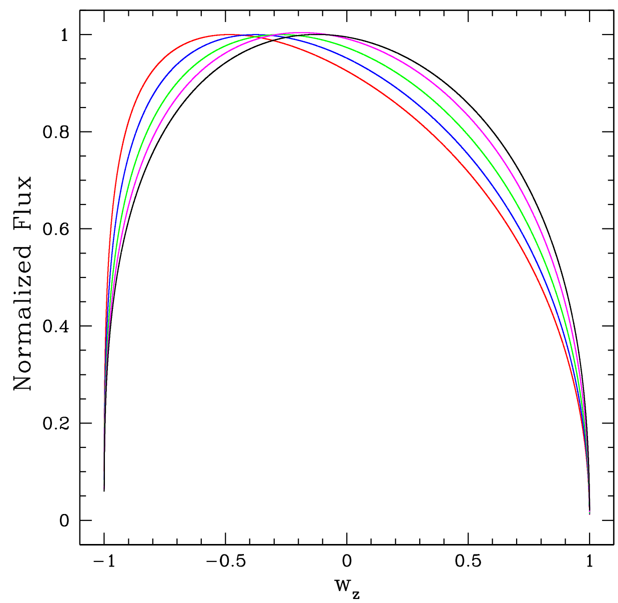

Fig. 5. The line profiles for the case $m = 0.0$ shown to highlight the evolution of line asymmetry as a function of t_{LC}. The line profiles have been continuum subtracted and normalized to a peak emission of unity. The parameter $\delta_{LC} = 0.5$ was held fixed. The line profiles are shown for $\log t_{LC} = -0.5$ (red), -0.125 (blue), $+0.25$ (green), $+0.625$ (magenta), and $+1.0$ (black). The color figure can be viewed online.

or $m = +1.0$. As m approaches -1, the line profile becomes perfectly symmetric, because the factor contributing to the line asymmetry cancels exactly when $2/(3+m) = 1$. As m increases, the line shapes become increasingly asymmetric with the line skewed preferentially toward blueshifted velocities. This is natural generally because the attentuation of line emission from the far-side hemisphere of the wind is greater than from the near-side hemisphere. When $S_L = S_C$, absorption is exactly compensated by emission, and no asymmetry in the line can result. For the given assumptions, the line asymmetry occurs only when the source functions are unequal.

The line profiles display some degeneracy between δ_{LC} and t_{LC}. As t_{LC} becomes large, asymmetry in the line shape lessens, in the sense that the peak emission shifts closer to line center. A large line optical depth means that a (positive) δ_{LC} has less influence on the line shape. Generally, t_{LC} controls the degree of asymmetry in the line, and δ_{LC} acts as an overall amplitude for the line emission (or line equivalent width).

4. CONCLUSIONS

The focus of this contribution has been to highlight the asymmetry of RRLs arising from a spherical wind using an analytic derivation. Previous analytic work produced symmetric line shapes. Numerical calculations have demonstrated that asymmetric lines can be produced. Here, with the assumption of constant but unequal line and continuum source functions, asymmetric line shapes are produced. The derivation allows for the presence of microclumping in the wind in terms of a power-law distribution (rising or declining with radius from the star). While the clumping distribution can impact line asymmetry, the line asymmetry results even with constant clumping, or no clumping whatsoever. Under the model assumptions, emission line asymmetry arises from the continuum opacity (specifically the appearance of the term with $G_{\rm m}(\theta)$ in equation [27]) that absorbs the redshifted emission from the far hemisphere more than the blueshifted emission from the near hemisphere. The result is a line shape with blueshifted emission peak. (The same effect arises in X-ray lines; c.f., Ignace 2016b).

RRLs are vigorously pursued as a diagnostic of source properties, from kinematics to geometrical aspects. Peters, Longmore, & Dullemond (2012) have made an in-depth study of various factors that affect the flux of line emission and the shape of the line profile, including line asymmetry. Observational motivation for understanding line asymmetry of RRLs includes some objects as the early-type binary MWC349, specifically the H76α line (Escalante et al. 1989). Understanding the line formation is key for distinguishing between radiative transfer effects for the line formation versus the influence of aspherical effects intrinsic to the source, such as binarity, or asymmetric mass-loss, or flow geometry. Applications for such effects include emission-line objects like MWC349 (e.g., LkHα 101; Thum et al. 2013), outflow from star-forming clumps (e.g., Kim et al. 2018), and planetary nebulae (e.g., Ershov & Berulis 1989; Sánchez Contreras et al. 2017). Analytic solutions are valuable to these studies in two main respects: (a) they allow for rapid evaluation of parameter space that can be honed with more detailed numerical calculations to fit the data, and (b) they are important for providing non-trivial benchmarks against which numerical codes can be tested.

The author expresses appreciation to an anonymous referee for several helpful comments.

REFERENCES

Abbott, D. C., Bieging, J. H., Churchwell, E., Cassinelli, J. P. 1980, ApJ, 238, 196
Abbott, D. C., Bieging, J. H., & Churchwell E. B. 1981, ApJ, 250, 645
Abbott, D. C., Bieging, J. H., Churchwell, E. B., & Torres, A. 1986, ApJ, 280, 671
Bieging, J., Abbott, D., & Churchwell, E., 1989, ApJ, 340, 518
Blomme, R., Prinja, R., Runacres, M., Colley, S. 2002, A&A, 382, 921
Blomme, R., van de Steene, G., Prinja, R., Runacres, M., & Clark, J., 2003, A&A, 408, 715
Cassinelli, J. P. & Hartmann, L. 1977, ApJ, 212, 488
Castor, J., Abbott, D., & Klein, R. 1975, ApJ, 195, 157
Cox, A. (ed.), 2000, Allen's Astrophysical Quantities, (New York: AIP Press, Spring)
Dessart, L., Crowther, P., Hillier, D., et al. 2000, MNRAS, 315, 407
Dulk, G. A. 1985, ARA&A, 23, 169
Escalante, V., Rodríguez, L. F., Moran, J., & Cantó, J. 1989, RMxAA, 17, 11
Friend, D. & Abbott, D. 1986, ApJ, 311, 701
Gordon, M. & Sorochenko, R. 2002, Radio Recombination Lines. Their Physics and Astronomical Applications, (Kluwer: Dordrecht)
Güdel, M. 2002, ARA&A, 40, 217
Hamann, W.-R. & Koesterke, L. 1998, A&A, 335, 1003
Hamann, W.-R., Feldmeier, A., & Oskinova, L. (eds.) 2008, Clumping in Hot-Star Winds (Potsdam: Universitätsverlag Potsdam)
Hamann, W.-R., Gräfener, G., & Liermann, A. 2006, A&A, 457, 1015
Hillier, D. I., Jones, T. J., & Hyland, A. R. 1983, ApJ, 271, 221
Hillier, D. I. & Miller, D. L. 1999, ApJ, 519, 354
Ignace, R. 2009, AN, 330, 717
Ignace, R. 2016a, MNRAS, 457, 4123
Ignace, R. 2016b, AdSpR, 58, 694
Kim, W.-J., Urquhart, J., Wyrowski, F., Menten, K., & Csengeri, T. 2018, A&A, 616, A107
Leitherer, C., Chapman, J. M., & Koribalski, B. 1995, ApJ, 450, 289
Lucy, L. & White, R. 1980, ApJ, 241, 300
Nugis, T., Crowther, P. A., & Willis A. J. 1998, A&A, 333, 956
Owocki, S., Castor, J., & Rybicki, G. 1988, ApJ, 335, 914
Panagia, N. & Felli, M. 1975, A&A, 39, 1
Pauldrach, A., Puls, J., & Kudritzki, R. 1986, A&A, 164, 86
Puls, J., Markova, N., Scuderi, S., et al. 2006, A&A, 454, 625
Rodríguez, L. F., 1982, RMxAA, 5, 179
Runacres, M. & Owocki, S. 2002, A&A, 381, 1015
Sánchez Contreras, C., Báez-Rubio, A., Alcolea, J., Bujarrabal, V., & Martín-Pintado, J. 2017, A&A, 603, A67
Sobolev, V. 1960, Moving Envelopes of Stars (Cambridge, MA: CUP)
Peters, P., Longmore, S., & Dullemond, C. 2012, MNRAS, 425, 2352
Thum, C, Neri, R., Báez-Rubio, A., & Krips, M. 2013, A&A, 556, A129
Weiler, K., Panagia, N., Monte, M., & Sramek, R. 2002, ARA&A, 40, 387
Wright, A. E. & Barlow, M. J. 1975, MNRAS, 170, 41

Richard Ignace: Department of Physics & Astronomy, East Tennessee State University, Johnson City, TN 37614, USA (ignace@etsu.edu).

Revista Mexicana de Astronomía y Astrofísica, **55**, 39–54 (2019)

OPTIMAL TRAJECTORIES TO KUIPER BELT OBJECTS

D. M. Sanchez[1], A. A. Sukhanov[1,2], and A. F. B. A. Prado[1]

Received June 22 2018; accepted November 14 2018

ABSTRACT

The present paper searches for transfers from the Earth to three of the Kuiper Belt Objects (KBO): Haumea, Makemake, and Quaoar. These trajectories are obtained considering different possibilities of intermediate planet gravity assists. The model is based on the "patched-conics" approach. The best trajectories are found by searching for the minimum total ΔV transfer for a given launch window, inside the 2023-2034 interval, and disregarding the ΔV required for the capture at the target object. The results show transfers with duration below 20 years that spend a total ΔV under 10 km/s. There is also one trajectory for each of the KBOs with ΔV under 10 km/s and duration below 10 years, using the Jupiter swingby. For the 20-year trajectories, there are also asteroids in the main belt that could be encountered with low additional ΔV, so increasing the scientific return of the mission.

RESUMEN

Se buscan trayectorias de transferencia entre la Tierra y tres objetos del Cinturón de Kuiper (KBO): Haumea, Makemake y Quaoar. Las trayectorias se obienen considerando distintas posibilidades para la influencia gravitatoria de los planetas intermedios. El modelo se basa en el enfoque de "cónicas empalmadas". Se encuentran las mejores trayectorias buscando la transferencia con una ΔV total mínima, para una ventana de lanzamiento en el intervalo 2023-2034, y despreciando la ΔV necesaria para la captura en la meta. Se encuentran transferencias con duración de menos de 20 años que requieren una ΔV menor que 10 km/s. También se encuentra una trayectoria para cada uno de los objetos KB con ΔV menor que 10 km/s y duración de menos de 10 años, empleando la atracción de Júpiter. Las trayectorias de 20 años podrían usarse también para encuentros con asteroides del cinturón central, lo cual aumentaría el valor científico de la misión.

Key Words: methods: numerical — Kuiper belt objects: individual: Haumea — Kuiper belt objects: individual: Makemake — Kuiper belt objects: individual: Quaoar — space vehicles

1. INTRODUCTION

The exploration of the Kuiper Belt Objects (KBOs) is an important step to improve the theories of the formation of the Solar System, since these bodies probably preserved material from the earlier Solar System (Luu & Jewitt 2002). Furthermore, due to the large distance to these bodies from the Sun, the development of new technologies and techniques for their exploration is required.

A few years ago these objects were thought to be single bodies with no atmosphere, except for Pluto. However, with the advances of observational techniques, it was discovered that several of these bodies are orbited by one or more small moons, like Haumea, Makemake, and Quaoar[3]. Another interesting point is that the New Horizons spacecraft, when passing by Pluto, discovered that Pluto has signs of recent surface activity (less than 10 million years old) (Moore et al. 2016). This fact can be an indication that other KBOs with sizes comparable to Pluto could also present recent geological activity. One example of this possibility is the potential presence of cryovolcanism in Quaoar (Barucci

[1]National Institute for Space Research, INPE, Brazil.

[2]Space Research Institute of the Russian Academy of Sciences, IKI, Russia.

[3]http://www.cbat.eps.harvard.edu/minorsats.html

et al. 2015). However, due to the large distance of the KBOs from the Sun, observational data were not enough to significantly improve our knowledge about these bodies, to carry out comparative planetology. Spacecraft missions to one or more of these bodies beyond Pluto are necessary to provide us with more detailed features of the KBOs. The present paper searches for optimal trajectories to (136108) Haumea, (136472) Makemake, and (50000) Quaoar. These three bodies were chosen as targets because they are good representatives of the KBOs and they can also be classified as Trans-Neptunian Objects (TNOs). Haumea and Makemake were recognized by the International Astronomical Union (IAU) as dwarf planets, but Quaoar is just a candidate to this classification. Haumea is probably the most intriguing of the TNOs, because it is a triaxial ellipsoid with fast rotation (3.9154 h), possesses two moons, Namaka and Hi'iaka, and a recently discovered ring (Ortiz et al. 2017). The thin layer of carbon depleted ice that surrounds the rocky core of Haumea is another important characteristic of this dwarf planet (Pinilla-Alonso et al. 2009).

Makemake is the third largest TNO, after Pluto and Eris. It also has a recently discovered moon, which has no official name yet, and its general designation is "S/2015 (136472) 1" (Parker et al. 2016). Quaoar also has a small moon, named Weywot. This moon seems to be in an eccentric orbit. Like Haumea, Quaoar has a rocky core covered by a thin layer of ice, but differently from Haumea, Quaoar has a high density and probably its core is entirely formed by silicate material (Fraser et al. 2013). Then, Quaoar probably is the densest TNO, which makes it a good target for spacecraft exploration. Table 1 presents some orbital and physical characteristics of Haumea (Ragozzine & Brown 2009; Ortiz et al. 2017), Makemake (Brown 2013; Parker et al. 2016), and Quaoar (Fraser et al. 2013). The values of the semi-major axes (a), eccentricities (e) and inclinations (I) are approximate. The inclinations are given with respect to the ecliptic plane. Table 1 also presents the masses (m), densities (ρ), and the moons of these bodies.

We analyzed the dates of launch in the 2023-2034 interval. The only exception was direct flight to Haumea with launch in 2058. The optimal transfer trajectories in terms of the minimum fuel consumption were found. Instead of the fuel consumption an equivalent parameter was considered, namely the total ΔV, which is the sum of the launch ΔV in the low Earth parking orbit and all necessary ΔVs during the flight.[4] This was done considering various possible transfer schemes for the given launch windows assuming that the dwarf planets will be flown by without capture. If capture is required for these specific trajectories, a new optimization should be made taking into account the capture maneuver. Most of the transfer schemes considered include various gravity assists of the planets, which lowers the fuel consumption and/or shortens the time of flight. Furthermore, multi-body missions are more interesting from the scientific point of view, since scientific data could be acquired during the flybys. However, since the limited time of flight is considered, the number of bodies in a single trajectory may be limited. Thus, the number of the planets was maximized for trajectories with 20 years of total time of flight, leaving a smaller number of planets for trajectories with total time of flight less than 20 years. The main difficulty in the design of these trajectories is to find feasible combinations of planets, within the proposed time interval, in a realistic time of flight. Some combinations are not always possible. For example, the combination used by the mission of the Voyager 2 (Kohlhase & Penzo 1977), Earth-Jupiter-Saturn-Uranus-Neptune-Outer space, cannot be reproduced in this century anymore. This technique was widely used in missions to the outer planets and outer space, such as in the Voyager 1 (Kohlhase & Penzo 1977), with the scheme E-J-S-Outer space, Galileo (D'Amario et al. 1982), with the scheme E-V-E-E-A-A-J, Ulysses (Wenzel et al. 1992), with the scheme E-A-DV-E-A, Cassini (Peralta & Flanagan 1995), with the scheme E-V-V-E-A-J-S, and the New Horizons (Guo & Farquhar 2005), with the scheme E-A-J-P-Kuiper Belt, where E, V, J, S, U, N, P, A stand for Earth, Venus, Jupiter, Saturn, Uranus, Neptune, and anăasteroid, respectively.ăDV means a deep space propulsive maneuver. All of these schemes, except E-V-V-E, which areăpossible for launch in 2023-2034 areăanalyzed in this paper. Also transfer schemes E-V-E-E-S andăE-V-E-DV-E-S are considered.

The method of patched-conics is a well-known technique and was used for the planning of several interplanetary missions (Kohlhase & Penzo 1977; D'Amario et al. 1982; Sukhanov 1999; Strange & Longusky 2002; Solórzano et al. 2008). The description of the method can be found in several publi-

[4]In fact this is not quite correct because the launch and deep space maneuvers will be made by different engines and cannot be simply summed. Although since the characteristics of the engines are not known in advance the sum of the ΔVs is the only way to estimate optimality of the transfers.

TABLE 1

SOME PHYSICAL AND ORBITAL CHARACTERISTICS OF HAUMEA, MAKEMAKE, AND QUAOAR

Body	m (kg)	ρ (g/cm^3)	a (AU)	e	I (deg)	Moon(s)
Haumea	4.006×10^{21}	1.885	43	0.19	28.2	Namaka, Hi'iaka
Makemake	$< 4.4 \times 10^{21}$	1.4 – 3.2	46	0.15	29.0	S/2015 (136472) 1
Quaoar	1.3 – 1.5$\times 10^{21}$	4.2	44	0.04	8.0	Weywot

cations, like Escobal (1968). The transfer trajectories shown here can be useful for future missions to Haumea, Makemake, and Quaoar, which are important targets in the future exploration of the Solar System.

2. METHODOLOGY

The patched-conic technique, making close approaches of the spacecraft to the planets of the Solar System, is used to generate sets of trajectories between Earth and Haumea, Makemake, and Quaoar. The software implemented to solve this problem generates all possible trajectories between the Earth and the final destination, choosing as optimal trajectory the one with the minimum ΔV required, for a given a launch window. This means that extended launch, swingby, and arrival time windows, up to a few and sometimes several months, were specified and optimal transfers within the windows were sought for. Thus, the trajectories found are optimal from the fuel consumption point of view. As mentioned above, this minimum ΔV does not consider the ΔV required to place the spacecraft in a close orbit around the dwarf planet, since the arrival velocity is too high: it can vary from 10 km/s to 22 km/s in trajectories with 10 to 20 years of time of flight, as shown in the next section. Then, the minimum ΔV to generate the optimal trajectory comprises the launch ΔV and mid-course maneuvers. The orbits of the planets were calculated using the JPL DE405 ephemerides. Orbital elements of the dwarf planets were taken from the Edward Bowell's Asteroid Orbital Elements Database and then numerically propagated to the arrival time. In order not to make the transfers too long the time of flight was limited by some values and the optimal transfers (*i.e.* transfers with minimal total ΔV) for that limited time of flight were calculated.

3. RESULTS

All types of the trajectories found for each of the dwarf planets are presented in this section. First, the direct Earth to the dwarf planet transfer is considered. Then transfers including gravity assists of the planets are considered, which increases the spacecraft velocity and decreases the launch ΔV. To decrease the launch ΔV, the classical combination of multiple gravity assist maneuvers in Earth and Venus are used, such as EVEE (Earth-Venus-Earth-Earth) and EVEdvE (Earth-Venus-Earth-deep space maneuver-Earth). However, these maneuvers may increase the total time of flight, because the duration of the EVEE and EVEdvE maneuvers is about 3.5 years, and, consequently, it may not be possible to find transfer trajectories with less than 20 years and a total ΔV less than 10 km/s. This value for the total ΔV is a limit in the present research, when searching for transfers in the 2023-2034 interval and 2058 for the direct flight to Haumea.

The last planet in the way to the dwarf planet is the one responsible for changing the orbital inclination of the spacecraft, since all dwarf planets have considerable inclination to the ecliptic plane, as seen in Table 1. This gravity assist maneuver is used also to minimize the cost of the inclination change, which is a very expensive maneuver if made using the fuel consumption. The types of transfers are ordered by the number of the planets involved, beginning with the direct transfer. The name of the trajectory indicates the first letter of the planets involved and the constraint in the time of flight, where "nc" stands for "no constraints". For example, the trajectory EJH60y is a type B trajectory, representing the Earth to Haumea passing by Jupiter with a maximum of 60 years of time of flight. It is worth mentioning that not all types of trajectories are possible for all the dwarf planets. The types of trajectories are the following:

A - Direct trajectory, with no constraint.

B - Earth to the dwarf planet passing by Jupiter.

C - Earth to the dwarf planet passing by Saturn.

D - Trajectory that includes the EVEE maneuver and the Jupiter gravity assist.

E - Trajectory that includes the EVEdvE maneuver and the Jupiter gravity assist.

F - The same as E, but with Saturn instead of Jupiter.

G - Trajectory that includes the EVEE maneuver and the Jupiter and Uranus gravity assists.

H - Trajectory that includes the EVEdvE maneuver and the Jupiter and Uranus gravity assists.

I - Trajectory that includes the EVEE maneuver and the Jupiter and Saturn gravity assists.

If there is more than one transfer of the same type, it will be numbered along the type of the transfer, *e. g.*, A1, A2, and so on.

Since Haumea, Makemake, and Quaoar are KBOs, all transfer trajectories pass by the main asteroid belt. This makes it possible to encounter and observe a main belt asteroid (or asteroids), increasing the scientific output of the mission. However, since the trajectories with smaller time of flight pass through the main belt with high velocity, the additional ΔV required to encounter an asteroid could increase too much the total ΔV. This is why only the 20-year trajectories include possible encounters with the asteroids. The results are shown for each individual target. The next three subsections give the main results for the trajectories to Haumea (Table 2), Makemake (Table 3), and Quaoar (Table 4). Plots of some of the trajectories are also shown, to illustrate the transfers. The results are summarized in the last subsection. All the dates presented in the results are in format dd.mm.yyyy, where dd = day, mm = month and yyyy = year.

3.1. *Transfers to Haumea*

Since inclination of the Haumea orbit to the ecliptic plane is about 28.2 degrees, the direct transfer to this body would have its minimum fuel consumption if the spacecraft reaches Haumea at the node line, *i.e.*, the intersection of the Haumea orbital plane with the ecliptic plane. The reason is the very high cost of maneuvers to change the inclination of the spacecraft orbit. Then, the first trajectory presented in Table 2, the EHnc (type A), is a direct transfer using the best scenario, with the launch date of (23.01.2058) and the arrival date of (11.03.2100), just when Haumea is passing by the line of nodes. In Table 2, ΔV_L is the launch ΔV, V_A is the arrival velocity, ΔV_T is the total ΔV, and TOF is the time of flight. Figure 1 shows the trajectory for the direct transfer.

The addition of the Jupiter swingby during the Earth to Haumea transfer allows to decrease the launch ΔV, the arrival velocity, the total ΔV and the time of flight, if compared with the EHnc transfer with launch in 2058. In the EJH60y transfer, the total ΔV decreased from 8.27 km/s to 6.84 km/s, a difference of 1.43 km/s compared to the transfer EHnc. The decrease of the ΔV at launch is 1.43 km/s, almost the same as the total ΔV. The same proportion was followed by the arrival velocity, which has a decrease of 1.43 km/s. This indicates that the arrival velocity is more sensitive to variations in the time of flight, since the arrival time for the EHnc transfer is almost the same as for the EJH60y transfer.

Figure 2 shows the EJH20y transfer trajectory, and Figure 3 shows the EJH10y trajectory. The latter transfer is the best solution found for the relatively short time of flight, since the total ΔV was kept under 10 km/s.

The launch ΔV can be reduced by means of the EVEE or EVEdvE maneuver. As an example, Figure 4 shows the EVEEJH20y transfer for launch in 2023. If we compare this transfer with the EJH20y shown in Table 2, there is decrease in the total ΔV of 1.43 km/s and decrease of 3.69 km/s in the launch ΔV. However, since the spacecraft passed by more planets in the same period of time as the EJH20y transfer, the mid-course velocity increment of the spacecraft in EVEEJH20y is larger than the one for the EJH20y situation, leading to a 1.93 km/s higher arrival velocity.

The EVEdvEJH20y transfer trajectory that uses the deep space maneuver is shown in Figure 5. The use of the deep space maneuver between the two Earth swingbys leads to a small decrease of the total ΔV, namely, of 0.11 km/s. We used the EVEdvEJH20y transfer to search for the asteroids that could be encountered in the 20-year trajectory. Just one asteroid that could be reached during the transfer with an additional $\Delta V < 0.5$ km/s was found. This asteroid is (11023) 1986 QZ. Figure 6 includes the orbit of the asteroid, the date of the encounter, and the trajectory EVEdvEJH20y. Characteristics of the original EVEdvEJH20y transfer and the transfer with the asteroid encounter are shown in Table 2, as E3 and E4. The additional ΔV necessary for the asteroid is 0.10 km/s.

The existence of launch windows with the Saturn gravity assist in the 2023-2034 interval allows another possibility of transfers to Haumea using the EVEdvE maneuver. However, compared with the similar combination, but using Jupiter instead of Saturn, all transfers that involve Saturn have a larger total ΔV, as can be seen in Table 2. There are also launch windows with Uranus swingby after Jupiter,

TABLE 2

TYPES OF OPTIMAL TRAJECTORIES TO SEND A SPACECRAFT TO HAUMEA

Type	Trajectory	Launch date	ΔV_L, km/s	V_A, km/s	ΔV_T, km/s	TOF, years
A1	EHnc	23.01.2058	8.24	4.22	8.24	42.26
B1	EJH60y	21.09.2025	6.84	2.88	6.84	59.99
B2	EJH40y	17.08.2024	6.96	4.52	8.24	37.54
B3	EJH20y	18.08.2024	7.30	11.20	7.30	20.00
B4	EJH10y	01.10.2025	9.79	25.05	9.98	10.00
C1	ESHnc	13.07.2027	7.39	4.80	7.39	42.42
C2	ESH20y	15.07.2028	7.32	16.27	9.39	19.99
D1	EVEEJH20y	21.05.2023	3.62	13.13	5.87	20.00
D2	EVEEJH15y	24.05.2023	3.63	20.20	7.09	15.00
E1	EVEdvEJH60y	14.05.2023	3.61	3.15	4.41	59.97
E2	EVEdvEJH30y	14.05.2023	3.61	7.11	5.09	29.92
E3	EVEdvEJH20y	12.05.2023	3.62	13.27	5.76	19.89
E4	EVEdvEJH20y+ast	21.05.2023	3.62	13.13	5.86	20.00
E5	EVEdvEJH15y	24.05.2023	3.63	20.20	7.08	15.00
F1	EVEdvESHnc	30.11.2024	4.18	4.43	5.03	46.94
F2	EVEdvESH30y	10.12.2024	4.11	10.82	5.65	30.00
F3	EVEdvESH25y	16.12.2024	4.07	15.66	6.65	25.00
F4	EVEdvESH20y	23.11.2024	4.27	22.28	10.30	20.00
G1	EVEEJUHnc	05.08.2026	3.90	5.75	3.91	55.30
G2	EVEEJUH40y	14.08.2026	3.92	11.27	6.50	40.00
G3	EVEEJUH30y	03.08.2026	3.91	19.44	13.76	30.00
H1	EVEdvEJUHnc	13.05.2023	3.62	6.50	5.25	49.92

but they also have a large total ΔV compared with other trajectories with the same time of flight, as also shown in Table 2. Transfer trajectories passing by Uranus exceed our limit of 10 km/s in all transfers that have total time of flight smaller than 25 years.

3.2. *Transfers to Makemake*

Characteristics of the transfers to Makemake are given in Table 3, where ΔV_L is the launch ΔV, V_A is the arrival velocity, ΔV_T is the total ΔV, and TOF is the time of flight. Makemake is three astronomical units farther from the Sun than Haumea. This fact, associated with an inclination larger by one degree, makes the fuel consumption larger. It can be seen, from the total ΔV for the transfer trajectories to Makemake, that, for all the transfers, the fuel expenditures are slightly larger than the ones for the transfers to Haumea. Comparing Table 2 with Table 3, one can see that the same type of trajectory has larger values of the total ΔV for Makemake. As an example, for the transfer type A, which is a direct transfer to the body, the total ΔV is 8.24 km/s for the Earth-Haumea flight and 8.33 km/s for the Earth-Makemake flight. Transfer A1 for Makemake is shown in Figure 7.

Similarly to what occurs for Haumea, transfer trajectories using the Jupiter swingby spend less total ΔV compared to transfers using the Saturn swingby, as is shown in Table 3. Very large variations in the costs for different types of trajectories are noted. As an example of this variation, note that the B3 type of transfer (Earth-Jupiter-Makemake) has a total ΔV of 10.43 km/s, which is almost half of the total ΔV for the transfer C3 (Earth-Saturn-Makemake), which is 17.72 km/s. Both transfers considered a time of flight of 10 years. The transfer B3 is shown in Figure 8.

However, if we consider the EVEdvE maneuver before the Saturn or Jupiter swingby, our simulations show that Saturn is more efficient in terms of reducing the total ΔV. In the same way as transfers to Haumea, a 20-year transfer is feasible if a mission passing by multiple bodies is designed, having the total ΔV around 10 km/s. Therefore, regarding

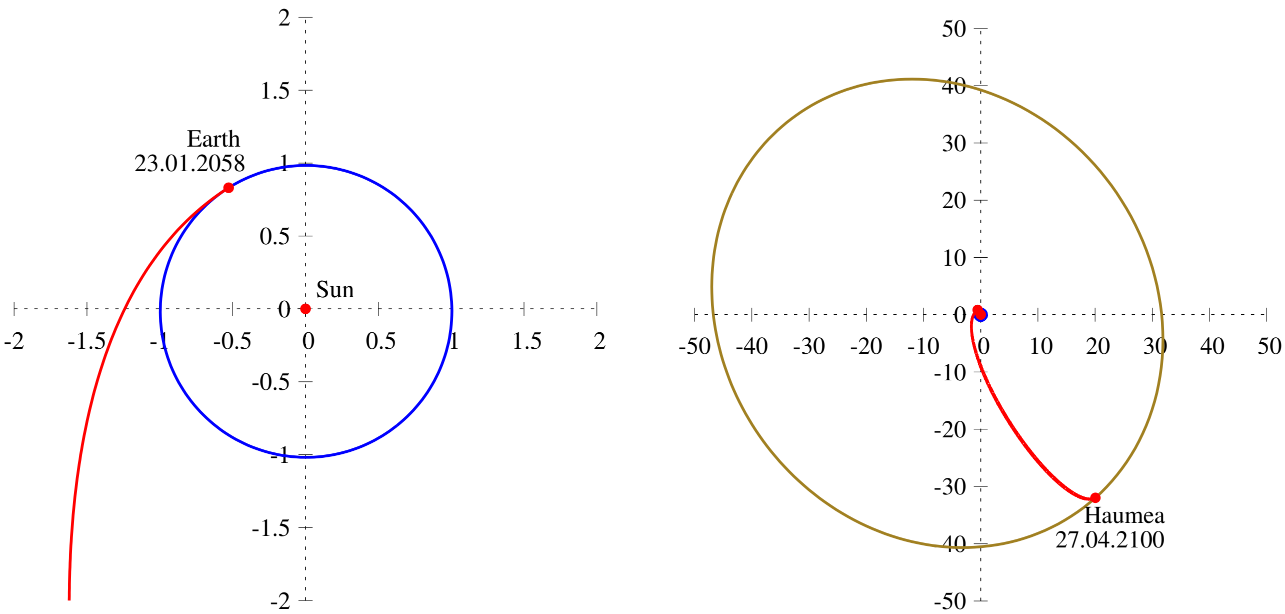

Fig. 1. Optimal transfer trajectory (red) to Haumea in the ecliptic plane. The orbit of the Earth is shown in blue and the orbit of Haumea in olive. The departure from the Earth is shown on the left and the whole trajectory on the right. The distances are given in astronomical units. The color figure can be viewed online.

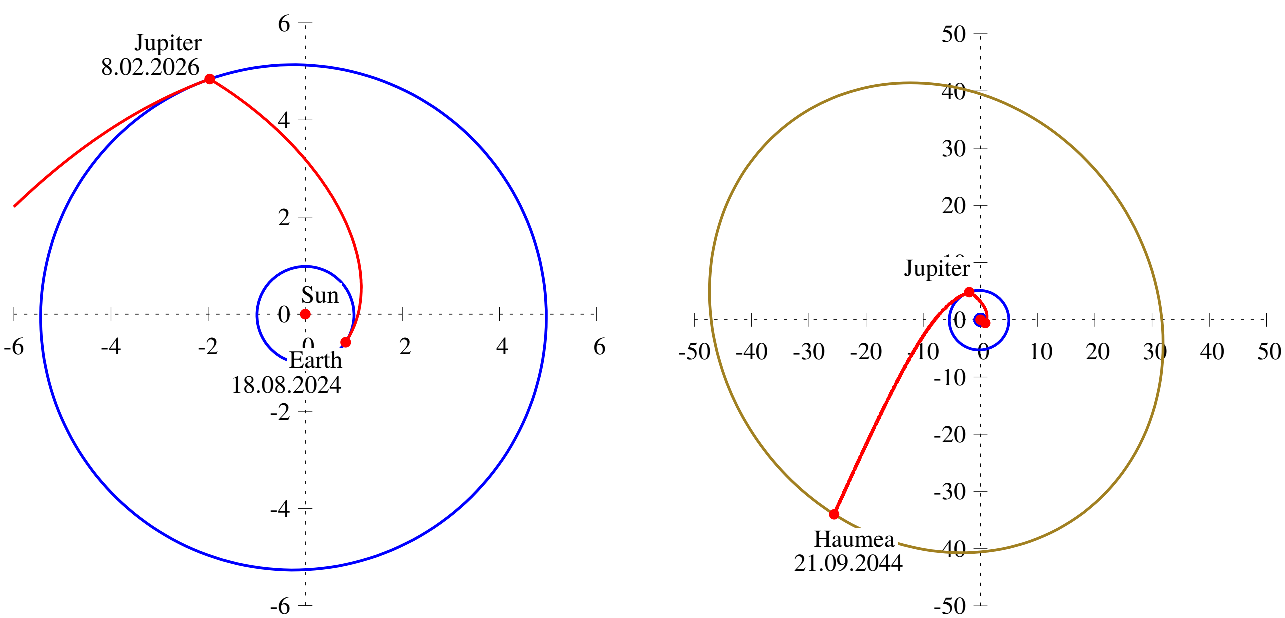

Fig. 2. Optimal transfer trajectory (red) to Haumea in the ecliptic plane, including a Jupiter swingby. The orbits of the planets are shown in blue, and the orbit of Haumea in olive. The Earth to Jupiter flight is shown on the left and the whole transfer trajectory on the right. The distances are given in astronomical units. The total time of flight was constrained to 20 years. The color figure can be viewed online.

the search of asteroids that can be encountered in the way from Earth to Makemake, the F2 transfer (EVEdvESM20y) is chosen. This transfer is shown in Figure 9. Three asteroids can be encountered with an additional ΔV of less than 1 km/s, which is not too much considering the scientific gains of the mission. The asteroids are: (96168) 1981 ER23, with an additional ΔV of only 0.04 km/s; (12062)

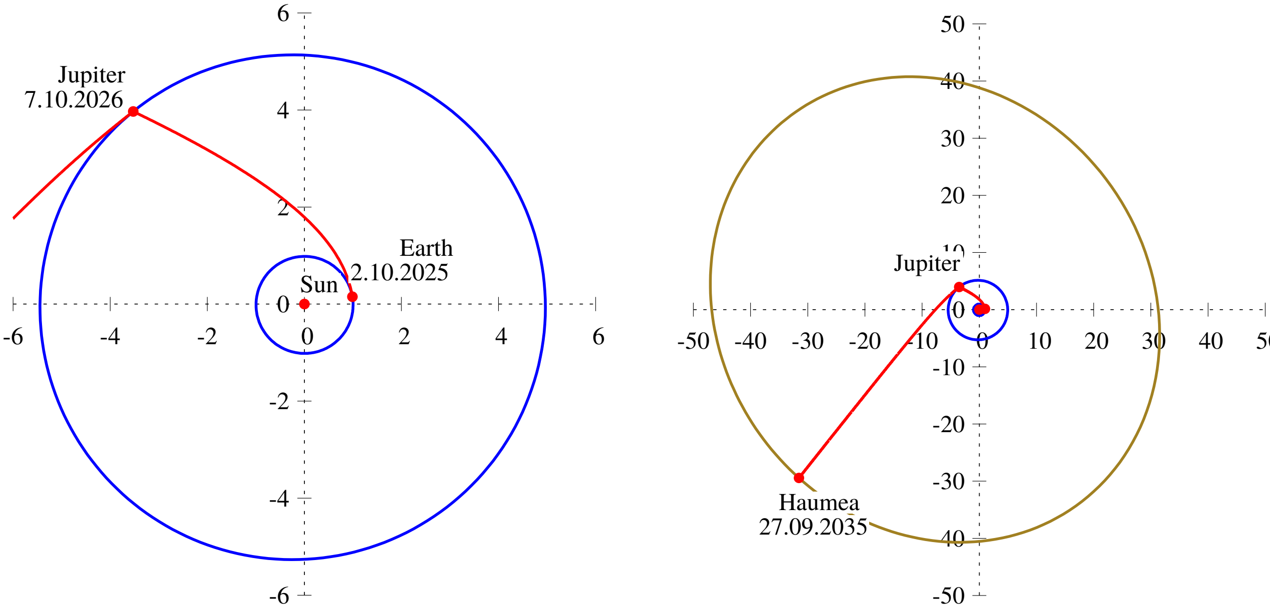

Fig. 3. The same as in Figure 2, but with a 10-year time of flight. The color figure can be viewed online.

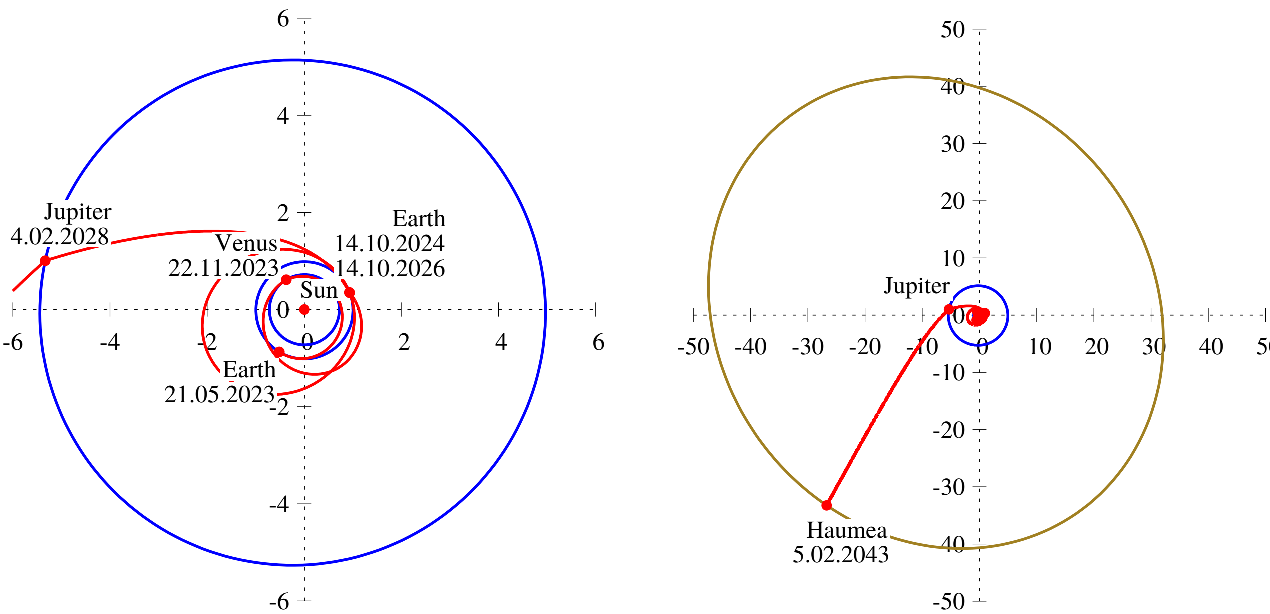

Fig. 4. Optimal transfer trajectory (red) to Haumea in the ecliptic plane, including the EVEE maneuver and the Jupiter swingby. The orbits of the planets are marked in blue, and the orbit of Haumea in olive. The departure from the Earth is shown on the left and the whole trajectory on the right. The distances are given in astronomical units. The total time of flight is constrained to 20 years. The color figure can be viewed online.

1998 FB10, with an additional ΔV of 0.12 km/s; and (135420) 2001 UT44, with additional ΔV of 0.14 km/s. The transfer trajectories reaching these three asteroids are shown in Figures 10, 11, and 12, respectively.

3.3. *Transfers to Quaoar*

Characteristics of the transfers to Quaoar are given in Table 4, where ΔV_L is the launch ΔV, V_A is the arrival velocity, ΔV_T is the total ΔV, and TOF is the time of flight. The orbit of Quaoar

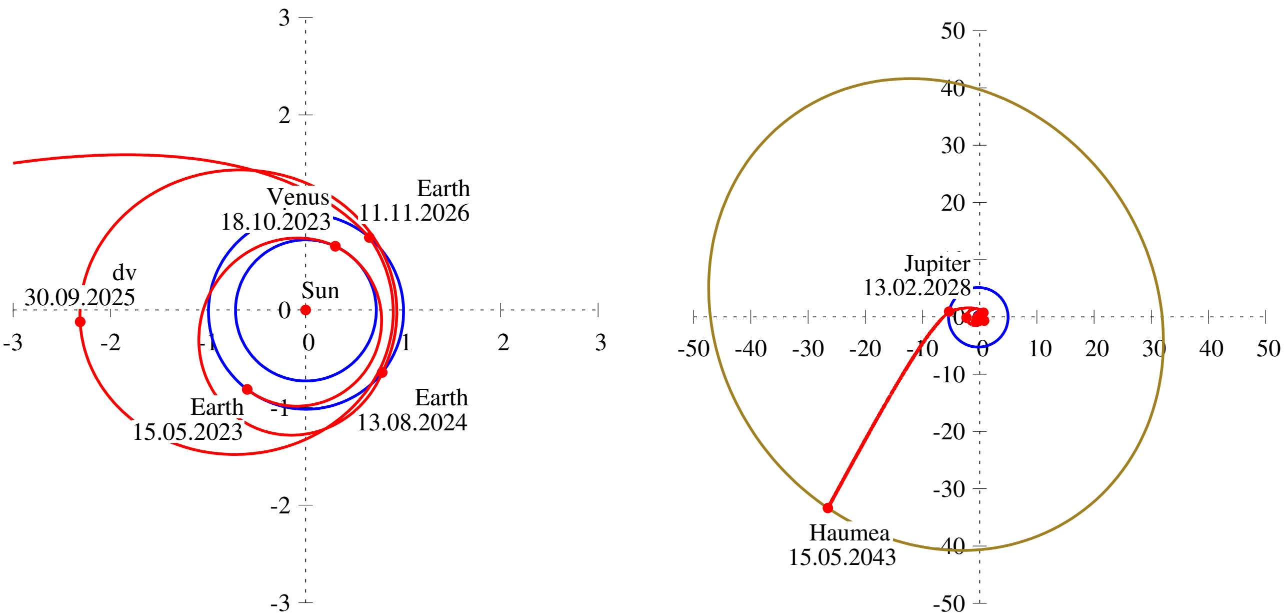

Fig. 5. Optimal transfer trajectory (red) to Haumea in the ecliptic plane, including the EVEdvE maneuver and the Jupiter swingby. The orbits of the planets are marked in blue and the orbit of Haumea in olive. The departure from the Earth is shown on the left and the whole trajectory on the right. The distances are given in astronomical units. The total time of flight is constrained to 20 years. The color figure can be viewed online.

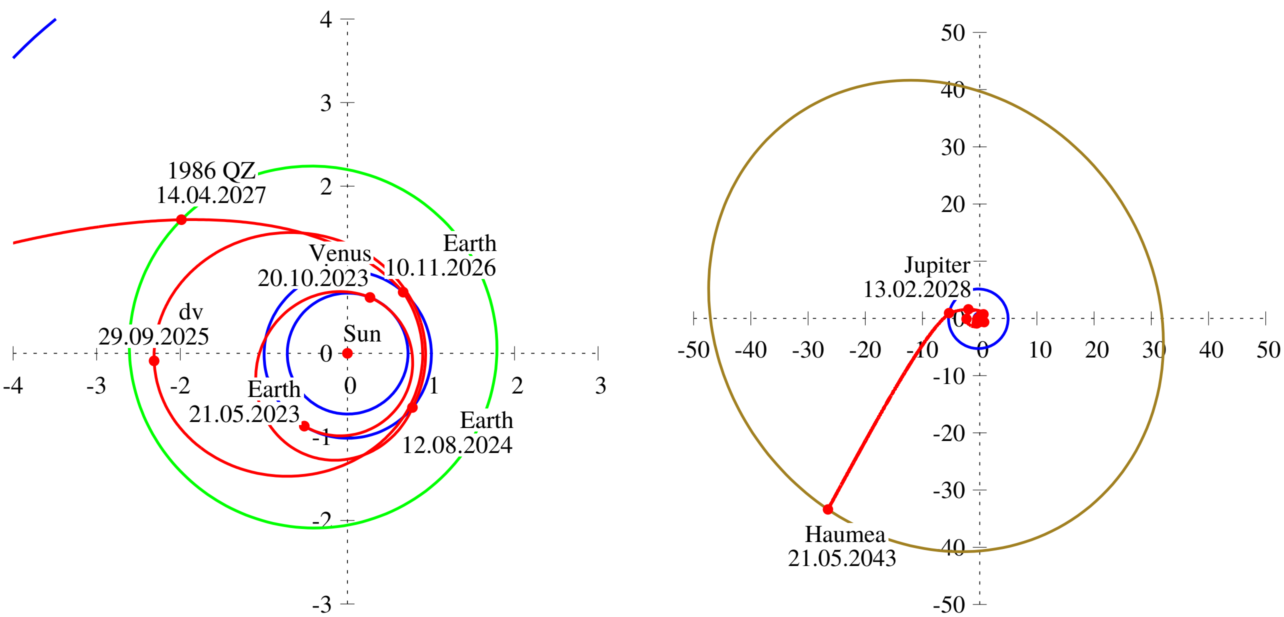

Fig. 6. Optimal transfer trajectory (red) to Haumea in the ecliptic plane, including the EVEdvE maneuver, the (11023) 1986 QZ asteroid encounter, and the Jupiter swingby. The orbits of the planets are marked in blue, the orbit of the asteroid in green, and the orbit of Haumea in olive. The departure from the Earth is shown on the left and the whole trajectory on the right. The distances are given in astronomical units. The total time of flight is constrained to 20 years. The color figure can be viewed online.

has a semi-major axis of 44 astronomical units, and this number places its orbit between the orbits of Haumea and Makemake, because the eccentricity of Quaoar is low. However, the orbital inclination of Quaoar to the ecliptic plane is 8 degrees. In this case, due to the lower inclination compared to Haumea

TABLE 3

TYPES OF OPTIMAL TRAJECTORIES TO SEND A SPACECRAFT TO MAKEMAKE

Type	Trajectory	Launch date	ΔV_L, km/s	V_A, km/s	ΔV_T, km/s	TOF, years
A1	EMnc	10.12.2034	8.33	3.42	8.33	68.39
B1	EJMnc	23.06.2034	6.39	3.24	6.39	53.36
B2	EJM20y	12.07.2034	6.57	13.95	7.36	20.00
B3	EJM10y	03.10.2025	10.41	25.78	10.43	10.00
C1	ESMnc	15.07.2028	7.31	7.21	7.31	34.52
C2	ESM20y	15.08.2031	7.86	13.60	7.87	19.99
C3	ESM10y	16.09.2033	8.26	31.88	17.72	10.00
F1	EVEdvESMnc	22.11.2024	4.21	7.390	5.00	37.68
F2	EVEdvESM20y	16.11.2024	4.28	22.25	11.83	20.00
F3	EVEdvESM20y+ast1	17.11.2024	4.29	21.97	11.87	20.00
F4	EVEdvESM20y+ast2	13.11.2024	4.30	21.97	11.96	20.00
F5	EVEdvESM20y+ast3	21.11.2024	4.24	22.83	11.97	20.00

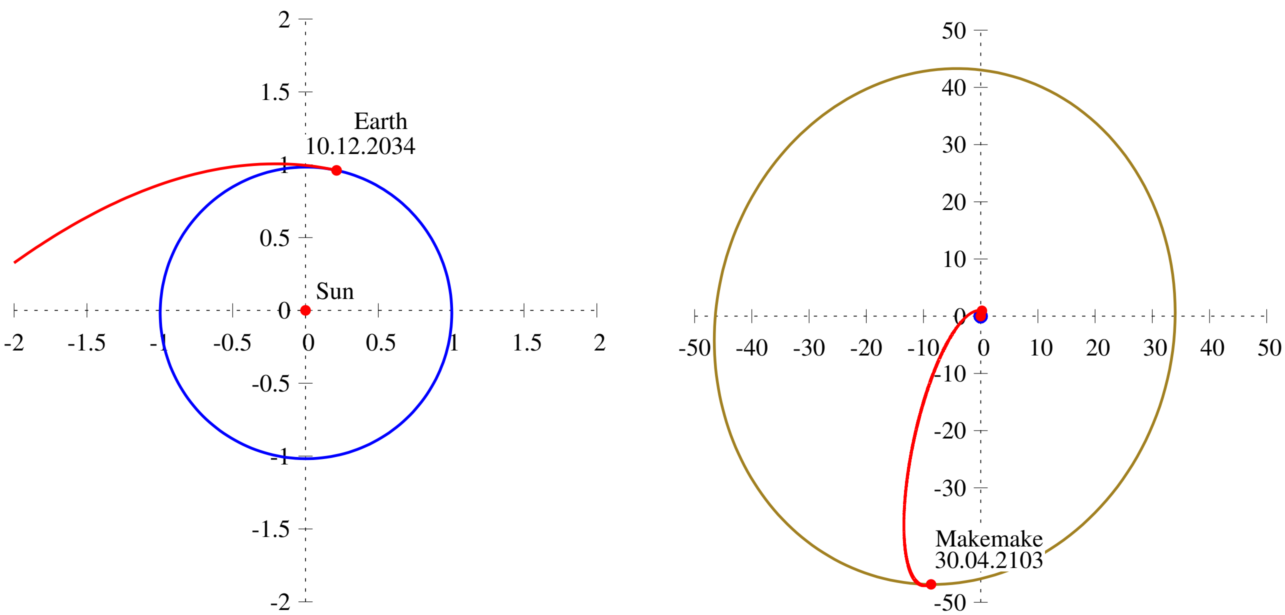

Fig. 7. Optimal transfer trajectory (red) to Makemake in the ecliptic plane. The orbit of the Earth is marked in blue, and the orbit of Makemake in olive. The departure from the Earth is shown on the left and the whole trajectory on the right. The distances are given in astronomical units. The color figure can be viewed online.

and Makemake, all transfer trajectories from Earth to Quaoar have fuel consumption, expressed by the total ΔV, smaller than the ones required for the transfers to Haumea or to Makemake. This fact can be seen if Tables 2, 3, and 4 are compared with each other. To exemplify this fact, the transfer using a Jupiter swingby and considering a 10-year time of flight can be used for comparisons. In the case of Haumea, this transfer requires a total ΔV of 9.98 km/s to be executed. For Makemake, the value is $\Delta V = 10.43$ km/s; while for Quaoar it is $\Delta V = 8.34$ km/s. Since, in this paper, we fixed a limit of 10 km/s for the total ΔV, it is possible to obtain a transfer to Quaoar with a flight time of 8 years and total $\Delta V = 9.73$ km/s. This means that Quaoar can be reached in less than a decade of flight, which makes it a very convenient target. Figure 13 shows the 8-year Earth-Jupiter-Quaoar transfer.

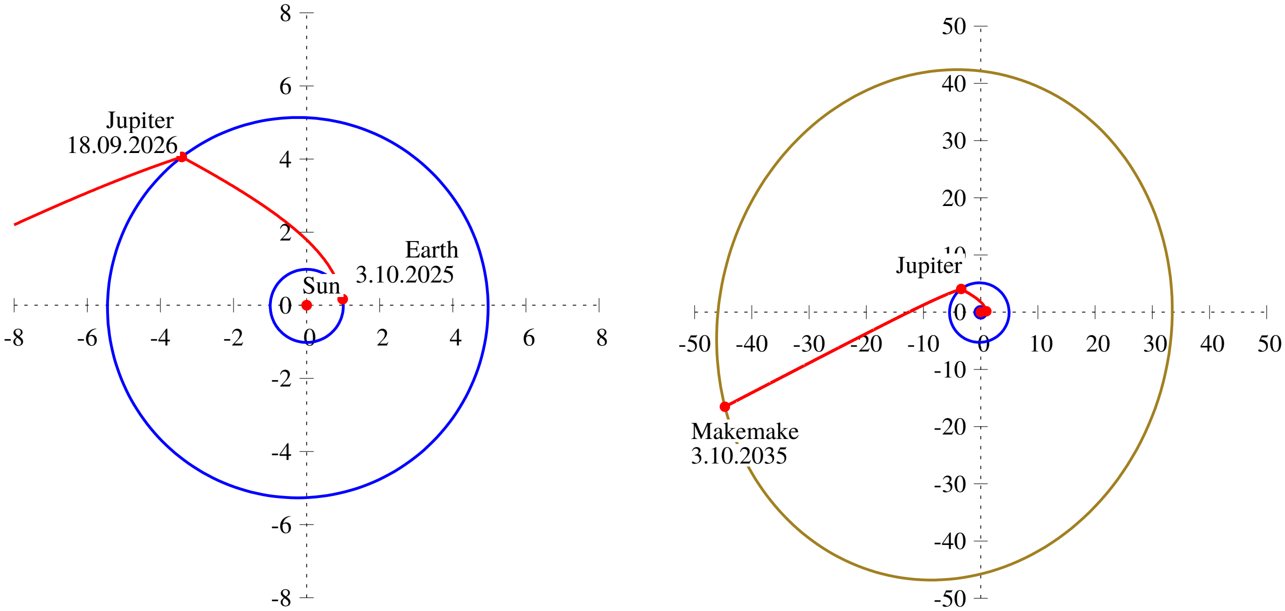

Fig. 8. Optimal transfer trajectory (red) to Makemake in the ecliptic plane, including a Jupiter swingby. The orbits of the planets are marked in blue, and the orbit of Makemake in olive. The distances are shown in astronomical units. The total time of flight is constrained to 10 years. The color figure can be viewed online.

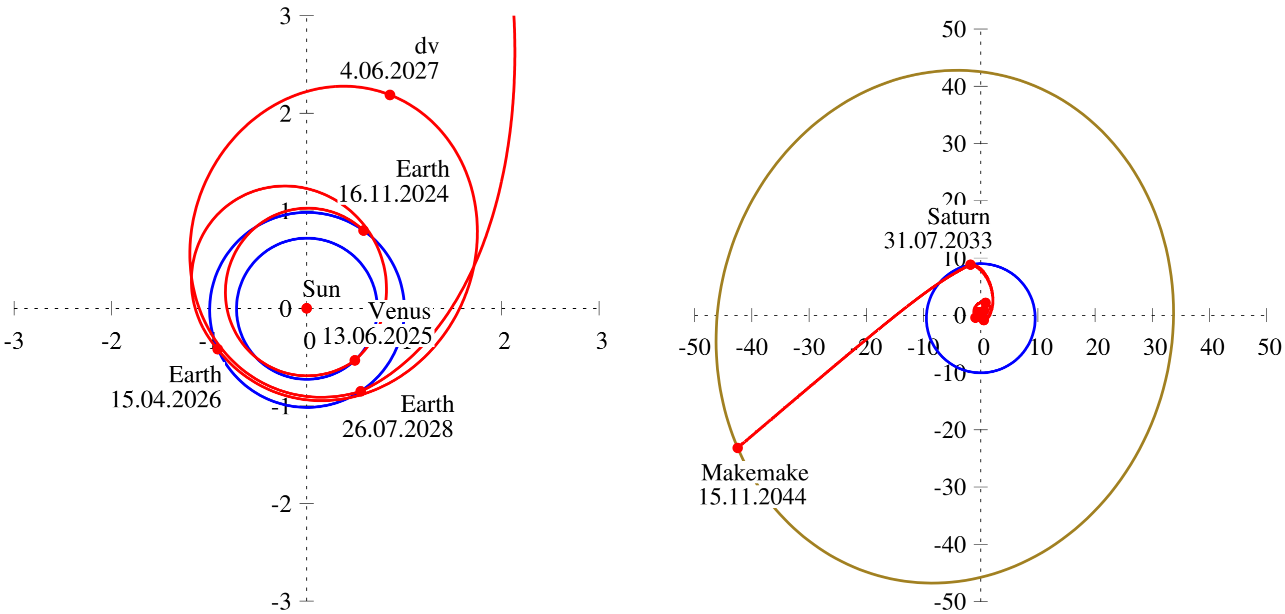

Fig. 9. Optimal transfer trajectory (red) to Makemake in the ecliptic plane, including the EVEdvE maneuver and the Saturn swingby. The orbits of the planets are marked in blue, and the orbit of Makemake in olive. The departure from the Earth is shown on the left and the whole trajectory on the right. The distances are given in astronomical units. The total time of flight is constrained to 20 years. The color figure can be viewed online.

In the case of Quaoar, similarly to that of Haumea, all the Earth-Jupiter-Quaoar transfers are more efficient, in terms of total ΔV, than the Earth-Saturn-Quaoar transfers. This fact can be seen in Table 4. Similarly to what occurred for Haumea, the EVEdvE transfer is more efficient if combined with a Jupiter swingby. Therefore, the transfer E1 (EVEdvEJQ20y) is used to search for possible as-

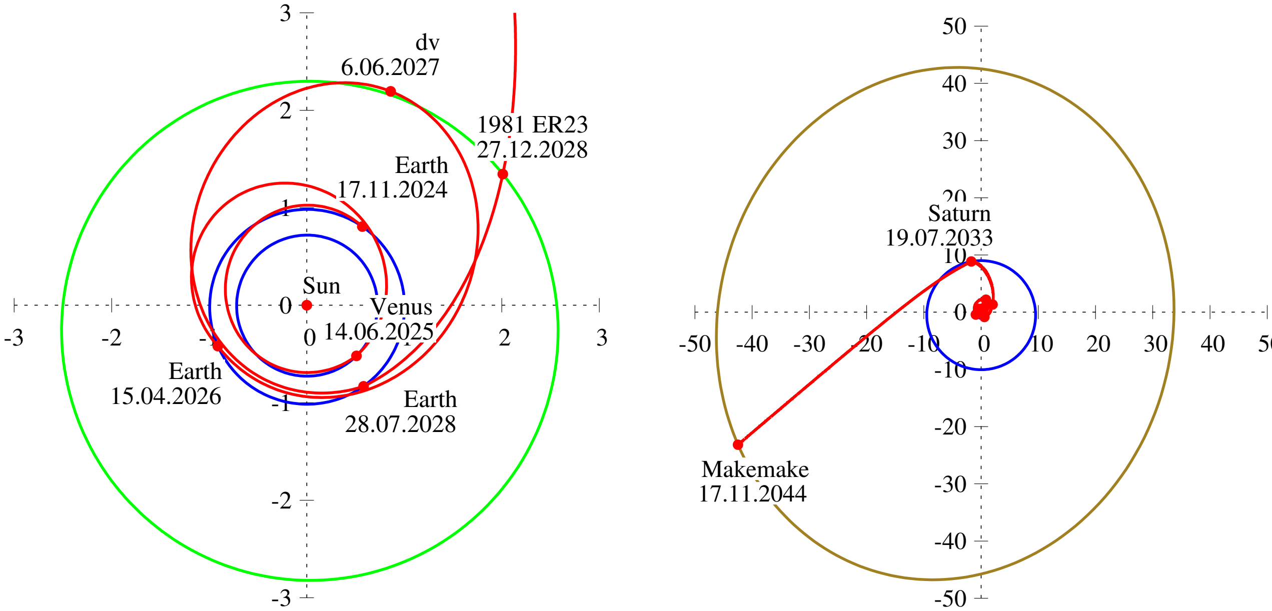

Fig. 10. Optimal transfer trajectory (red) to Makemake in the ecliptic plane, including the EVEE maneuver, the Jupiter swingby and the (96168) 1981 ER23 asteroid encounter. The departure from the Earth is shown on the left and the whole trajectory on the right. The orbits of the planets are marked in blue, the orbits of the asteroid in green, and the orbit of Makemake in olive. The distances are given in astronomical units. The total time of flight is constrained to 20 years. The color figure can be viewed online.

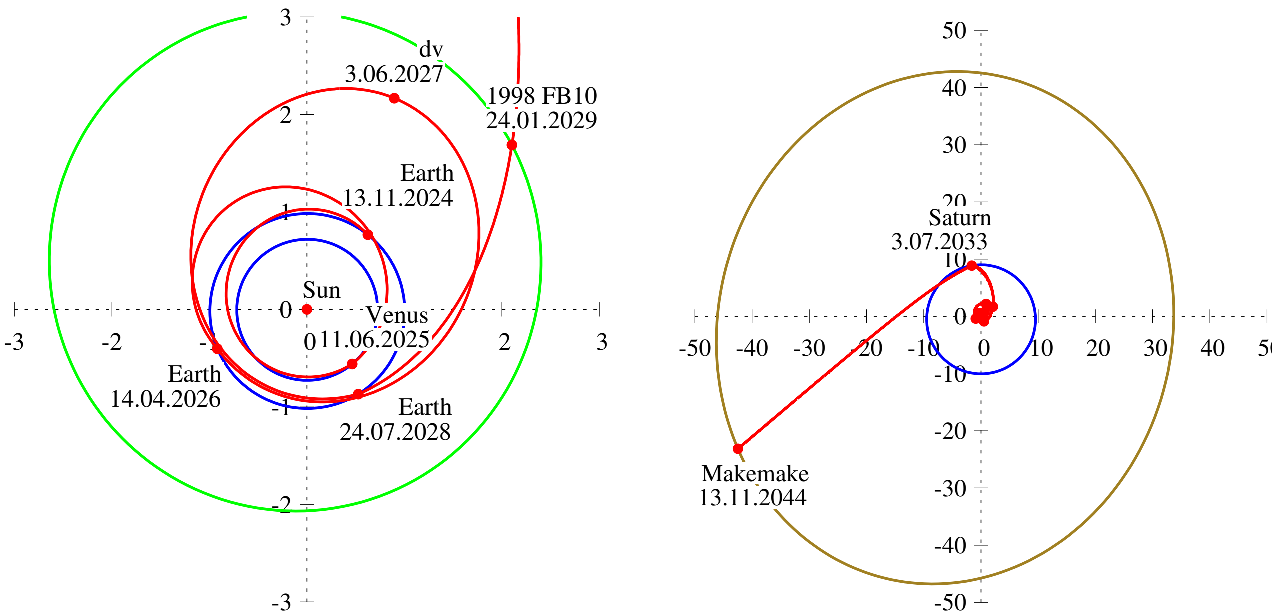

Fig. 11. Transfer type F4. The same as in Figure 10, but with the (12062) 1998 FB10 asteroid encounter. The color figure can be viewed online.

teroids encounters in the way from Earth to Jupiter. In this case, although the total ΔV of this transfer is 6.13 km/s, and this fact makes it possible to find transfers of the same type in shorter times of flight, we decided to keep the limit of 20 years of time of flight to allow the reader to compare this type of

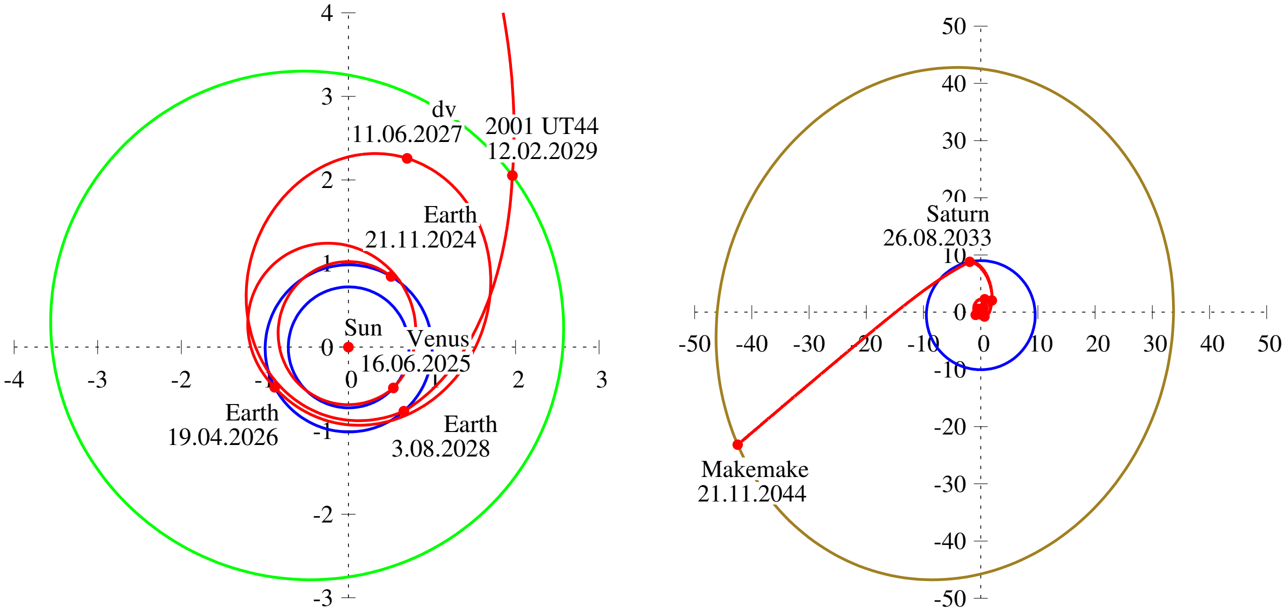

Fig. 12. Transfer type F5. The same as in Figure 10, but with the (135420) 2001 UT44 asteroid encounter. The color figure can be viewed online.

TABLE 4

TYPES OF OPTIMAL TRAJECTORIES TO SEND A SPACECRAFT TO QUAOAR

Type	Trajectory	Launch date	ΔV_L, km/s	V_A, km/s	ΔV_T, km/s	TOF, years
A1	EQnc	27.03.2023	8.84	3.98	8.39	68.46
B1	EJQnc	23.11.2027	6.70	3.08	6.70	42.74
B2	EJQ20y	22.11.2027	6.82	9.21	6.82	19.63
B3	EJQ10y	26.12.2028	8.34	20.59	8.34	9.98
B4	EJQ8y	31.12.2028	9.73	26.64	9.73	7.99
C1	ESQnc	04.07.2024	7.51	4.39	7.51	45.06
C2	ESQ20y	19.07.2029	7.43	13.36	10.10	19.99
E1	EVEdvEJQ20y	19.06.2026	4.12	10.54	6.13	19.98
E2	EVEdvEJQ20y+ast1	16.06.2026	4.14	10.54	6.39	19.99
E3	EVEdvEJQ20y+ast2	13.06.2026	4.16	10.71	7.26	19.81
I1	EVEdvEJSQ30y	06.06.2026	4.21	13.22	5.39	30.00
I2	EVEdvEJSQ25y	05.06.2026	4.24	20.61	8.71	25.00
I3	EVEdvEJSQ20y	05.06.2026	4.22	28.85	17.68	20.00

transfer for the three bodies Haumea, Makemake, and Quaoar. The transfer E1 is shown in Figure 14 as an example.

Two asteroids can be reached with an additional ΔV of around 1 km/s, a value that is not too large. The asteroid (155385) 1993 UO6 can be reached with an additional ΔV of only 0.26 km/s, while the asteroid (64378) 2001 UE122 can be visited with an additional ΔV of 1.13 km/s. The transfers that contain the passage by these asteroids are shown in Figures 15 and 16, respectively. The orbital geometry of the transfers to Quaoar also allows both Jupiter and Saturn swingbys. In a transfer with 30 years of time of flight, the total ΔV is 5.39 km/s; reducing this limit to 25 years, the total ΔV is increased to 8.71 km/s; and, finally, with a limit of 20 years, the total ΔV goes up to 17.68 km/s. This sensitive growth of the total ΔV in a period of five years of

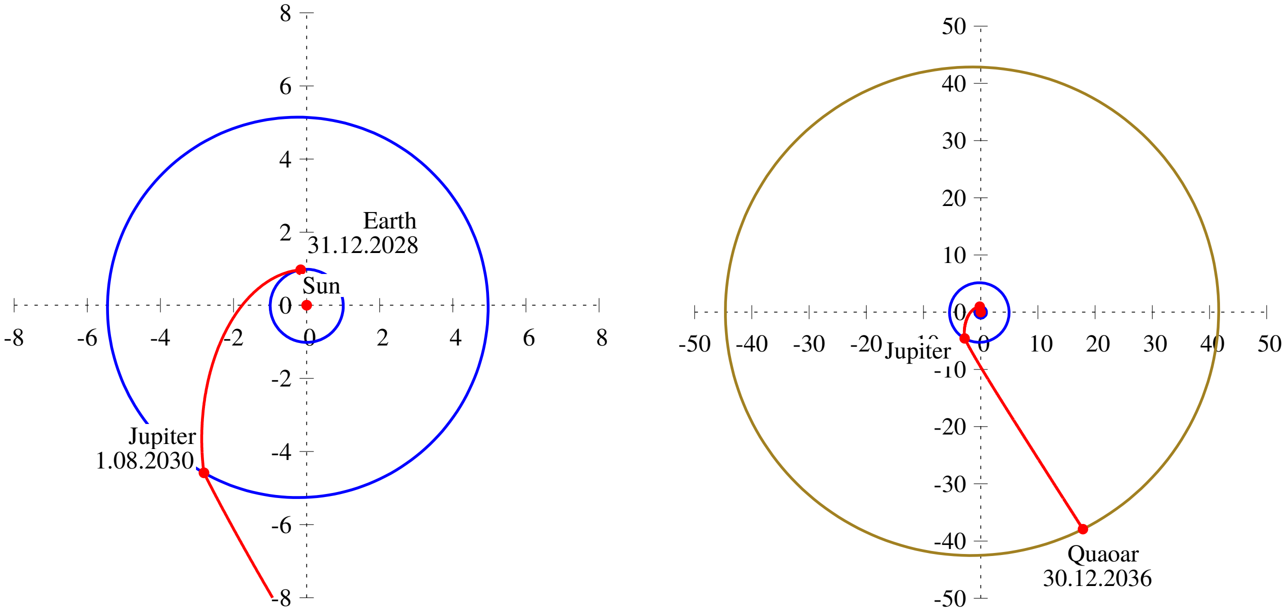

Fig. 13. Optimal transfer trajectory (red) to Quaoar in the ecliptic plane, including the Jupiter swingby. The orbits of the planets are marked in blue and the orbit of Quaoar in olive. The departure from the Earth is shown on the left and the whole trajectory on the right. The distances are given in astronomical units. The time of flight is 8 years. The color figure can be viewed online.

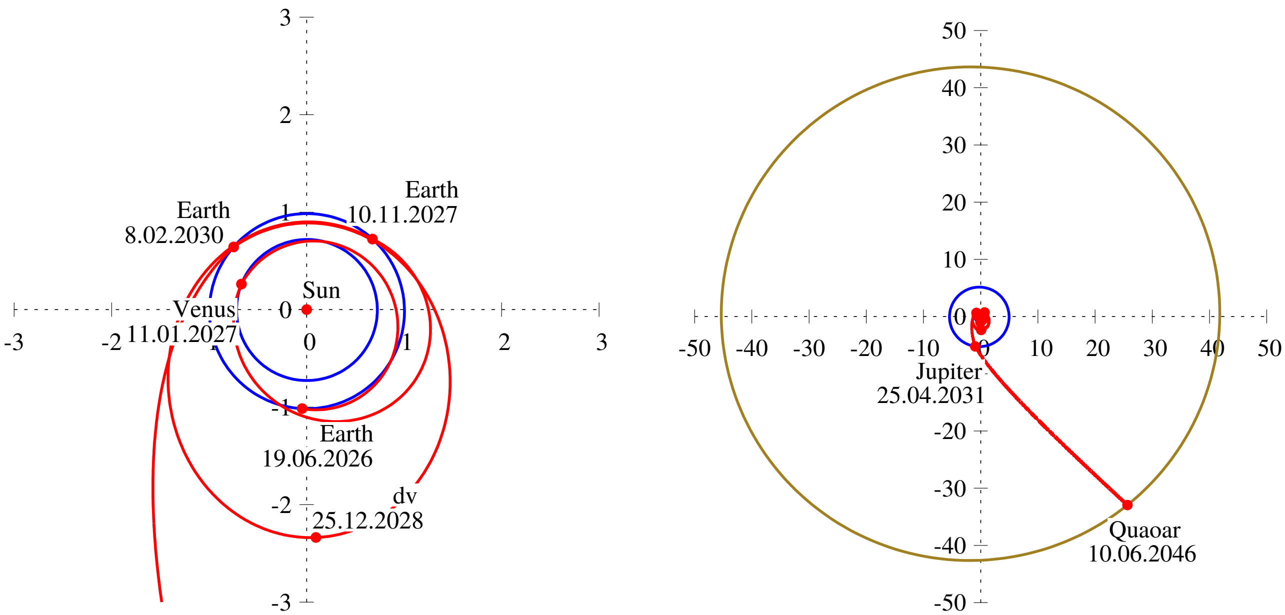

Fig. 14. Optimal transfer trajectory (red) to Quaoar in the ecliptic plane, including the EVEdvE maneuver and the Jupiter swingby. The orbits of the planets are marked in blue and the orbit of Quaoar in olive. The departure from the Earth is shown on the left and the whole trajectory on the right. The distances are given in astronomical units. The total time of flight is constrained to 20 years. The color figure can be viewed online.

time of flight indicates that the alignment of Jupiter and Saturn allows only a limited launch window for these transfers. This also indicates that the trajectory using 25 years and a total ΔV less that 10 km/s is a rare opportunity.

3.4. *Summary of the transfers*

The summary of all optimal transfers shown in this paper is presented here. Figure 17 shows the total ΔV as a function of the time of flight for all transfers. The transfers are represented by their type,

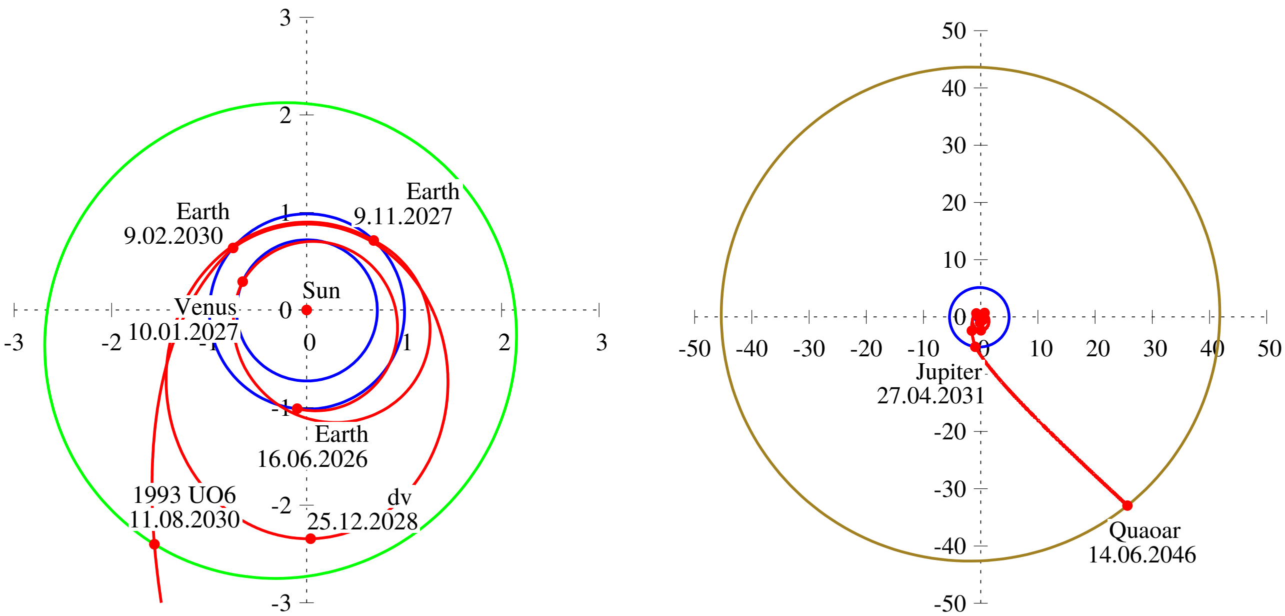

Fig. 15. Optimal transfer trajectory (red) to Quaoar in the ecliptic plane, including the EVEE maneuver, the Jupiter swingby and the (155385) 1993 UO6 asteroid encounter. The orbits of the planets are marked in blue, the orbits of the asteroids in green, and the orbit of Quaoar in olive. The departure from the Earth is shown on the left and the whole trajectory on the right. The distances are given in astronomical units. The total time of flight is constrained to 20 years. The color figure can be viewed online.

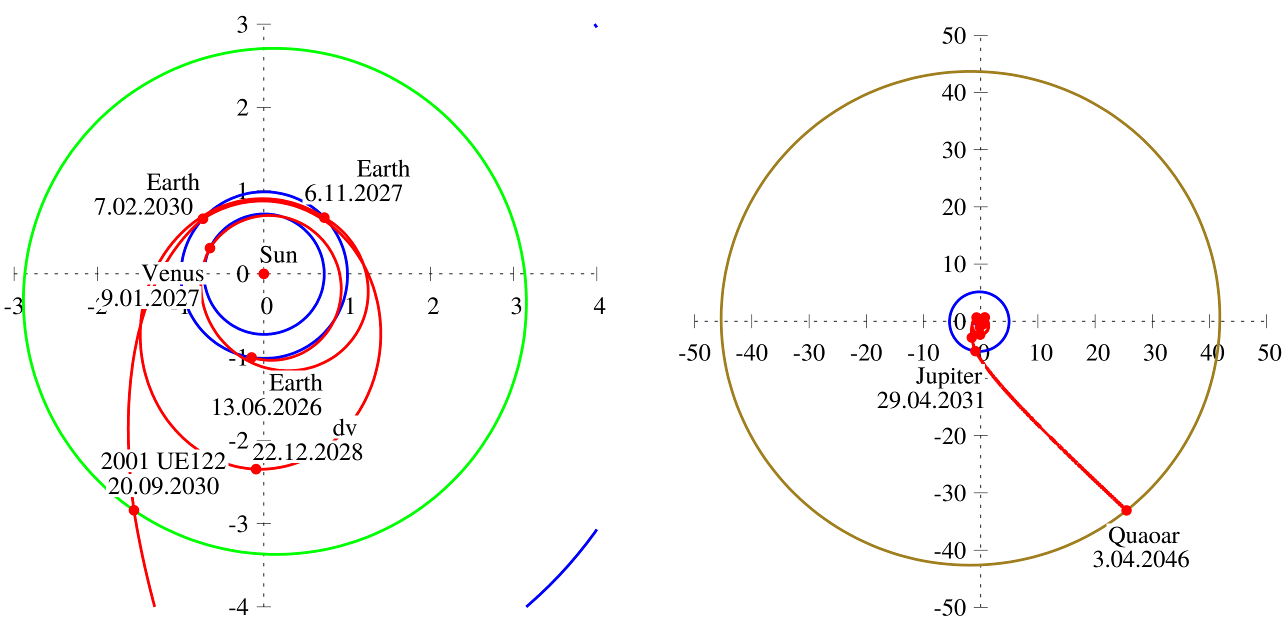

Fig. 16. Transfer type E3. The same as Figure 15, but including the (64378) 2001 UE122 asteroid encounter. The color figure can be viewed online.

with the red ones for transfers to Haumea, blue ones for Makemake, and green ones for Quaoar. Figure 18 shows the ΔV of launch for all trajectories, with the same color code as used in Figure 17.

4. CONCLUSIONS

The present paper gives results of an analysis of the spacecraft trajectories from the Earth to three of the most interesting Kuiper Belt Objects: Haumea,

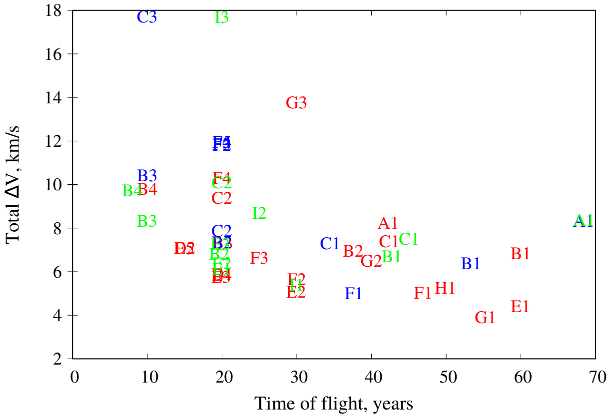

Fig. 17. Total ΔV for all types of optimal transfers as a function of the time of flight. Red: optimal transfers to Haumea; blue: optimal transfers to Makemake; green: optimal transfers to Quaoar. The color figure can be viewed online.

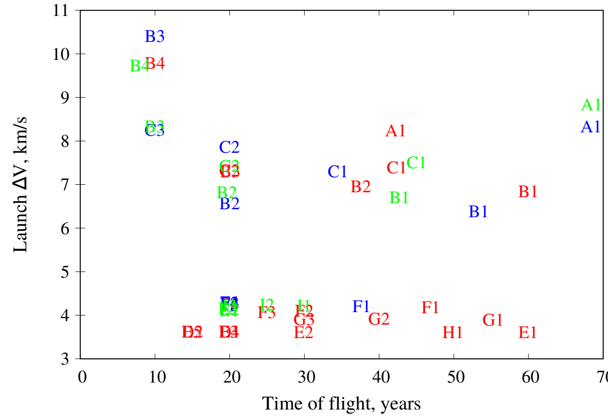

Fig. 18. ΔV at launch for all types of optimal transfers as a function of the time of flight. Red: optimal transfers to Haumea; blue: optimal transfers to Makemake; green: optimal transfers to Quaoar. The color figure can be viewed online.

Makemake, and Quaoar. The trajectories were obtained using different planets to make one or more intermediate swingby(s). The criterion to choose the best trajectories is the minimization of the total ΔV, which does not include the ΔV of the capture maneuver. The 2023-2034 interval is used as a baseline for the launch times for the mission. The results identify trajectories using a total ΔV below 10 km/s with times of flight below 20 years for all the three bodies considered as targets of the mission. Using a multi-gravity assist maneuver with the Jupiter swingby, one trajectory to each of the bodies is found with a ΔV under 10 km/s and a time of flight below 10 years. Those opportunities are not often repeated, and should be taken into account in the future plans of deep space missions. Considering the less expensive and longer transfers with a duration of 20 years, the possibility of visiting some asteroids of the main belt during the flight is shown, which increases the scientific return of the mission. Those extra observations can be made with only a small increase in the fuel consumed, sometimes below 0.1 km/s.

The authors wish to express their appreciation for the support provided by grants #406841/2016-0 and 301338/2016-7 from the National Council for Scientific and Technological Development (CNPq); Grants #2016/24561-0, 2014/22295-5, 2015/19880-6 and 2016/14665-2 from São Paulo Research Foundation (FAPESP) and for the financial support from the Coordination for the Improvement of Higher Education Personnel (CAPES).

REFERENCES

Barucci, M. A., Dalle Ore, C. M., Perna, D., et al. 2015, A&A, 584, A107

Brown, M. E. 2013, ApJ, 767, L7

D'Amario, L. A., Byrnes, D. V., & Stanford, R. H. 1982, JGCD, 5, 465

Escobal, P. R. 1968, Methods of Astrodynamics, (New York, NY: Wiley)

Fraser, W. C., Batygin, K., Brown, M. E., & Bouchez, A. 2013, Icar, 222, 357

Guo, Y. & Farquhar, R. W. 2005, AcAau, 56, 421

Kohlhase, C. E. & Penzo, P. A. 1977, SSRv, 21, 77

Luu, J. X. & Jewitt, D. C. 2002, ARA&A, 40, 63

Moore, J. M., McKinnon, W. B., Spencer, J. R., et al. 2016, Sci, 351, 1284

Ortiz, J. L., Santos-Sanz, P., Sicardy, B., et al. 2017, Natur, 550, 219

Parker, A. H., Buie, M. W., Grundy, W. M., & Noll, K. S. 2016, ApJ, 825, L9

Peralta, F. & Flanagan, S. 1995, Control Eng. Practice, 3, 1621

Pinilla-Alonso, N., Brunetto, R., Licandro, J. et al. 2009, A&A, 496, 547

Ragozzine, D. & Brown, M. E. 2009, AJ, 137, 4766

Solórzano, C. R. H., Sukhanov, A. A., & Prado, A. F. B. A. 2008, Nonlinear Dyn. and System Theory, 8, 205

Strange, N. J. & Longuski, J. M. 2002, JSpRo, 39, 9

Sukhanov, A. A. 1999, AcAau, 45, 177

Wenzel, K. P., Marsden, R. G., Page, D. E., & Smith, E. J. 1992, A&AS, 92, 207

Antonio F. B. A. Prado and Diogo. M. Sanchez: National Institute for Space Research - INPE, Av. dos Astronautas, 1758, 12227-010 São José dos Campos - SP, Brazil (antonio.prado, diogo.sanchez@inpe.br).

Alexander A. Sukhanov: Space Research Institute of the Russian Academy of Sciences, Moscow, 117997 Russia (sasha.su@hotmail.com).

Revista Mexicana de Astronomía y Astrofísica, **55**, 55–63 (2019)

MULTIWAVELENGTH OBSERVATIONS OF MASTER OT 075353.88+174907.6: A LIKELY SUPEROUTBURST OF A LONG PERIOD DWARF NOVA SYSTEM

A. S. Parikh[1], J. V. Hernández Santisteban[1], R. Wijnands[1], and D. Page[2]

Received September 18 2018; accepted November 14 2018

ABSTRACT

MASTER OT 075353.88+174907.6 was a blue optical transient reported by the MASTER-Net project on 2017 Oct 31. We carried out multiwavelength follow-up observations of this source during its 2017 outburst using *Swift* and RATIR. The source was found to be $\gtrsim$4.4 mag above its quiescent level during the peak of the outburst and the outburst lasted $\gtrsim$19 days. Our observations suggest that it was a superoutburst of a long period U Geminorum type dwarf nova system. The spectral energy distribution during the initial slow decay phase of the outburst was consistent with a disk-dominated spectrum (with spectral indices $\Gamma \approx$1.5–2.3). Afterwards, the UV flux decreased slowlier than the optical and the spectral energy distribution was very steep with indices $\Gamma \approx 3.7 \pm 0.7$. This slow UV decay may be the emission from a cooling white dwarf heated during the outburst. No X-ray emission was detected from the source since it is likely located at a large distance >2.3 kpc.

RESUMEN

MASTER OT 075353.88+174907.6 fue un objeto transitorio reportado por el proyecto MASTER-Net en 2017 Oct 31. Realizamos una campaña multi-onda de este objeto durante su erupción en 2017 con *Swift* y RATIR. La fuente fue descubierta $\gtrsim$4.4 mag por encima de su nivel mínimo en el máximo de la erupción, la cual duró $\gtrsim$19 días. Nuestras observaciones sugieren que se trata de una supererupción de un sistema tipo U Geminorum de largo período. La distribución espectral de energía en la fase inicial de la caída es consistente con un espectro dominado por el disco de acreción (con índices espectrales $\Gamma \approx$1.5–2.3). Después, el flujo UV decreció más lentamente que el óptico, con una distribución espectral de energía con indices $\Gamma \approx 3.7 \pm 0.7$. El lento declive en el UV puede deberse al enfriamiento de la enana blanca, la cual fue calentada durante la erupción. No se detectó emisión de la fuente en rayos-X, lo cual sugiere una distancia mucho mayor que 2.3 kpc.

Key Words: accretion, accretion discs — novae, cataclysmic variables — stars: dwarf novae — stars: individual: MASTER OT 075353.88+174907.6 — ultraviolet: stars

1. INTRODUCTION

Dwarf novae are a sub-set of cataclysmic variables — binary systems hosting a white dwarf and a low-mass main sequence star. In these systems, the companion is transferring mass to the white dwarf via Roche-lobe overflow and an accretion disk is formed around it. Dwarf novae can undergo outbursts, thought to occur due to thermal instabilities in the disk (see Lasota 2001, for details) resulting in a brightness increase of $\approx$6–100 times than its quiescence level (Osaki 1996). While these dwarf novae outbursts can be very homogeonous from a single source, occasionally they exhibit 'superoutbursts'. These are different from normal outbursts as they are brighter and can last 5–10 times longer

[1]Anton Pannekoek Institute for Astronomy, University of Amsterdam, The Netherlands.

[2]Instituto de Astronomía, UNAM, Mexico.

(≈15–40 days compared to ≈2–20 days in normal outbursts, the exact values depend on the type of system; Mauche et al. 2001).

MASTER OT 075353.88+174907.6 (hereafter OT 0753) was reported as a optical transient on 2017 October 31 (Balanutsa et al. 2017) by the MASTER-Net project (Kornilov et al. 2012). This transient had a B magnitude of 18.6 during the discovery observation. The Sloan Digital Sky Survey (SDSS) had previously observed the source position of OT 0753 and did not detect any source. The sensitivity limit of the SDSS in the *g'* band (which is the closest one to the Johnson B band from the MASTER-Net project) is ≈23 mag. This indicates (see also Balanutsa et al. 2017) that during the MASTER-Net detection OT 0753 was $\gtrsim$4.4 mag brighter than during its known quiescent level. Furthermore, a NUV detection within 5 arcsec of this source position was found in the *Galaxy Evolution Explorer* mission (*GALEX*; Martin et al. 2005) database. This source was observed on 2006 February 7 using *GALEX* and during that observation it had a magnitude of ≈22.9 in the NUV (Balanutsa et al. 2017). The source was not detected in the *GALEX*/FUV band. The *GALEX*/NUV detection and SDSS non-detection suggest that the source hosts a blue object when in quiescence.

To investigate the nature of this source, we carried out a multiwavelength campaign across the near-infrared, optical, UV, and X-ray bands during its 2017 outburst. We discuss the results of our observing campaign and show that this blue optical transient is likely a superoutburst of a dwarf nova which hosts a hot white dwarf that dominates the emission in quiescence.

2. OBSERVATIONS AND DATA ANALYSIS

We requested follow-up observations of OT 0753 using the *Neil Gehrels Swift Observatory* (Gehrels et al. 2004). We observed OT 0753 a total of 9 times using *Swift* (see Table 1 for a log of these observations). We obtained the first observation within a day of the initial report of the transient (see also Parikh & Wijnands 2017). This observation was carried out over all six optical and UV bands using the Ultraviolet and Optical Telescope (UVOT; Roming et al. 2005). Subsequent observations using the UVOT only observed the source in the three UV bands. Further UV and X-ray data of the source were obtained using *Swift* up to ≈1 month after the initial detection, until the source had approached its assumed quiescent level.

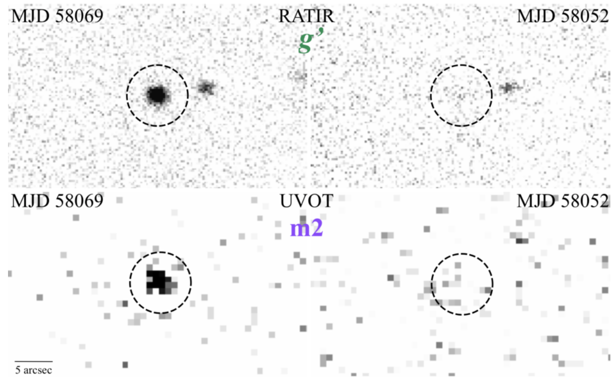

Fig. 1. The detection of OT 0753 (indicated by the dashed black circle) in outburst and its subsequent quiescence phase is shown. Top two panels: the RATIR images in the optical *g'* band; bottom two panels: the *Swift*/UVOT images in the UV m2 band. The color figure can be viewed online.

We analysed all the *Swift*/UVOT data using the Level 2 products. We added all the individual exposures (in the same band) of a given observation using `uvotimsum`. We selected a circular source extraction region having a radius of 5 arcsec. The background used was a circular region having a radius of 10 arcsec, placed on a source-free location on the CCD. The source magnitude and flux were extracted using the `uvotsource` tool. The results of this analysis is shown in Table 1.

The source was not detected in X-rays throughout our observing campaign. The upper limits on the source count rate (in the 0.5-10 keV energy range) during the individual observations taken with the X-ray Telescope (XRT; Burrows et al. 2005) observations were $\lesssim (0.8-2.4)\times 10^{-3}$ counts s^{-1} (depending on the exposure time of each observation; calculated using the 90% prescription by Gehrels 1986). To obtain the flux upper limits, we simulated X-ray spectrum using `Xspec` (Arnaud 1996) employing an absorbed power-law model and assuming that a power-law index of 2 was representative of the spectrum (similar to what has been observed from cataclysmic variables that were detected in the X-rays; Done & Osborne 1997; Balman 2015). The equivalent hydrogen column density $N_{\rm H}$ was obtained using the `HEASARC` $N_{\rm H}$ tool[3] and was found to be 3.8×10^{20} cm^{-2}. Our obtained count rate upper limits corresponded to flux upper limits of $\lesssim (4-9)\times 10^{-14}$ erg cm^{-2} s^{-1} in the 0.5–10 keV

[3] This was done using the `HEASARC` $N_{\rm H}$ tool: `https://heasarc.gsfc.nasa.gov/cgi-bin/Tools/w3nh/w3nh.pl`; (Dickey & Lockman 1990).

range. We stacked all the XRT observations using `ximage` to check whether the source could be detected if we used all available data. We found that the source was still not detected in ≈13.4 ksec of stacked XRT images and we obtained a stricter X-ray upper limit of $\lesssim 1.7 \times 10^{-4}$ counts s^{-1} (corresponding to a flux upper limit of $\lesssim 6 \times 10^{-15}$ erg cm^{-2} s^{-1}, again assuming a photon index of 2).

The optical and near-infrared follow-up was carried out by a ground-based campaign using the 1.5 m RATIR (Reionization and Transients InfraRed) telescope located at the Mexican Observatorio Astronómico Nacional (OAN) on the Sierra San Pedro Mártir (SPM) in Baja California (Watson et al. 2012). This campaign lasted from 2017 November 12 to 2017 November 25 and included 12 nights of observations with exposure times ranging from ≈0.8–2.4 hours per night (see Table 1 for a log of the RATIR observations). On each night, the source was observed using the SDSS *g'*, *i'*, and *z'* bands. We analysed the RATIR data using the `PYTHON` package `PhotoPipe`[4]. This pipeline automatically reduced all the data, carrying out the following processing steps: (1) calibrating the images using the bias, dark, and flat fields, (2) performing astrometry, and (3) co-adding the data and performing absolute photometry. For both the RATIR as well as the UVOT results, all errors are given for the 1σ confidence level and all magnitudes correspond to the AB system. The light curve constructed using these data is shown in Figure 2.

3. RESULTS

The first notice of the outburst of OT 0753 was published by the MASTER-Net Project on 2017 October 31 (in the *B* band, indicated by the blue diamond in the upper panel of Figure 2; Balanutsa et al. 2017). The rise to outburst of OT 0753 was not detected and the exact day on which the outburst began is not known. We examined the *Gaia* alerts[5] and found that it was detected by *Gaia* on 2017 October 28 (≈3 days before the reported detection from the MASTER-Net project; the source was observed twice using the *Gaia G* broadband filter, indicated by the blue-green squares in the upper panel of Figure 2). However, this information was not immediately publicly available and could only be retrospectively obtained. We examined the pre-outburst *GALEX* and SDSS data for this source. We assumed that the archival *GALEX* data (detected in the NUV and not detected in the FUV) and the non-detection by the SDSS are representative of our system in (pre-outburst) quiescence (see also Balanutsa et al. 2017). These data are summarized in Table 1. We estimated the upper limit of the source magnitude in the *GALEX*/FUV band using the known sensitivity versus exposure time relation[6].

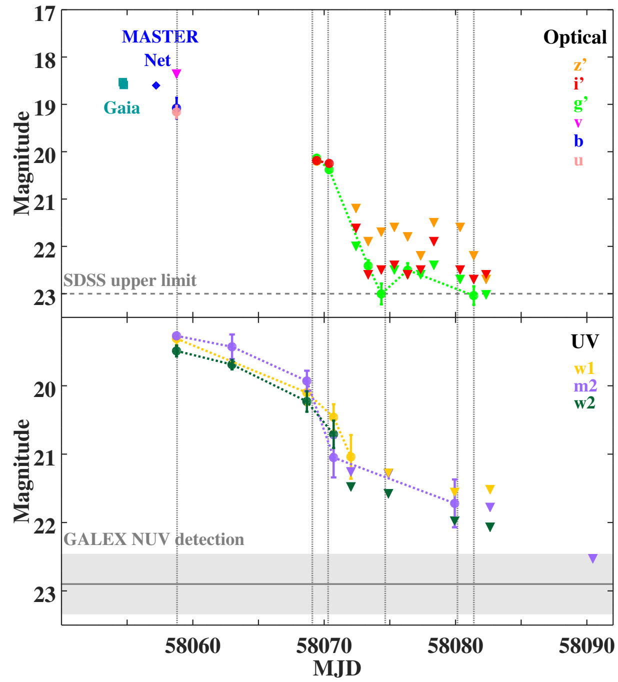

Fig. 2. The evolution of OT 0753 across the various optical/near-infrared (upper panel) and UV bands (lower panel) is shown. The upper panel also shows the detection of OT 0753 as reported by the *Gaia* Photometric Alert (blue-green squares) and the MASTER-Net project (blue diamond; Balanutsa et al. 2017). The SDSS detection limit is shown in the upper panel and the *GALEX*/NUV detection level (along with its error bar as indicated by the grey band) is shown in the lower panel. All magnitudes correspond to the AB system. The grey vertical dashed lines indicate the times for which we have constructed the SEDs shown in Figure 3. The color figure can be viewed online.

The RATIR and *Swift*/UVOT light curves are shown in Figure 2. The outburst displayed a slowly decaying phase that lasted $\gtrsim$16 days from MJD 58054 to 58070. The first RATIR observation was only obtained near the end of this slow decay phase. OT 0753 was only detected in the *i'* and *z'* near-infrared bands using RATIR during this slowly decaying outburst phase. After MJD 58070 the optical magnitude rapidly decayed, by a factor

[4]https://github.com/maxperry/photometrypipeline.
[5]http://gsaweb.ast.cam.ac.uk/alerts/alertsindex.
[6]http://www.galex.caltech.edu/DATA/gr1_docs/GR1_Observers_guide_v1.htm.

TABLE 1

LOG OF OBSERVATIONS OF OT 0753 WITH *SWIFT*/UVOT AND RATIR.*

***Swift*/UVOT**

MJD	Observation ID	Total exposure (s)	Magnitude (AB)						Flux ($\times 10^{-17}$ erg s^{-1} cm^{-2} Å^{-1})					
			v	b	u	w1	m2	w2	v	b	u	w1	m2	w2
58058.8	00010373001	988	<18.36	19.1±0.2	19.2±0.1	19.3±0.1	19.3±0.1	19.5±0.1	<16.8	13.4±2.7	19.5±2.4	43.0±2.1	43.0±2.1	42.1±3.0
58063.0	00010373002	1788	–	–	–	–	19.4±0.2	19.7±0.1	–	–	–	–	37.1±6.1	35.0±2.2
58068.7	00010373003	1982	–	–	–	20.1±0.2	19.9±0.2	20.2±0.2	–	–	–	14.6±2.1	23.5±3.3	21.4±2.9
58070.7	00010373004	951	–	–	–	20.5±0.2	21.1±0.3	20.7±0.2	–	–	–	10.4±1.9	8.4±2.3	13.7±2.5
58072.0	00010373005	1033	–	–	–	21.0±0.3	<21.3	<21.5	–	–	–	6.12±1.8	<6.91	<6.8
58075.0	00010373006	1627	–	–	–	<21.3	<21.3	<21.6	–	–	–	<4.93	<6.71	<6.1
58079.9	00010373008	946	–	–	–	<21.6	21.7±0.4	<22.0	–	–	–	<3.81	4.5±1.5	<4.3
58082.6	00010373009	1062	–	–	–	<21.5	<21.8	<22.1	–	–	–	<3.93	<4.3	<3.9
58090.5	00010373010	2948	–	–	–	–	<22.5	–	–	–	–	–	<2.2	–

RATIR

MJD	Total exposure (s)	Magnitude (AB)			Flux ($\times 10^{-18}$ erg s^{-1} cm^{-2} Å^{-1})		
		g'	*i'*	*z'*	*g'*	*i'*	*z'*
58069.4	8580	20.1±0.1	20.2±0.02	20.2±0.1	42.2±1.8	15.8±0.49	10.8±0.8
58070.4	3480	20.4±0.1	20.3±0.1	–	33.7±2.2	14.9±1.1	–
58072.4	3900	<22	<21.62	<21.2	<7.6	<4.2	<4.3
58073.4	3000	22.4±0.1	<22.6	<21.9	5.2±0.5	<1.7	<2.3
58074.4	3000	23.0±0.2	<22.5	<21.7	3.0±0.5	<1.9	<2.7
58075.3	3000	<22.5	<22.4	<21.6	4.8±0.0	<2.1	<3.0
58076.4	3000	22.5±0.2	<22.6	<21.8	4.8±0.6	<1.7	<2.5
58077.4	3000	<22.6	<22.5	<22.2	<4.4	<1.9	<1.7
58078.4	3000	<22.4	<21.9	<21.5	<5.3	<3.3	<3.3
58080.4	3000	<22.7	<22.5	<21.6	<4.0	<1.9	<3.0
58081.4	3000	23.0±0.2	<22.7	<22.2	2.9±0.5	<1.6	<1.7
58082.3	3000	<23.0	<22.6	<22.7	<3.0	<1.7	<1.1

Summary of observations using other instruments

Instrument	MJD	Band	Magnitude	Flux ($\times 10^{-18}$ erg s^{-1} cm^{-2} Å^{-1})
SDSS	–	*g'*	$\lesssim$23	$\lesssim$3.0
GALEX	53773.4	NUV	22.9±0.5	14.3±8.3
GALEX	53773.4	FUV	$\lesssim$21.5	$\lesssim$117.1
Gaia	58054.7	*G*	≈18.5	≈93.1
Gaia	58054.8	*G*	≈18.6	≈88.1
MASTER-Net	58057.2	*B*	≈18.6	≈14.8

*The log of the observations of OT 0753 of our *Swift*/UVOT and RATIR observing campaign is tabulated. The outburst observations obtained by *Gaia* and the MASTER-Net project and the archival quiescent observations using SDSS and *GALEX* are also shown. All the errors are presented for the 1σ confidence level and all magnitudes correspond to the AB system.

≈3 in ≈3–5 days, to values close to the SDSS upper limit determined when OT 0753 was (assumed to be) in quiescence. Around this time the UV magnitude also began to decrease but this decrease was slow compared to the optical decay. The UV magnitude only decreased by a factor of $\gtrsim$1.5 over the same time (as compared to a drop by a factor ≈3 in the optical in ≈3–5 days). In spite of this decrease, during the next observations (at MJD 58075) the UV magnitude did not approach its assumed pre-outburst quiescent level and continued to decay slowly. The last observation of the source, carried out on MJD 58091, indicated an upper limit of $\lesssim$22.5 mag in the m2 band. This band is similar to the NUV band on board *GALEX*. Thus, our last UVOT observation of OT 0753 indicated an upper limit consistent with the known *GALEX*/NUV quiescent level (of ≈22.9±0.5 mag; see also Figure 2), suggesting that the source was (likely) back in quiescence.

We constructed several spectral energy distributions (SEDs; see Figure 3) of OT 0753 to understand the broadband evolution of the source during its outburst. The (quasi-)simultaneous SEDs were constructed at the times indicated by the vertical dotted grey lines in Figure 2. We calculated the spectral indices (Γ) corresponding to these SEDs using the relation

$$F_\lambda \propto \lambda^{-\Gamma}. \quad (1)$$

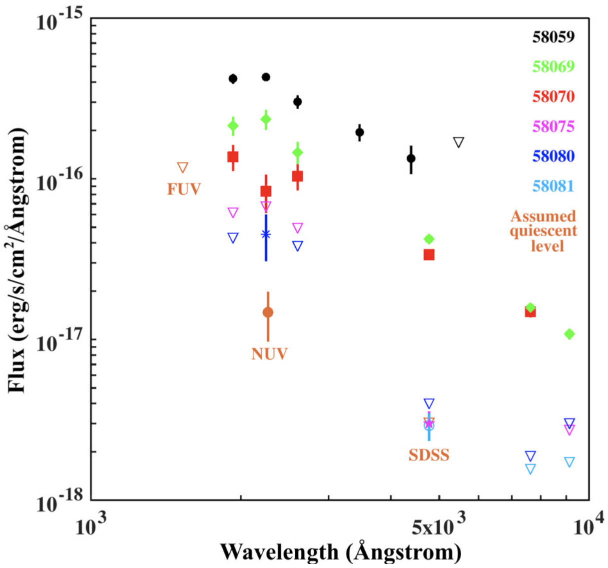

Fig. 3. The SED evolution of OT 0753 at various times is shown. The vertical dotted grey lines in Figure 2 indicate the times for which these SEDs were constructed. The assumed quiescent level using the pre-outburst *GALEX* and SDSS data is shown in orange. The color figure can be viewed online.

The SEDs corresponding to the broadband coverage of the initial slow outburst decay (over MJD 58059 to 58070) are shown in Figure 3 (as black •, green ◆, and red ■, respectively; upper limits are always shown using ∇ in the appropriate colour). These SEDs fit well a blackbody model. The spectral indices corresponding to these SEDs were $\Gamma \approx$1.5–2.3 and such values are consistent with the expected emission from a disk-like spectrum (Frank et al. 2002).

Several observations during the subsequent rapid outburst decay stage (after MJD 58070) yielded only upper limits with very few detections across the various bands. The SED constructed for the observations around MJD 58075 is unconstrained with $\Gamma \lesssim$4.1 (plotted as magneta ★ in Figure 3).

Further, we examined the SED shape around MJD 58080 and 58081 (near the end of the rapid optical and corresponding slow UV decay phase, as shown by the dark blue ✳ and light blue ○, respectively, in Figure 3). Unfortunately, detections were only obtained in either the UV *or* the optical bands for each of these days. However, the source magnitude level at this stage of the outburst is not expected to vary much across time scales of day.[7] Thus, we have a quasi-simultaneous detection in the optical and UV bands which suggests a very steep SED, with $\Gamma \approx$3.7±0.7.

The discussion in § 4 shows that this very steep SED a few days after the end of its outburst might not be unrealistic for the quiescent state of OT 0753. Fitting a blackbody model to this SED indicated a temperature of $\gtrsim$20,000 K. The actual temperature may also be indicative of significantly higher temperatures since for an SED corresponding to these high spectral indices our coverage over the optical and UV bands only probes the tail of the Rayleigh-Jeans distribution ($F_\lambda \propto \lambda^{-4}$). A further increase in this temperature does not significantly change the spectral index calculated over the wavelength range we probe.

If the pre-outburst flux is indeed representative of the quiescent flux level of the source, then the source flux must drop further after MJD 58080–58081. This is confirmed by the UV upper limit we obtained around MJD 58091 (see Table 1 and Figure 2) which indeed demonstrates that the source decreased further (at least in the UV).

We also constructed an SED at the assumed pre-outburst quiescent level, using the *GALEX* and SDSS data, as is shown in orange in Figure 3. The spectral index obtained for our assumed pre-outburst quiescent level is $5.3 \gtrsim \Gamma \gtrsim 2.5$. The upper limit determined using the *GALEX*/FUV band is unconstraining. We fit this pre-outburst quiescent level SED with a blackbody model which results in a blackbody temperature $\gtrsim$12,000 K.

4. DISCUSSION

We report on the near-infrared, optical, and UV behavior of the transient source OT 0753 during its 2017 outburst and subsequent quiescence. The broadband spectral behavior of the source, the length of the outburst ($\gtrsim$19 days), and the increase in magnitude above its quiescent level ($\gtrsim$ 4.4 mag) indicates that this is likely a superoutburst of a dwarf nova.

Otulakowska-Hypka et al. (2016) have presented the statistical properties of several dwarf nova by studying their outbursts. We use their study to learn more about OT 0753 based on its properties that we observe. We note that their study is based only on optical data and therefore we will only use properties determined from our optical observations to compare them to their results. The duration of the superoutburst of OT 0753 in the optical was $\gtrsim$19 days. From

[7]Our source does not exhibit rebrightenings (see discussion in § 4.3). Furthermore, photometric studies of sources that do not exhibit rebrightenings during this stage of their outburst (when they are returning to quiescence) do not show large variations on time scales of a day (Cannizzo 2012).

this value we can infer (using the trend they observe of the duration of the superoutburst versus the amplitude of the superoutburst; see their Figure 16) an expected optical amplitude increase of $\gtrsim$4 mag which is consistent with what we have observed for OT 0753. This supports the inference that OT 0753 is a superoutburst of a dwarf nova.

The 2017 superoutburst is the first reported outburst from this system. Using the relationship between the amplitude of the superoutburst and the amplitude of the normal outburst presented by Otulakowska-Hypka et al. (2016, see their Figure 13), we find that the amplitude of the normal outburst is $\approx$1–1.5 magnitude fainter than the superoutburst. This indicates that normal outbursts of OT 0753 will only have a magnitude of $\approx$20 in the optical bands meaning that the peak amplitude of such normal outbursts from this source may not be detectable by the various sky surveys. For example, the survey limit of the MASTER-Net project (based on its individual snapshots) is $\approx$20–21 mag and that of the Catalina Real Time Survey (Drake et al. 2009), which also observes this part of the sky, is only $\approx$19–19.5 mag. This could explain why the superoutburst of this source was the first activity to be detected and reported and why any previous normal outbursts were missed.

The relation between the amplitude of the superoutburst and the recurrence time between two consecutive superoutbursts presented by Otulakowska-Hypka et al. (2016, see their Figure 9) predicts that superoutbursts in this source should recur every $\approx$230 days. It is unknown why the source has not been observed before its 2017 superoutburst. During a superoutburst, similar to the 2017 one we study, the source is above the survey limit of several all sky surveys only for $\lesssim$5 days. Since the observation cadence of the source location by the various sky surveys is relatively sparse and since the number of days on which the source would be detected is small, it is not very surprising that the source has not been previously detected during a superoutburst. Alternatively, it could also be that OT 0753 has a superoutburst recurrence time longer than the $\approx$230 days predicted using the relation presented by Otulakowska-Hypka et al. (2016). Such a longer recurrence time is observed for sources that have a lower mass transfer rate (e.g., WZ Sge; Lasota et al. 1995).

4.1. *Cooling of the White Dwarf?*

Observations of white dwarfs after the end of dwarf nova outbursts show that they may be heated during the outburst and cool once the outburst ceases. White dwarfs in both short and long orbital period systems were found to have cooled by $\approx$ 4,000–7,000 K, $\approx$40–70 days after the end of their outbursts (Gänsicke & Beuermann 1996; Long et al. 1994; Godon et al. 2017).

We examined OT 0753 during its 2017 outburst and subsequent quiescence. We found that the SED evolves from resembling emission from a hot accretion disk to one that has a very steep spectral index (of $\Gamma\approx3.7\pm0.7$, indicating a blackbody temperature of $\gtrsim$20,000 K; see also § 3) when the source transitions from the slow decay during the outburst to quiescence. During this transition, the optical magnitude of OT 0753 fell off faster than the UV magnitude, as shown in Figure 2. The abrupt drop in the optical magnitude is likely representative of the cessation of the outburst and the retreat of the disk. The slow decay in the UV magnitude may be the white dwarf cooling after the superoutburst during which it may have been significantly heated due to the accretion. This suggests that the post-outburst spectrum may be dominated by a hot white dwarf. However, it is unknown if the quiescent disk provides a large contribution to this slowly decaying UV flux.

OT 0753 could be a promising source to study cooling in white dwarfs after being heated during its outburst (see discussion above). However, from its position in the sky and its peak outburst flux it seems to be located in the Galactic halo and it may not be close enough (see discussion in § 4.5 for a distance estimate) to allow a sensitive study of this possible cooling.

4.2. *OT 0753 Hosts a Hot White Dwarf in Quiescence*

Before its 2017 outburst, OT 0753 had only been detected in the NUV band on board the *GALEX* satellite. The source was not detected by the SDSS. The assumed quiescent level inferred using the *GALEX* and SDSS data also exhibits a steep spectral index in quiescence (with $5.3 \gtrsim \Gamma \gtrsim 2.5$). Such a blue quiescent spectrum is likely indicative of the tail of a Rayleigh-Jeans distribution and further supports that OT 0753 may host a hot white dwarf in quiescence even after all the heat deposited on the star during the outburst has been radiated away.

4.3. *Orbital Period of OT 0753*

The length of a superoutburst is not enough to definitively infer the orbital period of a dwarf nova system, because there exists a degeneracy between the length of the superoutburst and the orbital period as both systems having a short and long (above the gap) orbital period can exhibit superoutbursts of similar duration. This can be seen from Figure 18 of Otulakowska-Hypka et al. (2016). The effective white dwarf temperature can help break this degeneracy since systems located above the period gap host hot white dwarfs (likely due to the high mass accretion rate on to the white dwarf; see Figure 21 of Pala et al. 2017). Studying the SED we find that OT 0753 likely hosts a hot white dwarf that has an effective temperature $\gtrsim$20,000 K (see § 3). From Figure 21 in Pala et al. (2017) it can be seen that only one short period system has an effective temperature >20,000 K. Thus, this suggests that our source is likely a long period system having a period of ≈4–5 hours.

Several dwarf nova sources exhibit 'rebrightenings' which are episodes of increase of flux after the end of the initial outburst (see for e.g., WZ Sge; Patterson et al. 2002; Kato et al. 2009). Their peak fluxes are observed to reach the flux level observed at the end of the slow decay stage of the outburst. These rebrightenings are hypothesized to be caused by a 3:1 resonance, by the interaction between a precessing eccentric accretion disk and the secondary star in certain specific system configurations (O'Donoghue 2000). These systems have a mass ratio that is small enough ($q = \mathrm{M}_2/\mathrm{M}_1 < 0.25$, where M_1 is the mass of the white dwarf and M_2 is the mass of the donor; Whitehurst 1988) to accommodate a large accretion disk where a 3:1 resonance can occur (O'Donoghue 2000). It is found that these are systems that have short orbital periods ($\lesssim$2.4 hours). OT 0753 was observed almost every day and showed a continuous decay trend towards the end of its outburst. The subsequent detection and upper limits indicated that likely no rebrightenings occurred and none have been missed by our coverage. This evidence further supports our inference that OT 0753 is likely a source above the period gap and not a short period system. Alternatively, it could also be a short period dwarf nova that experiences a type D outburst. Type D outbursts are outbursts in short period dwarf nova systems that do not exhibit 'rebrightenings' because of their specific configuration (see Kato et al. 2009, for details). However, further evidence presented in the discussion (such as evidence of the steep blue spectrum in quiescence dominated by emission from a hot white dwarf) reinforces the suggestion that OT 0753 belongs to the sample of dwarf nova sources that are above the period gap.

4.4. *OT 0753 is a U Gem Like System*

The source properties of OT 0753 (the inferred white dwarf temperature, the inferred orbital period, and the SED evolution) indicate that it is very similar to U Geminorum. U Gem was studied using the *Hopkins Ultraviolet Telescope* in the UV and was found to have a very blue quiescent spectrum very soon (≈10 days) after the end of one of its outbursts (Long et al. 1993). This hot blue spectrum was dominated by emission from the white dwarf and the inferred temperature of this white dwarf was very high at ≈38,000 K (assuming all the UV light came only from the white dwarf; Long et al. 1993). Similar sources (e.g., UZ Serpentis and SS Aurigae; Lake & Sion 2001) also show a blue white dwarf dominated spectra in quiescence and have orbital periods (≈4 hours) similar to that inferred for OT 0753. Thus, OT 0753 is probably also a U Gem type system which is dominated by the hot white dwarf in quiescence.

4.5. *No X-ray Detection During the Dwarf Nova Outburst*

OT 0753 was not detected in X-rays. Güver et al. (2006) studied U Gem during its outburst and hypothesize that its X-ray activity arises from optically thin plasma close to the white dwarf or from the optically thick boundary layer during the outburst. If all dwarf novae are expected to show X-ray emission, albeit faint, due to similar mechanisms when they are in outbursts, then the lack of any X-ray detection from the source may be evidence that the source is located relatively far away. The X-ray flux from U Gem around the peak of its normal 2002 optical outburst, observed using *Chandra*, was found to be $F_{\mathrm{X}} = 3.3 \times 10^{-11}$ erg cm^{-2} s^{-1} (0.8–7.5 keV). U Gem is located at a distance of around 100 pc (Harrison et al. 2004) which corresponds to an outburst luminosity $\approx 4.1 \times 10^{31}$ erg s^{-1}. Assuming that our X-ray upper limit determined at the time close to the outburst peak (see § 2) corresponds to the same luminosity as observed for U Gem the distance to OT 0753 would be $\gtrsim$2.3 kpc. This is a very rough estimate that makes several assumptions (such as all dwarf novae should show X-ray emission at similar luminosities during their outbursts, that the peak X-ray luminosity from a normal outburst of U Gem and the superoutburst of OT 0753 are similar, and that our first XRT observation is representative of the peak of the superoutburst); however, it suggests that OT 0753 is relatively far away.

4.6. *The Insight Obtained from the UV Coverage*

OT 0753 was observed in the optical and UV bands during its outburst and subsequent decay. The UV probes hotter components of the system compared to the optical. For example, it can probe the inner hot accretion flow and, in this case, also the hot white dwarf. We wish to emphasize the importance of UV coverage of dwarf nova outbursts as this coverage can provide insights into the physics of the system which are unavailable when studying the source only in the optical. For example, if we only studied the optical light curve in Figure 2 we would had only been able to conclude that OT 0753 likely experienced a superoutburst which was not followed by any subsequent rebrightenings. The additional UV coverage after the end of the outburst showed that the source magnitude decayed relatively slowly in this band as compared to the optical. This allowed us to infer that the source likely hosts a cooling white dwarf which may have been heated during the preceding accretion outburst. Similarly, the spectrum covering the UV and optical wavelengths gave us more insight than would be inferred by only studying the optical spectral evolution. The optical spectral evolution alone indicated that a strong disk contribution present during the outburst gradually decreased as the outburst transitioned to quiescence. The additional UV coverage indicated that although the disk component faded away the spectrum remained very steep, suggesting the presence of a hot white dwarf. Furthermore, the assumed quiescent spectrum determined using the SDSS optical data and UV data from *GALEX* also exhibited a very steep spectral index which suggested that even after cooling the source hosts a hot white dwarf.

4.6.1. *Further Studies of Cooling White Dwarfs*

Without the accompanying UV coverage we would have missed the potential cooling of the hot white dwarf that OT 0753 hosts. This source is estimated to be at a large distance away (see § 4.5) and is not an excellent candidate to study the cooling in white dwarfs after the end of its accretion outburst. However, similar UV and optical coverage of nearby promising sources that may exhibit cooling will allow us to learn not only about the accretion physics but also to monitor the cooling white dwarf more accurately, thereby allowing us to infer the physics of the white dwarf. Photometry using the *Swift*/UVOT and similar instruments will allow us to sample a large population of cooling white dwarfs and infer thermal properties of the white dwarf.

AP and RW are supported by a NWO Top Grant, Module 1, awarded to RW. JVHS is supported by a Vidi grant awarded to Nathalie Degenaar by the Netherlands Organization for Scientific Research (NWO). DP is partially supported by the Consejo Nacional de Ciencia y Tecnología with a CB-2014-1 grant #240512. We thank the *Swift* team for scheduling our observations. We thank the RATIR project team, in particular C. Román-Zúñiga, and the staff of the Observatorio Astronómico Nacional on Sierra San Pédro Mártir. RATIR is a collaboration between the University of California, the Universidad Nacional Autonóma de México, NASA Goddard Space Flight Center, and Arizona State University, benefiting from the loan of an H2RG detector and hardware and software support from Teledyne Scientific and Imaging. RATIR, the automation of the Harold L. Johnson Telescope of the Observatorio Astronómico Nacional on Sierra San Pedro Mártir, and the operation of both are funded through NASA grants NNX09AH71G, NNX09AT02G, NNX10AI27G, and NNX12AE66G, CONACyT grants INFR-2009-01-122785 and CB-2008-101958, UNAM PAPIIT grant IN113810, and UC MEXUS-CONACyT grant CN 09-283.

REFERENCES

Arnaud, K. 1996, ASPC, 101, 17
Balanutsa, P., Gress, O., Shumkov, V., et al. 2017, ATel, 10915, 1
Balman, S. 2015, AcPPP, 2, 116
Burrows, D. N., Hill, J., Nousek, J., et al. 2005, SSRv, 120, 165
Cannizzo, J. K. 2012, ApJ, 757, 174
Dickey, J. M. & Lockman, F. J. 1990, ARA&A, 28, 215
Done, C. & Osborne, J. P. 1997, MNRAS, 288, 649
Drake, A. J., Djorgovski, S. G., Mahabal, A., et al. 2009, ApJ, 696, 870
Frank, J., King, A., & Raine, D. J. 2002, Accretion Power in Astrophysics, (3rd ed.; Cambridge, UK:CUP)
Gänsicke, B. T. & Beuermann, K. 1996, A&A, 309, L47
Gehrels, N. 1986, ApJ, 303, 336
Gehrels, N., Chincarini, G., Giommi, P., et al. 2004, ApJ, 611, 1005
Godon, P., Shara, M. M., Sion, E. M., & Zurek, D. 2017, ApJ, 850, 146
Güver, T., Uluyazı, C., Özkan, M. T., & Göğüş, E. 2006, MNRAS, 372, 450
Harrison, T. E., Johnson, J. J., McArthur, B. E., et al. 2004, AJ, 127, 460
Kato, T., Imada, A., Uemura, M., et al. 2009, PASJ, 61, S395
Kornilov, V. G., Lipunov, V. M., Gorbovskoy, E. S., et al. 2012, ExA, 33, 173
Lake, J. & Sion, E. M. 2001, AJ, 122, 1632

Lasota, J.-P. 2001, NewAR, 45, 449
Lasota, J. P., Hameury, J. M., & Hure, J. M. 1995, A&A, 302, L29
Long, K. S., Blair, W. P., Bowers, C. W., et al. 1993, ApJ, 405, 327
Long, K. S., Sion, E. M., Huang, M., & Szkody, P. 1994, ApJ, 424, L49
Martin, D. C., Fanson, J., Schiminovich, D., et al. 2005, ApJ, 619, L1
Mauche, C. P., Mattei, J. A., & Bateson, F. M. 2001, ASPC 229, Evolution of Binary and Multiple Star Systems, ed. P. Podsiadlowski, S. Rappaport, A. R. King, F. D'Antona, & L. Burder(ASP), 367
O'Donoghue, D. 2000, NewAR, 44, 45
Osaki, Y. 1996, PASP, 108, 39
Otulakowska-Hypka, M., Olech, A., & Patterson, J. 2016, MNRAS, 460, 2526
Pala, A. F., Gänsicke, B. T., Townsley, D., et al. 2017, MNRAS, 466, 2855
Parikh, A. S. & Wijnands, R. 2017, ATel, 10922, 1
Patterson, J., Masi, G., Richmond, M. W., et al. 2002, PASP, 114, 721
Roming, P. W. A., Kennedy, T. E., Mason, K. O., et al. 2005, SSRv, 120, 95
Watson, A. M., Richer, M. G., Bloom, J. S., et al. 2012, SPIE, 8444, Ground-based and Airborne Telescopes IV
Whitehurst, R. 1988, MNRAS, 232, 35

Juan V. Hernández Santisteban, Aastha S. Parikh, and Rudy Wijnands: Anton Pannekoek Institute for Astronomy, University of Amsterdam, Postbus 94249, 1090 GE Amsterdam, The Netherlands (a.s.parikh@uva.nl).
Dany Page: Instituto de Astronomía, Universidad Nacional Autónoma de México, Ciudad de México, 04510, México (page@astro.unam.mx).

Revista Mexicana de Astronomía y Astrofísica, **55**, 65–72 (2019)

MULTICOLOR STUDY OF V1009 PER, A CLOSE BINARY SYSTEM AT THE BEGINNING OF THE OVERCONTACT PHASE, AND OF CRTS J031642.2+332639, A NEW BINARY SYSTEM IN THE SAME FIELD

Raúl Michel[1], Francesco Acerbi[2], Carlo Barani[2], and Massimiliano Martignoni[2]

Received June 6 2018; accepted January 8 2019

ABSTRACT

The first multicolor observations and light curve solutions of the eclipsing binary systems V1009 Per and CRTS J031642.2+332639 are presented. Using the 2005 version of the Wilson-Devinney code, both systems are found to be W UMa contact binaries. V1009 Per has a mass ratio of $q = 0.362 \pm 0.002$ and a shallow fill out parameter of $f = 11.8 \pm 0.6\%$ while CRTS J031642.2+332639 has a mass ratio of $q = 2.507 \pm 0.006$ and a fill out of $f = 13.6 \pm 0.4\%$. High orbital inclinations, $i = 85^\circ.9$ for V1009 Per and $i = 83^\circ.2$ for CRTS J031642.2+332639, imply that both systems are total eclipsing binaries and that the photometric parameters here obtained are reliable. Based on 16 times of minimum the orbital period variations of V1009 Per are discussed. The absolute dimensions of the systems are estimated and, from the $\log M - \log L$ diagram, it is found that both components of the systems follow the general pattern of the W subtype W Ursae Majoris systems.

RESUMEN

Se presentan las primeras observaciones multicolor y las curvas de luz de las binarias eclipsantes V1009 Per y CRTS J031642.2+332639. Con la versión 2005 del código Wilson-Devinney se encuentra que ambos sistemas son binarias en contacto del tipo W UMa. El cociente de masas de V1009 Per es $q = 0.362 \pm 0.002$ y el factor de llenado es $f = 11.8 \pm 0.6\%$; CRTS J031642.2+332639 tiene los valores $q = 2.507 \pm 0.006$ y $f = 13.6 \pm 0.4\%$. Las inclinaciones orbitales, $i = 85^\circ.9$ para V1009 Per e $i = 83^\circ.2$ para CRTS J031642.2+332639, implican que ambas son binarias totalmente eclipsantes y que los parámetros fotométricos obtenidos son confiables. Con base en 16 tiempos de mínimo, se discuten las variaciones del período orbital de V1009 Per. Se calculan las dimensiones absolutas de los sistemas y, con el diagrama $\log M - \log L$, se encuentra que ambos componentes de los sistemas siguen el patrón general del subtipo W de las W Ursae Majoris.

Key Words: binaries: eclipsing — stars: individual: CRTS J031642.2+332639 — stars: individual: V1009 Per — techniques: photometric

1. INTRODUCTION

The creation of a stellar evolutionary scheme requires a knowledge of the fundamental parameters of stars in different stages of their evolution. Eclipsing binary systems, especially the W Ursae Majoris type, are among the most important sources of such information (Kjurkchieva et al. 2017).

W UMa systems have orbital periods, typically, between 0.2 days and 0.8 days and consist of two dwarf stars with spectral types ranging from A to K sharing a common convective envelope resulting in a near equalization of the surface temperature with differences of no more than a few percent (Christopoulou et al. 2011).

Light curves of W UMa stars show continuous changes in brightness with nearly equal depth minima and maxima that are not always symmetric. This difference in maximum light levels, sometimes referred to as the O'Connell effect (O'Connell 1951), is caused by the inhomogeneity in the surface brightness distribution of one or both stars, commonly as-

[1]Instituto de Astronomía, Universidad Nacional Autónoma de México, México.

[2]Stazione Astronomica Betelgeuse, Magnago, Italy.

sociated with dark or hot spots. The difference between the maxima can change from orbit to orbit because of the motion and evolution of these active regions. This phenomenon may indicate the presence of an activity cycle similar to that of the Sun (Mitnyan et al. 2018).

According to our modern understanding, these systems are most likely formed from the moderately close binaries (Chen et al. 2016) through either nuclear evolution of the most massive component in the detached phase or angular momentum evolution of the two component stars within a convective envelope (Hilditch et al. 1988; Tutukov et al. 2004; Yildiz & Doğan 2013).

V1009 Per (GSC 2344-00092, NSVS 6662264, $\alpha_{2000} = 03^h16^m49^s.62, \delta_{2000} = +33°30'14''.1$) was first reported by Kuruslov (2011) as a short-period contact eclipsing binary candidate with an orbital period of about 0.23414 days. The published light curve presented the typical EW-type behavior. However, the data of its light curve are scattered to some extent, and it is not clear that the light curve shows the O'Connell effect or argues about the features of the light curve at the time of the observations. We found the O'Connell effect in our observed light curves and adopted a bright spot model to interpret it.

CRTS J031642.2+332639 (hereinafter J031642, $\alpha_{2000} = 03^h16^m42^s.23, \delta_{2000} = +33°26'39''.0$) is listed as a variable star with a period of 0.3009380 days, in the Catalina Surveys Periodic Variable Star Catalog (Drake et al. 2014). This object also shows the typical behavior of W UMa type systems.

Since no photometric or spectroscopic studies are found in the literature, the aim of the present study is to analyze our B, V, R_c and I_c light curves to obtain the first orbital and fundamental parameters of these eclipsing binaries.

2. OBSERVATIONS

Photometric observations were carried out at the San Pedro Martir Observatory, on December 16, 2017 and January 18, 2018, with the 0.84-m telescope, a filter-wheel and the *Spectral Instruments 1* CCD detector (a deep depletion e2v CCD42-40 chip with a gain of 1.39 e^-/ADU and a readout noise of 3.54 e^-). The field of view was $7.6' \times 7.6'$ and a binning of 2×2 was used during all the observations. Alternated exposures were taken in filters B, V, R_c and I_c with exposure times of 40, 25, 15 and 15 seconds respectively. A total of 371 target images were acquired during the first night covering an interval of 5.7 hours while 414 images were acquired during the second night over 6.3 hours. Flat field and bias frames were taken during both observing runs.

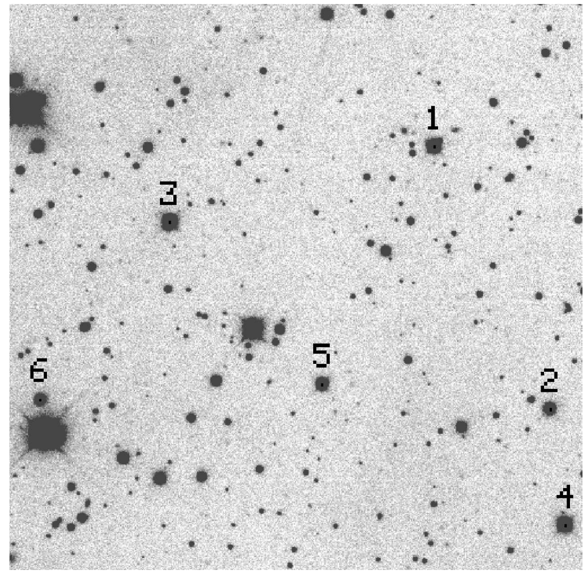

Fig. 1. Observed field. This finding chart was generated by aligning and adding all the images acquired during the second night of observation. The calibrated $UBV(RI)_c$ magnitudes of the marked stars can be found in Table 1.

All images were processed using IRAF[3] routines. Images were bias subtracted and flat field corrected before the instrumental magnitudes of the marked stars in Figure 1 were computed with the standard aperture photometry method. This field was also calibrated in the $UBV(RI)_c$ system and the results, along with the 2MASS magnitudes, are presented in Table 1. Based on this information, we decided to use Object #3 as comparison star since it has a magnitude and color similar to both V1009 Per and J031642, making differential extinction corrections negligible. Objects #4, #5 and #6 were used as check stars to confirm that the comparison star is not variable. All data can be provided by the first author upon request.

3. LIGHT ELEMENTS AND ORBITAL PERIOD VARIATIONS OF V1009 PER

The measured times of minimum (ToM) of J031642, determined by the polynomial fits, are presented in Table 2. These new data permit us to refine the orbital period as:

$$HJD(Min.I) = 2458136.8210(5) + 0^d.2996181(83) \times E, \tag{1}$$

[3]IRAF is distributed by the National Optical Observatories, operated by the Association of Universities for Research

TABLE 1

$UBV(RI)_C$ AND 2MASS MAGNITUDES OF THE FIELD STARS. IDS AS IN FIGURE 1

ID	Name	RA (2000)	DEC (2000)	U	B	V	R_c	I_c	J	H	K_s
1	V1009 Per	49.206375	33.504269	15.938	15.406	14.351	13.716	13.112	12.307	11.734	11.619
2	CRTS J031642.2+332639	49.175527	33.444546	16.397	16.002	15.046	14.437	13.920	13.207	12.737	12.599
3	LAM260516231	49.278550	33.487820	15.482	15.071	14.109	13.567	13.042	12.228	11.779	11.681
4	LAM260516226	49.171755	33.418138	15.461	15.157	14.227	13.698	13.205	12.452	12.061	11.935
5	2MASSJ03165701+3327025	49.237512	33.450702	16.434	15.955	14.987	14.458	13.988	13.186	12.837	12.680
6	2MASSJ03171542+3326522	49.314234	33.447899	16.961	16.525	15.523	14.927	14.401	13.602	13.131	13.012

TABLE 2

CCD (BVRI) TIMES OF MINIMA OF J031642

HJD	Epoch	O-C
2458102.665	-114	0
2458136.671	-0.5	-0.0005
2458136.822	0	0.0005

TABLE 3

CCD (BVRI) TIMES OF MINIMA OF V1009 PER

Band	HJD	Epoch	O-C	Source
Rotse	2451491.536	0	-0.0143	Kuruslov (2011)
Rotse	2451491.653	0.5	-0.014	NSVS
SWASP	2453250.281	7511.5	0.0111	SWASP
SWASP	2453250.397	7512	0.0109	SWASP
SWASP	2454045.87	10909.5	0.0031	SWASP
SWASP	2454045.988	10910	0.0045	SWASP
SWASP	2454320.981	12084.5	0.0039	SWASP
SWASP	2454321.098	12085	0.0037	SWASP
CCD	2455846.852	18601.5	0.0043	Diethelm (2012)
CCD	2455846.968	18602	0.0031	Diethelm (2012)
CCD(V)	2456227.909	20229	0.0034	Diethelm (2013)
CCD	2457387.23	25180.5	-0.0037	Nosal P.
BVRI	2458102.635	28236	-0.0038	This paper
BVRI	2458102.752	28236.5	-0.0046	This paper
BVRI	2458136.702	28381.5	-0.0039	This paper
BVRI	2458136.819	28382	-0.0037	This paper

Based on a careful search for all available eclipsing times of V1009 Per, we collected a total of 16 ToM that, with the new four ToM observed by us (Table 3), permit the revision of the ephemeris and the construction of the O-C diagram depicted in Figure 2.

$$HJD(Min.I) = 2451491.5503(37) + 0^d.2341369(2) \times E. \quad (2)$$

Applying the ephemeris of equation 2 to those minima, we notice that the trend of the residual has a parabolic shape as shown in Figure 2. A second order polynomial ephemeris, fitting all the minima, gives:

in Astronomy, Inc., under cooperative agreement with the National Science Foundation.

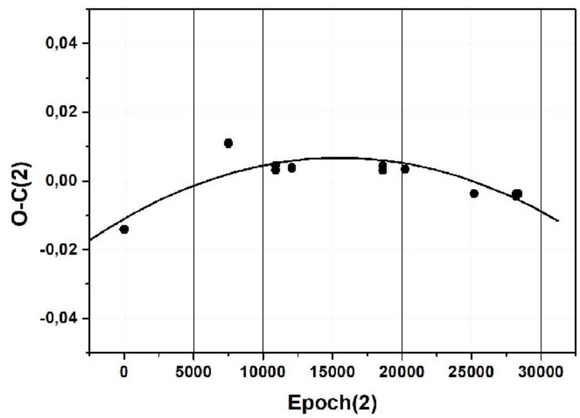

Fig. 2. O-C diagram of V1009 Per. The solid curve shows the second-order polynomial fit to the data points as given by equation 2.

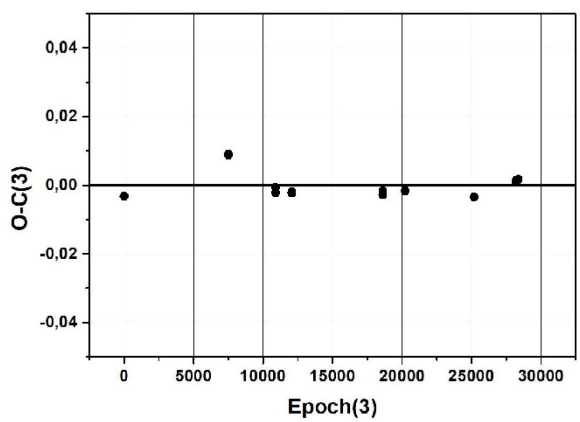

Fig. 3. O-C diagram of V1009 Per. The solid curve shows the second-order polynomial fit to the data points as given by equation 3.

$$HJD(Min.I) = 2451491.5393(28) + 0^d.2341392(4) \times E - 7.4(1.2) \times 10^{-11} \times E^2, \quad (3)$$

whose residual behavior is shown in Figure 3.

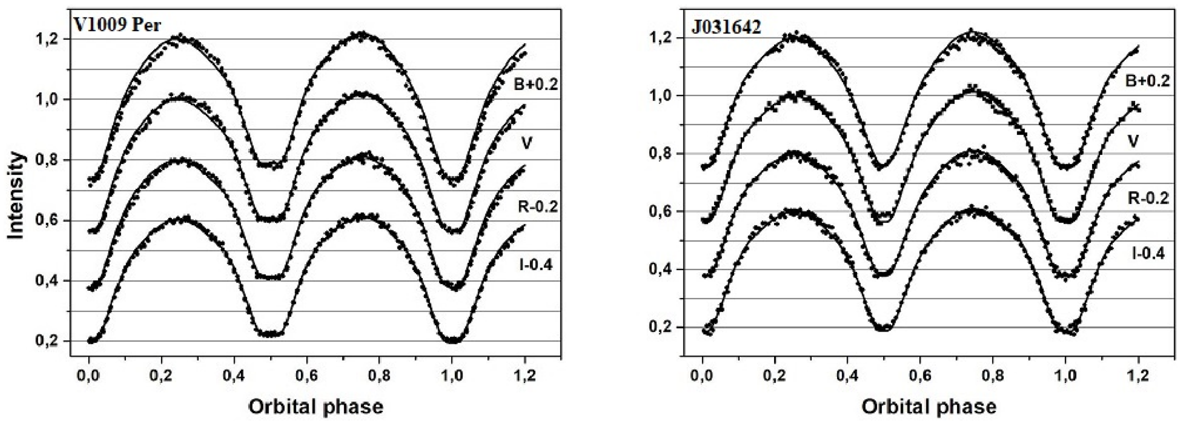

Fig. 4. CCD B, V, R and I light curves of V1009 Per (left) and J031642 (right). Points are the original observations and lines the theoretical light curves with the spot contribution.

Since the temporal distribution of the O-C values is rather small (covering only 18 years, spanning nearly 28,400 orbits), the downward parabolic change shown in Figure 2 may be only a part of a long-period cyclic oscillation that may be caused be the presence of a third body. To confirm this conclusion more times of light minimum are required.

From the quadratic term of equation (3), it follows that the orbital period may be decreasing at a rate of $\dot{P} = -2.31 \times 10^{-7}$days/yr^{-1}. With the orbital period decrease, the primary component transfers mass to the secondary, the mass ratio increases and eventually the system evolves into the contact phase. The period decrease might be caused by mass or angular momentum loss (AML) due to a magnetic stellar wind (magnetic braking) and/or mass transfer from the more massive to the less massive component.

According to the formula given by Bradstreet & Guinan (1994): $\dot{P}_{AML} = -6.30 \times 10^{-9}$days/yr^{-1}; this suggests that magnetic braking is not the main cause of the period decrease. The mass transfer from M_1 to M_2 or the mass loss from the system can be evaluated using equations 4 and 5 of Hilditch (2001) for conservative and non-conservative mass loss, respectively. We obtain for V1009 Per $\dot{M}_1 = -1.63 \times 10^{-7} M_{\odot}$yr^{-1} and $\dot{M}_1 = -1.91 \times 10^{-7} M_{\odot}$yr^{-1} for conservative and non-conservative mass transfer, respectively.

The timescale of the conservative mass transfer (i.e. the dynamical timescale) can be estimated to be approximately τdy= 5.35×10^6 yrs and 4.59×10^6 yrs for the non-conservative mass transfer.

On the other hand, the thermal timescale of the massive component can be estimated as $\tau_{th} \approx 3.0 \times 10^7 (M/M_{\odot})^2 (R/R_{\odot})^{-1} (L/L_{\odot})^{-1} \approx 5.8\times 10^7$ yrs (Hilditch 2001) which is longer than the conservative mass-transfer duration. This suggests that the primary component cannot stay in thermal equilibrium and the mass transfer in V1009 Per is unstable.

4. PHOTOMETRIC ANALYSIS USING THE WD CODE

There are no reported spectroscopic mass ratios for these systems. In order to derive reliable geometric and astrophysical elements, the present observations were analyzed simultaneously using the 2003 (October 2005 revision) version of the Wilson–Devinney (WD) program (Wilson & Devinney 1971; Wilson 1990; Wilson 1994; Wilson & van Hamme 2004).

We applied the q–search method to find the best initial value to be used for q during the light curve analysis.

From Figure 4 left, it is clearly seen that the light curves of V1009 Per present a flatter bottom secondary eclipse covering approximately 0.07 in phase; this possibly indicates a total eclipse configuration of the system.

We used the NASA IPAC database (NASA 2015), interstellar extinction and reddening calculator to compute the $E(B-V)$ value for both the systems which, due to the low galactic latitude ($-20°$), could be significant.

We have checked the consistency of our determined $(B-V)_0$ values using the period-color relation discovered by Eggen and revised by Wang (1994) as $(B-V)_0 = 0.062 - 1.310 \log P$(days). The results are the following:

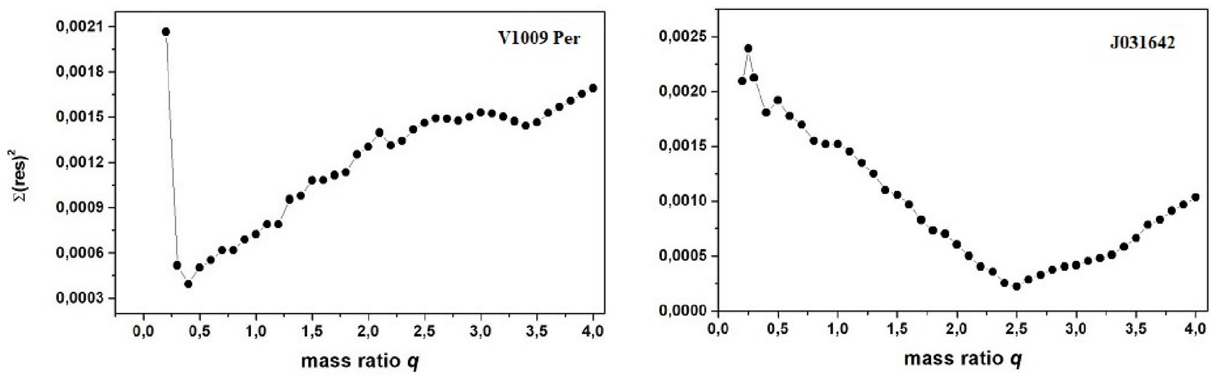

Fig. 5. The relation $\Sigma(res)^2$ versus mass ratio q in Mode 3 in the WD code for V1009 Per (left) and J031642 (right).

TABLE 4

LIGHT CURVES SOLUTIONS FOR V1009 PER AND J032642.[1]

	V1009 Per	J032642
i	85.971±0.145	83.245±0.148
$T_1(K)$	5280*	5544*
$T_2(K)$	5253±6	5416±6
$\Omega_1 = \Omega_2$	2.534±0.004	5.872+0.009
$q = m_2/m_1$	0.362±0.002	0.398±0.006
$A_1 = A_2$	0.5*	0.5*
$g_1 = g_2$	0.32*	0.32*
L_{1B}	0.681±0.002	0.318±0.002
L_{1V}	0.687±0.001	0.311±0.001
L_{1R}	0.687±0.001	0.308±0.001
L_{1I}	0.690±0.001	0.307±0.001
L_{2B}	0.268±0.002	0.634±0.003
L_{2V}	0.267±0.002	0.639±0.003
L_{2R}	0.269±0.002	0.645±0.002
L_{2I}	0.271±0.002	0.654±0.002
f	0.118±0.06	0.136±0.04
$X_{1B} = X_{2B}$	0.749*	0.624*
$X_{1V} = X_{2V}$	0.422*	0.319*
$X_{1R} = X_{2R}$	0.244*	0.168*
$X_{1I} = X_{2I}$	0.131*	0.075*
L_3	0	0
$r_1(pole)$	0.453±0.001	0.289±0.001
$r_1(side)$	0.488±0.001	0.302±0.001
$r_1(back)$	0.591±0.001	0.339±0.002
$r_2(pole)$	0.289±0.001	0.429±0.001
$r_2(side)$	0.303±0.001	0.470±0.001
$r_2(back)$	0.247±0.003	0.499±0.001
lat spot (°)	89±1.8	51±2
long spot(°)	310.1±3.1	270.4±2.7
radius(°)	24.8±0.92	25.4±0.88
Temp fac.Spot	1.055±0.017	1.03±0.02
Star	2	2
Sum (res)2	0.00030	0.00022

[1] Assumed parameters are marked with *.

TABLE 5

DIFFERENCES IN THE HEIGHT OF THE MAXIMA

	V1009 Per	J032642
Max II-Max I B	0.008	0.011
Max II-Max I V	0.007	0.006
Max II-Max I R	0.016	0.008
Max II-Max I I	0.006	0.006

For V1009 Per; NASA's calculator gives a value of $(B-V)_0 = 0.830$, i.e. $T_1 = 5280K$, while Wang's equation gives $(B-V)_0 = 0.736$, i.e. $T_1 = 5140K$ (a difference of $140K$). For CRTS J031642; NASA's calculator gives $(B-V)_0 = 0.736$, i.e. $T_1 = 5544K$, while Wang's equation gives $(B-V)_0 = 0.747$, i.e. $T_1 = 5505K$ (a difference of $39K$). The differences between the two values are smaller than the error bars. The $(B-V)$ color values obtained from our observations were corrected with the relative $E(B-V)$ and the resulting values of $(B-V)_0$ were adopted for the determination of the temperature of Star 1.

Following Lucy (1967), the gravity-darkening coefficients of the two components were taken to be 0.32 and the bolometric albedo coefficients were set at 0.50 for stars with a convective envelope, (Ruciński 1973). Limb-darkening coefficients of the components were interpolated with a square root law from the van Hamme (1993) tables.

The shapes of the light curves of these systems are similar to the usual light curve shapes of the W UMa-type binary stars. This prompted us to start the W-D analysis directly in Mode 3. Mode 3 in the W-D Code is used for over-contact binaries

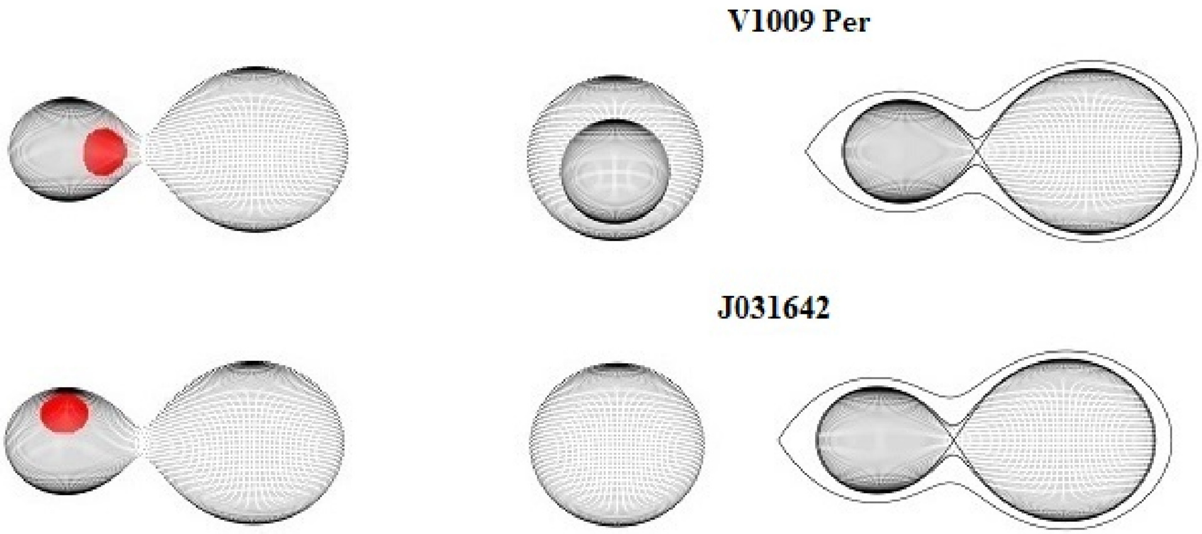

Fig. 6. Graphic representations of V1009 Per and J031642 according to our solution at quadrature (left) and at primary minimum (center). Right: the configuration of the components of the systems in the orbital plane is shown.

TABLE 6

ESTIMATED ABSOLUTE ELEMENTS FOR V1009 PER AND J031642

	V1009 Per		J032642	
	Primary star	Secondary star	Primary star	Secondary star
Mass ($M_{\odot}$)	0.874±0.001	0.317±0.007	1.037±0.010	0.414±0.030
Radius ($R_{\odot}$)	0.865±0.003	0.474±0.003	1.002±0.009	0.661±0.014
Luminosity ($L_{\odot}$)	0.521±0.004	0.153±0.002	0.770±0.010	0.370±0.020
a ($R_{\odot}$)	1.694±0.006		2.133±0.029	

(W UMa stars) in which the adjustable parameters used in the differential correction calculation are the orbital inclination, i, the mean surface effective temperature of the secondary component, T_2, the dimensionless surface potentials of the two components, $\Omega_1 = \Omega_2$, and the monochromatic luminosity of the primary component L_1.

Due to the common occurrence of third bodies in WUMa systems (Pribulla & Ruciński 2006), third light was included as an adjustable parameter. The results showed that the values for third light were negligible (smaller than the uncertainties). To search for a reliable mass ratio q, we made test solutions at the outset using the four light curves in BVR_cI_c colors simultaneously.

The test solutions were computed for a series of assumed mass ratios q, with the values from 0.2 to 4 in steps of 0.1 for both systems; the behavior of the sum of squares of residuals, $\Sigma(res)^2$, was used to estimate their values. The relation between the resulting sum of weighted square deviations and q is plotted in Figure 5. A minimum value was obtained at $q = 0.40$ for V1009 Per and $q = 2.5$ for J031642. Therefore, we chose the above initial values for the mass ratios q and made them adjustable parameters. Then, we performed a differential correction until it converged and final solutions were derived (Table 4). It should be noted that the errors of the parameters given in this paper are the formal errors from the WD code and are known to be unrealistically small (Maceroni & Ruciński 1997). For a discussion see Barani et al. (2017).

The results of our analysis confirm that both the system are shallow contact binaries in good thermal contact. For systems exhibiting high inclination, the mass ratios can be inferred from purely geometric arguments even in the absence of complementary spectroscopic data (Terrell & Wilson 2005). As shown in Figure 4, the light curves of both systems display an inverse O'Connell effect (O'Connell 1951). The maximum at phase 0.25 (Max I) is slightly fainter than the one at phase 0.75 (Max II), see Table 5.

These features usually indicate wavelength-dependent hot spot activity (rather than a cool spots) on the surface of one component due to the probable impact from the mass transfer between the components. The final synthetic light curves calculated using the whole set of parameters of Table 4 are shown in Figure 4 as continuous lines. The observed and the theoretical light curves are in good agreement. A graphic representations and the Roche geometries of the systems is shown in Figure 6.

5. EVOLUTIONARY STATUS OF THE SYSTEMS AND CONCLUSIONS

Since at present there is no spectroscopic determination of the orbital elements available, the absolute parameters of the system cannot be determined directly. We use the 3D empirical laws of Gazeas (2009) where the physical parameters of contact binaries are closely correlated with the orbital period and mass ratio. Then with the mass ratio determined from the photometry, we can derive the individual masses and radii.

Luminosities were calculated using the Stefan-Boltzmann law. The physical parameters listed in Table 6 are used to investigate the current evolutionary status of both systems.

Recently, Yildiz & Doğan (2013), developed a method for the computation of initial masses of contact binaries based on stellar modelling with mass loss. Their main assumption was that the mass transfer starts near or after the TAMS phase of the massive component (the progenitor of the secondary component). They found that binary systems with initial mass of the secondary, M_{2i}, higher than $1.8M_\odot$ become A-subtype, but if M_{2i} is lower than $1.8M_\odot$ then the systems exhibit W-subtype properties. Applying this method we find $M_{2i} = 1.3M_\odot$ for V1009 Per and $M_{2i} = 1.4M_\odot$ for J031642. These results agree with the determination of the W-subtype based on the above criterion for the initial mass of the secondary.

In Figure 7 we plot the components of V1009 Per and J031642 together with other W- and A-type W UMa systems collected by Yildiz & Doğan (2013) in the logarithmic mass-luminosity (M-L) relations along with the ZAMS and TAMS computed by Girardi et al. (2000). It is clear that both components of our systems follow the general pattern of the W-subtype systems and seem to be in good agreement with the well known W-type W UMa systems on the $\log M - \log L$ plane.

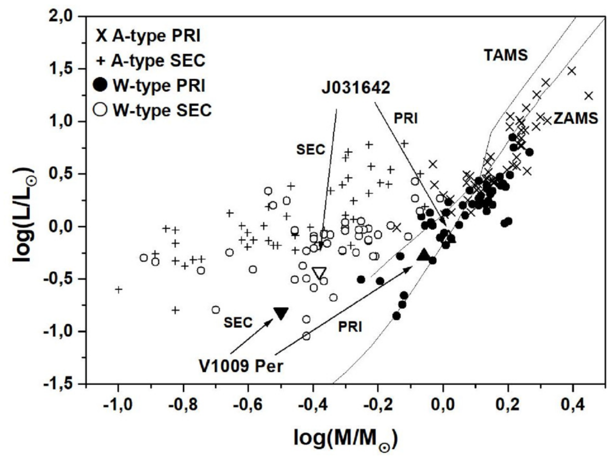

Fig. 7. Location of the components of V1009 Per and J031642 on the $\log M - \log L$ diagram. The sample of W UMa type systems was obtained from a compilation of Yildiz & Doğan (2013) Zero Age Main Sequence (ZAMS) and Terminal Age Main Sequence (TAMS) are taken from Girardi et al. (2000) for the solar chemical composition.

The light curves of both systems exhibit the inverse O'Connell effect with the maximum at phase 0.25 (Max I) slightly fainter than that at phase 0.75 (Max II). For this reason a hot spot, indicating a probable impact from mass transfer between the components, was placed on the surface of the secondary component.

RM acknowledges financial support from UNAM under DGAPA grant PAPIIT IN 100918. This paper is based on observations acquired at the OAN-SPM, Baja California, Mexico. This research has made use of the International Variable Star Index (VSX) database, operated at AAVSO, Cambridge, Massachusetts, USA, of the VizieR catalogue access tool, CDS, Strasbourg, France. The original description of the VizieR service was published in A&AS 143, 23. We acknowledge our anonymous referee for comments that helped to improve this work.

REFERENCES

Barani, C., Martignoni, M., & Acerbi, F. 2017, NewA, 50, 73

Bradstreet, D. H. & Guinan, E. F. 1994, ASPC 56, Interacting binaries stars, ed. A. W. Shafter (San Francisco, CA: ASP), 228

Chen, X., Deng, L., de Grijs, R., et al. 2016, AJ 152, 129

Christopoulou, P.-E., Parageorgiou, A., & Chrysopoulos, I. 2011, AJ 142, 99
Diethelm, R. 2012, IBVS, 6011, 1
__________. 2013, IBVS, 6042, 1
Drake, A. J., Graham, M. J., Djorgovski, S. G., et al. 2014. ApJS, 213, 9
Gazeas, K. D. 2009, CoAst, 159, 129
Girardi, L., Bressan, A., Bertelli, G., & Chiosi, C. 2000, A&AS 141, 371
Hilditch, R. W., King, D. J., & McFarlane, T. M. 1988, MNRAS, 231, 341
Hilditch, R. W. 2001, An introduction to Close Binary Stars, (Cambridge, MA: CUP)
Kjurkchieva, D. P., Popov, V. A., Ibryamov, S. I., Vasileva, D. L., & Petrov, N. I. 2017, RAA, 17, 42
Kuruslov, A. V. 2011, PZP, 11, 1
Lucy, L. B. 1967, ZA, 65, 89
Maceroni, C. & Ruciński, S. M. 1997, PASP, 109, 782
Mitnyan, T., Bódi, A., Szalai, T., et al. 2018, A&A, 612, 91
NASA. 2015, `http://irsa.ipac.caltech.edu/applications/DUST/`
Nosal, P., O-C gateway, `http://var2.astro.cz/ocgate/`
O'Connell, D. J. K. 1951, PRCO, 2, 85
Pribulla, T. & Ruciński, S. M. 2006, AJ, 131, 2986
Ruciński, S. M. 1973, AcA, 23, 79
Terrell, D. & Wilson, R. E. 2005, Ap&SS, 296, 221
Tutukov, A. N., Dremova, G. N., & Svechnikov, M. A. 2004, ARep, 48, 219
van Hamme, W. 1993, AJ, 106, 2096
Wang, J. M. 1994, ApJ, 434, 277
Wilson, R. E. & Devinney, E. J. 1971, ApJ, 166, 605
Wilson, R. E. 1990, ApJ, 356, 613
__________. 1994, PASP, 106, 921
Wilson, R. E. & van Hamme, W. 2004, Computing binary stars observables, `http://ftp.astro.ufl.edu`, directory `pub/wilson/lcdc2003`
Worthey, G. & Lee, H. C. 2011, ApJs, 193, 1
Yildiz, M., & Doğan, T. 2013, MNRAS, 430, 2029

F. Acerbi: Via Zoncada 51, Codogno, LO, 26845, Italy (acerbifr@tin.it).
C. Barani: Via Molinetto 35, Triulza di Codogno, LO, 26845, Italy (cvbarani@alice.it).
M. Martignoni: Via Don G. Minzoni 26/D, Magnago, MI, 20020, Italy (massimiliano.martignoni@alice.it).
R. Michel: Universidad Nacional Autónoma de México. Observatorio Astronómico Nacional. Apartado Postal 877, C.P. 22800, Ensenada, B. C., México (rmm@astro.unam.mx).

Revista Mexicana de Astronomía y Astrofísica, **55**, 73–92 (2019)

ON THE CHROMOSPHERIC ACTIVITY NATURE OF A LOW-MASS CLOSE BINARY: KIC 12004834

E. Yoldaş and H. A. Dal

Department of Astronomy and Space Sciences, University of Ege, Bornova, İzmir, Turkey.

Received June 10 2018; accepted January 17 2019

ABSTRACT

We study the nature of the chromospheric activity of an eclipsing binary KIC 12004834, using Kepler data. We analyse the light curve of the system, the sinusoidal variations at out-of-eclipses and detected flare events. The secondary component's temperature is found to be 4001±11 K, the mass ratio is 0.743±0.001, and the orbital inclination is $75^{\circ}.89 \pm 0^{\circ}.03$. The analysis indicates a stellar spot effect on the variation. Moreover, the OPEA model has been derived over 149 flares. The saturation level called *Plateau* value, is found to be 2.093±0.236 s. The flare number per hour (known as flare frequency N_1) is found to be 0.06644 h^{-1}, while the flare-equivalent duration per hour (known as flare frequency N_2) is found to be 0.59 second/hour. According to these results, KIC 12004834 is a very low-mass close binary system with high level of flare activity.

RESUMEN

Estudiamos la actividad cromosférica de la binaria eclipsante KIC 12004834 utilizando datos de Kepler. Analizamos la curva de luz y la variación sinusoidal fuera de eclipse, y detectamos ráfagas. Encontramos que la temperatura de la secundaria es de 4001±11 K, que el cociente de masas es 0.743±0.001 y la inclinación orbital es $75^{\circ}.89 \pm 0^{\circ}.03$. El análisis indica que hay un efecto de manchas en la variabilidad. Obtenemos el modelo OPEA para 149 ráfagas. El nivel de saturación, llamado *Plateau* tiene un valor de 2.093±0.236 s. El número de ráfagas por hora, conocido como la frecuencia de ráfagas N_1, es 0.06644 h^{-1}, mientras que la duración de la emisión equivalente a las ráfagas, conocida como la frecuencia N_2 es 0.59 s/hora. De acuerdo con estos resultados, KIC 12004834 es una binaria cerrada, de muy baja masa, y con frecuentes ráfagas.

Key Words: binaries: eclipsing — methods: data analysis — stars: flare — stars: individual: KIC 12004834 — stars: low-mass — techniques: photometric

1. INTRODUCTION

The nature of a low-mass eclipsing binary KIC 12004834 with $14^{m}.7180$ in Kepler band is studied here. KIC 12004834, whose nature is different from the classical UV Ceti type stars of spectral type dMe due to its being a binary system, was observed by Watson (2006) for the first time. Magnitudes of the system were given as $J = 12^{\mathrm{m}}.007$, $H = 11^{\mathrm{m}}.407$, $K = 11^{\mathrm{m}}.170$ by Cutri et al. (2003). Although there are no further studies in the literature, some estimated parameters of the system were given by Coughlin et al. (2011), using calibrations to derive the parameters. Taking $T_{\mathrm{eff}} = 3576$ K, the orbital inclination (i) was found to be $72^{\circ}.47$, while the masses were found to be $M_1 = 0.48\ M_{\odot}$ and $M_2 = 0.34\ M_{\odot}$. In addition, the radii were computed as $R_1 = 0.48\ R_{\odot}$ and $R_2 = 0.35\ R_{\odot}$. Like Coughlin et al. (2011), taking $T_{\mathrm{eff}} = 3576$ K, Slawson et al. (2011) found $\log(g)$ as 4.217 cm/s^2. There are several approaches to obtain the temperatures of its components. Coughlin et al. (2011) gave the temperatures as T_1 =3620 K for the primary and T_2 =3468 K for the secondary. Armstrong et al. (2014) gave T_1 =3511 K for the primary and T_2 =3512 K for the secondary.

KIC 12004834 was mentioned as a chromospherically active system for the first time by Debosscher et al. (2011). In addition, a dominant flare activity was also reported by Balona (2015). Considering the estimated parameters of the system; KIC 12004834 is a low-mass close binary with a chromospherically active component. This makes the system an important object in the astrophysical sense. This is because the system exhibits not only spots, but also flare activity. A flaring star being a component of an eclipsing binary system is a rare phenomenon among the UV Ceti type stars. However, the red dwarf abundance is about 65% in our Galaxy, and seventy-five percent of them exhibit flare activity (Rodonó 1986). Thus, almost half of the stars in our galaxy should exhibit flare activity. The number of eclipsing binaries with a flaring component is nowadays increasing, thanks to space missions such the Kepler and Corot satellites.

Because of its effects on stellar evolution, flare activity is very important in astrophysics in terms of its sources and mechanism. Although the first flare was observed on the solar surface by R. C. Carrington and R. Hodgson on September 1, 1859 (Carrington 1859; Hodgson 1859), there are still unsolved problems, for instance, the different mass loss rate seen among stars of different spectral types, the different flare energy levels detected for stars of different spectral types (Gershberg & Shakhovskaya 1983; Haisch et al. 1991; Gershberg 2005; Benz 2008).

At this point, photometric data accumulated from the eclipsing binaries with a chromospherically active component can give some clues for these problems. Recently, several eclipsing binary stars, where one of the components is chromospherically active have been discovered by the Kepler Mission (Borucki et al. 2010; Koch et al. 2010; Caldwell et al. 2010). Most of them have an interesting nature. These chromospherically active components exhibit flare events and also rapidly evolving stellar spots (Balona 2015). Although the light variations due to the cool spots have remarkably small amplitudes, their shapes change over short time intervals, from one cycle to the next one (Yoldaş & Dal 2016, 2017; Özdarcan et al. 2017).

In this study, the variations of the times of minima are analysed (see § 2.1). The light curve of KIC 12004834 is studied (§ 2.2) for the first time in the literature in order to find the physical properties of the components. Then, the flares occurring on the chromospherically active component are used to model the nature of the magnetic activity of the system as described in § 2.3. The results obtained are given in § 3, comparing the active component with its analogue discovered in the Kepler Mission.

2. DATA AND ANALYSES

The data analysed in this study are the detrended short cadence data from the Kepler Mission Database (Borucki et al. 2010; Koch et al. 2010; Caldwell et al. 2010; Slawson et al. 2011; Matijevič et al. 2012). In the analyses, the data of quarters Q10.1, Q10.2 and Q10.3 are used (Murphy 2012; Murphy et al. 2013), whose quality and sensitivity are the highest ones ever reached (Jenkins et al. 2010a,b).

After removing all the observations with large errors from the data, and using the ephemeris taken from the Kepler Mission database, the phases are computed for all data, and the obtained light curves are shown in Figure 1. Because of the study's format, the detrended short cadence data were used in the analysis instead of those of the long cadence. The data were arranged in suitable formats for different analyses, such as the light curve analysis and the flare event calculations.

2.1. *Orbital Period Variation*

The times of minima in the light curves were computed from short cadence data without any corrections. We used just short cadence data, because the system has a very short orbital period. The whole shape of the minima is not seen in the long cadence data. The minima times were computed with a script according to the method described by Kwee & van Woerden (1956). The $(O-C)_I$ residuals were determined for each minimum time. Examining the times of minima indicated that some of them have very large errors. These errors are sometimes caused by scattered observations; while some of them are caused by the flare activity occurring during these minima. All the minima times with large errors were removed from the $(O-C)$ data. Finally, 688 minima times were determined in the analyses.

Using the epoch of 2455002.041 and the orbital period of 0.2623168 day given in the Kepler Eclipsing Binary Catalogue[1] by Slawson et al. (2011), we computed the $(O-C)_I$ residuals. Then, using the Least-Squares method, we applied a linear correction to these residuals. The linear correction revealed that the $(O-C)_I$ residuals had a linear trend with

[1] http://keplerebs.villanova.edu/.

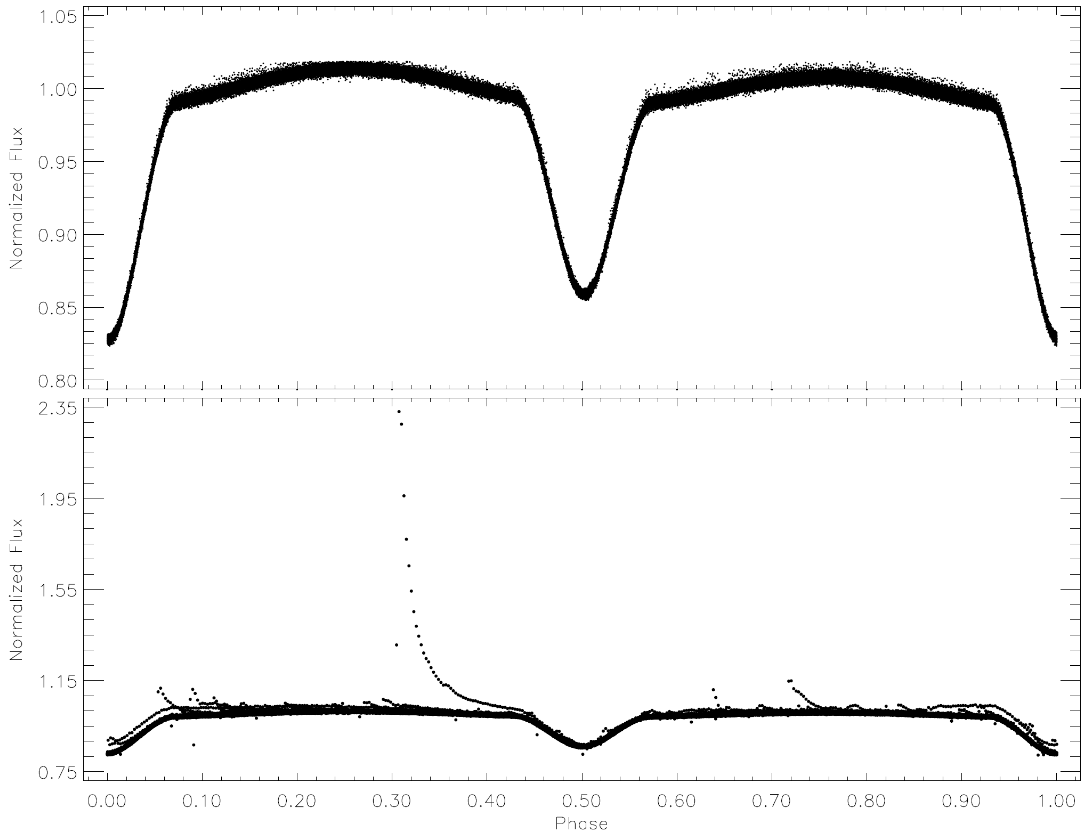

Fig. 1. Whole light curve of KIC 12004834 obtained from the data taken from the Kepler Mission database. In the bottom panel, the light curve is plotted along the orbital cycle with the flare activity, while it is plotted without the flare activity in the upper panel.

a small slope; the distribution of the $(O-C)_I$ residuals seems to be linear, needing just a zero point correction. After the linear correction, we obtained the new ephemerides given in equation (1) and the $(O-C)_{II}$ residuals:

$$JD(Bary.) = 24\,55002.04164(14) + 0^d.262317(1) \times E. \quad (1)$$

The $(O-C)_I$ and $(O-C)_{II}$ residuals are listed in Table 1. In the table, the minima times, cycles, the minima type, $(O-C)_I$ and $(O-C)_{II}$ residuals are listed, respectively. An interesting variation is seen in the $(O-C)_{II}$ residuals plotted versus time in Figure 2.

According to the studies of Tran et al. (2013) on contact binaries, if one of the components of an eclipsing binary system exhibits stellar spot activity on its surface, there must be a separation between the $(O-C)_{II}$ residuals of the primary and secondary minima. Debosscher et al. (2011) and Balona (2015) mentioned that the system exhibits chromospheric activity. In the case of KIC 12004834 considered as a very close binary, we firstly examined whether there was any separation in the primary and secondary minimum $(O-C)_{II}$ residuals. As shown in the upper panel of Figure 2, there is an evident separation between the primary and secondary minima residuals. Secondly, the analysis indicates that the best fit is derived by a linear function for the distribution of $(O-C)_I$. The obtained fit is shown in the lower panel of is Figure 2.

2.2. *Light Curve Analysis*

The light curve of KIC 12004834 was analyzed by the PHOEBE V.0.32 software (Prša & Zwitter 2005) which depends on the 2003 version of the Wilson-Devinney Code (Wilson & Devinney 1971; Wilson 1990) to compute the physical parameters of each component. In the analyses, the averaged data were computed phase by phase with an interval of 0.001 to decrease the scattering. Although several modes

TABLE 1

MINIMA TIMES AND THEIR RESIDUALS

BJD (+24 50000)	E	Type	$(O-C)_I$ (day)	$(O-C)_{II}$ (day)	BJD (+24 50000)	E	Type	$(O-C)_I$ (day)	$(O-C)_{II}$ (day)
5739.93853	2813.0	I	0.00037	−0.00014	5833.06104	3168.0	I	0.00041	−0.00008
5740.20090	2814.0	I	0.00042	−0.00009	5740.06987	2813.5	II	0.00055	0.00004
5740.46318	2815.0	I	0.00039	−0.00013	5740.33222	2814.5	II	0.00059	0.00007
5740.72552	2816.0	I	0.00041	−0.00010	5740.59460	2815.5	II	0.00065	0.00013
5740.98782	2817.0	I	0.00040	−0.00012	5740.85687	2816.5	II	0.00060	0.00008
5741.25018	2818.0	I	0.00044	−0.00008	5741.11948	2817.5	II	0.00090	0.00038
5741.51253	2819.0	I	0.00047	−0.00004	5741.38143	2818.5	II	0.00053	0.00001
5741.77485	2820.0	I	0.00047	−0.00004	5741.64370	2819.5	II	0.00049	−0.00003
5742.03709	2821.0	I	0.00040	−0.00011	5741.90610	2820.5	II	0.00056	0.00005
5742.29950	2822.0	I	0.00049	−0.00002	5742.16839	2821.5	II	0.00054	0.00003
5742.56182	2823.0	I	0.00049	−0.00002	5742.43077	2822.5	II	0.00060	0.00008
5742.82406	2824.0	I	0.00042	−0.00009	5742.69298	2823.5	II	0.00049	−0.00002
5743.08650	2825.0	I	0.00054	0.00003	5742.95537	2824.5	II	0.00057	0.00006
5743.34869	2826.0	I	0.00041	−0.00010	5743.21765	2825.5	II	0.00053	0.00002
5743.61107	2827.0	I	0.00048	−0.00003	5743.47996	2826.5	II	0.00052	0.00001
5743.87339	2828.0	I	0.00048	−0.00003	5743.74229	2827.5	II	0.00054	0.00003
5744.13561	2829.0	I	0.00038	−0.00013	5744.00469	2828.5	II	0.00062	0.00011
5744.39801	2830.0	I	0.00046	−0.00005	5744.26691	2829.5	II	0.00052	0.00001
5744.66025	2831.0	I	0.00038	−0.00013	5744.52938	2830.5	II	0.00068	0.00016
5744.92283	2832.0	I	0.00065	0.00014	5744.79153	2831.5	II	0.00051	0.00000
5745.18490	2833.0	I	0.00041	−0.00010	5745.05391	2832.5	II	0.00058	0.00006
5745.44729	2834.0	I	0.00048	−0.00003	5745.31632	2833.5	II	0.00067	0.00015
5745.70963	2835.0	I	0.00050	−0.00001	5745.57862	2834.5	II	0.00065	0.00013
5745.97188	2836.0	I	0.00044	−0.00007	5745.84093	2835.5	II	0.00064	0.00013
5746.23418	2837.0	I	0.00041	−0.00010	5746.10319	2836.5	II	0.00059	0.00008
5746.49653	2838.0	I	0.00046	−0.00006	5746.36550	2837.5	II	0.00058	0.00007
5746.75883	2839.0	I	0.00044	−0.00007	5746.62782	2838.5	II	0.00058	0.00007
5747.02101	2840.0	I	0.00030	−0.00021	5746.89012	2839.5	II	0.00057	0.00006
5747.28347	2841.0	I	0.00044	−0.00007	5747.15246	2840.5	II	0.00059	0.00008
5747.54575	2842.0	I	0.00040	−0.00011	5747.41478	2841.5	II	0.00060	0.00008
5747.80808	2843.0	I	0.00042	−0.00009	5747.67710	2842.5	II	0.00059	0.00008
5748.07045	2844.0	I	0.00047	−0.00005	5747.93950	2843.5	II	0.00068	0.00017
5748.33278	2845.0	I	0.00048	−0.00003	5748.20170	2844.5	II	0.00056	0.00005
5748.59497	2846.0	I	0.00035	−0.00016	5748.46406	2845.5	II	0.00061	0.00009
5748.85738	2847.0	I	0.00045	−0.00006	5748.72647	2846.5	II	0.00069	0.00018
5749.11974	2848.0	I	0.00049	−0.00002	5748.98876	2847.5	II	0.00067	0.00016
5749.38192	2849.0	I	0.00036	−0.00016	5749.25105	2848.5	II	0.00065	0.00013
5749.64431	2850.0	I	0.00043	−0.00008	5749.51321	2849.5	II	0.00049	−0.00002
5749.90661	2851.0	I	0.00042	−0.00009	5749.77566	2850.5	II	0.00062	0.00011
5750.16895	2852.0	I	0.00043	−0.00008	5750.03785	2851.5	II	0.00050	−0.00002
5750.43123	2853.0	I	0.00040	−0.00011	5750.30019	2852.5	II	0.00052	0.00001
5750.69361	2854.0	I	0.00046	−0.00005	5750.56269	2853.5	II	0.00070	0.00019
5750.95592	2855.0	I	0.00046	−0.00005	5750.82496	2854.5	II	0.00066	0.00014
5751.21813	2856.0	I	0.00035	−0.00016	5751.08720	2855.5	II	0.00058	0.00007
5751.48043	2857.0	I	0.00033	−0.00018	5751.34962	2856.5	II	0.00068	0.00017
5751.74287	2858.0	I	0.00045	−0.00006	5751.61171	2857.5	II	0.00046	−0.00005
5752.00513	2859.0	I	0.00039	−0.00012	5751.87418	2858.5	II	0.00060	0.00009
5752.26744	2860.0	I	0.00039	−0.00012	5752.13672	2859.5	II	0.00083	0.00032
5752.52964	2861.0	I	0.00027	−0.00024	5752.39881	2860.5	II	0.00060	0.00009
5752.79203	2862.0	I	0.00034	−0.00017	5752.66107	2861.5	II	0.00055	0.00004
5753.05428	2863.0	I	0.00028	−0.00023	5752.92340	2862.5	II	0.00056	0.00005
5753.31685	2864.0	I	0.00054	0.00003	5753.18572	2863.5	II	0.00056	0.00005

TABLE 1 (CONTINUED)

BJD (+24 50000)	E	Type	$(O-C)_I$ (day)	$(O-C)_{II}$ (day)	BJD (+24 50000)	E	Type	$(O-C)_I$ (day)	$(O-C)_{II}$ (day)
5753.57902	2865.0	I	0.00039	−0.00012	5753.44802	2864.5	II	0.00054	0.00003
5753.84128	2866.0	I	0.00033	−0.00018	5753.71046	2865.5	II	0.00067	0.00016
5754.10358	2867.0	I	0.00031	−0.00020	5753.97273	2866.5	II	0.00063	0.00012
5754.36600	2868.0	I	0.00042	−0.00009	5754.23500	2867.5	II	0.00058	0.00007
5754.62820	2869.0	I	0.00030	−0.00021	5754.49742	2868.5	II	0.00068	0.00017
5754.89082	2870.0	I	0.00060	0.00009	5754.75969	2869.5	II	0.00063	0.00012
5755.15292	2871.0	I	0.00039	−0.00012	5755.02200	2870.5	II	0.00062	0.00011
5755.41537	2872.0	I	0.00053	0.00001	5755.28431	2871.5	II	0.00062	0.00011
5755.67762	2873.0	I	0.00045	−0.00006	5755.54643	2872.5	II	0.00042	−0.00009
5755.93995	2874.0	I	0.00047	−0.00004	5755.80900	2873.5	II	0.00068	0.00017
5756.20219	2875.0	I	0.00039	−0.00013	5756.07126	2874.5	II	0.00062	0.00011
5756.46450	2876.0	I	0.00038	−0.00013	5756.33364	2875.5	II	0.00068	0.00017
5756.72679	2877.0	I	0.00036	−0.00015	5756.59594	2876.5	II	0.00066	0.00015
5757.25137	2879.0	I	0.00030	−0.00021	5756.85817	2877.5	II	0.00058	0.00007
5757.51358	2880.0	I	0.00019	−0.00032	5757.12057	2878.5	II	0.00066	0.00015
5757.77606	2881.0	I	0.00036	−0.00015	5757.38280	2879.5	II	0.00058	0.00007
5758.03841	2882.0	I	0.00039	−0.00012	5757.64519	2880.5	II	0.00065	0.00014
5758.30065	2883.0	I	0.00032	−0.00019	5757.90742	2881.5	II	0.00056	0.00005
5758.56303	2884.0	I	0.00037	−0.00014	5758.16977	2882.5	II	0.00060	0.00009
5758.82529	2885.0	I	0.00032	−0.00019	5758.43218	2883.5	II	0.00069	0.00018
5759.08774	2886.0	I	0.00045	−0.00006	5758.69452	2884.5	II	0.00071	0.00020
5759.35011	2887.0	I	0.00051	−0.00001	5758.95684	2885.5	II	0.00072	0.00021
5759.61229	2888.0	I	0.00037	−0.00014	5759.21913	2886.5	II	0.00068	0.00017
5759.87448	2889.0	I	0.00025	−0.00026	5759.48141	2887.5	II	0.00065	0.00014
5760.13695	2890.0	I	0.00039	−0.00012	5759.74364	2888.5	II	0.00056	0.00005
5760.39929	2891.0	I	0.00042	−0.00009	5760.00603	2889.5	II	0.00063	0.00012
5760.66157	2892.0	I	0.00038	−0.00013	5760.26829	2890.5	II	0.00058	0.00007
5760.92396	2893.0	I	0.00046	−0.00005	5760.53054	2891.5	II	0.00052	0.00001
5761.18628	2894.0	I	0.00046	−0.00005	5760.79294	2892.5	II	0.00059	0.00008
5761.44852	2895.0	I	0.00039	−0.00012	5761.05529	2893.5	II	0.00063	0.00012
5761.71085	2896.0	I	0.00040	−0.00011	5761.31752	2894.5	II	0.00054	0.00003
5761.97323	2897.0	I	0.00046	−0.00005	5761.57990	2895.5	II	0.00061	0.00010
5762.23551	2898.0	I	0.00042	−0.00009	5761.84227	2896.5	II	0.00066	0.00015
5762.49784	2899.0	I	0.00043	−0.00008	5762.10455	2897.5	II	0.00062	0.00011
5762.76015	2900.0	I	0.00043	−0.00008	5762.36681	2898.5	II	0.00056	0.00005
5763.02252	2901.0	I	0.00048	−0.00003	5762.62918	2899.5	II	0.00062	0.00011
5763.28483	2902.0	I	0.00047	−0.00004	5762.89124	2900.5	II	0.00037	−0.00014
5763.54712	2903.0	I	0.00045	−0.00006	5763.15403	2901.5	II	0.00083	0.00032
5763.80947	2904.0	I	0.00048	−0.00003	5763.41597	2902.5	II	0.00046	−0.00005
5764.07172	2905.0	I	0.00041	−0.00010	5763.67842	2903.5	II	0.00059	0.00008
5764.33411	2906.0	I	0.00049	−0.00002	5763.94075	2904.5	II	0.00061	0.00010
5764.59645	2907.0	I	0.00051	0.00000	5764.20278	2905.5	II	0.00032	−0.00019
5764.85872	2908.0	I	0.00047	−0.00004	5764.46537	2906.5	II	0.00059	0.00008
5765.12109	2909.0	I	0.00052	0.00001	5764.72771	2907.5	II	0.00062	0.00011
5765.38338	2910.0	I	0.00049	−0.00002	5764.99002	2908.5	II	0.00061	0.00010
5765.64561	2911.0	I	0.00040	−0.00011	5765.25234	2909.5	II	0.00061	0.00010
5765.90796	2912.0	I	0.00044	−0.00007	5765.51464	2910.5	II	0.00059	0.00008
5766.17027	2913.0	I	0.00043	−0.00008	5765.77706	2911.5	II	0.00070	0.00019
5766.43259	2914.0	I	0.00043	−0.00008	5766.03932	2912.5	II	0.00064	0.00013
5766.69492	2915.0	I	0.00045	−0.00006	5766.30149	2913.5	II	0.00049	−0.00002
5766.95725	2916.0	I	0.00046	−0.00005	5766.56391	2914.5	II	0.00059	0.00008
5767.21957	2917.0	I	0.00046	−0.00004	5766.82620	2915.5	II	0.00057	0.00006
5767.48203	2918.0	I	0.00060	0.00010	5767.08856	2916.5	II	0.00061	0.00010
5767.74426	2919.0	I	0.00053	0.00002	5767.35084	2917.5	II	0.00057	0.00006

TABLE 1 (CONTINUED)

BJD (+24 50000)	E	Type	$(O-C)_I$ (day)	$(O-C)_{II}$ (day)	BJD (+24 50000)	E	Type	$(O-C)_I$ (day)	$(O-C)_{II}$ (day)
5768.00651	2920.0	I	0.00045	−0.00006	5767.61314	2918.5	II	0.00056	0.00005
5768.26882	2921.0	I	0.00044	−0.00006	5767.87550	2919.5	II	0.00060	0.00009
5768.53113	2922.0	I	0.00044	−0.00006	5768.13771	2920.5	II	0.00049	−0.00001
5768.79353	2923.0	I	0.00052	0.00002	5768.40024	2921.5	II	0.00071	0.00020
5769.05572	2924.0	I	0.00040	−0.00011	5768.66241	2922.5	II	0.00056	0.00006
5769.31808	2925.0	I	0.00044	−0.00007	5768.92476	2923.5	II	0.00059	0.00009
5769.58036	2926.0	I	0.00041	−0.00010	5769.18702	2924.5	II	0.00053	0.00003
5769.84269	2927.0	I	0.00042	−0.00009	5769.44938	2925.5	II	0.00058	0.00007
5770.89201	2931.0	I	0.00047	−0.00004	5769.71170	2926.5	II	0.00058	0.00007
5771.15430	2932.0	I	0.00044	−0.00007	5771.02329	2931.5	II	0.00059	0.00009
5771.41653	2933.0	I	0.00035	−0.00015	5771.28561	2932.5	II	0.00059	0.00008
5771.67891	2934.0	I	0.00042	−0.00009	5771.54806	2933.5	II	0.00073	0.00022
5771.94126	2935.0	I	0.00045	−0.00006	5771.81024	2934.5	II	0.00059	0.00008
5772.20359	2936.0	I	0.00047	−0.00004	5772.07252	2935.5	II	0.00055	0.00004
5772.46592	2937.0	I	0.00048	−0.00003	5772.33480	2936.5	II	0.00052	0.00001
5772.72823	2938.0	I	0.00047	−0.00003	5772.59722	2937.5	II	0.00062	0.00011
5772.99053	2939.0	I	0.00046	−0.00005	5772.85951	2938.5	II	0.00060	0.00009
5773.25281	2940.0	I	0.00041	−0.00009	5773.12172	2939.5	II	0.00048	−0.00002
5773.77750	2942.0	I	0.00047	−0.00004	5773.38416	2940.5	II	0.00061	0.00011
5774.03976	2943.0	I	0.00042	−0.00009	5773.64643	2941.5	II	0.00057	0.00006
5774.30213	2944.0	I	0.00047	−0.00004	5773.90875	2942.5	II	0.00056	0.00005
5774.56442	2945.0	I	0.00044	−0.00007	5774.17113	2943.5	II	0.00063	0.00012
5774.82673	2946.0	I	0.00044	−0.00007	5774.43336	2944.5	II	0.00055	0.00004
5775.08902	2947.0	I	0.00041	−0.00010	5774.69576	2945.5	II	0.00063	0.00012
5775.35138	2948.0	I	0.00045	−0.00006	5774.95804	2946.5	II	0.00059	0.00008
5775.61364	2949.0	I	0.00040	−0.00011	5775.22027	2947.5	II	0.00051	0.00000
5775.87595	2950.0	I	0.00039	−0.00011	5775.48274	2948.5	II	0.00065	0.00014
5776.13830	2951.0	I	0.00042	−0.00009	5775.74500	2949.5	II	0.00060	0.00009
5776.40067	2952.0	I	0.00047	−0.00004	5776.00734	2950.5	II	0.00062	0.00011
5776.66298	2953.0	I	0.00047	−0.00003	5776.26960	2951.5	II	0.00057	0.00006
5776.92523	2954.0	I	0.00041	−0.00010	5776.53194	2952.5	II	0.00059	0.00008
5777.18759	2955.0	I	0.00044	−0.00006	5776.79429	2953.5	II	0.00062	0.00011
5777.44985	2956.0	I	0.00039	−0.00011	5777.05653	2954.5	II	0.00055	0.00004
5777.71216	2957.0	I	0.00038	−0.00013	5777.31886	2955.5	II	0.00056	0.00005
5777.97445	2958.0	I	0.00036	−0.00015	5777.58118	2956.5	II	0.00056	0.00005
5778.23677	2959.0	I	0.00036	−0.00015	5777.84361	2957.5	II	0.00067	0.00017
5778.49912	2960.0	I	0.00039	−0.00011	5778.10584	2958.5	II	0.00059	0.00008
5778.76147	2961.0	I	0.00042	−0.00008	5778.36816	2959.5	II	0.00059	0.00008
5779.02378	2962.0	I	0.00042	−0.00009	5778.63048	2960.5	II	0.00060	0.00009
5779.28609	2963.0	I	0.00041	−0.00009	5778.89269	2961.5	II	0.00049	−0.00002
5779.54846	2964.0	I	0.00047	−0.00004	5779.15504	2962.5	II	0.00052	0.00001
5779.81070	2965.0	I	0.00039	−0.00012	5779.41739	2963.5	II	0.00056	0.00005
5780.07298	2966.0	I	0.00035	−0.00015	5779.67979	2964.5	II	0.00063	0.00013
5780.33536	2967.0	I	0.00042	−0.00009	5779.94215	2965.5	II	0.00068	0.00017
5780.59768	2968.0	I	0.00042	−0.00009	5780.20452	2966.5	II	0.00073	0.00022
5780.85996	2969.0	I	0.00038	−0.00012	5780.46661	2967.5	II	0.00051	0.00000
5781.12228	2970.0	I	0.00039	−0.00012	5780.72892	2968.5	II	0.00050	−0.00001
5781.38458	2971.0	I	0.00037	−0.00014	5780.99127	2969.5	II	0.00053	0.00003
5781.64690	2972.0	I	0.00037	−0.00014	5781.25359	2970.5	II	0.00053	0.00003
5781.90926	2973.0	I	0.00042	−0.00009	5781.51601	2971.5	II	0.00063	0.00013
5782.17159	2974.0	I	0.00042	−0.00008	5781.77844	2972.5	II	0.00075	0.00025
5782.43385	2975.0	I	0.00037	−0.00014	5782.04071	2973.5	II	0.00071	0.00020
5782.69628	2976.0	I	0.00049	−0.00002	5782.30292	2974.5	II	0.00059	0.00009
5782.95845	2977.0	I	0.00033	−0.00017	5782.56533	2975.5	II	0.00070	0.00019

TABLE 1 (CONTINUED)

BJD (+24 50000)	E	Type	$(O-C)_I$ (day)	$(O-C)_{II}$ (day)	BJD (+24 50000)	E	Type	$(O-C)_I$ (day)	$(O-C)_{II}$ (day)
5783.22076	2978.0	I	0.00033	−0.00017	5782.82763	2976.5	II	0.00067	0.00017
5783.48316	2979.0	I	0.00042	−0.00009	5783.08978	2977.5	II	0.00051	0.00000
5783.74559	2980.0	I	0.00052	0.00002	5783.35222	2978.5	II	0.00063	0.00013
5784.00765	2981.0	I	0.00027	−0.00023	5783.61454	2979.5	II	0.00064	0.00013
5784.27018	2982.0	I	0.00049	−0.00002	5783.87685	2980.5	II	0.00063	0.00012
5784.53237	2983.0	I	0.00036	−0.00015	5784.13909	2981.5	II	0.00055	0.00004
5784.79470	2984.0	I	0.00037	−0.00014	5784.40146	2982.5	II	0.00061	0.00010
5785.05708	2985.0	I	0.00043	−0.00007	5784.66373	2983.5	II	0.00056	0.00005
5785.31938	2986.0	I	0.00041	−0.00009	5784.92628	2984.5	II	0.00079	0.00029
5785.58162	2987.0	I	0.00033	−0.00017	5785.18850	2985.5	II	0.00070	0.00019
5785.84400	2988.0	I	0.00040	−0.00011	5785.45072	2986.5	II	0.00060	0.00010
5786.10633	2989.0	I	0.00041	−0.00009	5785.71294	2987.5	II	0.00050	0.00000
5786.36872	2990.0	I	0.00049	−0.00002	5786.23768	2989.5	II	0.00060	0.00010
5786.63076	2991.0	I	0.00021	−0.00029	5786.49999	2990.5	II	0.00060	0.00009
5786.89323	2992.0	I	0.00036	−0.00014	5786.76227	2991.5	II	0.00057	0.00006
5787.15562	2993.0	I	0.00044	−0.00007	5787.02466	2992.5	II	0.00064	0.00013
5787.41789	2994.0	I	0.00039	−0.00012	5787.28710	2993.5	II	0.00076	0.00025
5787.68022	2995.0	I	0.00040	−0.00011	5787.54920	2994.5	II	0.00054	0.00003
5787.94251	2996.0	I	0.00038	−0.00013	5787.81157	2995.5	II	0.00060	0.00009
5788.20475	2997.0	I	0.00030	−0.00020	5788.07397	2996.5	II	0.00068	0.00018
5788.46720	2998.0	I	0.00043	−0.00007	5788.33633	2997.5	II	0.00072	0.00021
5788.72942	2999.0	I	0.00034	−0.00017	5788.59842	2998.5	II	0.00050	−0.00001
5788.99177	3000.0	I	0.00037	−0.00014	5788.86078	2999.5	II	0.00053	0.00003
5789.25408	3001.0	I	0.00036	−0.00014	5789.12328	3000.5	II	0.00072	0.00022
5789.51641	3002.0	I	0.00038	−0.00013	5789.38556	3001.5	II	0.00069	0.00018
5789.77866	3003.0	I	0.00031	−0.00020	5789.64780	3002.5	II	0.00061	0.00010
5790.04109	3004.0	I	0.00042	−0.00008	5789.91000	3003.5	II	0.00050	−0.00001
5790.30352	3005.0	I	0.00053	0.00003	5790.17263	3004.5	II	0.00080	0.00030
5790.56574	3006.0	I	0.00044	−0.00007	5790.43473	3005.5	II	0.00058	0.00008
5790.82787	3007.0	I	0.00025	−0.00025	5790.69702	3006.5	II	0.00056	0.00006
5791.09036	3008.0	I	0.00042	−0.00008	5790.95941	3007.5	II	0.00064	0.00013
5791.35262	3009.0	I	0.00037	−0.00014	5791.22160	3008.5	II	0.00051	0.00000
5791.61493	3010.0	I	0.00037	−0.00014	5791.48409	3009.5	II	0.00068	0.00017
5791.87739	3011.0	I	0.00050	0.00000	5791.74635	3010.5	II	0.00062	0.00012
5792.13963	3012.0	I	0.00043	−0.00008	5792.00872	3011.5	II	0.00068	0.00017
5792.40196	3013.0	I	0.00044	−0.00007	5792.27091	3012.5	II	0.00055	0.00005
5792.66439	3014.0	I	0.00056	0.00005	5792.53334	3013.5	II	0.00066	0.00015
5792.92667	3015.0	I	0.00052	0.00002	5792.79570	3014.5	II	0.00071	0.00020
5793.18883	3016.0	I	0.00036	−0.00014	5793.05791	3015.5	II	0.00059	0.00009
5793.45125	3017.0	I	0.00046	−0.00004	5793.32014	3016.5	II	0.00051	0.00001
5793.71356	3018.0	I	0.00045	−0.00005	5793.58251	3017.5	II	0.00057	0.00007
5793.97583	3019.0	I	0.00042	−0.00009	5793.84439	3018.5	II	0.00013	−0.00038
5794.23824	3020.0	I	0.00050	0.00000	5794.10726	3019.5	II	0.00068	0.00018
5794.50047	3021.0	I	0.00042	−0.00009	5794.36953	3020.5	II	0.00063	0.00013
5795.02511	3023.0	I	0.00042	−0.00008	5794.63184	3021.5	II	0.00063	0.00012
5795.28743	3024.0	I	0.00042	−0.00008	5794.89418	3022.5	II	0.00065	0.00015
5795.54970	3025.0	I	0.00038	−0.00012	5795.15639	3023.5	II	0.00055	0.00004
5795.81201	3026.0	I	0.00037	−0.00013	5795.41861	3024.5	II	0.00045	−0.00006
5796.07435	3027.0	I	0.00040	−0.00011	5795.68117	3025.5	II	0.00069	0.00019
5796.33660	3028.0	I	0.00033	−0.00017	5795.94344	3026.5	II	0.00064	0.00014
5796.59882	3029.0	I	0.00023	−0.00027	5796.20583	3027.5	II	0.00072	0.00022
5796.86132	3030.0	I	0.00042	−0.00008	5796.46806	3028.5	II	0.00063	0.00013
5797.12378	3031.0	I	0.00056	0.00006	5796.73036	3029.5	II	0.00062	0.00011
5797.38596	3032.0	I	0.00042	−0.00008	5796.99260	3030.5	II	0.00054	0.00003

TABLE 1 (CONTINUED)

BJD (+24 50000)	E	Type	$(O-C)_I$ (day)	$(O-C)_{II}$ (day)	BJD (+24 50000)	E	Type	$(O-C)_I$ (day)	$(O-C)_{II}$ (day)
5797.64831	3033.0	I	0.00046	−0.00005	5797.25499	3031.5	II	0.00061	0.00011
5797.91059	3034.0	I	0.00042	−0.00008	5797.51730	3032.5	II	0.00060	0.00010
5798.17290	3035.0	I	0.00041	−0.00009	5797.77958	3033.5	II	0.00056	0.00006
5798.43522	3036.0	I	0.00042	−0.00008	5798.04192	3034.5	II	0.00059	0.00009
5798.69750	3037.0	I	0.00038	−0.00012	5798.30430	3035.5	II	0.00065	0.00015
5798.95987	3038.0	I	0.00044	−0.00007	5798.56658	3036.5	II	0.00061	0.00011
5799.22219	3039.0	I	0.00044	−0.00007	5798.82883	3037.5	II	0.00055	0.00004
5799.48450	3040.0	I	0.00042	−0.00008	5799.09109	3038.5	II	0.00049	−0.00001
5799.74680	3041.0	I	0.00041	−0.00009	5799.35343	3039.5	II	0.00052	0.00002
5800.00915	3042.0	I	0.00045	−0.00006	5799.61583	3040.5	II	0.00060	0.00010
5800.27136	3043.0	I	0.00033	−0.00017	5799.87847	3041.5	II	0.00092	0.00042
5800.53375	3044.0	I	0.00041	−0.00009	5800.14042	3042.5	II	0.00055	0.00005
5800.79601	3045.0	I	0.00035	−0.00015	5800.40276	3043.5	II	0.00058	0.00007
5801.05841	3046.0	I	0.00044	−0.00006	5800.66503	3044.5	II	0.00053	0.00003
5801.32068	3047.0	I	0.00039	−0.00011	5800.92739	3045.5	II	0.00058	0.00008
5801.58306	3048.0	I	0.00045	−0.00005	5801.18955	3046.5	II	0.00042	−0.00008
5801.84539	3049.0	I	0.00046	−0.00004	5801.45207	3047.5	II	0.00062	0.00012
5803.15703	3054.0	I	0.00052	0.00002	5801.71447	3048.5	II	0.00070	0.00020
5803.41922	3055.0	I	0.00040	−0.00010	5803.28830	3054.5	II	0.00064	0.00013
5803.68156	3056.0	I	0.00042	−0.00008	5803.55064	3055.5	II	0.00065	0.00015
5803.94397	3057.0	I	0.00051	0.00001	5803.81290	3056.5	II	0.00061	0.00010
5804.20622	3058.0	I	0.00044	−0.00006	5804.07518	3057.5	II	0.00056	0.00006
5804.46852	3059.0	I	0.00043	−0.00007	5804.33752	3058.5	II	0.00059	0.00009
5804.73098	3060.0	I	0.00057	0.00007	5804.59987	3059.5	II	0.00062	0.00012
5804.99308	3061.0	I	0.00036	−0.00015	5804.86217	3060.5	II	0.00060	0.00010
5805.25550	3062.0	I	0.00046	−0.00004	5805.12447	3061.5	II	0.00059	0.00008
5805.51784	3063.0	I	0.00048	−0.00002	5805.38688	3062.5	II	0.00068	0.00018
5805.78006	3064.0	I	0.00038	−0.00012	5805.64934	3063.5	II	0.00082	0.00032
5806.04238	3065.0	I	0.00039	−0.00011	5805.91151	3064.5	II	0.00068	0.00018
5806.30477	3066.0	I	0.00046	−0.00005	5806.17373	3065.5	II	0.00058	0.00008
5806.56712	3067.0	I	0.00050	−0.00001	5806.43608	3066.5	II	0.00062	0.00011
5806.82940	3068.0	I	0.00045	−0.00005	5806.69838	3067.5	II	0.00059	0.00009
5807.09167	3069.0	I	0.00041	−0.00009	5806.96067	3068.5	II	0.00057	0.00007
5807.35401	3070.0	I	0.00043	−0.00007	5807.22302	3069.5	II	0.00060	0.00010
5807.61627	3071.0	I	0.00038	−0.00012	5807.74772	3071.5	II	0.00067	0.00017
5807.87864	3072.0	I	0.00043	−0.00008	5808.00991	3072.5	II	0.00054	0.00004
5808.14096	3073.0	I	0.00043	−0.00007	5808.27221	3073.5	II	0.00053	0.00002
5808.40327	3074.0	I	0.00043	−0.00007	5808.53459	3074.5	II	0.00059	0.00009
5808.66558	3075.0	I	0.00042	−0.00008	5808.79695	3075.5	II	0.00063	0.00013
5808.92788	3076.0	I	0.00040	−0.00010	5809.05922	3076.5	II	0.00059	0.00008
5809.19021	3077.0	I	0.00042	−0.00008	5809.32162	3077.5	II	0.00067	0.00017
5809.71445	3079.0	I	0.00003	−0.00047	5809.58393	3078.5	II	0.00066	0.00016
5809.97705	3080.0	I	0.00030	−0.00020	5809.84621	3079.5	II	0.00063	0.00013
5810.23950	3081.0	I	0.00044	−0.00006	5810.10852	3080.5	II	0.00062	0.00012
5810.50178	3082.0	I	0.00040	−0.00010	5810.37081	3081.5	II	0.00059	0.00009
5810.76405	3083.0	I	0.00035	−0.00015	5810.63311	3082.5	II	0.00057	0.00007
5811.02640	3084.0	I	0.00039	−0.00011	5810.89550	3083.5	II	0.00064	0.00014
5811.28878	3085.0	I	0.00045	−0.00005	5811.15768	3084.5	II	0.00051	0.00001
5811.55104	3086.0	I	0.00040	−0.00010	5811.42012	3085.5	II	0.00063	0.00013
5811.81335	3087.0	I	0.00039	−0.00011	5811.68243	3086.5	II	0.00063	0.00013
5812.07572	3088.0	I	0.00044	−0.00006	5811.94482	3087.5	II	0.00070	0.00020
5812.33787	3089.0	I	0.00028	−0.00022	5812.20700	3088.5	II	0.00057	0.00007
5812.60016	3090.0	I	0.00025	−0.00025	5812.46930	3089.5	II	0.00055	0.00005
5812.86218	3091.0	I	−0.00004	−0.00055	5812.73176	3090.5	II	0.00069	0.00019

TABLE 1 (CONTINUED)

BJD (+24 50000)	E	Type	$(O-C)_I$ (day)	$(O-C)_{II}$ (day)	BJD (+24 50000)	E	Type	$(O-C)_I$ (day)	$(O-C)_{II}$ (day)
5813.12485	3092.0	I	0.00030	−0.00020	5812.99405	3091.5	II	0.00066	0.00016
5813.38697	3093.0	I	0.00010	−0.00040	5813.51857	3093.5	II	0.00055	0.00005
5813.64950	3094.0	I	0.00032	−0.00018	5813.78083	3094.5	II	0.00049	−0.00001
5813.91198	3095.0	I	0.00048	−0.00002	5814.04320	3095.5	II	0.00055	0.00005
5814.17418	3096.0	I	0.00037	−0.00013	5814.30553	3096.5	II	0.00056	0.00006
5814.43651	3097.0	I	0.00038	−0.00013	5814.56796	3097.5	II	0.00067	0.00017
5814.69876	3098.0	I	0.00031	−0.00019	5814.83014	3098.5	II	0.00054	0.00004
5814.96114	3099.0	I	0.00037	−0.00013	5815.09257	3099.5	II	0.00065	0.00015
5815.22344	3100.0	I	0.00036	−0.00014	5815.35425	3100.5	II	0.00001	−0.00049
5815.48564	3101.0	I	0.00024	−0.00026	5815.61713	3101.5	II	0.00057	0.00007
5815.74811	3102.0	I	0.00040	−0.00010	5815.87944	3102.5	II	0.00057	0.00007
5816.01052	3103.0	I	0.00049	−0.00001	5816.14174	3103.5	II	0.00055	0.00005
5816.27266	3104.0	I	0.00031	−0.00019	5816.40395	3104.5	II	0.00044	−0.00006
5816.53504	3105.0	I	0.00037	−0.00013	5816.66593	3105.5	II	0.00010	−0.00040
5816.79728	3106.0	I	0.00030	−0.00020	5816.92880	3106.5	II	0.00066	0.00016
5817.05964	3107.0	I	0.00034	−0.00016	5817.19100	3107.5	II	0.00054	0.00004
5817.32198	3108.0	I	0.00037	−0.00013	5817.45352	3108.5	II	0.00075	0.00025
5817.58428	3109.0	I	0.00035	−0.00015	5817.71574	3109.5	II	0.00065	0.00015
5817.84666	3110.0	I	0.00041	−0.00009	5817.97813	3110.5	II	0.00073	0.00023
5818.10956	3111.0	I	0.00100	0.00050	5818.24076	3111.5	II	0.00104	0.00054
5818.37127	3112.0	I	0.00039	−0.00011	5818.50250	3112.5	II	0.00046	−0.00004
5818.63346	3113.0	I	0.00026	−0.00024	5818.76494	3113.5	II	0.00058	0.00008
5818.89586	3114.0	I	0.00034	−0.00016	5819.02721	3114.5	II	0.00054	0.00004
5819.15825	3115.0	I	0.00041	−0.00009	5819.28957	3115.5	II	0.00058	0.00008
5819.42062	3116.0	I	0.00047	−0.00003	5819.55194	3116.5	II	0.00063	0.00013
5819.68287	3117.0	I	0.00040	−0.00010	5819.81412	3117.5	II	0.00050	0.00000
5819.94514	3118.0	I	0.00036	−0.00014	5820.07665	3118.5	II	0.00071	0.00021
5820.20747	3119.0	I	0.00037	−0.00013	5820.33886	3119.5	II	0.00061	0.00011
5820.46980	3120.0	I	0.00038	−0.00012	5820.60122	3120.5	II	0.00064	0.00014
5820.73204	3121.0	I	0.00031	−0.00019	5820.86365	3121.5	II	0.00076	0.00026
5820.99433	3122.0	I	0.00028	−0.00022	5821.12575	3122.5	II	0.00054	0.00004
5821.25663	3123.0	I	0.00026	−0.00024	5821.38816	3123.5	II	0.00064	0.00014
5821.51917	3124.0	I	0.00049	−0.00001	5821.65047	3124.5	II	0.00063	0.00013
5821.78135	3125.0	I	0.00035	−0.00015	5821.91268	3125.5	II	0.00052	0.00002
5822.04365	3126.0	I	0.00033	−0.00017	5822.17504	3126.5	II	0.00057	0.00007
5822.30599	3127.0	I	0.00036	−0.00014	5822.43737	3127.5	II	0.00058	0.00008
5822.56831	3128.0	I	0.00036	−0.00014	5822.69969	3128.5	II	0.00058	0.00008
5822.83056	3129.0	I	0.00029	−0.00021	5822.96218	3129.5	II	0.00075	0.00025
5823.09302	3130.0	I	0.00044	−0.00006	5823.22431	3130.5	II	0.00057	0.00007
5823.35536	3131.0	I	0.00046	−0.00004	5823.48652	3131.5	II	0.00046	−0.00004
5823.61756	3132.0	I	0.00034	−0.00016	5823.74905	3132.5	II	0.00067	0.00018
5823.88003	3133.0	I	0.00049	−0.00001	5824.01127	3133.5	II	0.00058	0.00008
5824.14225	3134.0	I	0.00040	−0.00010	5824.27361	3134.5	II	0.00060	0.00010
5824.40453	3135.0	I	0.00036	−0.00014	5824.53601	3135.5	II	0.00068	0.00018
5824.66695	3136.0	I	0.00047	−0.00003	5824.79824	3136.5	II	0.00060	0.00010
5824.92924	3137.0	I	0.00044	−0.00006	5825.06050	3137.5	II	0.00054	0.00004
5825.19154	3138.0	I	0.00043	−0.00007	5825.32279	3138.5	II	0.00051	0.00001
5825.45390	3139.0	I	0.00046	−0.00003	5825.58529	3139.5	II	0.00070	0.00020
5825.71621	3140.0	I	0.00046	−0.00004	5825.84753	3140.5	II	0.00062	0.00012
5825.97848	3141.0	I	0.00041	−0.00009	5826.10994	3141.5	II	0.00071	0.00021
5826.24082	3142.0	I	0.00043	−0.00006	5826.37214	3142.5	II	0.00060	0.00010
5826.50316	3143.0	I	0.00045	−0.00005	5826.63450	3143.5	II	0.00063	0.00014
5826.76539	3144.0	I	0.00037	−0.00013	5826.89681	3144.5	II	0.00063	0.00013
5827.02783	3145.0	I	0.00049	−0.00001	5827.15911	3145.5	II	0.00062	0.00012

TABLE 1 (CONTINUED)

BJD (+24 50000)	E	Type	$(O-C)_I$ (day)	$(O-C)_{II}$ (day)	BJD (+24 50000)	E	Type	$(O-C)_I$ (day)	$(O-C)_{II}$ (day)
5827.29006	3146.0	I	0.00041	−0.00009	5827.42147	3146.5	II	0.00066	0.00016
5827.55248	3147.0	I	0.00051	0.00001	5827.68367	3147.5	II	0.00054	0.00005
5827.81476	3148.0	I	0.00048	−0.00002	5827.94613	3148.5	II	0.00069	0.00019
5828.07705	3149.0	I	0.00044	−0.00005	5828.20842	3149.5	II	0.00066	0.00016
5828.33942	3150.0	I	0.00050	0.00000	5828.47068	3150.5	II	0.00060	0.00010
5828.60162	3151.0	I	0.00038	−0.00012	5828.73306	3151.5	II	0.00066	0.00016
5828.86430	3152.0	I	0.00074	0.00024	5828.99522	3152.5	II	0.00051	0.00001
5829.12629	3153.0	I	0.00042	−0.00008	5829.25755	3153.5	II	0.00052	0.00003
5829.38866	3154.0	I	0.00047	−0.00003	5829.51981	3154.5	II	0.00046	−0.00004
5829.65093	3155.0	I	0.00043	−0.00007	5829.78236	3155.5	II	0.00069	0.00020
5829.91329	3156.0	I	0.00047	−0.00003	5830.04457	3156.5	II	0.00059	0.00009
5830.17562	3157.0	I	0.00048	−0.00002	5830.30680	3157.5	II	0.00051	0.00001
5830.43787	3158.0	I	0.00042	−0.00008	5830.56913	3158.5	II	0.00051	0.00002
5830.70019	3159.0	I	0.00042	−0.00008	5830.83157	3159.5	II	0.00064	0.00014
5830.96248	3160.0	I	0.00039	−0.00011	5831.09376	3160.5	II	0.00052	0.00002
5831.22489	3161.0	I	0.00049	−0.00001	5831.35620	3161.5	II	0.00064	0.00014
5831.48711	3162.0	I	0.00039	−0.00011	5831.61846	3162.5	II	0.00058	0.00008
5831.74944	3163.0	I	0.00040	−0.00010	5831.88079	3163.5	II	0.00059	0.00009
5832.01179	3164.0	I	0.00044	−0.00006	5832.14315	3164.5	II	0.00064	0.00014
5832.27407	3165.0	I	0.00039	−0.00010	5832.40538	3165.5	II	0.00055	0.00005
5832.53641	3166.0	I	0.00042	−0.00007	5832.66774	3166.5	II	0.00059	0.00010
5832.79871	3167.0	I	0.00041	−0.00009	5832.92998	3167.5	II	0.00052	0.00002

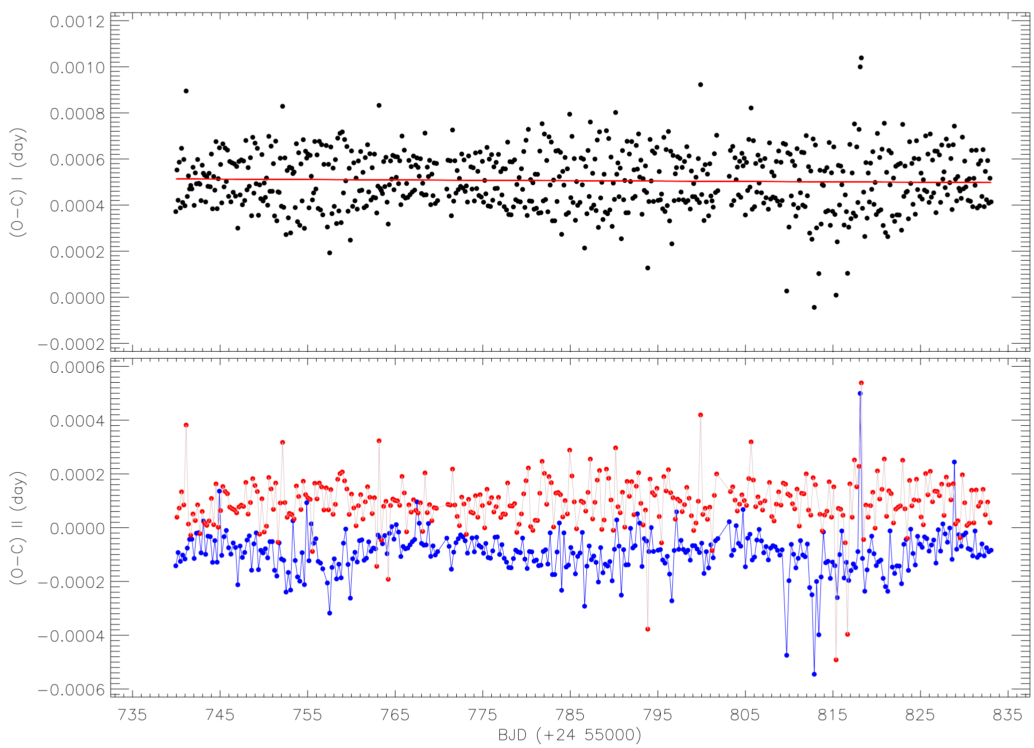

Fig. 2. The variations of time of minimum residuals of $(O-C)_I$ and $(O-C)_{II}$ obtained by applying a linear correction. In the bottom panel, the filled blue circles represent the primary minima; the filled red circles represent the secondary minima. In the upper panel all the residuals are plotted with filled black circles, while the red line represents a linear fit. The color figure can be viewed online.

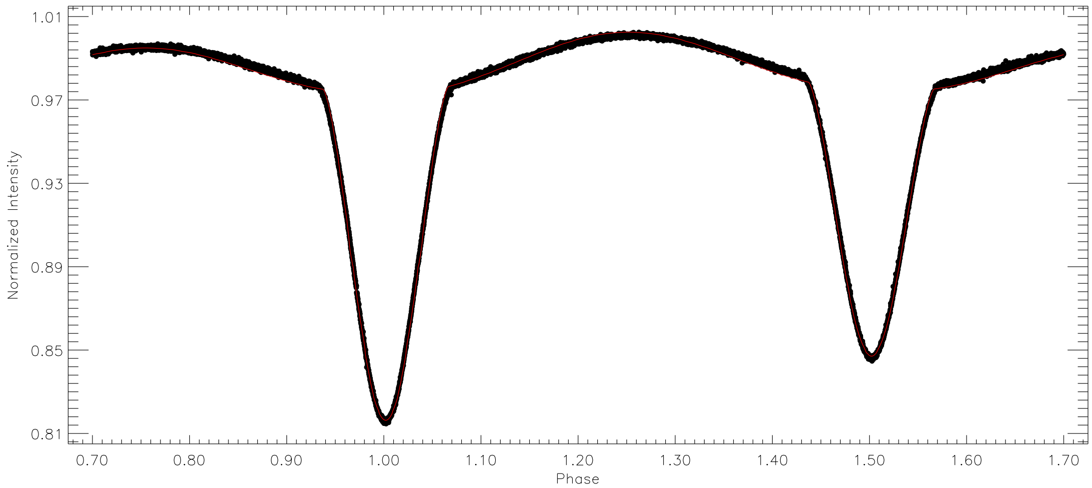

Fig. 3. The light curve along the orbital cycle, from BJD 2455739.94 to 2455829.13. In the figure, the filled circles represent the observations, while the red smooth line represents the synthetic light curve. The color figure can be viewed online.

were tried in the light curve analyses, astrophysically acceptable parameters were obtained only for the detached system mode.

The PHOEBE V.0.32, needs a temperature value for the primary component. We determined its temperature from the JHK brightness given by Cutri et al. (2003). The de-reddened colors were found to be $(H-K)_{\circ} = 0^{\rm m}.252$ and $(J-K)_{\circ} = 0^{\rm m}.629$. Then a temperature value of 4220±20 K corresponding to the de-reddened colours was obtained by using the calibrations given by Tokunaga (2000). We accepted this value as the primary component temperature. The temperature of the secondary component was taken as an adjustable free parameter. In the analyses, some coefficients, such as the albedos (A_1 and A_2), the gravity-darkening coefficients (g_1 and g_2) and the limb-darkening coefficients (x_1 and x_2), were taken from the tables given by Lucy (1967); Rucinski (1969); Van Hamme (1993), considering the possible temperatures of both components. The rest of the parameters, such as the dimensionless potentials (Ω_1 and Ω_2), the fractional luminosity (L_1) of the primary component, the inclination (i) and the mass ratio (q) of the system, were taken as adjustable free parameters.

The computed values of the free parameters are tabulated in Table 2, while the synthetic light curve derived by these parameters is shown in Figure 3. As the table shows, some errors are smaller than the expected values. However, the errors given in the table were computed by the PHOEBE V.0.32, depending on Taylor (1997). In fact the χ^2 was computed as 3.15×10^{-3} from the Kepler short cadence data. The 3D model of Roche geometry obtained with these parameters is shown in Figure 4.

It should be noted that we obtained a solution after some iterations in the detached system mode of the Wilson-Devinney Code (Wilson & Devinney 1971; Wilson 1990). Although the synthetic curve fitted the observations very well, it was revealed that it did not fit the observations around phase 0.27. To solve this mismatched part of synthetic light curve, we assumed that there is a spotted area on a component, considering the flare activity. We assumed that the spotted area was on the primary component. It could be assumed that the spotted star was the secondary component, which would lead to another acceptable solution.

The $(B-V)$ color indexes were computed as $1^{\rm m}.233$ and $1^{\rm m}.329$ for the primary and secondary components, respectively. The computed color indexes are in agreement with the values found by Walkowicz & Basri (2013). Considering these values, we determined the masses as $0.644M_{\odot}$ and $0.570M_{\odot}$ for primary and secondary components. Then, the semi-major axis of the system was found to be $1.84R_{\odot}$ (0.0086 AU) according to Kepler's third law. With this value for the semi-major axis, the radius of the primary component was found to be $0.701R_{\odot}$, while that of the secondary was $0.650R_{\odot}$.

2.3. *Flare Activity and the OPEA Model*

The main subject of this paper is about flare activity in KIC 12004834. To demonstrate the nature of the flare activity occurring in a star with

TABLE 2

PARAMETERS OBTAINED FROM THE LIGHT CURVE ANALYSIS OF KIC 12004834

Parameter	Value
q	0.743 ± 0.001
i (°)	75.89 ± 0.03
T_1 (K)	4220 (fixed)
T_2 (K)	4001 ± 11
Ω_1	4.308 ± 0.004
Ω_2	5.485 ± 0.007
L_1/L_2	0.245 ± 0.067
g_1, g_2	0.32 (fixed)
A_1, A_2	0.32 (fixed)
$x_{1,bol}$, $x_{2,bol}$	0.377, 0.001 (fixed)
x_1, x_2	0.369, 0.001 (fixed)
$< r_1 >$	0.287 ± 0.001
$< r_2 >$	0.172 ± 0.001
$Co - Lat^{(rad)}_{Spot}$	1.920 ± 0.004
$Long^{(rad)}_{Spot}$	1.710 ± 0.002
$R^{(rad)}_{Spot}$	0.244 ± 0.003
T_{fSpot}	0.960 ± 0.001

known photometric data, Dal & Evren (2010) and Dal (2012) described a simple way depending on the method mentioned by Gershberg (1972), which is just a smoothing out of the flares. However, apart from the flare activity, the light curve of KIC 12004834 exhibits other effects caused by both the geometrical nature of the components and the structures on them, such as eclipses and cool spots.

In order to determine and analyze the flares, first we removed the variations seen out-of-flares in the light curves. We follow the method of Dal & Evren (2010) for KIC 12004834. For this purpose, using the synthetic light curve derived from the light curve analyses described in the previous section, the residual data were obtained as a pre-whitened light curve, in which there was only flare activity variation. Following Dal (2012), 149 flares were detected from the available short cadence data. In the analyses, the synthetic light curve allowed us to fix the quiescent levels at the flare moment, which are shown in Figure 5.

Taking into account that the luminosity parameter enters in the energy calculations as described by Dal & Evren (2010, 2011), the equivalent duration parameter was computed for each flare, instead of its energy. According to the beginning and the end of a

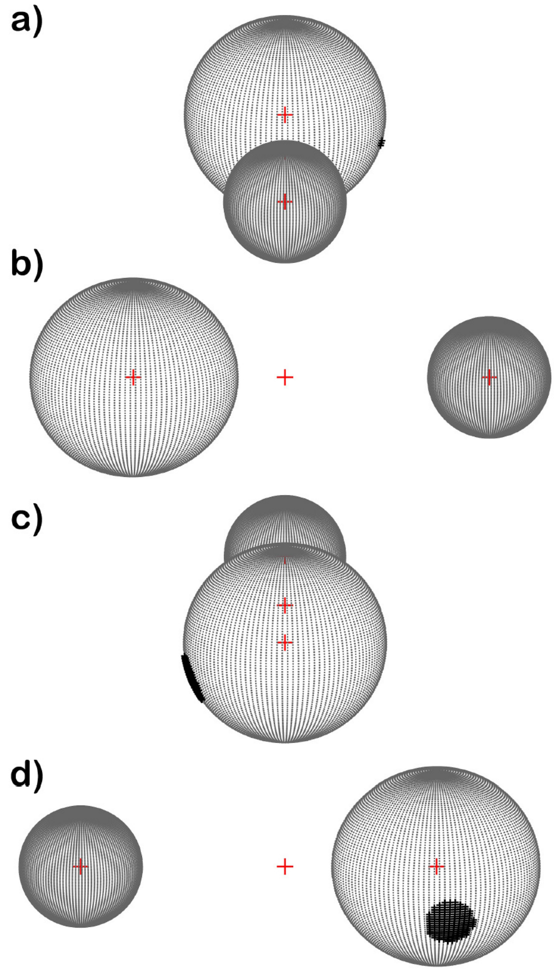

Fig. 4. The 3D model of Roche geometry and spotted area distribution derived from the light curve analysis is shown for different phases, such as (a) 0.00, (b) 0.25, (c) 0.50, (d) 0.75. The color figure can be viewed online.

flare, the desired parameters, such as flare rise times (T_r), decay times (T_d), amplitudes of flare maxima, flare equivalent durations (P), were computed for each flare. The flare equivalent durations were computed by equation (2) taken from Gershberg (1972):

$$P = \int [(I_{flare} - I_0)/I_0] dt \tag{2}$$

where I_0 is the flux of the star in the quiet state. As described above, the synthetic light curve derived by the light curve analysis was taken as I_0. $I_{\rm flare}$ is the intensity observed at the moment of the flare. P is the flare-equivalent duration in the observing band. All the computed parameters are listed in Table 3 for these 149 flares. The general standard errors were

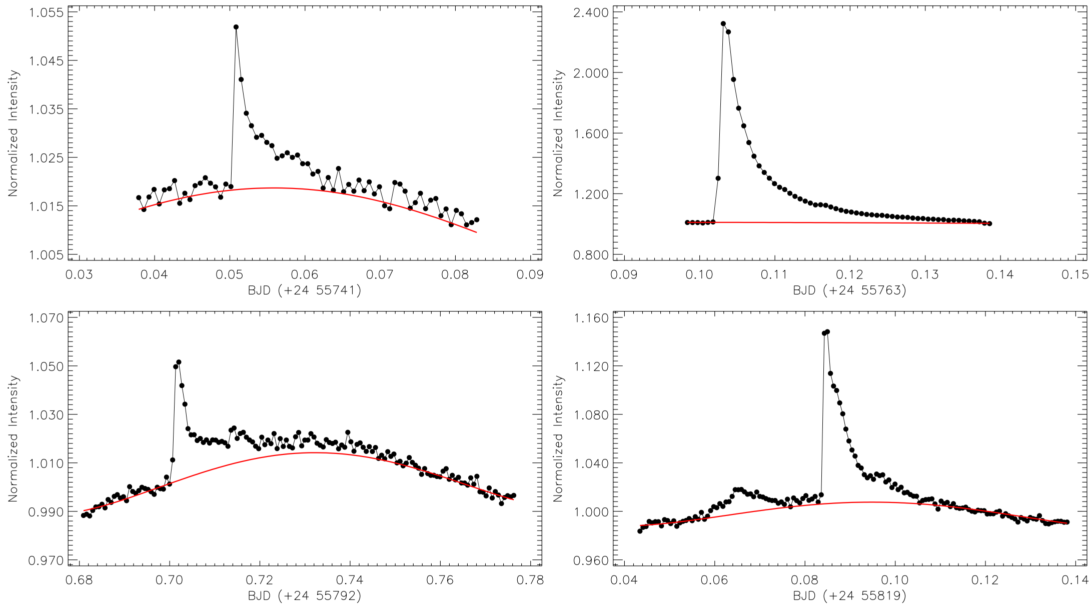

Fig. 5. Four different samples for the flare light variations are shown. In the figure, the filled circles represent the observations, while the (red) lines represent the synthetic light curve obtained from the light curve analysis, which was taken as the quiescent levels for each flare. The color figure can be viewed online.

computed by using the methods described by Taylor (1997) for the time scales such as flare rise and decay times.

The distributions of flare equivalent durations on a logarithmic scale versus flare total durations were modelled by the One Phase Exponential Association (hereafter OPEA) defined by equation (3), using the SPSS V17.0 (Green et al. 1999) and GrahpPad Prism V5.02 (Dawson & Trapp 2004) software:

$$y = y_0 + (Plateau - y_0) \times (1 - e^{-k \times x}) \quad (3)$$

where y is the flare equivalent duration, x is the flare total duration. According to the description of Dal & Evren (2010), the most important parameter in this equation is the $Plateau$ term to reveal the flare behavior of a star. Following three different methods described by D'Agostino & Stephens (1986), the probability values ($p-value$) were calculated to test the quality of the fit. The $p-value$ was found to be < 0.001 in all the methods. The derived OPEA model is shown in Figure 6 together with the observed flare equivalent durations. The parameters computed from the model are listed in Table 4.

In contrast to the known UV Ceti flare stars, KIC 12004834 is a binary system. It is well known that the flare events are generally random phenomena. To test this situation for a close binary like KIC 12004834, we calculated the phase distribution of the flares, depending on the orbital period of the system. The phase distribution is shown in Figure 7. In the figure, the distribution of the total number of flares computed in phase intervals of 0.05, for all 149 flares is shown.

We also derived the flare energy spectrum (Gershberg 1972) for KIC 12004834. Like for the OPEA model, we again used the flare equivalent duration instead of the flare energy. To derive the flare energy spectrum, the cumulative flare frequencies were computed for 149 flares, and then, its distribution was derived in order to compare KIC 12004834 to its analogues. The obtained cumulative flare frequency distribution and its models are shown in Figure 8.

In the literature there are two other flare frequency descriptions. Contrary to Gershberg (1972), Ishida et al. (1991) described the flare frequencies N_1 and N_2, a flare number and a total flare-equivalent duration emitting per hour, respectively. In this study, we detected 149 flares from the available observations lasting 89.19 days. We computed the frequencies by equations (4) and (5) (Ishida et al. 1991):

$$N_1 = \Sigma n_f \;/\; \Sigma DT \quad (4)$$

$$N_2 = \Sigma P \;/\; \Sigma DT \quad (5)$$

where Σn_f is the total flare number, ΣDT is the total observing duration, and ΣP is the total equivalent duration. We found that the N_1 frequency is 0.070 h^{-1}, while the N_2 frequency is 0.62 second/hour for KIC 12004834. It should be noted that

TABLE 3

THE FLARE PARAMETERS COMPUTED FROM KIC 12004834'S THE AVAILABLE SHORT CADENCE DATA IN THE KEPLER MISSION DATABASE

Tmax (BJD-2450000)	P (s)	T_r (s)	T_d (s)	T_t (s)	Amplitude (Relative Flux)
55806.51506	0.762	58.846 ± 3.616	58.846 ± 3.616	117.692 ± 5.114	0.01180
55804.54459	0.471	58.846 ± 3.616	58.847 ± 3.616	117.693 ± 5.114	0.01221
55811.74873	0.896	58.847 ± 3.616	58.846 ± 3.616	117.693 ± 5.114	0.01720
55766.08239	0.745	58.848 ± 3.616	117.686 ± 5.114	176.534 ± 6.264	0.00989
55830.23880	1.240	58.845 ± 3.616	176.538 ± 6.264	235.383 ± 7.233	0.01713
55801.66075	1.066	117.702 ± 5.114	117.685 ± 5.114	235.386 ± 7.233	0.00827
55794.32581	1.117	58.855 ± 3.617	176.532 ± 6.263	235.387 ± 7.233	0.00929
55831.45798	1.880	117.700 ± 5.114	117.692 ± 5.114	235.392 ± 7.233	0.01391
55822.77794	1.137	58.846 ± 3.616	176.546 ± 6.264	235.392 ± 7.233	0.01338
55801.95704	2.098	58.846 ± 3.616	235.386 ± 7.233	294.233 ± 8.086	0.01416
55804.71215	1.290	117.684 ± 5.114	176.549 ± 6.264	294.233 ± 8.086	0.01001
55823.82889	1.051	58.846 ± 3.616	235.393 ± 7.233	294.240 ± 8.086	0.01032
55822.73912	1.633	117.692 ± 5.114	235.384 ± 7.233	353.076 ± 8.858	0.01343
55760.03465	0.632	58.848 ± 3.616	294.239 ± 8.086	353.087 ± 8.858	0.01071
55801.75679	2.621	58.838 ± 3.616	294.251 ± 8.087	353.088 ± 8.858	0.01381
55799.55611	1.312	117.702 ± 5.114	235.387 ± 7.233	353.089 ± 8.858	0.00642
55780.13399	1.711	117.703 ± 5.114	235.389 ± 7.233	353.092 ± 8.858	0.01102
55766.07149	0.848	117.704 ± 5.114	235.391 ± 7.233	353.094 ± 8.858	0.01050
55768.37983	2.922	58.857 ± 3.617	294.255 ± 8.087	353.112 ± 8.858	0.01705
55756.03029	1.168	117.687 ± 5.114	294.257 ± 8.087	411.944 ± 9.568	0.00935
55756.56293	1.245	117.696 ± 5.114	294.248 ± 8.086	411.944 ± 9.568	0.01079
55740.56791	2.973	117.696 ± 5.114	294.251 ± 8.087	411.947 ± 9.568	0.01556
55831.96472	4.468	58.846 ± 3.616	411.929 ± 9.568	470.775 ± 10.228	0.03456
55778.12332	2.165	117.694 ± 5.114	353.093 ± 8.858	470.787 ± 10.229	0.01238
55776.73927	1.898	117.695 ± 5.114	353.093 ± 8.858	470.788 ± 10.229	0.00963
55792.90704	6.883	117.694 ± 5.114	411.937 ± 9.568	529.631 ± 10.849	0.02718
55779.79002	9.266	117.694 ± 5.114	411.940 ± 9.568	529.634 ± 10.849	0.04237
55755.22928	3.861	176.552 ± 6.264	353.087 ± 8.858	529.640 ± 10.849	0.01210
55772.93588	0.849	117.704 ± 5.114	411.941 ± 9.568	529.644 ± 10.849	0.01032
55761.90026	1.219	117.704 ± 5.114	411.943 ± 9.568	529.648 ± 10.849	0.01217
55755.87908	1.132	294.248 ± 8.086	235.400 ± 7.233	529.648 ± 10.849	0.00573
55783.26307	0.793	58.856 ± 3.617	470.794 ± 10.229	529.650 ± 10.849	0.00322
55762.79935	1.244	117.704 ± 5.114	411.952 ± 9.568	529.655 ± 10.849	0.01132
55766.10282	2.214	294.247 ± 8.086	294.238 ± 8.086	588.485 ± 11.436	0.01453
55792.98265	2.377	117.693 ± 5.114	470.793 ± 10.229	588.486 ± 11.436	0.01164
55825.24424	2.172	117.700 ± 5.114	470.786 ± 10.229	588.486 ± 11.436	0.01260
55810.05753	1.166	176.557 ± 6.264	411.933 ± 9.568	588.489 ± 11.436	0.01357
55742.47985	1.287	176.545 ± 6.264	411.946 ± 9.568	588.490 ± 11.436	0.01300
55747.50593	1.506	117.696 ± 5.114	470.802 ± 10.229	588.498 ± 11.436	0.01536
55742.24282	3.543	294.241 ± 8.086	294.259 ± 8.087	588.500 ± 11.436	0.01447
55829.60128	2.781	117.692 ± 5.114	529.629 ± 10.849	647.322 ± 11.994	0.01256
55826.06293	3.057	176.546 ± 6.264	470.776 ± 10.228	647.323 ± 11.994	0.00379
55792.31311	1.336	176.540 ± 6.264	470.793 ± 10.229	647.333 ± 11.994	0.00897
55762.79186	3.297	117.686 ± 5.114	529.648 ± 10.849	647.334 ± 11.994	0.01830
55779.32482	2.116	117.703 ± 5.114	529.635 ± 10.849	647.337 ± 11.994	0.01469
55748.36688	1.896	235.392 ± 7.233	411.963 ± 9.568	647.355 ± 11.994	0.01075
55776.23933	3.682	117.694 ± 5.114	588.491 ± 11.436	706.185 ± 12.527	0.00924
55796.02792	3.817	117.703 ± 5.114	588.485 ± 11.436	706.188 ± 12.527	0.01597
55765.69482	5.587	235.408 ± 7.233	470.789 ± 10.229	706.197 ± 12.528	0.01827
55763.59627	1.525	117.704 ± 5.114	588.495 ± 11.436	706.199 ± 12.528	0.00532
55811.84817	9.222	176.539 ± 6.264	588.481 ± 11.436	765.020 ± 13.039	0.02482

TABLE 3 (CONTINUED)

Tmax (BJD-2450000)	P (s)	T_r (s)	T_d (s)	T_t (s)	Amplitude (Relative Flux)
55808.84242	3.326	176.548 ± 6.264	588.472 ± 11.436	765.020 ± 13.039	0.01629
55806.89444	2.641	294.241 ± 8.086	470.781 ± 10.229	765.022 ± 13.039	0.04012
55810.38923	3.032	176.548 ± 6.264	588.481 ± 11.436	765.029 ± 13.039	0.00910
55779.65108	6.755	176.551 ± 6.264	588.481 ± 11.436	765.031 ± 13.039	0.02747
55777.26170	2.436	58.847 ± 3.616	706.185 ± 12.527	765.032 ± 13.039	0.01427
55800.70583	1.053	176.549 ± 6.264	588.483 ± 11.436	765.032 ± 13.039	0.01235
55773.50393	2.461	235.407 ± 7.233	529.627 ± 10.849	765.034 ± 13.039	0.04477
55762.69582	2.510	58.839 ± 3.616	706.199 ± 12.528	765.038 ± 13.039	0.01041
55748.38868	3.771	117.704 ± 5.114	647.337 ± 11.994	765.042 ± 13.039	0.01522
55746.66405	1.236	117.704 ± 5.114	647.338 ± 11.994	765.043 ± 13.039	0.01060
55743.15553	2.308	353.098 ± 8.858	411.946 ± 9.568	765.043 ± 13.039	0.01575
55745.65597	2.618	117.705 ± 5.114	647.347 ± 11.994	765.052 ± 13.039	0.01126
55821.60644	2.042	294.230 ± 8.086	529.632 ± 10.849	823.862 ± 13.531	0.00904
55798.75171	4.518	58.838 ± 3.616	765.032 ± 13.039	823.871 ± 13.531	0.02078
55794.34352	4.924	58.856 ± 3.617	765.026 ± 13.039	823.882 ± 13.531	0.01618
55783.25353	3.925	235.388 ± 7.233	588.498 ± 11.436	823.886 ± 13.531	0.01514
55763.58673	4.125	176.551 ± 6.264	647.342 ± 11.994	823.893 ± 13.531	0.01013
55775.11139	3.272	117.704 ± 5.114	706.194 ± 12.528	823.897 ± 13.531	0.01310
55740.48481	2.590	294.250 ± 8.087	529.652 ± 10.849	823.902 ± 13.531	0.01744
55747.88464	3.972	58.857 ± 3.617	765.051 ± 13.039	823.908 ± 13.531	0.02227
55820.70669	11.448	176.546 ± 6.264	706.171 ± 12.527	882.717 ± 14.006	0.02987
55812.88346	5.447	58.855 ± 3.617	823.865 ± 13.531	882.720 ± 14.006	0.02041
55792.81781	3.461	411.937 ± 9.568	470.783 ± 10.229	882.720 ± 14.006	0.01339
55809.54465	3.030	117.693 ± 5.114	765.029 ± 13.039	882.722 ± 14.006	0.01444
55807.14032	3.450	411.934 ± 9.568	470.789 ± 10.229	882.723 ± 14.006	0.01147
55815.95868	2.639	58.856 ± 3.617	823.872 ± 13.531	882.728 ± 14.006	0.01146
55744.32436	4.279	176.553 ± 6.264	706.196 ± 12.528	882.749 ± 14.006	0.01569
55742.23055	5.768	117.705 ± 5.114	765.052 ± 13.039	882.757 ± 14.006	0.01393
55817.51569	6.776	117.701 ± 5.114	823.864 ± 13.531	941.565 ± 14.465	0.02661
55792.21979	1.686	176.541 ± 6.264	765.026 ± 13.039	941.567 ± 14.465	0.00954
55806.74527	3.401	176.548 ± 6.264	765.021 ± 13.039	941.569 ± 14.465	0.01014
55804.56094	2.295	176.539 ± 6.264	765.031 ± 13.039	941.571 ± 14.465	0.00944
55743.93339	1.965	176.553 ± 6.264	765.043 ± 13.039	941.597 ± 14.466	0.00956
55818.95147	5.622	58.846 ± 3.616	941.564 ± 14.465	1000.410 ± 14.911	0.02512
55820.43834	4.285	117.701 ± 5.114	882.718 ± 14.006	1000.419 ± 14.911	0.00997
55800.59413	2.617	117.702 ± 5.114	882.725 ± 14.006	1000.427 ± 14.911	0.01204
55773.99094	2.775	58.848 ± 3.616	941.585 ± 14.465	1000.433 ± 14.911	0.01211
55760.96984	3.584	117.696 ± 5.114	882.743 ± 14.006	1000.439 ± 14.911	0.01461
55777.94827	9.265	176.542 ± 6.264	823.897 ± 13.531	1000.439 ± 14.911	0.02508
55756.66238	4.502	176.552 ± 6.264	823.888 ± 13.531	1000.440 ± 14.911	0.01090
55755.86341	3.832	176.552 ± 6.264	823.897 ± 13.531	1000.449 ± 14.911	0.00772
55752.17713	3.504	176.553 ± 6.264	823.897 ± 13.531	1000.451 ± 14.911	0.01063
55803.99153	3.654	294.233 ± 8.086	765.022 ± 13.039	1059.254 ± 15.343	0.01084
55826.07315	3.786	176.546 ± 6.264	882.715 ± 14.006	1059.261 ± 15.343	0.00801
55741.05083	10.207	58.849 ± 3.616	1000.455 ± 14.911	1059.304 ± 15.343	0.03355
55805.48113	6.780	235.386 ± 7.233	882.724 ± 14.006	1118.109 ± 15.763	0.01629
55792.62642	8.534	353.090 ± 8.858	765.027 ± 13.039	1118.117 ± 15.763	0.02378
55751.93397	6.862	117.696 ± 5.114	1000.442 ± 14.911	1118.138 ± 15.763	0.03174
55765.32020	4.999	176.551 ± 6.264	941.589 ± 14.466	1118.140 ± 15.763	0.01279
55807.98013	4.321	117.702 ± 5.114	1059.261 ± 15.343	1176.963 ± 16.173	0.01249
55792.84574	5.480	176.549 ± 6.264	1000.423 ± 14.911	1176.972 ± 16.173	0.02244
55804.36682	5.572	235.386 ± 7.233	1000.417 ± 14.911	1235.803 ± 16.572	0.01366
55818.06535	18.899	117.692 ± 5.114	1118.111 ± 15.763	1235.803 ± 16.572	0.04024
55763.74271	5.420	235.399 ± 7.233	1000.445 ± 14.911	1235.845 ± 16.572	0.01580

TABLE 3 (CONTINUED)

Tmax (BJD-2450000)	P (s)	T_r (s)	T_d (s)	T_t (s)	Amplitude (Relative Flux)
55808.48143	6.886	294.241 ± 8.086	1000.415 ± 14.911	1294.656 ± 16.962	0.01014
55752.86099	2.487	470.793 ± 10.229	823.897 ± 13.531	1294.690 ± 16.962	0.01033
55748.43023	6.680	176.536 ± 6.264	1118.157 ± 15.764	1294.693 ± 16.962	0.01774
55757.40209	13.431	235.400 ± 7.233	1059.296 ± 15.343	1294.696 ± 16.962	0.02852
55740.24641	5.290	176.554 ± 6.264	1118.152 ± 15.764	1294.706 ± 16.962	0.01038
55755.23405	7.243	58.857 ± 3.617	1235.850 ± 16.572	1294.707 ± 16.962	0.02040
55799.53567	5.955	58.847 ± 3.616	1294.670 ± 16.962	1353.517 ± 17.343	0.02091
55759.69340	8.248	235.400 ± 7.233	1118.134 ± 15.763	1353.535 ± 17.344	0.01900
55748.56237	5.839	235.400 ± 7.233	1118.140 ± 15.763	1353.540 ± 17.344	0.01245
55746.72876	6.982	294.240 ± 8.086	1059.301 ± 15.343	1353.542 ± 17.344	0.01395
55759.69340	2.293	235.391 ± 7.233	1118.152 ± 15.764	1353.542 ± 17.344	0.00198
55820.42199	10.170	176.539 ± 6.264	1235.811 ± 16.572	1412.350 ± 17.716	0.01346
55797.44873	4.053	235.396 ± 7.233	1176.969 ± 16.173	1412.365 ± 17.716	0.01008
55807.03611	20.538	294.241 ± 8.086	1176.964 ± 16.173	1471.205 ± 18.082	0.03700
55791.63812	11.512	294.243 ± 8.086	1176.973 ± 16.173	1471.216 ± 18.082	0.02267
55746.15729	4.354	117.697 ± 5.114	1353.550 ± 17.344	1471.247 ± 18.082	0.01144
55806.00150	11.359	176.540 ± 6.264	1412.367 ± 17.716	1588.907 ± 18.791	0.02162
55787.89945	7.928	58.847 ± 3.616	1530.075 ± 18.440	1588.922 ± 18.791	0.00838
55768.84435	5.401	235.391 ± 7.233	1353.537 ± 17.344	1588.928 ± 18.791	0.01316
55833.09059	25.717	117.700 ± 5.114	1530.033 ± 18.440	1647.734 ± 19.136	0.07710
55819.06454	16.793	588.478 ± 11.436	1059.265 ± 15.343	1647.743 ± 19.136	0.02017
55766.87590	18.093	235.391 ± 7.233	1412.386 ± 17.717	1647.777 ± 19.136	0.03545
55773.95416	4.012	176.543 ± 6.264	1471.237 ± 18.082	1647.780 ± 19.136	0.01109
55790.05588	38.271	411.947 ± 9.568	1294.676 ± 16.962	1706.623 ± 19.475	0.16402
55816.58802	7.120	176.547 ± 6.264	1588.891 ± 18.791	1765.438 ± 19.807	0.01858
55793.88104	24.987	117.702 ± 5.114	1647.764 ± 19.136	1765.466 ± 19.808	0.11313
55826.02002	6.115	117.691 ± 5.114	1706.585 ± 19.475	1824.276 ± 20.135	0.01318
55827.89170	10.892	117.691 ± 5.114	1765.429 ± 19.807	1883.121 ± 20.457	0.02212
55819.08497	46.875	176.547 ± 6.264	1765.435 ± 19.807	1941.983 ± 20.774	0.14180
55780.39486	10.869	588.489 ± 11.436	1471.224 ± 18.082	2059.714 ± 21.395	0.01187
55765.45575	21.704	176.544 ± 6.264	1883.185 ± 20.457	2059.728 ± 21.395	0.04175
55822.75342	10.331	353.085 ± 8.858	2000.826 ± 21.087	2353.911 ± 22.872	0.01707
55828.63411	32.706	117.700 ± 5.114	2412.751 ± 23.156	2530.451 ± 23.714	0.04817
55821.43071	23.129	294.240 ± 8.086	2589.304 ± 23.988	2883.544 ± 25.314	0.01867
55756.89805	22.867	117.704 ± 5.114	2765.928 ± 24.793	2883.633 ± 25.315	0.03313
55763.10313	119.328	117.704 ± 5.114	2942.472 ± 25.572	3060.177 ± 26.078	1.31184
55764.80868	19.131	1059.301 ± 15.343	2059.729 ± 21.395	3119.030 ± 26.328	0.01630
55810.14130	28.083	176.548 ± 6.264	3118.961 ± 26.327	3295.509 ± 27.062	0.02015
55795.62606	59.471	117.703 ± 5.114	3236.660 ± 26.820	3354.362 ± 27.303	0.05526
55822.11727	32.769	235.392 ± 7.233	3177.782 ± 26.575	3413.175 ± 27.541	0.02822
55795.07436	37.409	353.089 ± 8.858	3589.768 ± 28.245	3942.857 ± 29.601	0.04263
55792.70202	36.928	176.541 ± 6.264	3766.321 ± 28.931	3942.862 ± 29.601	0.04881
55766.71856	117.197	235.391 ± 7.233	4119.463 ± 30.257	4354.854 ± 31.109	0.11637
55741.94107	52.968	1059.303 ± 15.343	4296.050 ± 30.899	5355.353 ± 34.498	0.02498

the N_2 frequency is a unitless parameter, because the unit of ΣDT is time as well as the unit of ΣDT. However, the N_2 frequency is given in units of second/hour to facilitate the reading of the manuscript.

3. RESULTS AND DISCUSSION

We analysed the light curve and $(O-C)$ residuals of the system for the first time in the literature. The mass ratio of the system (q) was found to be 0.743 ± 0.001, while the inclination (i) was found to be $75^\circ.89 \pm 0^\circ.03$. This inclination ($i$) value is in agreement with the inclination (i) value of $72^\circ.47$ given by Coughlin et al. (2011). The mass of the primary component was found to be $0.64 M_\odot$ with a radius of $0.70 R_\odot$, while it was found to be $0.57 M_\odot$ for the secondary component with a radius of $0.65 R_\odot$. Although these parameters are a bit larger than those found by Coughlin et al. (2011),

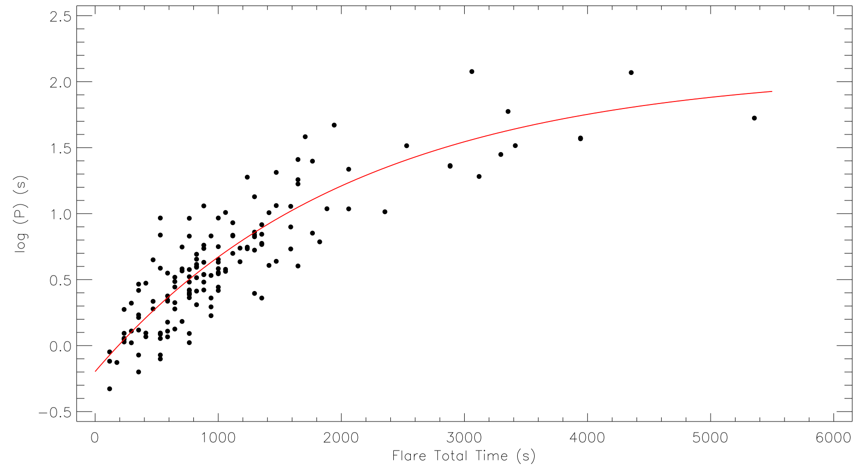

Fig. 6. The OPEA model derived from 149 flares detected in the available short cadence data of KIC 12004834 is shown. In the figure, the filled circles represent the calculated $\log(P)$ values from observations, while the red line represents the OPEA model. The color figure can be viewed online.

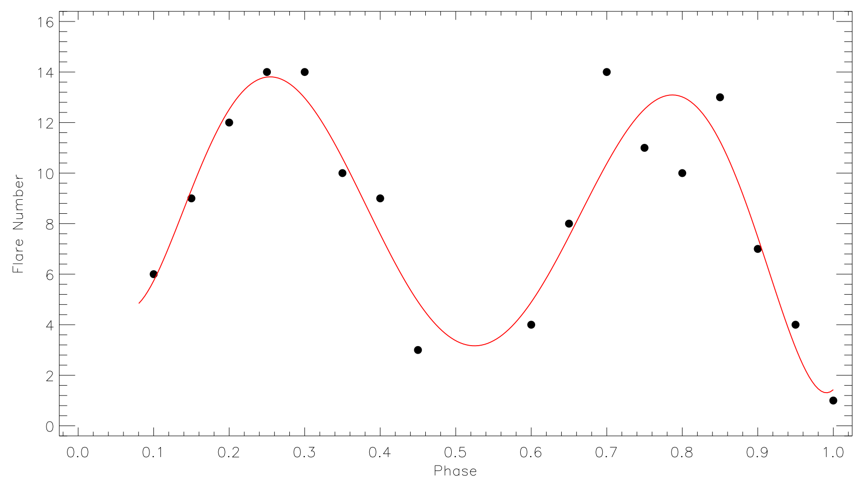

Fig. 7. The distribution of flare total number in each phase interval of 0.05, plotted versus phase for 149 flares. The color figure can be viewed online.

it can be assumed that they are in agreement. In addition, these values indicate that KIC 12004834 is a simple close binary system. Indeed, the possible semi-major axis was found to be as small as $1.84 R_{\odot}$ (≈ 0.0086 AU), which indicates that there must be a distance of $0.49 R_{\odot}$ between the surfaces of the components. In this case, it is possible that each component can trigger the magnetic activity of the other.

If being in a very close binary affects the chromospheric patterns of the active component, we should see an effect: an increase of the flare frequency or of the *Plateau* value. KIC 12004834 was continuously observed over 89.19 days from JD 24 55739.83568694 to JD 24 55833.27789066, and we detected 149 flare events. The flare frequency N_1, the general flare number per an hour, was found to be 0.070 h^{-1}, while the flare frequency N_2, the averaged flare energy per an hour, was computed as 0.62 second/hour. However, according to these results, KIC 12004834 did not show a high magnetic activity, not at the expected level.

Comparing the target to similar systems, we can easily notice that like KIC 12004834, both FL Lyr and KIC 9761199 are binary systems, but with high level chromospheric activity. Indeed, the flare frequencies of FL Lyr were recently found to be $N_1 = 0.41632\ h^{-1}$ and $N_2 = 0.00027$ by (Yoldaş & Dal 2016). However, the radii of the FL Lyr components were given as $R_1 = 1.283 R_{\odot}$, $R_2 = 0.963 R_{\odot}$

TABLE 4

THE OPEA MODEL PARAMETERS DERIVED BY USING THE LEAST-SQUARES METHOD

Parameter	Value
Y_0	-0.197 ± 0.081
$Plateau$	2.093 ± 0.236
K	0.00048 ± 0.00010
Tau	2098.68
$Half-life$	1454.7
95% Confidence Intervals	
Y_0	-0.355 to -0.038
$Plateau$	1.630 to 2.556
K	0.00029 to 0.00067
Tau	1497.65 to 3505.49
$Half-life$	1038.09 to 2429.82
Goodness of Fit	
R^2	0.7628
$p-value$ (D'Agostino-Pearson)	0.0001
$p-value$ (Shapiro-Wilk)	0.0001
$p-value$ (Kolmogorov-Smirnov)	0.0005

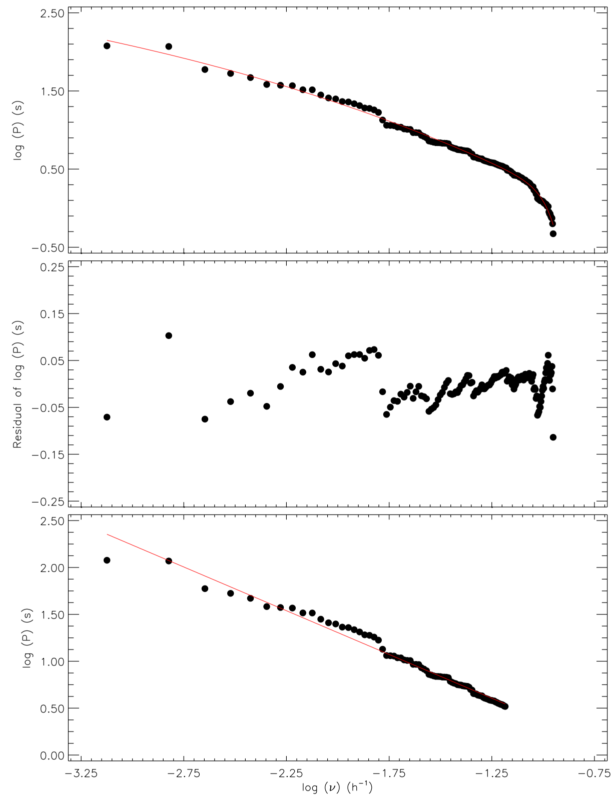

Fig. 8. Cumulative flare frequencies and model computed for 149 flares obtained from KIC 12004834. In the upper panel, the variation of the flare equivalent durations versus the cumulative flare frequency is shown, while the residuals obtained from the model are shown in the middle panel. The bottom panel shows the linear part of the flare energy spectrum and its linear representation. The color figure can be viewed online.

with a semi-major axis of $a = 9.17R_{\odot}$ by Eker et al. (2014). In the case of KIC 9761199, Yoldaş & Dal (2017) found the $Plateau$ value as 1.951 s, while the flare frequencies, N_1 and N_2, were found to be $0.01351\,h^{-1}$ and 0.00006, respectively. The authors computed the masses of the primary and secondary components as $0.57M_{\odot}$, $0.39M_{\odot}$, and the radii of the components as $0.62R_{\odot}$ and $0.56R_{\odot}$ with a semi-major axis of $a = 5.16R_{\odot}$. According to these results, if being a close binary affects the surface magnetic activity, KIC 12004834 should exhibit more frequent or more powerful flares than FL Lyr. On the other hand, according to Dal & Evren (2011); Dal (2012), it is a controversial topic whether the flare frequencies are an indicator of flare activity level, or not. There is one more parameter that may be taken an indicator for the flare activity level, which is the $Plateau$ value. The $Plateau$ value was found to be 2.093 ± 0.236 s from the OPEA model of KIC 12004834. However, Yoldaş & Dal (2016) found the $Plateau$ value as 1.232 ± 0.069 s for FL Lyr. According to these results, the activity level of KIC 12004834 is nearly two times higher than FL Lyr, as expected. With an increasing number of eclipsing binaries with a flaring component, we may determine which parameter is real indicator for the flare activity level.

Using the regression calculations, the half−life value was found to be 1454.7 s from the OPEA model for KIC 12004834. In the case of FL Lyr, it is 2291.7 s (Yoldaş & Dal 2016). This means that a flare occurring on FL Lyr can reach the maximum energy level when the flare total duration reaches 38 minutes, while it takes 24.245 minutes for KIC 12004834. Moreover, the maximum flare rise time (T_r) obtained from the flares of KIC 12004834 was found to be 1059.303 s, while the maximum flare total time (T_t) was found to be 5355.050 s. However, these values are $T_r = 5179.00$ s and $T_t = 12770.62$ s for FL Lyr. As a result, the FL Lyr flare time scales are obviously larger than those obtained from KIC 12004834, which is in agreement with the results found by Dal & Evren (2011); Dal (2012) for single flare stars of type dMe.

However, there is one more controversial feature of KIC 12004834, which is stellar spot activity. During the analysis process, we recognised that the synthetic curve derived without any stellar spot does not fit the observations around phase 0.27. Because of this, the results of the light curve analysis point to the presence of stellar spot activity on one of the components. Considering the temperatures of the components we assumed that the flare activity is a sinusoidal variation caused by the rotational modulation due to the stellar cool spots. Indeed, this sinusoidal variation could be easily modelled with a cool spot on the primary component as seen in the 3D model of Roche geometry shown in Figure 4. However, the analyses indicated that the location of the spot is not changed on the primary component along 89.19 day despite the presence of high level flare activity. Considering the rapid variation in the flare behaviour, a stable spotted area on the component is very interesting. According to Hall et al. (1989) and Gershberg (2005), it is well known that the spotted areas on the active components of some RS CVn binaries can keep their shapes and locations for as long as two years. Therefore, the behavior of the cool spot activity observed for KIC 12004834 is not inconsistent with the stellar spot activity phenomenon.

In addition, considering the distribution of the total flare number in each phase interval of 0.05, it is noticed that the flares tend to occur in two specific phases, 0.25 and 0.75, as seen in Figure 7. Since the spotted area is seen around phase 0.27, the behavior of the flare activity of this close binary system KIC 12004834 can be understood.

At this point, one can question whether the sinusoidal variation out-of-eclipses is really caused by the stellar spots. In the literature, Tran et al. (2013) found a way to obtain the sign of the spot activity. They demonstrated that the spot activity remarkably affects the variations of the $(O-C)$ residuals, especially for the $(O-C)_{II}$ residuals. Tran et al. (2013) reported that the stellar spot activity occurring on the active component causes the $(O-C)_{II}$ residuals of both the primary and secondary minima to vary synchronously in a sinusoidal manner, but in opposite directions. We could not determine the minima times from the Kepler long cadence data because the orbital period of KIC 12004834 is short, $0^{d}.262317$. However, we determined all the minima times from the available short cadence data. In the Kepler Mission Database, the short cadence data of observations are covered over 100 days. Because of this, the sinusoidal variation cannot be properly seen. On the other hand, we determined that the minima times computed from the primary and the secondary minima are separated from each other. This is enough evidence for the spot presence on one component.

We wish to thank the Turkish Scientific and Technical Research Council for supporting this work through grant No. 116F213. We thank the referee for useful comments that have contributed to the improvement of the paper. We also thank Dr. O. Özdarcan for the useful scripts that have supported us, providing an easy way to solve hard calculations.

REFERENCES

Armstrong, D. J., Gómez Maqueo Chew, Y., Faedi, F., & Pollacco, D. 2014, MNRAS, 437, 3473

Balona, L. A. 2015, MNRAS, 447, 2714

Benz, A. O. 2008, LRSP, 5, 1

Borucki, W. J., Koch, D., Basri, G., et al. 2010, Sci, 327, 977

Caldwell, D. A., Kolodziejczak, J. J., & Van Cleve, J. E. 2010, ApJL, 713, L92

Carrington, R. C. 1859, MNRAS, 20, 13

Coughlin, J. L., López-Morales, M., Harrison, T. E., Ule, N., & Hoffman, D. I. 2011, AJ, 141, 78

Cutri, R. M., Skrutskie, M. F., van Dyk, S., et al. 2003, The IRSA 2MASS all sky point source catalog. NASA/IPAC Infrared Science Archive `http://irsa.ipac.caltech.edu/applications/Gator`

D'Agostino, R. B. & Stephens, M. A. 1986, Goodness-Of-Fit Techniques, ed. Ralph B. D'Agostino & M. A. Stephens (New York, NY: Dekker)

Dal, H. A. 2012, PASJ, 64, 82

Dal, H. A. & Evren, S. 2010, AJ, 140, 483

_________. 2011, AJ, 141, 33

Dawson, B. & Trapp, R. G. 2004, Basic and Clinical Biostatistics, (New York, NY: McGraw-Hill)

Debosscher, J., Blomme, J., Aerts, C., & De Ridder, J. 2011, A&A, 529, 89

Eker, Z., Bilir, S., Soydugan, F., et al. 2014, PASA, 31, 24

Gershberg, R. E. 2005, Solar-Type Activity in Main-Secauence Stars, (New York, NY: Springer)

Gershberg, R. E. & Shakhovskaya, N. I. 1983, Ap&SS, 95, 235

Gershberg, R. E. 1972, Ap&SS, 19, 75

Green, S. B., Salkind, N. J. & Akey, T. M. 1999, Using SPSS for Windows: Analyzing and Understanding Data (New Jersey, NJ: Perarson)

Haisch, B., Strong, K. T., & Rodonó, M. 1991, ARA&A, 29, 275

Hall D. S., Henry G. W., & Sowell J. R. 1989, AJ, 99, 396

Hodgson, R. 1859, MNRAS, 20, 15
Ishida, K., Ichimura, K., Shimizu, Y. & Mahasenaputra. 1991, Ap&SS, 182, 227
Jenkins, J. M., Caldwell, D. A., Chandrasekaran, H., et al. 2010a, ApJL, 713, L87
Jenkins, J. M., Chandrasekaran, H., McCauliff, S. D., et al. 2010b, SPIE, 7740, 77400
Kwee, K. K. & van Woerden, H. 1956, BAN, 12, 327
Koch, D. G., Borucki, W. J., Basri, G., et al. 2010, ApJL, 713, L79
Lucy, L. B. 1967, ZA, 65, 89
Matijevič, G., Prša, A., Orosz, J. A., et al. 2012, AJ, 143, 123
Murphy, S. J. 2012, MNRAS, 422, 665
Murphy, S. J., Shibahashi, H., & Kurtz, D. W. 2013, MNRAS, 430, 2986
Özdarcan, O., Yoldaş, E., & Dal, H. A. 2018, RMxAA, 54, 37
Prša, A. & Zwitter, T. 2005, ApJ, 628, 426
Rodonó, M. 1986, NASSP, 492, 409
Rucinski, S. M. 1969, AcA, 19, 245
Slawson, R., Prša, A., Welsh, W. F., et al. 2011, AJ, 142, 160
Taylor, J. 1997, Introduction to Error Analysis, the Study of Uncertainties in Physical Measurements, (2nd ed.; Sausalito, CA: University Science Books)
Tokunaga, A. T. 2000, in Allen's Astrophysical Quantities, ed. A. N. Cox (Springer)
Tran, K., Levine, A., Rappaport, S., et al. 2013, ApJ, 774, 81
Van Hamme, W. 1993, AJ, 106, 2096
Walkowicz, L. M. & Basri, G. S. 2013, MNRAS, 436, 1883
Watson, C. L. 2006, SASS, 25, 47
Wilson, R. E. 1990, ApJ, 356, 613
Wilson, R. E. & Devinney, E. J. 1971, ApJ, 166, 605
Yoldaş, E. & Dal, H. A. 2016, PASA, 33,16
__________. 2017, RMxAA, 53, 67

H. A. Dal and E. Yoldaş: Department of Astronomy and Space Sciences, University of Ege, Bornova, 35100 İzmir, Turkey (ezgiyoldas@gmail.com).

Revista Mexicana de Astronomía y Astrofísica, **55**, 93–104 (2019)

AN ALTERNATIVE APPROACH TO THE FINGER OF GOD IN LARGE SCALE STRUCTURES

L. Salas[1] and I. Cruz-González[2]

Received October 2 2018; accepted January 28 2019

ABSTRACT

It is generally accepted that linear theory of growth of structure under gravity produces a squashed structure in the two-point correlation function (2PCF) along the line of sight (LoS). The observed radial spread out structure known as Finger of God (FoG) is attributed to non-linear effects. We argue that the squashed structure associated with the redshift-space ($s-$) linear theory 2PCF is obtained only when this function is displayed in real-space ($r-$), or when the mapping from $r-$ to $s-$space is approximated. We solve for the mapping function $\boldsymbol{s}(\boldsymbol{r})$ that allows us to display the $s-$space 2PCF in a grid in $s-$space, by using plane of the sky projections of the $r-$ and $s-$ 2PCFs. Even in the simplest case of a linear Kaiser spectrum with a conservative power-law $r-$space 2PCF, a structure quite similar to the FoG is observed in the small scale region, while in the large scale the expected squashed structure is obtained. This structure depends on only three parameters.

RESUMEN

Comúnmente se acepta que la teoría de colapso lineal gravitacional produce una estructura comprimida a lo largo de la visual en la función de correlación de dos puntos (2PCF). La estructura conocida como *Finger of God* (FoG) se ha atribuido a efectos no-lineales. Argumentamos que la estructura asociada con el espacio de corrimiento al rojo ($s-$) de la 2PCF de la teoría lineal, sólo se obtiene cuando esta función se despliega en el espacio-real ($r-$) o cuando el mapeo de $r-$ al $s-$ se calcula mediante una aproximación. Resolvemos para la función de mapeo $\boldsymbol{s}(\boldsymbol{r})$, lo que permite visualizar correctamente la $s-$ 2PCF en una malla en $s-$, utilizando proyecciones en el plano del cielo para ambas 2PCFs, $r-$ y $s-$. Aún en el caso más simple, el de un espectro de Kaiser con ley de potencia para la 2PCF del $r-$, se aprecia a pequeña escala una estructura similar a FoG, mientras que a gran escala se obtiene la estructura comprimida esperada, que solo depende de tres parámetros.

Key Words: cosmology: theory — galaxies: clusters: general — large-scale structure of Universe — quasars: general

1. INTRODUCTION

A spherical object observed at a distance in its longitudinal ($||$) and transversal ($\perp$) dimensions, should provide a test of different cosmological models, as first proposed by Alcock & Paczyński (1979). The Alcock-Paczyński parameter, hereafter AP, basically the ratio of $||$ to $\perp$ dimensions, takes a value of one at redshift zero, and increases with z with a strong dependence on the value of the cosmological parameters that make up the Hubble function, introducing a cosmological distortion to the large scale structure observations. This apparently simple comparison is, however, greatly complicated by several factors. First, real-space measurements are not directly attainable and one has to rely on redshift-space. Then, if the proposed object consists of a cluster of quasars or galaxies, or a statistical ensemble of such, proper motions of its constituents (either derived from gravitational collapse or virialized conditions) distort redshift-space measurements causing a degeneracy problem (e.g., Hamilton 1998). On cosmological scales, clusters of galaxies or quasars are among the simplest geometric structures that

[1]Instituto de Astronomía, Universidad Nacional Autónoma de México, Ensenada, B. C., México.

[2]Instituto de Astronomía, Universidad Nacional Autónoma de México, Ciudad de México, México.

one may conceive. Even if single clusters should have non-spherical or filamentary structures, those should be randomly oriented. As we probe more distant clusters, observations become biased towards brighter and widely separated members, and the numbers become statistically insignificant. A superposition of many such clusters may reduce the problem while retaining spherical symmetry. For more than 40 years the two-point correlation function (2PCF), and its Fourier transform, the power spectrum, have been fundamental tools in these studies (e.g., Peebles 1980).

Overdense clusters or associations separate from the Hubble flow due to their own gravity, which results in peculiar velocities of its members that distort redshift-space observations. When gravitational fields are small, velocities are well described by the linear theory of gravitational collapse (Peebles 1980). In the study of these clusters, the 2PCF was initially conceived as a single entity ξ that could be evaluated in either real ($r-$) or redshift ($s-$) space (Peebles 1980). Davis & Peebles (1983) even mentioned that when observing the local universe, if the peculiar velocities were relatively small, $s-$space would directly reproduce $r-$space and one would have $\xi(\boldsymbol{r}) = \xi(\boldsymbol{s})$. That should be the case for distant objects, although one should be careful not to mix up the notions of distant from each other and distant from the observer. In the case of the CfA Redshift Survey (e.g., Huchra et al. 1983), as described in Davis & Peebles (1983) peculiar velocities were significant, and the authors chose to go from real $\xi(r)$ to observable $\xi(s)$ by means of a convolution with a pair-wise velocity distribution, tailored to approach the Hubble flow at large distances, known as the *streaming model*. The convolution integral would at the same time convert $r-$space to $s-$space coordinates. However, the same function ξ would be obtained as a result of the convolution of ξ with a function of velocity, which constitutes an inconsistency. Later on, Kaiser (1987), hereafter K87, showed that gravitationally induced peculiar velocities by gravitational collapse of overdense structures in the linear regime produced a power spectrum $P^{(s)}$ for $s-$space different from the one $P^{(r)}$ for $r-$space, that is, two different functions for the power spectrum. Both are, however, functions of the $r-$space Fourier frequency $\boldsymbol{k}$. Then, while $P^{(r)}(\boldsymbol{k})$ is a spherically symmetric function, $P^{(s)}(\boldsymbol{k})$ shows an elongation along the line of sight (LoS) direction. Later on, Hamilton (1992) translated these results to configuration space obtaining the 2PCF in its two flavors: $\xi^{(r)}(\boldsymbol{r})$ and $\xi^{(s)}(\boldsymbol{r})$. Again $\xi^{(r)}(\boldsymbol{r})$ is symmetric and the possibility of a power-law $r^{-\gamma}$ is considered, as had been historically accepted (e.g., Peebles 1980, who favored $\gamma = 1.8$). Also, in perfect agreement with K87, $\xi^{(s)}(\boldsymbol{r})$ shows a squashing along the LoS direction. Hamilton (1998) presented in great detail the assumptions that led to his results. He started by defining selection functions $n^{(r)}(r)$ and $n^{(s)}(s)$ for $r-$space and $s-$space and by numerical conservation obtained a complicated high order expression (his equation 4.28) for the density contrast $\delta^{(s)}$. From that one can obtain the 2PCF, but a series of approximations are needed (the linear case) to reduce the right hand side of the equation and to obtain his equation 4.30 for $\delta^{(s)}(\boldsymbol{s})$. Then, he introduced one extra assumption, $\delta^{(s)}(\boldsymbol{r}) = \delta^{(s)}(\boldsymbol{s})$, which is not justified by the linear approximation. This changes the left hand side of the equation directly to $\delta^{(s)}(\boldsymbol{r})$. It may be argued that this approximation is valid in the distant case mentioned above. Consequently, one could easily write $\xi^{(s)}(\boldsymbol{s})$ in place of $\xi^{(s)}(\boldsymbol{r})$, shifting between one form and the other as needed. That is an imperative because observable 2PCF are inevitably obtained in $s-$space.

Since then many authors have tried the Kaiser linear approximation facing this dilemma and have introduced similar approximations. In the description of 2PCF in redshift-space, due to the multipole expansion of the inverse Lagrangian operator derived from the corresponding power spectrum in Fourier space (Hamilton 1992), there appears a dependence with μ, the cosine of the angle between the $\boldsymbol{r}$ (real space) vector and the LoS: $\mu(\boldsymbol{r}) = r_{||}/|\boldsymbol{r}|$. However, it has been a common practice to approximate μ from redshift-space coordinates as either $\mu(\boldsymbol{s}) = s_{||}/|\boldsymbol{s}|$ or $\mu(\boldsymbol{cs}) = c_{||}s_{||}/\sqrt{c_\perp^2 s_\perp^2 + c_{||}^2 s_{||}^2}$ (e.g., Matsubara & Suto 1996; Nakamura et al. 1998; López-Corredoira 2014). Yet in some other cases the approximation $r_{||} = s_{||}$ is specifically made (e.g., Tinker et al. 2006) calling it the “distant observer" approximation. But, as mentioned above, this is really intended to mean a wide separation approximation and does not apply in the small scale regime. Furthermore, the “distant observer" name is also used for the plane-parallel case (e.g., Percival & White 2009), adding to the confusion. In some other cases the substitution $r_{||} = s_{||}$ is just performed with no further comment (e.g., Hawkins et al. 2003). Another facet of the same problem has been to expand the redshift-space correlation function as a series of harmonics of that same $\mu(\boldsymbol{s})$, rather than the actual $\mu(\boldsymbol{r})$ derived in linear theory (e.g., Guo et al. 2015; Chuang & Wang 2012; Marulli et al. 2017). While this is certainly a valid approach, the conclusions of linear theory, like the existence of only monopole, quadrupole and hexadecapole terms in the Legendre polynomial expansion, are not really applicable to the $\mu(\boldsymbol{s})$ case. All these forms of the approximation are really one and the same, and to avoid further confusion (like the term "distant observer") we decided to call it the $\mu(\boldsymbol{s})$ approximation.

When observational data are used to construct the 2PCF $\xi^{(s)}(\boldsymbol{s})$, it is generally true that simple linear theory predictions are not kept. On one hand, the predicted compression along the viewing direction is observed, but as one approaches the LoS axis the observed structure is mostly dominated by an elongated feature (e.g., Hamaus et al. 2015), usually called Finger of God (Huchra 1988), hereafter FoG. Prominent examples of FoG were found in the Coma Cluster by de Lapparent et al. (1986) and in the Perseus cluster by Wegner et al. (1993). The FoG feature is also commonly observed in the 2PCF of statistical aggregates (e.g., Hawkins et al. 2003), making it a common feature of large scale structures.

Many studies have been conducted to explain this discrepancy. In general, non-linear processes are invoked. Sometimes the non-linearities are assigned to virial relaxation in the inner regions of clusters, while others explore the non-linear terms of the approximation in the derivation of the K87 result. In these categories, we mention a small sample of the representative literature. Kinematic relaxation, like the virialized motion of cluster members in the inner regions (Kaiser 1987; Hamaus et al. 2015), are explored by introducing a distribution of pair-wise peculiar velocities for cluster components. There are at least two ways of doing so: First, the *streaming model* where a velocity distribution $f(V)$ is convolved with $\xi^{(r)}(\boldsymbol{r})$ to obtain $\xi^{(s)}(\boldsymbol{s})$, without using the K87 result, similar to Davis & Peebles (1983) but differentiating $\xi^{(s)}$ from $\xi^{(r)}$. More recent work on distribution functions take great care of this issue (Seljak & McDonald 2011; Okumura et al. 2012a,b) by directly obtaining the power spectra in redshift-space as a function of the $s-$space wave-number. Unfortunately, the expression that results for the power spectra is rather complicated, even when it is conveniently expressed as a series of mass weighted velocity moments. However, it is possible to obtain FoG structures in $\xi^{(s)}(\boldsymbol{s})$ maps by the convolution with simple velocity distributions, at the same time that a mapping from $r-$ to $s-$space takes place (e.g., Scoccimarro 2004). Paradoxically, it is not that easy to obtain the traditional peanut-shape structure that is generally recognized as the K87 limit in $\xi^{(s)}(\boldsymbol{s})$, unless the limit $s \sim r$ is once again invoked. Second, in the phenomenological *dispersion model* (c.f., Scoccimarro 2004; Tinker et al. 2006) a linear K87 spectrum is multiplied in Fourier space by a velocity distribution. This can be seen as a convolution in configuration space, as in Hawkins et al. (2003), but the procedure has the disadvantage that it obtains the same function $\xi^{(s)}$ as the result of the convolution of $\xi^{(s)}$ and $f(V)$. It has to be noted, however, that very good fits to the observed data are obtained by this procedure. The same is true for the fits to numerical simulation results at mid spatial frequencies obtained by similar procedures in e.g., Marulli et al. (2017). In the streaming model, the velocity distribution function can also be obtained from the interaction of galaxies with dark mater halos (e.g., Tinker et al. 2006; Tinker 2007), via the halo occupation distribution formalism.

Apart from kinematics, non-linear terms also arise in the expansion of the mass conservation or continuity equation in $r-$ and $s-$spaces to obtain the power spectrum or the 2PCF (e.g., Matsubara 2008; Taruya et al. 2010; Zheng & Song 2016). Preserving only first order terms yields the K87 result. However, a full treatment of all the terms is possible with the use of perturbative methods. There are diverse techniques: standard, Lagrangian, re-normalized, resumed Lagrangian (for a comparison see Percival & White 2009; Reid & White 2011). The latter authors however, conclude that the failure of these methods to fit the l=2 and 4 terms in the expansion $\xi_l^{(s)}(r)$ on quasi-linear scales of 30 to 80 h^{-1} Mpc, must be due to inaccuracies in the mapping between r- and s-spaces. So, they favor again the *streaming model*. Clearly, there is still substantial debate on this subject.

In most of these works the necessity to translate their results to observable 2PCFs, $\xi^{(s)}(\boldsymbol{s})$, is not really addressed. Most authors prefer to display their results in Fourier space as s-space power spectrum $P^{(s)}(\boldsymbol{k}_r)$ (e.g., Matsubara 2008; Okumura et al. 2012a), but with k_r in r-space; or display its moments $P_l^{(s)}(\boldsymbol{k}_r)$ (e.g., Taruya et al. 2010; Zheng & Song 2016); or the power spectra with k_s in $s-$space $P^{(s)}(\boldsymbol{k}_s, \mu_s)$ (e.g., Okumura et al. 2012b). Other authors display the correlation function in r-space, either as $\xi^{(r)}(\boldsymbol{r})$ (e.g., Matsubara 2008) or $\xi^{(s)}(\boldsymbol{r})$ (e.g., Tinker 2007; Reid & White 2011; Okumura et al. 2012a), or its moments $\xi_l^{(s)}(s)$ (e.g., Taruya et al. 2010) for l=2. Few works try to display directly the 2PCFs $\xi^{(s)}(\boldsymbol{s})$ (e.g., Matsubara & Suto 1996; Nakamura et al. 1998; Tinker et al. 2006; López-Corredoira 2014), but as already mentioned above, usually perform the $\mu(\boldsymbol{s})$ approximation; this amounts to really obtaining $\xi^{(s)}(\boldsymbol{r})$ instead.

To further complicate matters, redshift-space distortions are often treated separately from the cosmological distortions. Both are not easily discernible because both produce stretching or squashing in the LoS direction (Hamilton 1998; Hamaus et al. 2015). This degeneracy could in principle be resolved because the cosmological and peculiar velocity signals evolve differently with redshift, but in practice the uncertain evolution of bias (the dimensionless growth rate for visible matter, see equation 26) complicates the problem (Ballinger et al. 1996). Furthermore, Kaiser (1987) and Hamilton (1992, 1998) do not consider cosmological distortions in their analysis of peculiar motions. Since the earlier works, the inclusion of cosmological distortions has been attempted by several authors (e.g., Matsubara & Suto 1996; Hamaus et al. 2015).

In this paper, we show that a structure quite similar to FoG can be obtained in $\xi^{(s)}(\boldsymbol{s})$ directly in the linear theory limit of K87. That is, without invoking virial relaxation or the *streaming model*, nor the nonlinearities studied in perturbation theory, but just by avoiding the $\mu(\boldsymbol{s})$ approximation, in any of its forms ($\mu = s_{||}/|\boldsymbol{s}|$, "distant observer" or $r_{||} = s_{||}$), the FoG structure is recovered. This will be accomplished by solving for the function $\boldsymbol{r}(\boldsymbol{s})$ with the aid of the projected correlation function of both 2PCFs : $\xi^{(s)}(\boldsymbol{s})$ and $\xi^{(r)}(\boldsymbol{r})$. We will stay on the academic power-law approximation $\xi^{(r)}(\boldsymbol{r}) \sim r^{-\gamma}$ in order to be able to show a closed form for the result, and to prove the main point of this paper, i.e. that the FoG feature is derived in the simplest case.

We start with a detailed definition of $r-$ and $s-$space, noting that frequently $s-$space is expressed in distance units as is $r-$space. But in doing so, one multiplies by a scale factor that invariably introduces a cosmological parameter in the definition; and as a result the named $s-$space is no longer purely observational. Later on, the factor is solved by introducing a fiducial cosmology and solving for the real values. An example can be seen in the analysis made by Padmanabhan & White (2008) in Fourier space and Xu et al. (2013) in configuration space. The latter recognize the need of introducing a two-step transformation, one isotropic dilation and one warping transformation, to transform from real fiducial to real space. However, the real fiducial space is actually redshift-space, and this identification is missing in these works.

Therefore, we argue (c.f., § 2) that it is convenient to define the observable-redshift-space $\boldsymbol{\sigma}$ (σ-space) given by the simple redshift differences and subtended angles that are truly observable, and that do not depend on any choice of cosmological parameters. Multiplying by a unit function (scale factor) produces the physical redshift-space ($s-$space): $\boldsymbol{s} = K(\boldsymbol{\Omega}, z)\ \boldsymbol{\sigma}$, that is isomorphic to the observable σ-space, but has actual distance units that are dependent on a particular cosmological set of parameters Ω and on the redshift z. The $K(\boldsymbol{\Omega}, z)$ function is chosen so that the physical redshift-space is related to real space $\boldsymbol{r}$ by a unitary Jacobian independent of redshift. So, no additional scaling is needed, and the only remaining difference will be precisely in shape. That is why $\boldsymbol{\sigma}$ and $\boldsymbol{s}$ are more alike, and thus can both be named redshift-space; $\boldsymbol{\sigma}$ is the observable redshift-space while $\boldsymbol{s}$ is the physical redshift-space. Then, the transformation to real-space necessarily goes through redshift distortions.

Furthermore, when we introduce peculiar non-relativistic velocities in this scheme, we will show that it is possible to keep the same relation between observable and physical redshift-spaces, $\boldsymbol{s}$ and $\boldsymbol{\sigma}$, and that the Kaiser (1987) effect is recovered independently of redshift (see § 3). That is, now redshift-space will also show an additional gravitational distortion with respect to real-space.

To solve for the relation between real-space and redshift-space, we will rely on projected correlations. Projections of the 2PCF in the plane of the sky have been widely used to avoid the complications of dealing with unknown components in redshift-space (e.g., Davis & Peebles 1983). This has the advantage that in the case of a symmetric 2PCF in real-space, the 3-D structure can be inferred from the projection. We will show in § 4 that since the projections of the 2PCF in real-space and in redshift-space are bound to give the same profile, a relationship can be obtained for the real-space coordinate $r_{||}$ as a function of the corresponding one in redshift-space $s_{||}$. From this, we solve for $\mu(\boldsymbol{r})$ in real-space, and show that a different view of the redshift-space 2PCF emerges. The main result is that the redshift-space 2PCF presents a distortion in the LoS direction which looks similar to the ubiquitous FoG. This is due to a strong anisotropy that arises purely from linear theory and produces a change in scale as one moves into the on-axis LoS direction. As we move out of the LoS, a structure somewhat more squashed than the traditional result by the $\mu(\boldsymbol{s})$ approximation is obtained. As this effect has been missed before (to the best of our knowledge), we provide a detailed derivation in § 2 to 4, and show examples of the derived 2PCFs in redshift-space (§ 5). Finally, in § 6 we summarize our main conclusions.

2. REDSHIFT-SPACE

Consider the Friedmann-Lemaître-Robertson-Walker metric (e.g., Harrison 1993) written in units of distance and time as follows:

$$\begin{aligned} ds^2 &= c^2dt^2 - dr^2 \\ &= c^2dt^2 - a(t)^2\left[d\chi^2 + S_k(\chi)^2\left(d\theta^2 + \sin^2(\theta)d\varphi^2\right)\right], \end{aligned} \quad (1)$$

with $S_k = (\sin,\ Identity,\ \sinh)$ for $k = (1, 0, -1)$. Then the co-moving present-time length of an object dr^0 that is observed longitudinally is related to a variation in the observed redshift dz by

$$dr^0_{||} = \frac{cdz}{H(z)}, \quad (2)$$

where $H(z)$ is the Hubble function and the ^{0} superindex is used to define the present time t_0. Similarly, an object with a transversal co-moving dimension $dr^0_\perp$ subtends an angle $d\theta$ given by the angular co-moving distance (e.g., Hogg 1999) as

$$\frac{dr^0_\perp}{d\theta} = a_0 S_k\left(\frac{c}{a_0}\int_0^z \frac{dz'}{H(z')}\right), \quad (3)$$

where a_0 is the present day scaling parameter of the metric.

Observationally one measures redshift differences dz and subtended angles $d\theta$. We then define the observable redshift-space adimensional quantities $(d\sigma_{||}, d\sigma_\perp)$ as

$$d\sigma_{||} = dz, \quad (4)$$

and

$$d\sigma_\perp = zd\theta. \quad (5)$$

The physical redshift-space sizes $ds_{||}$ and $ds_\perp$ can then be defined in terms of $\boldsymbol{\sigma}$ as

$$ds_{||} = K(\mathbf{\Omega}, z)d\sigma_{||}, \quad (6)$$

and

$$ds_\perp = K(\mathbf{\Omega}, z)d\sigma_\perp, \quad (7)$$

where $K(\mathbf{\Omega}, z)$ has distance units and depends on the cosmology, represented here symbolically by the $\mathbf{\Omega}$ terms. The relation between real-space and physical redshift-space is then obtained from equations (2) to (7), that is:

$$dr^0_{||} = c_{||}ds_{||}, \quad (8)$$

and

$$dr^0_\perp = c_\perp ds_\perp, \quad (9)$$

with

$$c_{||} = \frac{c}{K(\mathbf{\Omega}, z)\ H(z)}, \quad (10)$$

and

$$c_\perp = \frac{a_0}{z\ K(\mathbf{\Omega}, z)}\ S_k\left(\frac{c}{a_0}\int_0^z \frac{dz'}{H(z')}\right). \quad (11)$$

It is clear then that the Alcock & Paczyński (1979) function $AP(z)$, that tests redshift distortions of a particular cosmology, can be written as

$$AP(z) = \frac{c_\perp(z)}{c_{||}(z)} = \frac{a_0}{c}\ \frac{H(z)}{z}\ S_k\left(\frac{c}{a_0}\int_0^z \frac{dz'}{H(z')}\right). \quad (12)$$

Furthermore, from the transformation of physical redshift-space with coordinates $(ds_\perp, ds_\perp, ds_{||})$ into real-space $(dr^0_\perp, dr^0_\perp, dr^0_{||})$ we get a Jacobian

$$\left|\frac{d^3\boldsymbol{s}}{d^3\boldsymbol{r}}\right| = \frac{1}{c_{||}(z)}\ \frac{1}{c^2_\perp(z)}. \quad (13)$$

In order for this transformation to preserve scale we need a unitary Jacobian. This condition can be achieved simply by the following condition:

$$K(\mathbf{\Omega}, z) = \frac{c}{H(z)}\ AP(z)^{2/3}, \quad (14)$$

as can be seen from equations (10) to (12). Here the dependence on the cosmology is made explicit through the Hubble function. Note that the resulting scale factor $K(\mathbf{\Omega}, z)$ approaches the Hubble radius $a_H = c/H_0$ as $z \to 0$ and decreases approximately as $1/(1+z)$ thereafter. Also note that for redshift $z > 0$, the physical scale that transforms all dimensions of redshift-space contracts isotropically. Also we remark that $c_{||}$ and $c_\perp$ are of order unity as $z \to 0$, and satisfy $c_\perp/c_{||} = AP(z)$ for all z. In fact we have (see also Xu et al. 2013):

$$c_{||}(z) = AP(z)^{-2/3}, \quad (15)$$

and

$$c_\perp(z) = AP(z)^{1/3}. \quad (16)$$

Peculiar velocities modify the observed redshift, and therefore alter the relation between real-space and redshift-space giving rise to kinematic distortions. Suppose the near-end of an object is at rest at redshift z, while the far-end is moving with peculiar non-relativistic velocity $\vec{\mathrm{v}}$. Then it will appear Doppler shifted to an observer at rest at the far-end position, causing equation (2) to get the form (see also Matsubara & Suto 1996; Hamaus et al. 2015):

$$cdz = H(z)\ dr^0_{||} + (1+z)\ (\vec{\mathrm{v}}\cdot\hat{r}), \quad (17)$$

where $\hat{r}$ points in the direction of the far-end, at an angle $d\theta$ from the near-end. Since $\vec{\mathrm{v}}\cdot\hat{r} = \mathrm{v}_{||} + \mathrm{v}_\perp\ d\theta$, then for small angular separations ($d\theta << 1$) the perpendicular component of the peculiar velocity may be trivialized. Therefore equation (8) is modified to

$$dr^0_{||} = c_{||}\ (ds_{||} - ds_{\rm v}). \tag{18}$$

where $ds_{\rm v}$ (in physical redshift-space) is given by

$$ds_{\rm v} = K(\boldsymbol{\Omega}, z)\ d\sigma_{\rm v}, \tag{19}$$

and $d\sigma_{\rm v}$ (in observable redshift-space) is given by

$$d\sigma_{\rm v} = (1+z)\ \frac{{\rm v}_{||}}{c}. \tag{20}$$

Through the similarity of equations (19) and (20) with equations (6) and (4), we note that the concepts of observable redshift-space and physical redshift-space can be extended to include peculiar motions as well.

3. TWO POINT CORRELATION FUNCTION

Let $\boldsymbol{r}$ be real-space Euclidean co-moving coordinates in the close vicinity of a point at redshift z, defined as dr in the previous section. Then for azimuthal symmetry around the line of sight (aligned to the third axis) we have $\boldsymbol{r} = (dr^0_\perp, dr^0_\perp, dr^0_{||})$. Let $\boldsymbol{s}$ denote physical redshift-space coordinates around the same point (in the same tangent subspace), with the third axis along the line of sight. Then, from equations (9) and (18), the Jacobian is

$$\begin{aligned}\left|\frac{d^3\boldsymbol{s}}{d^3\boldsymbol{r}}\right| =& \frac{1}{c_{||}(z)\ c_\perp^2(z)}\ \left(1 + \frac{(1+z)}{H(z)}\frac{\partial {\rm v}_{||}}{\partial r_{||}}\right)\\ =& 1 + \frac{(1+z)}{H(z)}\frac{\partial {\rm v}_{||}}{\partial r_{||}},\end{aligned} \tag{21}$$

where we have used the unitary condition on equation (13) to eliminate the $c_{||}(z)\ c_\perp^2(z)$ term. In going from $\boldsymbol{r}$ to $\boldsymbol{s}$ space, the density change can be related to the change in volume V, and the Jacobian by the equation

$$\left(\frac{d\rho}{\rho}\right)_{\boldsymbol{s}-r} = -\frac{dV}{V} = 1 - \left|\frac{d^3\boldsymbol{s}}{d^3\boldsymbol{r}}\right|. \tag{22}$$

This can also be expressed in terms of the contrast density ratios in $\boldsymbol{s}$ and $\boldsymbol{r}$ spaces defined such that

$$\left(\frac{d\rho}{\rho}\right)_{\boldsymbol{s}-r} = \delta^{(s)} - \delta^{(r)}, \tag{23}$$

where $\delta^{(s)}$ and $\delta^{(r)}$ are two distinct scalar functions of position in either space. This particular definition of $\delta^{(s)}$ requires knowledge of the real-space selection function (Hamilton 1998), which makes it rarely a first choice. However, the procedure given below allows us precisely to solve for the function $\boldsymbol{r}(\boldsymbol{s})$.

In linear theory, Peebles (1980) shows by equations 14.2 and 14.8 that an overdensity of mass $\delta(\boldsymbol{r})$ creates a peculiar velocity field similar to the acceleration field produced by a mass distribution. As such, it can be derived from a potential function whose Laplacian is the overdensity itself (e.g., Thornton & Marion 2004) times a constant which is time (or redshift) dependent. That is

$${\rm v}(\boldsymbol{r}) = -\frac{H(z)\ f(z)}{(1+z)}\ \boldsymbol{\nabla}\nabla^{-2}\delta_m^{(r)}(\boldsymbol{r}), \tag{24}$$

where ∇ is the gradient, ∇^{-2} is the inverse Laplacian, and

$$f(z) = \frac{a(z)}{D(z)}\frac{dD}{da}. \tag{25}$$

Here $D(z)$ is the growth factor, the temporal component of density. Note that in Peebles (1980) coordinates are given in the expanding background model $\boldsymbol{x}$, which relate to present time real-space coordinates by $\boldsymbol{r} = a_0\boldsymbol{x}$; this brings about the $(1+z)$ factor in equation (24). The m subscript to δ emphasizes that all mass is responsible for the velocity field, while δ without the subscript refers to visible mass in the form of galaxies or quasars. To account for the difference, it is customary to introduce a bias factor $b(z)$ and to define the dimensionless growth rate for visible matter

$$\beta(z) = \frac{f(z)}{b(z)}. \tag{26}$$

Then from equations (21) to (24) we get:

$$\delta^{(s)}(\boldsymbol{r}) = \Big(1 + \beta(z)\ \partial_{||}^2\ \nabla^{-2}\Big)\ \delta^{(r)}(\boldsymbol{r}), \tag{27}$$

where $\partial_{||}$ denotes $\partial/\partial r_{||}$ in real space. Note that if we had not required a unity Jacobian (c.f., equation 13), then equations (21) and (22) would not have canceled out the $1 - c_{||}(z)^{-1}c_\perp(z)^{-2}$ term. We note that this term is not small when $K(\Omega, z)$ is a constant, and will vary by one order of magnitude as $z \to 1$, and up to three orders of magnitude as $z \to 10$. So the transformation between observable and physical redshift-spaces cannot be neglected (contrary to the assumption of Matsubara & Suto 1996).

The square modulus of the Fourier transform of equation (27) gives an expression for the power spectrum, or the Fourier transform of the autocorrelation function (2PCF) ξ, which generalizes Kaiser (1987) results for any redshift z

$$\widetilde{\xi^{(s)}}(\boldsymbol{k}) = \big(1 + \beta(z)\ \mu_k^2\big)^2\ \widetilde{\xi^{(r)}}(\boldsymbol{k}), \tag{28}$$

where $\mu_k = k_{r3}/|\boldsymbol{k}_r|$ is the cosine of the angle between the k_{r3} component and the wave number vector $\boldsymbol{k}_r$ in real-space; it arises by the Fourier transform property of changing differentials into products. Note that wave number vectors in real-space also differ from their counterparts in redshift-space by the unknown velocity field in equation (17).

Fourier transforming back into coordinate space gives the Hamilton (1992) result:

$$\xi^{(s)}(\boldsymbol{r}) = \left(1 + \beta(z)\ \partial_{||}^2\ \nabla^{-2}\right)^2 \xi^{(r)}(\boldsymbol{r}). \tag{29}$$

Note that this equation is written in a way that all terms in the right hand side are real-space coordinates $\boldsymbol{r}$ dependent, as is the case for the derivatives and inverse Laplacian. Recalling that the solution of the Laplace equation in spherical coordinates consists of spherical harmonics in the angular coordinates and a power series in the radial part, one can write for the case of azimuthal symmetry

$$\xi^{(s)}(\boldsymbol{r}) = \sum_{l=0} \xi_l(r)\ P_l(\mu(\boldsymbol{r})) \tag{30}$$

where $P_l(\mu(\boldsymbol{r}))$ are the Legendre polynomials,

$$\mu(\boldsymbol{r}) = \frac{r_{||}}{|\boldsymbol{r}|}, \tag{31}$$

explicitly defined for real-space coordinates, and the harmonics are given by the coefficients $\xi_l(r)$ that can be obtained from equation (30) through orthogonality properties as

$$\xi_l(r) = \frac{(2l+1)}{2} \int_{-1}^{1} P_l(\mu(\boldsymbol{r}))\ \xi^{(s)}(\boldsymbol{r})\ d\mu(\boldsymbol{r}). \tag{32}$$

Substituting equation (29) in (32) for the case of spherical symmetry in real-space ($\xi^{(r)}(\boldsymbol{r}) = \xi^{(r)}(r)$), one gets by direct evaluation the classical result given by Hamilton (1992), see also Hawkins et al. (2003). That result consists of only three terms: monopole, quadrupole and hexadecapole ($l = 0, 2, 4$), all the others evaluate to zero. It is important to note that this is not true when the expansion of equation (30) is done in $\mu(\boldsymbol{s})$ as assumed by several authors (e.g., Guo et al. 2015; Chuang & Wang 2012; Marulli et al. 2017).

When the 2PCF can be approximated by a power-law, $\xi^{(r)}(r) = (r/r_0)^{-\gamma}$, the solution for equation (29) can be written as

$$\xi^{(s)}(\boldsymbol{r}) = g(\gamma, \beta, \mu(\boldsymbol{r}))\ \xi^{(r)}(r). \tag{33}$$

where $g(\gamma, \beta, \mu(\boldsymbol{r}))$ has been written in several equivalent forms (Hamilton 1992; Matsubara & Suto 1996; Hawkins et al. 2003). One of these is the following:

$$g(\gamma, \beta, \mu(\boldsymbol{r})) = 1 + 2\frac{1 - \gamma\,\mu(\boldsymbol{r})^2}{3-\gamma}\beta(z) + \frac{\gamma(\gamma+2)\,\mu(\boldsymbol{r})^4 - 6\gamma\,\mu(\boldsymbol{r})^2 + 3}{(3-\gamma)(5-\gamma)}\ \beta(z)^2. \tag{34}$$

This function takes values greater than 1 for the equatorial region ($\mu(\boldsymbol{r}) \to 0$), and less than 1 for the polar axis ($\mu(\boldsymbol{r}) \to 1$). Alternatively, it has been mentioned that the quadrupolar term in the multipole expansion dominates the hexadecapole. As a result of either argument the 2PCF $\xi^{(\boldsymbol{s})}(\boldsymbol{r})$ seems squashed with a peanut shape when displayed in r-space , in agreement with common knowledge.

However, we will show below that the stretching of redshift scale along the LoS will counteract this apparent squashing producing a structure similar to a FoG. In order to stay within the linear regime, we ensure not to reach the turnaround velocity by keeping $g(\gamma, \beta, \mu(\boldsymbol{r}))$ positive in the polar region. In that case β is limited from 0 to an upper limit which is a function of γ, and equals $2/3$ when $\gamma = 1.8$. The $\beta = 0$ case gives the no gravity one in which $\xi^{(s)}(\boldsymbol{r}) = \xi^{(r)}(\boldsymbol{r})$.

We now remark that $\mu(\boldsymbol{r}) = r_{||}/|\boldsymbol{r}|$ (see equation 31). But in some works (e.g., Matsubara & Suto 1996; Tinker et al. 2006; López-Corredoira 2014) it has been approximated as $\mu(\boldsymbol{s}) = s_{||}/|\boldsymbol{s}|$ or as $\mu(\boldsymbol{cs}) = c_{||}s_{||}/\sqrt{c_\perp^2 s_\perp^2 + c_{||}^2 s_{||}^2}$, or even as $r_{||} = s_{||}$. We have referred to this as the $\mu(\boldsymbol{s})$ approximation. In principle, given that μ is a scalar function, either form should be acceptable as long as the $\boldsymbol{s}$ and $\boldsymbol{r}$ vectors refer to the same point. However, we remark that $r_{||}$ differs from $c_{||}s_{||}$ (see equation 18), and that it is usually unknown, since in order to obtain it from $s_{||}$, the infall velocity field must be known. So these approximations should be carefully used.

The result in our equation (33) has been derived for r-space, profiting from the difference between r- and s- spaces. Plotting this function directly in r-space as the independent variable produces a squashed structure for $\xi^{(s)}(\boldsymbol{r})$. However, one wants to display the correlation function in s-space to compare it with observations, not in r-space. In order to do so, some authors perform the $\mu(\boldsymbol{s})$ approximation while others may plainly substitute s for r all the way in equation (33) and write $\xi^{(s)}(\boldsymbol{s}) = g(\gamma, \beta, \mu(\boldsymbol{s}))\ \xi^{(r)}(s)$ to be able to display $\xi^{(s)}$ in s-space. This is certainly wrong because $\boldsymbol{s}$

and $\boldsymbol{r}$ are not just independent names for position, and there exists a relation $\boldsymbol{s}(\boldsymbol{r})$ between them that is not linear. Specifically, the parallel component is $s_{||} \sim r_{||} + v_{||}$ (equation 18), with $v_{||}$ also a (yet unknown) function of position $\boldsymbol{r}$. In the case of small disturbances we expect small velocities (below turnover) that result in a bi-univocal map $\boldsymbol{s}(\boldsymbol{r})$ and its inverse. So, if we want to display the resulting $\xi^{(s)}$ in $\boldsymbol{s}$ space, we must proceed first to evaluate $\boldsymbol{r} = \boldsymbol{r}(\boldsymbol{s})$ and then $\xi^{(s)}(\boldsymbol{r})$ via equation (33), or in short $\xi^{(s)}(\boldsymbol{r}(\boldsymbol{s})) = g(\gamma, \beta, \mu(\boldsymbol{r}(\boldsymbol{s})))\ \xi^{(r)}(r(\boldsymbol{s}))$. We can therefore informally define $\xi^{(s)}(\boldsymbol{s}) \equiv \xi^{(s)}(\boldsymbol{r}(\boldsymbol{s}))$ and we claim that this is the correct way to evaluate the two-point correlation function on a grid in s-space.

On the other hand, if the $\mu(\boldsymbol{s})$ approximation is used one obtains structures that are squashed in the LoS direction, and with a characteristic peanut-shaped geometry close to the polar axis (see for example Hawkins et al. 2003). One concludes that this geometry fails to reproduce the structure known as “Finger of God" (FoG). The consequence is that other processes are called upon to account for it, such as random motions arising in the virialized inner regions of clusters. We show below that avoiding this approximation allows us to obtain a geometrical structure quite similar to the FoG feature.

4. PROJECTED CORRELATION FUNCTION

In order to avoid the complications that redshift-space distortions introduced in the correlation function, such as those produced by gravitationally induced motions or virialized conditions, the projected correlation function $w_\perp(r_\perp)$ is frequently preferred in the analysis. This approach was first suggested in the analysis of CfA data by Davis & Peebles (1983), who mention that at small redshift separations peculiar velocities may cause $\xi(s)$ to differ from $\xi(r)$. To avoid this effect, they integrate $\xi(r)$ along the redshift difference to obtain the projected function $w_\perp(r_\perp)$ on the plane of the sky. Then, from it, they recuperate $\xi(r)$ inverting the problem by solving Abel's integral equation (Binney & Tremaine 1987) numerically. See also Pisani et al. (2014) for other possibilities. In the case where $\xi(r)$ is a power-law, $w_\perp(r_\perp)$ will be one as well, and the relation between them is analytical (e.g., Krumpe et al. 2010).

We will show that the projected correlation function can be used to obtain the $r_{||}(s_{||})$ function that allows us to calculate $\mu(\boldsymbol{r})$. We start by noting that the projection on the plane of the sky may be performed either by using the $\xi^{(s)}$ function or its real space counterpart $\xi^{(r)}$. Then we define the projected correlation functions as

$$w_\perp^{(s)}(s_\perp, s_{||}^*) = \int_0^{s_{||}^*} \xi^{(s)}(\boldsymbol{r}(s_\perp, s_{||}))\ ds_{||}, \tag{35}$$

and

$$w_\perp^{(r)}(r_\perp, r_{||}^*) = \int_0^{r_{||}^*} \xi^{(r)}(r_\perp, r_{||})\ dr_{||}, \tag{36}$$

where $\xi^{(s)}(\boldsymbol{r}(s_\perp, s_{||}))$, given by equation (33), may be understood as $\xi^{(s)}(\boldsymbol{s})$, as mentioned above.

The integral limits should go to infinity to get the total projected functions. However, one can project the correlation function up to a particular real space distance $r_{||}^*$. Furthermore, if we assume that there exists a biunivocal function $s_{||}(r_{||})$, then we can find the corresponding $s_{||}^* = s_{||}(r_{||}^*)$. Boundary conditions are thus well defined (e.g., Nock et al. 2010). On the one hand, slices in r-space (equation 36) do not depend on the observer's perspective, while on the other (equation 35) the limit of the integral (boundary condition) becomes a function that is precisely going to be evaluated. Carrying on, due to number conservation, the projections in redshift- and real-space multiplied by the corresponding area elements that complete the volume where the number of pairs are counted, must be equal. This leads to

$$w_\perp^{(s)}(s_\perp, s_{||}^*)\ ds_\perp^2 = w_\perp^{(r)}(r_\perp, r_{||}^*)\ dr_\perp^2, \tag{37}$$

for all values of $r_\perp$ (or its corresponding $s_\perp$, see equation 9). Inverting the $s_{||}(r_{||})$ map and using equations (35) to (37), together with (33) and (9) we obtain

$$\int_0^{s_{||}^*} g(\gamma, \beta, \mu(\boldsymbol{r}))\ \xi^{(r)}(r_\perp, r_{||})\ ds_{||} = c_\perp^2 \int_0^{r_{||}(s_{||}^*)} \xi^{(r)}(r_\perp, r_{||})\ dr_{||}. \tag{38}$$

Then, changing variables to $r_{||}$ in the left ($ds_{||} = \frac{ds_{||}}{dr_{||}} dr_{||}$), and noting that the equality holds for all values of $s_{||}^*$, the integral signs can be omitted. Furthermore, using equations (15) and (16) the equation simplifies to

$$c_{||}\ ds_{||} = \frac{dr_{||}}{g(\gamma, \beta, \mu(\boldsymbol{r}(r_\perp, r_{||})))}, \tag{39}$$

where the dependence $\mu(\boldsymbol{r}(r_\perp, r_{||})) = r_{||}/\sqrt{r_\perp^2 + r_{||}^2}$ has been emphasized for clarity. Equation (39) completes the metric transformation between redshift-

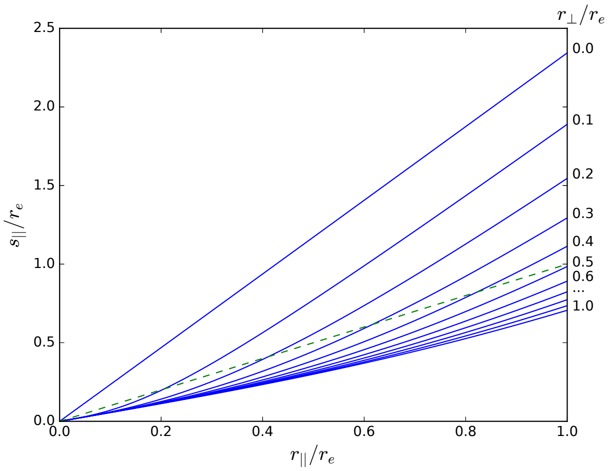

Fig. 1. $s_{||}/r_e$ vs. $r_{||}/r_e$ for $r_\perp/r_e$ from 0 to 1 as indicated in the figure, for $\gamma = 1.8$, $\beta = 0.4$, and $c_{||} = 1$, for any value of the scaling parameter r_e. The dashed line indicates the identity $s_{||} = r_{||}$ for reference. The color figure can be viewed online.

and real-spaces. As a consistency test, we note that in the limit of no gravitational disturbance ($\beta = 0$) we have $g(\gamma, \beta, \mu(\boldsymbol{r})) = 1$ and equation (8) is recovered.

5. RESULTING REDSHIFT-SPACE AND REAL-SPACE RELATION

We integrate equation (39) numerically using equation (34), to obtain the $s_{||}(r_{||})$ function shown in Figure 1 for different values of $r_\perp/r_e$, indicated for each curve in the figure, where r_e is an arbitrary scaling parameter, $\gamma = 1.8$, $\beta = 0.4$, and $c_{||} = 1$. Note that the relation is not linear. If we compare it to the identity line ($s_{||} = r_{||}$) shown as a dashed line, we note that sometimes the curves of constant $r_\perp$ lie above or below the identity line, or even cross it.

So, it can be noted that for on-axis separations (where $r_\perp = 0$), the spatial scale in redshift space is stretched, i.e. $s_{||} > r_{||}$, effectively opposing the squashing effect obtained by the rough $\mu(\boldsymbol{s})$ approximation. On the other hand, for $r_\perp \to 1$ a squashed structure is seen (even more so that the one obtained by the $\mu(\boldsymbol{s})$ approximation) that ultimately converges to the limit $s_{||} \to r_{||}$ as we approach the plane of the sky ($r_{||} = 0$).

These geometrical distortions can be better appreciated by their effect on the 2PCF presented in Figure 2. Here we start from a grid in $s-$space, and transform to r-space using the integral relation (equation 39) for the parallel component and equation (9) for the perpendicular one. From there, we calculate $\mu(\boldsymbol{r})$ (equation 31), $g(\gamma, \beta, \mu(\boldsymbol{r}))$ (equation 34), assuming that $\xi^{(r)}(\boldsymbol{r}) = (r/r_0)^{-\gamma}$; and finally, $\xi^{(s)}(\boldsymbol{s})$ (i.e. $\xi^{(s)}(\boldsymbol{r}(\boldsymbol{s}))$) from equation (33). The cosmological distortion is governed by the $c_{||}$ and $c_\perp$ parameters that depend on the Alcock-Paczyński function AP (see equation 12). Its value depends on the cosmological parameters $\boldsymbol{\Omega} = (\Omega_m, \Omega_k, \Omega_\Lambda)$ and increases with the redshift z (see Figure 1 in Alcock & Paczyński 1979).

Figure 2(a) shows the case that corresponds to the parameters used for Figure 1: $\gamma = 1.8$, $\beta = 0.4$ and $AP = 1$, where the geometrical distortions produced are evident, an elongation in the polar direction and a squashing in the equatorial direction. As can be noted the polar elongation resembles the structure known as FoG.

In the other three Figures, 2(b), 2(c) and 2(d), we explore the effect of cosmological and gravitational alterations. Figure 2(b) shows that the effect of increasing AP is a geometrical distortion that concentrates the structure towards the polar axis direction for $AP = 2$ that corresponds to ΛCDM cosmology at $z = 2.6$. In Figure 2(c) we explore the effect of changing the dimensionless growth-rate for visible mater β. This gravitational effect is to enhance the FoG structure as its value increases (recall that its limit value is 2/3). On the other hand, if β decreases the structure becomes rounder and the FoG fainter, as is shown in Figure 2(d). By comparing Figures 2(b) and 2(c) relative to 2(a), we note that the same enhanced strength of the FoG feature is obtained in the small scale regions, but the large scale structure is quite different. This is because in the first case the distortion is cosmological while on the second it is gravitational.

Although it has not been the purpose of this paper, we may consider different values of the power-law index γ and we obtain figures similar to those shown in Figure 2. In some cases they might even resemble some of the cases depicted here. It turns out that lower values may accommodate rounder 2PCFs at mid scales, while a steeper γ may also concentrate the structure towards the LoS. Note, however, that it is easy to discern those cases by a simple projection on the plane of the sky, as depicted through § 4. This is because such a projection will erase redshift distortions, both gravitational (β) and cosmological (AP), while preserving the radial structure γ.

As we have indicated, a rounder 2PCF at mid spatial scales is favored by some works that use the $\mu(s)$ approximation. As can be seen in Figure 2(b), rounder figures can be obtained with lower

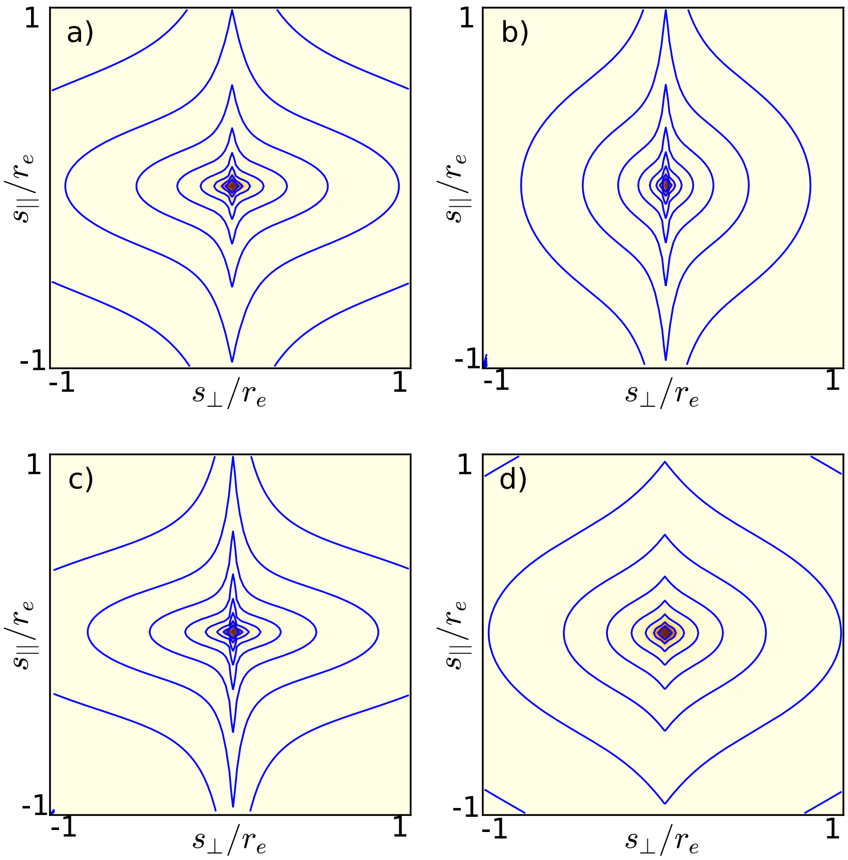

Fig. 2. Redshift-space two-point-correlation-function (2PCF) $\xi^{(s)}(s_\perp, s_{||})$ in logarithmically spaced contours at e intervals for any value of the scaling parameter r_e. The parameter values are: (a) $\gamma = 1.8$, $\beta = 0.4$ and $AP = 1$; (b) $\gamma = 1.8$, $\beta = 0.4$ and $AP = 2$; (c) $\gamma = 1.8$, $\beta = 0.5$ and $AP = 1$; (d) $\gamma = 1.8$, $\beta = 0.2$ and $AP = 1$. The color figure can be viewed online.

values of β. We have estimated that a $\beta = 0.25$ produces a 2PCF which is squashed equally to that obtained by the $\mu(s)$ approximation for the case $\beta = 0.4$ for most points in the s-space plane, those with $s_\perp > s_{||}$. An increase in the AP parameter may also contribute to alleviate the situation.

Another possibility, that was not intended to be covered here, is the case of a more realistic 2PCF $\xi^{(r)}(r)$ such as the ones inferred from baryon acoustic oscillations (BAOs) (e.g. Slosar et al. 2013) or those obtained by the CAMB code (Seljak & Zaldarriaga 1996). In order to apply the results of this paper to such cases, one could try breaking the inferred $\xi^{(r)}(r)$ profile into a series of power-laws, and then apply equation (39) to each section. If this is not possible, then we would have to give up equations (33) and (34) as a way of simplifying $\xi^{(s)}(\boldsymbol{r})$. However, the projections on the plane of the sky, i.e. equations (35) and (36) are still valid, and instead of using equation (33) to simplify, we would have to go back to the expansion of $\xi^{(s)}(\boldsymbol{r})$ in multipoles (equation 30). In that case one would end up with the following equation:

$$c_{||}\ ds_{||} = \frac{\xi^{(r)}(r)}{\sum_{l=0,2,4} \xi_l(r)\ P_l(\mu(\mathbf{r}))} dr_{||} \qquad (40)$$

instead of equation (39). We would also have to find a way to estimate the multipole moments $\xi_l(r)$. Another possibility is to leave $\xi^{(s)}(r)$ in the denominator. Considering these possibilities seems like an interesting task for future works, but it is beyond the scope of this paper.

We conclude that a whole range of possibilities in shape and strength of the FoG structure and the squashing of the equatorial zone can be obtained by tuning the parameters γ, β, and AP. This may provide a path towards solving the usual degeneracy problem between cosmological and gravitational distortions, which can still be seen at a level of 10% in 1σ correlated variations in recent work (e.g. Satpathy et al. 2017).

6. CONCLUSIONS

We emphasize the importance of distinguishing three spaces in cluster and large scale structure studies: the observable redshift-space $\boldsymbol{\sigma}$, the physical redshift-space $\boldsymbol{s}$, and the real-space $\boldsymbol{r}$. The transformation between $\boldsymbol{\sigma}$ and $\boldsymbol{s}$ is an isotropic dilation that introduces a scale factor dependent on the cosmology.

On the other hand, the transformation between $\boldsymbol{s}$ and $\boldsymbol{r}$ occurs through a unitary Jacobian independent of redshift, and only distorts the space by factors related to the Alcock-Paczyński AP function (c.f., equations 15 and 16).

Furthermore, when we introduce non-relativistic peculiar velocities in this scheme, we demonstrate that the same relation between observable and physical redshift-spaces $\boldsymbol{s} = K(\boldsymbol{\Omega}, z)\ \boldsymbol{\sigma}$ is kept. In the analysis of the 2PCF in the physical redshift-space $\boldsymbol{s}$, we recover the Kaiser (1987) effect independent of redshift in Fourier space, and Hamilton (1992) results in configuration space.

We remark that a dependence with μ in real-space ($\mu(\boldsymbol{r}) = r_{||}/|\boldsymbol{r}|$) appears, and that it has been a common practice to approximate it from redshift-space coordinates as either $\mu(\boldsymbol{s}) = s_{||}/|\boldsymbol{s}|$ or $\mu(\boldsymbol{cs}) = c_{||}s_{||}/\sqrt{c_\perp^2 s_\perp^2 + c_{||}^2 s_{||}^2}$ or $r_{||} = s_{||}$, sometimes called the“distant observer approximation", or simply to substitute $\boldsymbol{s}$ for $\boldsymbol{r}$ in the equations. To avoid further confusion we have called this the $\mu(\boldsymbol{s})$ approximation in any of its forms. We argue that this wrong assumption produces either a squashed or a peanut-shaped geometry close to the LoS axis, for the 2PCF in redshift-space.

Since $r_{||}$ is usually unknown, we propose a method to derive it from $s_{||}$ using number conservation in the projected correlation function in both real- and redshift-spaces. This leads to a closed form equation (39) for the case where the real 2PCF can be approximated by a power-law. From this, we solve for $\mu(\boldsymbol{r})$ in real-space, and show that a different view of the redshift-space 2PCF emerges. The main result is that the redshift-space 2PCF presents a distortion in the LoS direction which looks quite similar to the ubiquitous FoG. This is due to a strong anisotropy that arises purely from linear theory and produces a stretching of the scale as one moves into the on-axis LoS direction. Moving away from the LoS the structures appear somewhat more squashed than those obtained by the $\mu(s)$ approximation for equivalent values of β. The implications of this remains an open question.

The development presented here produces structures that qualitatively reproduce the observed features of the 2PCF of galaxies and quasars large scale structure. A squashing distortion in the equatorial region is attributed to a mixture of cosmological and gravitational effects. The FoG feature that is usually attributed to other causes is instead ascribed to the same gravitational effects derived from linear theory.

We conclude that a whole range of possibilities in shape and strength of the FoG structure, and the squashing of the equatorial zone, can be obtained by tuning the parameters γ, β, and AP. This provides a path towards solving the usual degeneracy problem between cosmological and gravitational distortions. In a future paper (Salas & Cruz-González in preparation) we will apply these results to the galaxies and quasar data obtained by current large scale surveys.

I.C.G. acknowledges support from DGAPA-UNAM (Mexico) Grant IN113417.

REFERENCES

Alcock, C. & Paczyński, B. 1979, Natur, 281, 358
Ballinger, W. E., Peacock, J. A., & Heavens, A. F. 1996, MNRAS, 282, 877
Binney, J. & Tremaine, S. 1987, Galactic Dynamics (Princeton, NJ: PUP)
Chuang, C.-H. & Wang, Y. 2012, MNRAS, 426, 226
Davis, M. & Peebles, P. J. E. 1983, ApJ, 267, 465
de Lapparent, V., Geller, M. J., & Huchra, J. P. 1986, ApJL, 302, L1
Guo, H., Zheng, Z., Zehavi, I., et al. 2015, MNRAS, 446, 578
Hamaus, N., Sutter, P. M., Lavaux, G., & Wandelt, B. D. 2015, JCAP, 11, 036
Hamilton, A. J. S. 1992, ApJ Letters, 385, L5
Hamilton, D. 1998, Astrophysics and Space Science Library, 231, Linear Redshift Distortions: a Review, ed. D. Hamilton, 185
Harrison, E. 1993, ApJ, 403, 28
Hawkins, E., Maddox, S., Cole, S., et al. 2003, MNRAS, 346, 78
Hogg, D. W. 1999, ArXiv Astrophysics e-prints /9905116
Huchra, J. P., Davis, M., Latham, D., & Tonry, J. 1983, ApJS, 52, 89
Huchra, J. P. 1988, in ASPC 5, The Minnesota lectures on Clusters of Galaxies and Large-Scale Structure, ed. J. M. Dickey, (San Francisco, CA: ASP), 41
Kaiser, N. 1987, MNRAS, 227, 1
Krumpe, M., Miyaji, T., & Coil, A. L. 2010, ApJ, 713, 558
López-Corredoira, M. 2014, ApJ, 781, 96
Marulli, F., Veropalumbo, A., Moscardini, L., Cimatti, A., & Dolag, K. 2017, A&A, 599, A106
Matsubara, T. 2008, PhRvD, 77, 063530
Matsubara, T. & Suto, Y. 1996, ApJ Letters, 470, L1

Nakamura, T. T., Matsubara, T., & Suto, Y. 1998, ApJ, 494, 13
Nock, K., Percival, W. J., & Ross, A. J. 2010, MNRAS, 407, 520
Okumura, T., Seljak, U., & Desjacques, V. 2012a, JCAP, 11, 014
Okumura, T., Seljak, U., McDonald, P., & Desjacques, V. 2012b, JCAP, 2, 010
Padmanabhan, N. & White, M. 2008, PhRvD, 77, 123540
Peebles, P. J. E. 1980, The large-scale structure of the universe, (Princeton NJ: PUP)
Percival, W. J. & White, M. 2009, MNRAS, 393, 297
Pisani, A., Lavaux, G., Sutter, P. M., & Wandelt, B. D. 2014, MNRAS, 443, 3238
Reid, B. A. & White, M. 2011, MNRAS, 417, 1913
Satpathy, S., Alam, S., Ho, S., et al. 2017, MNRAS, 469, 1369
Scoccimarro, R. 2004, PhRvD, 70, 3007
Seljak, U. & McDonald, P. 2011, JCAP, 11, 039
Seljak, U. & Zaldarriaga, M. 1996, ApJ, 469, 437
Slosar, A., Iršič, V., Kirkby, D., et al. 2013, JCAP, 4, 026
Taruya, A., Nishimichi, T., & Saito, S. 2010, PhRvD, 82, 3522
Thornton, S. T. & Marion, J. B. 2004, Classical Dynamics of Particles and Systems, (5th ed. Brooks/Cole, a division of Thomson Learning Inc.)
Tinker, J. L. 2007, MNRAS, 374, 477
Tinker, J. L., Weinberg, D. H., & Zheng, Z. 2006, MNRAS, 368, 85
Wegner, G., Haynes, M. P., & Giovanelli, R. 1993, AJ, 105, 1251
Xu, X., Cuesta, A. J., Padmanabhan, N., Eisenstein, D. J., & McBride, C. K. 2013, MNRAS, 431, 2834
Zheng, Y. & Song, Y.-S. 2016, JCAP, 8, 050

Irene Cruz-González: Instituto de Astronomía, Universidad Nacional Autónoma de México, Circuito Exterior, Ciudad Universitaria, Ciudad de México 04510 (irene@astro.unam.mx).
Luis Salas: Instituto de Astronomía, Universidad Nacional Autónoma de México, México, Apdo. Postal 877, Ensenada B. C. 22810, México (salas@astro.unam.mx).

Revista Mexicana de Astronomía y Astrofísica, **55**, 105–116 (2019)

SELECTION EFFECTS AND STRUCTURAL SYMMETRIES IN THE ORIENTATION BASED UNIFIED SCHEME

C. C. Onuchukwu[1] and A. A. Ubachukwu[2]

Received November 1 2018; accepted February 6 2019

ABSTRACT

Using the projected linear size, (D) as an orientation parameter, the arm-length ratio, (Q) and the lobe-luminosity ratio, (R) as asymmetry parameters, we test the FR-II galaxies (Gs) and radio-loud quasar (Qs) unification scheme. Using the median values of our binned sample, our results, generally indicate that the D of the radio sources are smaller at higher redshifts z and at larger Q values, with the D of Qs smaller than those of Gs across all Q, z and R bins. Also, the D of Gs appear smaller for lower values of Q, if $R \leq 1.0$ but become larger at higher values of Q if $R > 1.0$. For Qs, the D decreases with increasing Q, R and z. These results imply that the beaming effect is more important in Qs than in Gs. The $D - R$ regression analyses for different Q and z subsamples suggest the importance of factors other than beaming and orientation in the interpretation of the evolution of these radio sources.

RESUMEN

Con el tamaño lineal proyectado (D) como parámetro para la orientación, el cociente de las longitudes de los brazos (Q) y el cociente de las luminosides de los lóbulos (R) como parámetros de asimetría, ponemos a prueba el esquema unificado para galaxias FR-II (GS) y cuasares radio-intensos (Qs). Usando las medianas para nuestras muestras agrupadas, encontramos que en general las D de las radio fuentes son menores para corrimientos al rojo z y valores Q mayores, siendo las D de los Qs menores que las de las Gs para todos los grupos de Q, z y R. Las D de las Gs son menores para valores menores de Q si $R \leq 1.0$ pero aumentan para valores mayores de Q si $R > 1.0$. Para los Qs, las D disminuyen al aumentar Q, R y z. Estos resultados implican que el efecto de colimación es más importante para las Qs que para las Gs. Las regresiones $D - R$ para distintas submuestras de Q y z sugieren la importancia de otros efectos para interpretar la evolución de estos objetos, además de la colimación y la orientación.

Key Words: general: method — method: data analysis — miscellaneous: galaxies — galaxies: active

1. INTRODUCTION

Generally, Extragalactic Radio Sources (EGRS) are classified based on their observed geometric structures, and the amount and variability of the magnitude of radio power they emit (e.g. Fanarof & Riley 1974; Scheuer & Readhead, 1979; Barthel 1989). With improved observations and better theoretical foundation, the general understanding is that the nature and processes that govern the generation and dynamical evolution of EGRS is common to them all. Thus, unification schemes have been developed which posit that, fundamentally, all EGRS are similar in nature and differ only by the factors limiting/affecting their observations. These factors include the viewing angle, relativistic beaming, screens through which the sources are viewed; obscuring torus, time travel and time delay effects (Rees 1967; Ryle & Longair 1967; Zensus 1997; Urry & Padovani 1995; Laing 1988; Garrington et al. 1988; Garring-

[1]Department of Industrial Physics, Chukwuemeka Odumegwu Ojukwu University, Anambra State, Nigeria.

[2]Department of Physics and Astronomy, Faculty of Physical Sciences, Carver Building, University of Nigeria Nsukka, Enugu State, Nigeria.

ton & Conway 1991; Willot et al. 1998; Barthel 1989; Ubachukwu & Ogwo, 1998; Antonucci 1993; Ubachukwu 2002; Gopal-Krishna & Wiita 2004).

In the relativistic beaming and orientation based unification scheme, the projected linear size D of a radio source is believed to be fore-shortened due to orientation effect and is given by (e.g. Ubachukwu 2002)

$$D = D_0 \sin\theta, \tag{1}$$

where D_0 in the intrinsic linear size of the radio source in its rest frame and θ the viewing angle with respect to a distant observer. In the relativistic beaming scenario, the observed arm-length ratio, Q, generally defined as the ratio of the approaching core-lobe length D_a to that of the receding core-lobe length D_r, is given by (e.g. Rees 1967; Ryle & Longair 1967; Ubachukwu 2002; Gopal-Krishna & Wiita 2004)

$$Q = \frac{D_a}{D_r} = \frac{1+\beta\cos\theta}{1-\beta\cos\theta}, \tag{2}$$

where β is the bulk advance speed of the radio emitting plasma in unit of c (the speed of light). Similarly, the observed lobe luminosity ratio R is defined as the ratio of the luminosity of the lobe of the approaching arm to that of the receding arm, and is given by (e.g. Rees 1967; Ryle & Longair 1967; Ubachukwu 2002; Gopal-Krishna & Wiita 2004),

$$R = \left(\frac{1+\beta\cos\theta}{1-\beta\cos\theta}\right)^{n+\alpha}, \tag{3}$$

where n is a factor which depends on the jet flow model, where $n = 3$ is assumed for jet consisting of blobs and $n = 2$ is assumed for jets consisting of continuous flow. The spectral index, α, is defined by $S_{(\nu)} \approx \nu^{-\alpha}$ where $S_{(\nu)}$ is the flux density at the frequency of observation ν. From equations (1)-(3), it follows that as $\theta \longrightarrow \theta_{\min}$, $Q \longrightarrow Q_{\max}$ and $R \longrightarrow R_{\max}$ while $D \longrightarrow D_{\min}$; here min/max is the minimum/maximum value (see Ubachukwu 2002; Onuchukwu & Ubachukwu 2013). We therefore should expect some form of inverse $D - Q$ and $D - R$ relations from pure orientation arguments.

In the orientation based unification scheme of extragalactic radio sources, radio loud quasars and FR-II radio galaxies are expected to differ only in their orientation dependent properties, since FR-II radio galaxies are believed to lie closer to the plane of the sky than radio loud quasars (e.g. Barthel 1989). Thus, we expect a stronger anti-correlation between the projected linear size (D) and the asymmetry parameters (Q/R) for radio-loud quasars than for radio galaxies (Barthel 1989; Urry & Padovani 1995) if pure orientation is the only factor responsible for the differences between these two classes of radio sources. However, in flux density limited source samples, there is a strong selection effect due to the ubiquitous Malmquist bias which must be taken into account while considering quasars/galaxy unification schemes (e.g. Ubachukwu and Ogwo 1998).

In this paper, using the projected linear size as orientation parameter, the arm-length ratio and the lobe-luminosity ratio as asymmetry parameters, we test the FR-II radio galaxy and radio-loud quasar unification scheme for a well-defined sample (e.g Nilsson 1998), and the effect of selection bias in the two classes of radio sources in their luminosity-redshift plane.

2. DATA

The data used for this analysis comprises 1045 heterogeneous sources (543 FR-II radio galaxies (Gs), 366 radio loud quasars (Qs) and 135 unidentified radio sources based on optical classification) taken from Nilsson (1998). For the present analysis, we selected the sources with complete information on the parameters: the redshift (z), the log of luminosity at 178 MHz ($\log P_{178\mathrm{MHz}}$), the lobe-luminosity asymmetry parameter (R), the arm-length asymmetry parameter (Q), the spectral index (α) and the projected linear size of the radio source (D). The final sample consists of 495 radio sources with 243 FR-II radio galaxies and 252 radio-loud quasars. We also form subsamples of highly asymmetric sources defined by $Q > 1.5$ (93 radio quasars and 63 FR-II radio galaxies) and less asymmetric sources defined by $Q \leq 1.5$ (159 radio quasars and 180 FR-II radio galaxies). Though the break at $Q \leq 1.5/Q > 1.5$ was chosen arbitrarily, we are aware of the result obtained in Teerikorpi (2001), which suggests the existence of a correlation between radio source linear size and core luminosity for less asymmetric sources ($Q \leq 1.5$) than for more asymmetric sources ($Q > 1.5$).

Figure 1 shows the $P - z$ plot for our sample which indicates a change in slope at about $z = 0.3$. This change in slope believed to be due to selection effect is shown in Table 1. The quasar subsample with $z \leq 0.3$ indicates a negative $P - z$ slope while others are positive. In our sample, there are only 11 radio loud quasars with $z \leq 0.3$; this low number statistics may have been responsible for the observed negative slope. We note that several authors have pointed out the slope change in the P/z relation from low z radio sources to high z radio sources (See Ubachukwu and Ogwo 1998; Onuchukwu 2014;

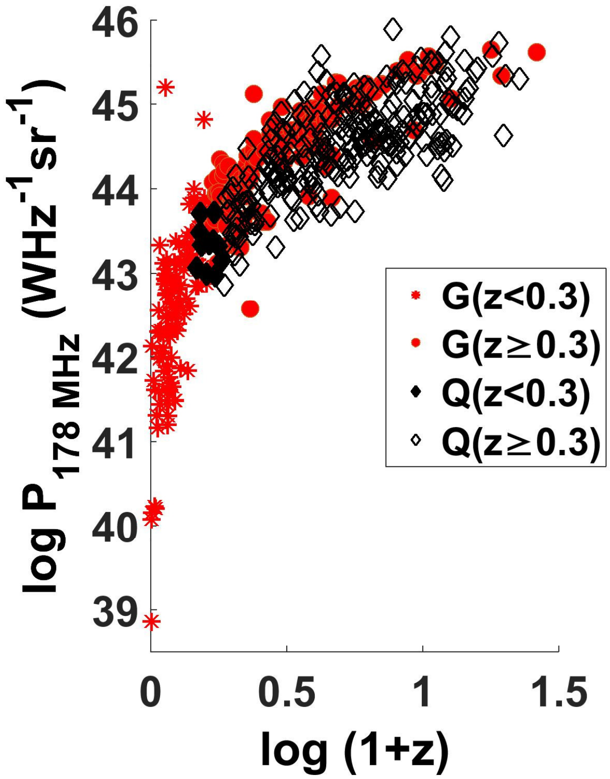

Fig. 1. Distribution plot $\log P_{178\mathrm{MHz}}$ against $\log(1+z)$ for $z < 0.3$ and $z \geq 0.3$ for galaxies (red) and quasars (black). The color figure can be viewed online.

Onah et al. 2018). Thus, we form a subsample of sources with $z \geq 0.3$ and compare the results of our analysis with those of the whole redshift range. There are 112 FR-II radio galaxies at $z \geq 0.3$ in our sample, with 77 having $Q \leq 1.5$ while 35 have $Q > 1.5$. For the radio-loud quasars, we have 242 sources at $z \geq 0.3$, with 150 having $Q \leq 1.5$ while 92 have $Q > 1.5$. For our analyses and results, we have the z-samples (for all z and with $z \geq 0.3$) and two Q-subsamples (with $Q \leq 1.5$ and > 1.5).

3. ANALYSES, RESULTS AND DISCUSSION

We show in Table 2 the results of the average values (the means with the associated error and the median values) for the analysed radio source parameters (D, Q and R) for the different ranges of z and Q subsamples. Generally, the projected linear sizes of galaxies (D_{G}) appear to be larger than those of quasars (D_{Q}). Based on the median value data, the ratio $D_{\mathrm{G}}/D_{\mathrm{Q}} \approx 1.7 - 1.8$ for the whole sample and for the two Q-subsamples (for all z), but it decreases to $D_{\mathrm{G}}/D_{\mathrm{Q}} \approx 1.4 - 1.5$ for the z-subsample ($z \geq 0.3$) and the two Q-subsamples (for $z \geq 0.3$). This is consistent with the quasar-galaxy unification scheme, in which quasars are believed to be the beamed counterpart of radio galaxies which form the parent objects (e.g. Barthel 1989).

TABLE 1

CORRELATION COEFFICIENT.*

	r	Slope
G($z < 0.3$)	0.7	26.2 ± 0.7
Q($z < 0.3$)	-0.1	-2.6 ± 0.3
G($z \geq 0.3$)	0.8	4.6 ± 0.4
Q($z \geq 0.3$)	0.7	3.6 ± 0.4

*Results and slope of the regression fit to $\log P_{178\mathrm{MHz}}$ against $\log(1+z)$ for $z < 0.3$ and $z \geq 0.3$.

Generally, for the sample and z-subsamples considered, the ratio $Q_{\mathrm{G}}/Q_{\mathrm{Q}} \approx 1$ for various Q-subsamples. The similarity of Q-values for quasars and galaxies for different Q and z subsamples may be regarded as a pointer to the same micro-physics at work in the evolution of these radio sources (see Ryś 1994, 2000).

For all the samples and z-subsamples considered, and for the $Q \leq 1.5$ subsample, the ratio $R_{\mathrm{G}}/R_{\mathrm{Q}} \approx 1$ but it decreases to $R_{\mathrm{G}}/R_{\mathrm{Q}} \approx 0.6$ for the $Q > 1.5$ subsample. The observed similarities/differences between the lobe-luminosity ratio of galaxies and quasars for $Q \leq 1.5/Q > 1.5$ suggest that the beaming/orientation effects that foreshorten the observed projected size of quasars (note $D_{\mathrm{G}}/D_{\mathrm{Q}}$ is systematically smaller for $Q > 1.5$ than $Q \leq 1.5$ - see the median values) may also be responsible for enhancing its brightness, thus the lower values of $R_{\mathrm{G}}/R_{\mathrm{Q}}$ obtained for $Q > 1.5$. We also note that several authors (e.g. Ingham & Morrison 1975; Valtonen 1979; Macklin 1981; McCarthy et al. 1991; Best et al. 1995; Wardle & Aaron 1997; Jeyakumar & Saikia 2000; Saikia et al. 2003; Arshakian & Longair 2004; Jeyakumar et al. 2005; Subrahmanyan et al. 2008; Safouris et al. 2009; Priya et al. 2012; Onuchukwu & Ubachukwu 2013; Onuchukwu 2017)) have pointed at other factors (e.g. environment/intrinsic) as being important in the interpretation of the dynamics and evolution of such highly asymmetric radio sources. We also observe that the quasars in our sample are located in denser environments than galaxies (the density (ρ) of the universe scales as $\rho \propto (1+z)^x$, where x is positive), with the median redshift for quasars and galaxies in our sample being 1.1 and 0.3 respectively; while for the subsample with $z \geq 0.3$, the median redshift for the galaxy subclass is ≈ 0.8. and that of the quasar subclass is ≈ 1.1.

TABLE 2

AVERAGE VALUES (MEAN WITH ASSOCIATED ERROR & MEDIAN) OF THE PROJECTED LINEAR SIZE (D).*

z Range		D(kpc) mean	D(kpc) median	Q mean	Q median	R mean	R median
z(All)	Gs(All Q)	401.5 ± 308.4	270.0	1.4 ± 0.3	1.3	1.1 ± 0.6	0.9
z(All)	Qs(All Q)	221.4 ± 162.0	146.6	1.6 ± 0.5	1.3	2.0 ± 1.8	1.0
z(All)	Gs($Q \leq 1.5$)	380.2 ± 255.8	300.3	1.2 ± 0.1	1.2	1.1 ± 0.5	0.9
z(All)	Qs($Q \leq 1.5$)	257.8 ± 181.8	167.0	1.2 ± 0.1	1.2	2.2 ± 2.1	1.0
z(All)	Gs($Q > 1.5$)	462.2 ± 465.5	185.0	2.0 ± 0.4	1.8	1.1 ± 0.8	0.7
z(All)	Qs($Q > 1.5$)	159.3 ± 115.4	106.3	2.2 ± 0.7	1.8	1.6 ± 1.3	1.2
$z \geq 0.3$	Gs(All Q)	310.6 ± 222.3	223.9	1.5 ± 0.4	1.3	1.2 ± 0.8	0.9
$z \geq 0.3$	Qs(All Q)	205.9 ± 146.8	141.5	1.6 ± 0.5	1.3	2.0 ± 1.8	1.0
$z \geq 0.3$	Gs($Q \leq 1.5$)	322.6 ± 213.7	241.0	1.2 ± 0.1	1.2	1.2 ± 0.6	1.0
$z \geq 0.3$	Qs($Q \leq 1.5$)	234.8 ± 160.4	160.1	1.2 ± 0.1	1.2	2.2 ± 2.2	1.0
$z \geq 0.3$	Gs($Q > 1.5$)	284.4 ± 236.9	151.9	2.2 ± 0.5	2.0	1.4 ± 1.2	0.7
$z \geq 0.3$	Qs($Q > 1.5$)	158.8 ± 116.0	105.5	2.2 ± 0.7	1.8	1.7 ± 1.3	1.2

*Redshift and log $P_{178\mathrm{MHz}}$ estimated using all the sources in the sample for radio-loud quasars and FR-II radio galaxies, and for the sample and the subsample with $z \geq 0.3$.

TABLE 3

CORRELATION COEFFICIENT RESULTS FOR $D - Q/R$.*

		Gs	Qs	Gs	Qs
	R (All)	D/Q	D/Q	D/R	D/R
z(All)	Q(All)	−0.2	−0.2	0.1	−0.1
z(All)	$Q \leq 1.5$	0.0	0.0	0.1	−0.2
z(All)	$Q > 1.5$	−0.2	−0.1	0.1	0.0
$z \geq 0.3$	Q(All)	−0.3	−0.2	0.2	−0.1
$z \geq 0.3$	$Q \leq 1.5$	−0.2	0.0	0.2	−0.2
$z \geq 0.3$	$Q > 1.5$	−0.4	−0.1	0.3	0.1
	$R > 1.0$				
z(All)	Q(All)	−0.2	−0.2	0.1	−0.3
z(All)	$Q \leq 1.5$	−0.2	−0.1	0.1	−0.5
z(All)	$Q > 1.5$	−0.3	0.0	0.2	0.1
$z \geq 0.3$	Q(All)	−0.4	−0.2	0.0	−0.3
$z \geq 0.3$	$Q \leq 1.5$	−0.5	−0.1	−0.2	−0.5
$z \geq 0.3$	$Q > 1.5$	−0.1	0.0	0.5	0.1
	$R \leq 1.0$				
z(All)	Q(All)	−0.1	−0.3	0.2	0.2
z(All)	$Q \leq 1.5$	0.1	0.1	0.2	0.1
z(All)	$Q > 1.5$	−0.2	−0.2	0.1	0.1
$z \geq 0.3$	Q(All)	−0.2	−0.3	0.2	0.2
$z \geq 0.3$	$Q \leq 1.5$	0.1	0.1	0.1	0.1
$z \geq 0.3$	$Q > 1.5$	−0.5	−0.2	0.4	0.1

*Relations for different redshift and Q subsamples for radio-loud quasars and FR-II radio galaxies.

In Figures 2-7 we display the distribution plots of D, Q and R of the radio sources for different Q and z subsamples. In Figure 2, the distribution plots of D for all Q, $Q \leq 1.5$ and $Q > 1.5$ for the sample and the z-subsample indicate a lognormal distribution for both galaxies and quasars, though with a seemingly increasing tendency to be more left-skewed for the galaxy subclass than for the quasar subclass of radio sources. We have used the natural logarithm considering the range in values of D in our sample 1.1 - 5853.3 kpc.

At $z > 0.3$, there is a noticeable difference in the distribution of the linear sizes of galaxies and quasars (shown in Figure 3), which seems to increase with increasing Q. For quasars at all Q ($Q \leq 1.5$ and $Q > 1.5$ combined) sample, the D distribution approximates lognormal; but for the galaxies, for $Q > 1.5$ subsample, the projected linear size distribution seems constant from above 100 kpc to more than 1000 kpc. The remarkable differences in the distribution of D for $Q > 1.5; z > 0.3$ between galaxies and quasars may be due to selection and beaming effects. At large z, it is expected that only relatively large sized galaxies of higher luminosity will be easily observable (the median luminosity of galaxies for $Q > 1.5, z \geq 0.3$ is a factor of 7 higher than that of $Q > 1.5, z < 0.3$). The median redshift for $Q > 1.5; z > 0.3$ is: for quasars ($z_{\mathrm{median}} \approx 1.0$) and for galaxies ($z_{\mathrm{median}} \approx 0.7$). Environmental differ-

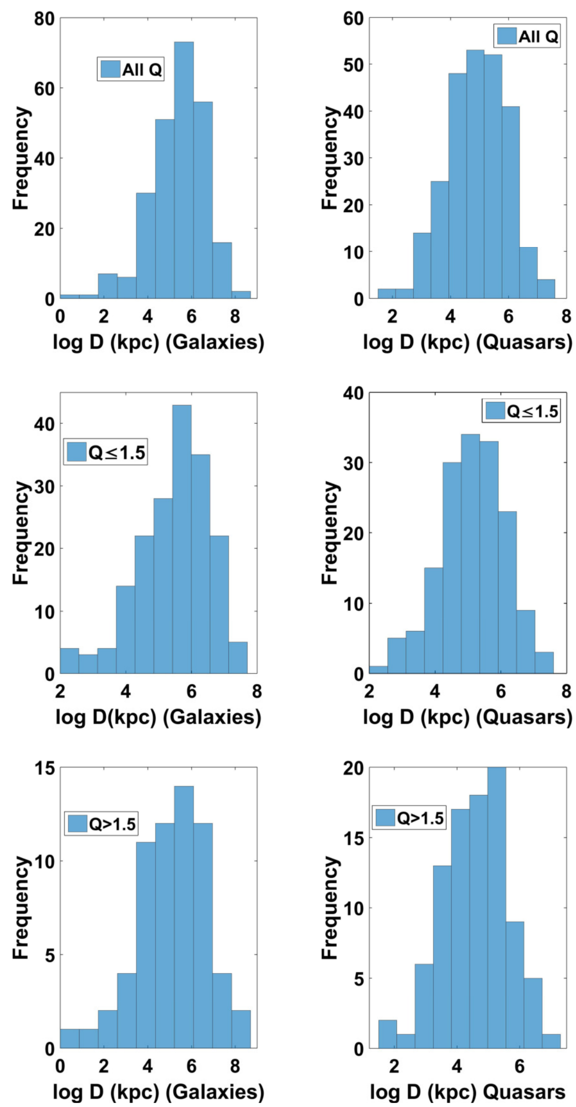

Fig. 2. Distribution plots of $\log D$ for galaxies and quasars for all Q (Top Panel), $Q \leq 1.5$ (Centre Panel), and $Q > 1.5$ (Bottom Panel) for all z.

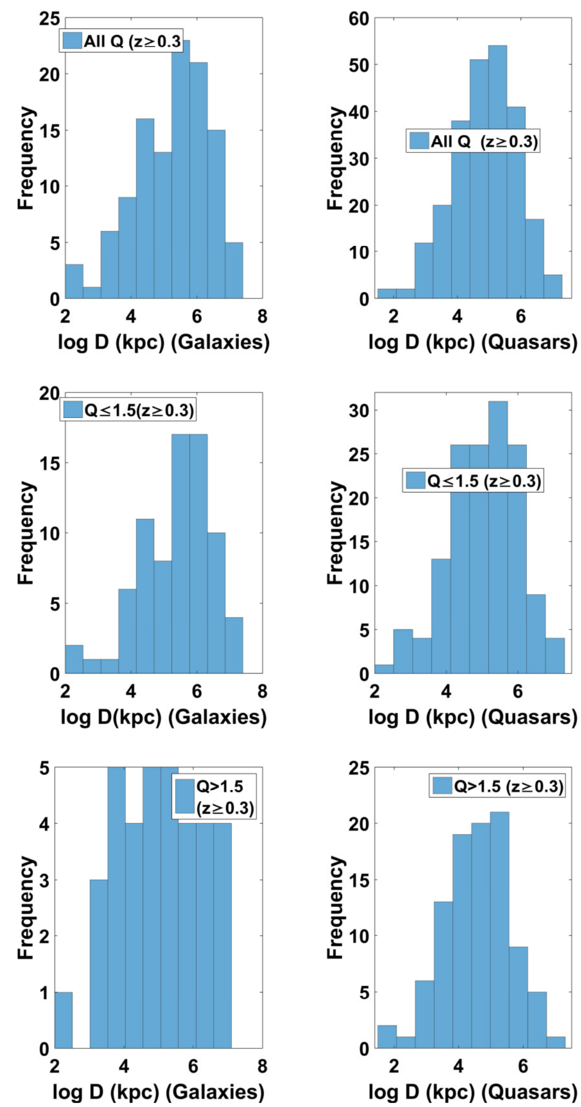

Fig. 3. Distribution plots of $\log D$ for galaxies and quasars for all Q (Top Panel), $Q \leq 1.5$ (Centre Panel), and $Q > 1.5$ (Bottom Panel) for the $z \geq 0.3$ subsample.

ences, if present in the host galaxies, may be responsible for this observed difference, since the density of the universe scales as $\rho \approx (1+z)^x$. By implication, the observed quasars in our sample are found in more dense environments and may suffer greater restraint in expanding to all possible dimensions, while galaxies suffer less restraint and may attain all possible sizes.

Figure 4 shows the distribution plots of Q for the whole sample and the z-subsample.The distributions appear similar for quasars and galaxies for all the different Q-subsamples (right skewed for $Q > 1.5$ and for all Q subsamples but seem to have a constant distribution for the subsample $1 \leq Q \leq 1.5$). For the $z > 0.3$ subsample, (see Figure 5), the Q distributions for the quasar and galaxy subclasses are similar as is the case for the all $-z$ sample. In Figures 6 and 7 we display the distribution plots of lobe-luminosity ratio, R, for radio-loud quasars and FR-II radio galaxies for the whole samples and various z and Q subsamples. The distributions appear lognormal for both classes of object. These distributions show that the observed asymmetries must have been caused by a number of independent factors (relativistic beaming, selection effects, environmental effects, etc.).

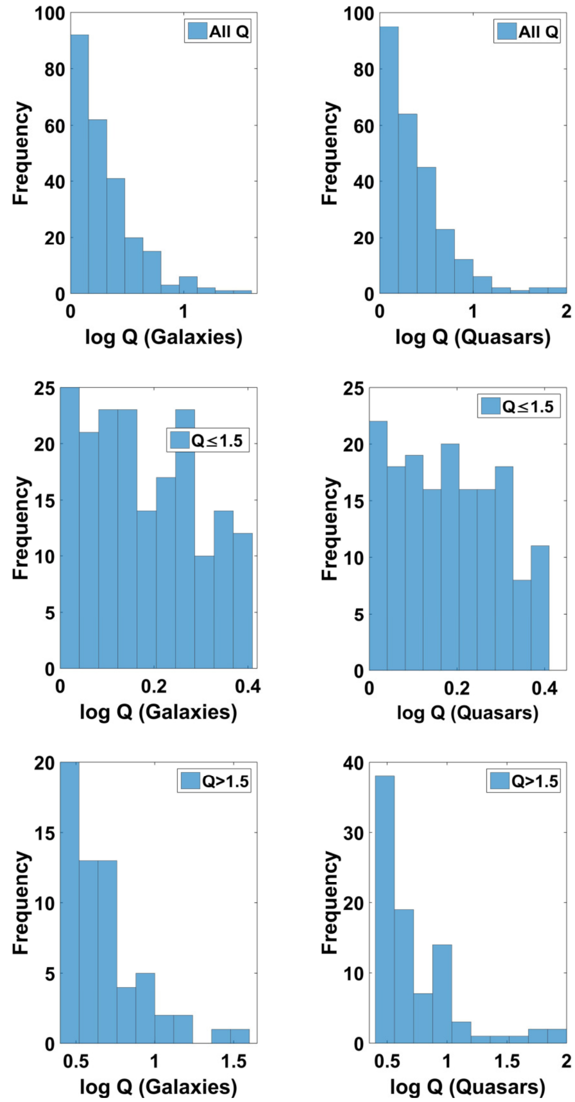

Fig. 4. Distribution plots of Q for galaxies and quasars for all Q (Top Panel), $Q \leq 1.5$ (Centre Panel), and $Q > 1.5$ (Bottom Panel) for all z.

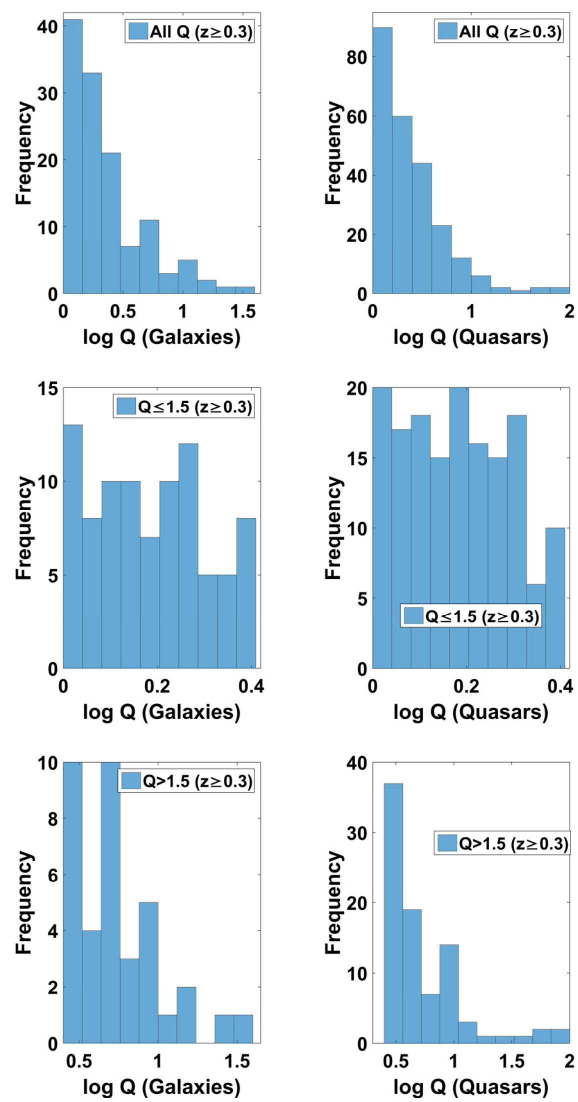

Fig. 5. Distribution plots of Q for galaxies and quasars for all Q (Top Panel), $Q \leq 1.5$ (Centre Panel), and $Q > 1.5$ (Bottom Panel) for the $z \geq 0.3$ subsample.

In Figures 8 and 9 we show the $D-Q/R$ data for the different z and Q subsamples. The results of the one-dimensional regression analyses of the plots are shown in Table 3. Equations (2) and (3) imply that if $Q \geq 1$, then $R \geq 1$. Our sample however shows that 49 % of the quasars and 57 % of the galaxies have $R \leq 1$, implying that relativistic beaming alone cannot explain the observed R-data. We have further subdivided our sample and subsamples to include sources with $R \leq 1.0$ and $R > 1.0$ (see Table 3). We hereby show the average values of the observed parameters in Table 4, the orientation and the asymmetry parameters in Table 5 (in form of the ratios of $D_{\rm G}/D_{\rm Q}$, $Q_{\rm G}/Q_{\rm Q}$ and $R_{\rm G}/R_{\rm Q}$ for the different z and Q subsamples) and the matrix of their correlations in Table 6.

Analyses based on $R > 1.0$ follow the same trend as that of the sample where all the R values were used but with a slight improvement in the strength of the correlation, especially for the quasar subsample with $Q \leq 1.5$. For the subsample based on $R \leq 1.0$, both galaxy and quasar subclasses showed no $D-R$ correlation, and a slight inverse $Q-D$ correlation for the galaxy subclass for $z \geq 0.3; Q > 1.5$. Actually, Onuchukwu (2017) pointed out that environmental/intrinsic factors (e.g. dense environment) may

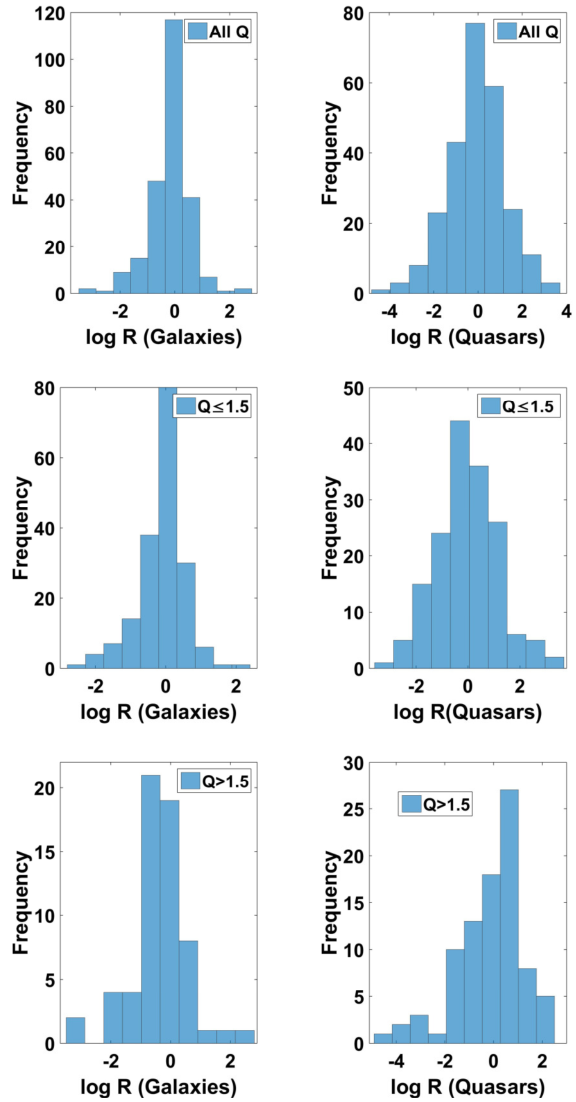

Fig. 6. Distribution plots of R for galaxies and quasars for all Q (Top Panel), $Q \leq 1.5$ (Centre Panel), and $Q > 1.5$ (Bottom Panel) for all z.

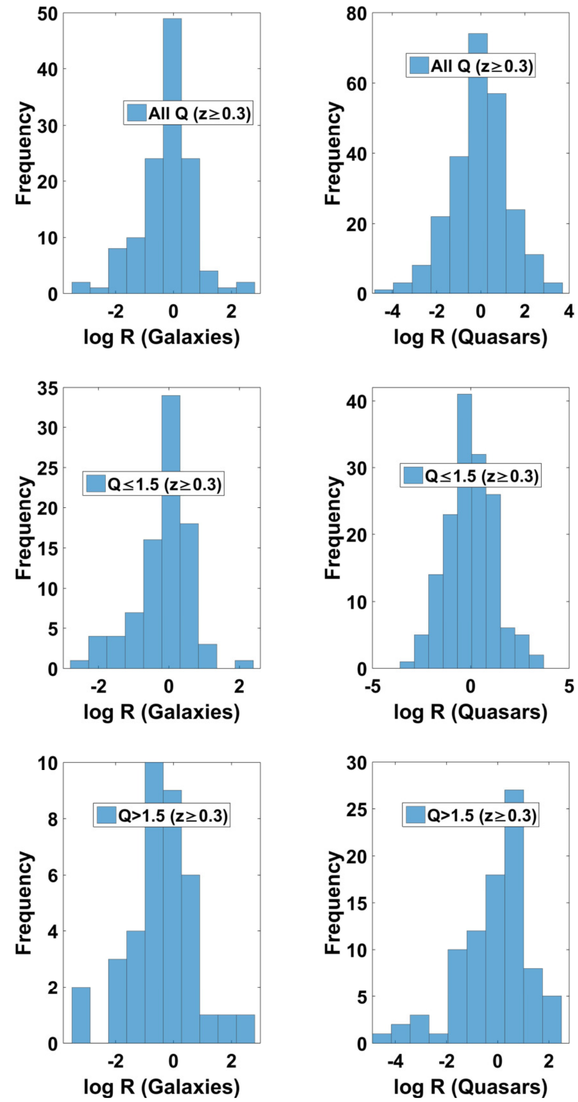

Fig. 7. Distribution plots of R for galaxies and quasars for all Q (Top Panel), $Q \leq 1.5$ (Centre Panel), and $Q > 1.5$ (Bottom Panel) for the $z \geq 0.3$ subsample.

limit the growth of one arm, thereby impeding large values of Q and D, and will also enhance the luminosity of the arm (thereby increasing/decreasing the value of R depending on whether it is assumed to be the approaching/receding side). In Nilsson (1998), the longer side, which may not be the physically approaching side, is assumed to be the approaching side (there was no determination of the jet/counterjet in the sources of the sample).

Table 4 indicates that linear sizes of FR-II radio galaxies depend on both Q and R; being larger for less asymmetric sources ($Q \leq 1.5$) than for more asymmetric sources ($Q > 1.5$) with $R \leq 1.0$ and the reverse for $R > 1.0$. For the quasar subclass, D decreases with Q independent of R. From Table 5, it can be seen that the asymmetry ratio $Q_{\mathrm{G}}/Q_{\mathrm{Q}}$ appears independent of R and z, while $R_{\mathrm{G}}/R_{\mathrm{Q}}$ appears dependent on z. If radio loud quasars and FR-II radio galaxies differ by simple orientation, these ratios are expected to be independent of z, especially for all sources with $R > 1.0$. Similarly, the orientation parameter $D_{\mathrm{G}}/D_{\mathrm{Q}}$ is expected to be dependent on Q and R for all $R > 1.0$ but independent of z for all sources with $z \geq 0.3$. This is generally true from Table 5, where it can be seen that $D_{\mathrm{G}}/D_{\mathrm{Q}}$ is smaller for more asymmetric than for less asymmetric sources.

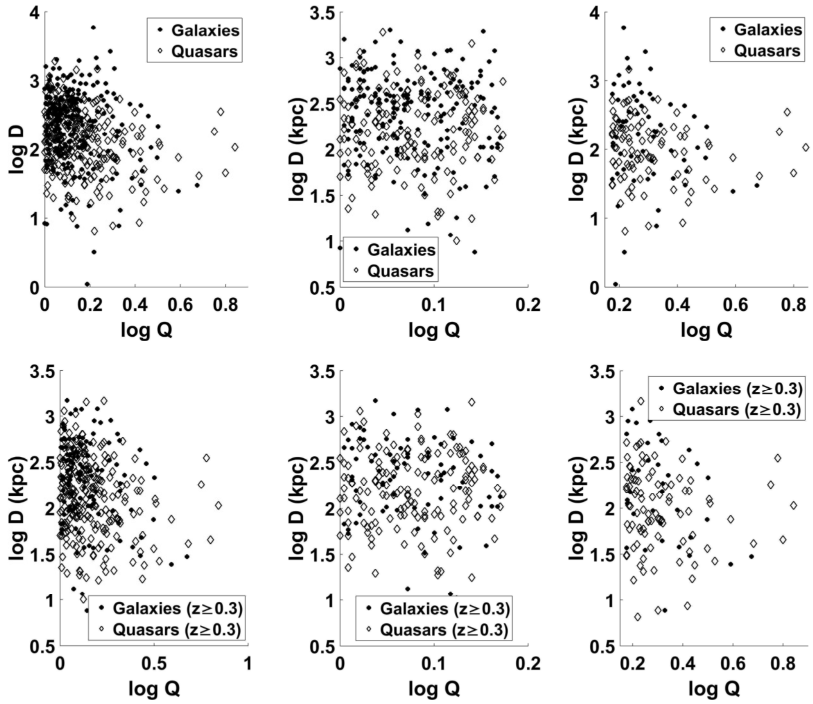

Fig. 8. log − log plots of D against Q for galaxies and quasars for all Q (Right), $Q \leq 1.5$ (Centre), and $Q > 1.5$ (Left) for all z (Top Panel) and for the $z \geq 0.3$ subsample (Bottom Panel).

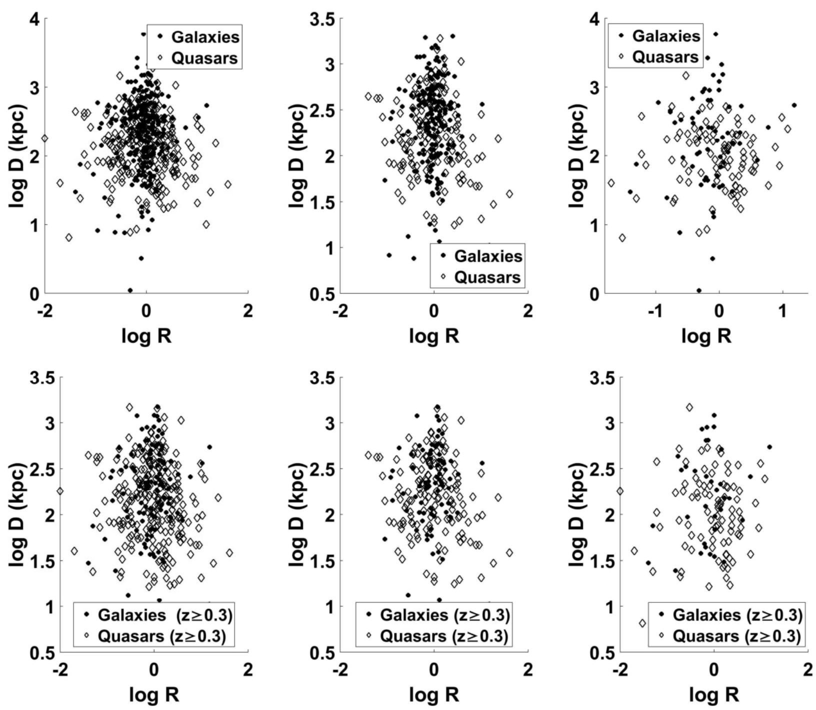

Fig. 9. log − log plots of D against R for galaxies and quasars for all Q (Right), $Q \leq 1.5$ (Centre), and $Q > 1.5$ (Left) for all z (Top Panel) and for the $z \geq 0.3$ subsample (Bottom Panel).

TABLE 4

AVERAGE VALUES OF D, Q, AND R.*

		D	D	Q	Q	R	R
Galaxy	Mean	$R \leq 1.0$	$R > 1.0$	$R \leq 1.0$	$R > 1.0$	$R \leq 1.0$	$R > 1.0$
z(all)	QAll	399.5	398.7	1.5	1.3	0.6	1.8
z(all)	$Q \leq 1.5$	359.8	406.6	1.2	1.2	0.7	1.7
z(all)	$Q > 1.5$	488.1	364.9	2.1	1.9	0.5	2.5
$z \geq 0.3$	QAll	268.6	346.0	1.6	1.4	0.5	2.1
$z \geq 0.3$	$Q \leq 1.5$	251.1	400.0	1.2	1.2	0.6	1.8
$z \geq 0.3$	$Q > 1.5$	300.3	188.3	2.3	2.0	0.5	3.0
Quasar	Mean						
z(all)	QAll	229.3	216.8	1.6	1.6	0.5	3.5
z(all)	$Q \leq 1.5$	251.6	270.6	1.2	1.2	0.5	4.0
z(all)	$Q > 1.5$	187.3	135.2	2.2	2.2	0.4	2.7
$z \geq 0.3$	QAll	221.2	194.1	1.6	1.6	0.5	3.5
$z \geq 0.3$	$Q \leq 1.5$	240.2	235.0	1.2	1.2	0.5	4.1
$z \geq 0.3$	$Q > 1.5$	186.8	135.2	2.2	2.2	0.4	2.7
Galaxy	Median						
z(all)	QAll	255.0	276.0	1.3	1.2	0.7	1.3
z(all)	$Q \leq 1.5$	282.4	312.0	1.2	1.1	0.7	1.3
z(all)	$Q > 1.5$	228.6	151.9	1.9	1.8	0.6	1.4
$z \geq 0.3$	QAll	189.7	256.4	1.3	1.2	0.6	1.4
$z \geq 0.3$	$Q \leq 1.5$	178.5	327.0	1.2	1.2	0.6	1.4
$z \geq 0.3$	$Q > 1.5$	228.6	149.7	2.0	2.1	0.6	1.4
Quasar	Median						
z(all)	QAll	168.5	131.2	1.3	1.3	0.4	2.0
z(all)	$Q \leq 1.5$	196.9	157.5	1.2	1.2	0.5	2.2
z(all)	$Q > 1.5$	153.8	93.7	1.8	1.9	0.3	1.9
$z \geq 0.3$	QAll	164.7	128.3	1.3	1.3	0.4	2.0
$z \geq 0.3$	$Q \leq 1.5$	182.5	153.4	1.2	1.2	0.5	2.3
$z \geq 0.3$	$Q > 1.5$	130.2	93.7	1.8	1.9	0.4	1.9

*For different redshift, Q and R subsamples for radio-loud quasars, and FR-II radio galaxies.

Note that for the comparison we used the ratio obtained from the median value data due to the wide dispersion of the D-values.

It should be noted that the original sample is quite heterogeneous, and contains both lobe- and core- dominated quasars (which may also exhibit different types of D/R & D/Q relations) and covers a wide range of redshifts ($0.0 \leq z \leq 2.87$) and luminosities ($38.86 \leq \log P_{178\mathrm{MHz}} \leq 48.89$, a 7 orders of magnitude difference). This implies a wide range of plausible different host galaxies with differing environment). We believe that binning will smooth out randomly induced characteristics/values in the radio source parameters, and may reveal possible correlations between parameters of radio sources. One possible source of error is the binning range which was done to obtain equal representation in each bin (e.g see Ubachukwu 1998; Onuchukwu & Ubachukwu 2013).

We divided each subsample into 10 (this choice is arbitrary, though motivated by the fact that the histogram plots were arranged into 10 bins). We evaluated the averages (mean and median) of each bin, which we used in the regression analysis shown in Table 6. In the power-law fitted to the $D-Q/D-R$ relations, we have assumed that the power-law index is an indication of the strength of the relation, while the associated error indicates the level of scatter.

The $D - Q$ relation using the mean and the median values of the binned samples indicates a strong anti-correlation for both quasar and galaxy subclasses, except for the quasar subsample with

TABLE 5

RATIO $D_{\rm G}/D_{\rm Q}$, $Q_{\rm G}/Q_{\rm Q}$ AND $R_{\rm G}/R_{\rm Q}$.*

		$D_{\rm G}/D_{\rm Q}$	$D_{\rm G}/D_{\rm Q}$	$Q_{\rm G}/Q_{\rm Q}$	$Q_{\rm G}/Q_{\rm Q}$	$R_{\rm G}/R_{\rm Q}$	$R_{\rm G}/R_{\rm Q}$
		$R \leq 1.0$	$R > 1.0$	$R \leq 1.0$	$R > 1.0$	$R \leq 1.0$	$R > 1.0$
Median							
z(all)	Q(All)	1.5	2.1	1.0	0.9	1.5	0.7
z(all)	$Q \leq 1.5$	1.4	2.0	1.0	1.0	1.6	0.6
z(all)	$Q > 1.5$	1.5	1.6	1.1	0.9	1.6	0.7
$z \geq 0.3$	Q(All)	1.2	2.0	1.0	0.9	1.3	0.7
$z \geq 0.3$	$Q \leq 1.5$	1.0	2.1	1.0	1.0	1.3	0.6
$z \geq 0.3$	$Q > 1.5$	1.8	1.6	1.1	1.1	1.5	0.7
Mean							
z(all)	Q(All)	1.7	1.8	0.9	0.8	1.3	0.5
z(all)	$Q \leq 1.5$	1.4	1.5	1.0	1.0	1.4	0.4
z(all)	$Q > 1.5$	1.6	1.7	0.9	0.9	1.3	0.9
$z \geq 0.3$	Q(All)	1.2	1.8	1.0	0.9	1.2	0.6
$z \geq 0.3$	$Q \leq 1.5$	1.0	1.7	1.0	1.0	1.2	0.4
$z \geq 0.3$	$Q > 1.5$	1.6	1.4	1.0	0.9	1.1	0.8

*For different redshift and Q subsamples using the average (mean and median) values.

$Q \leq 1.5$ for both $z \geq 0.3$ and all z bins, which suggest no correlation (with $r \approx -0.1 \ldots 0.0$). This result is consistent with beaming and orientation effects for both quasars and galaxies, even at large scales, and seems independent of redshift. The power-law index is similarly strong for both redshift bins. The observed absence of any significant correlation for quasar subsamples with $Q \leq 1.5$ is an indication that for such less asymmetric quasars there are other important factors that interfere with the beaming effect.

The $D-R$ correlation is mildly strong and inverse for quasars, decreasing with increasing Q, while it is mild and direct for galaxies, and seems not to vary with Q. The fairly strong inverse $D-R$ correlation for quasars supports the beaming hypotheses while the observed direct $D-R$ correlation for galaxies suggests other factors at play in the evolution of this class of radio sources.

4. CONCLUSION

We have compared the radio size (D) and radio asymmetry parameters Q/R relations based on the pure orientation and relativistic beaming unification scheme for FR-II radio galaxies and radio loud quasars. Using the median values, our results in general indicate that the projected linear sizes of the radio sources are smaller at higher redshift and at larger Q values, with the linear size of quasars generally smaller than those of galaxies across all Q, z and R bins. Moreover, the linear sizes of galaxies seem smaller at lower values of Q if $R \leq 1.0$ but become larger at higher values of Q if $R > 1.0$. For quasars, the linear size decreases with increasing Q, R and z.

On the assumption that as $Q \longrightarrow Q_{\rm max}, R \longrightarrow R_{\rm max}, D \longrightarrow D_{\rm min}$ being a consequence of beaming and projection effects, our results suggest that beaming effect is more important in quasars than in galaxies. Moreover, the results of the $D-R$ regression analyses for the Q and z subsamples reveal that factors other than beaming and orientation are important in the interpretation of the evolution and dynamics of these radio sources. These other factors may include intrinsic asymmetries and environmentally induced asymmetries in radio sources (Ryś 1994, 2000; O'Dea 1998; Mackay's Rule-Mackay 1971; Ingham & Morrison 1975; Gopal-Krishna & Wiita 1996, 2000).

According to the orientation and unification scheme, the Q/R analysis should indicate a stronger beaming effect in quasars than in galaxies. We note that in the sample we have used no effort was made originally to identify the "approaching" and "receding" side (Nilsoon 1988). The longer side was assumed to be the "approaching" side. Thus, a simple Q/R analysis from this sample will give an inconclusive result. This is because, for most of the sources, to assume the longer side as the approaching side may be incorrect. Moreover, environmental factors (Onuchukwu 2017) that may shorten a side can

TABLE 6

CORRELATION COEFFICIENT RESULTS FOR $D-Q/R$ RELATIONS.*

Mean		D/Q	D/Q	D/R	D/R
z	Q	r		r	
z(All)	Gs(ALL Q)	−0.8	$D \propto Q^{-9.3\pm0.3}$	0.4	$D \propto R^{1.7\pm0.5}$
z(All)	Qs(ALL Q)	−0.9	$D \propto Q^{-8.6\pm0.2}$	−0.9	$D \propto R^{-2.4\pm0.2}$
z(All)	Gs($Q \leq 1.5$)	−0.2	$D \propto Q^{-5.9\pm0.5}$	0.2	$D \propto R^{0.8\pm0.5}$
z(All)	Qs($Q \leq 1.5$)	−0.1	$D \propto Q^{-2.0\pm0.5}$	−0.8	$D \propto R^{-1.4\pm0.3}$
z(All)	Gs($Q > 1.5$)	−0.7	$D \propto Q^{-9.1\pm0.5}$	0.2	$D \propto R^{0.5\pm0.7}$
z(All)	Qs($Q > 1.5$)	−0.5	$D \propto Q^{-4.6\pm0.4}$	0.2	$D \propto R^{0.4\pm0.5}$
$z \geq 0.3$	Gs(ALL Q)	−0.9	$D \propto Q^{-6.9\pm0.3}$	0.5	$D \propto R^{1.5\pm0.4}$
$z \geq 0.3$	Qs(ALL Q)	−0.7	$D \propto Q^{-5.8\pm0.3}$	−0.8	$D \propto R^{-2.1\pm0.3}$
$z \geq 0.3$	Gs($Q \leq 1.5$)	−0.4	$D \propto Q^{-8.6\pm0.4}$	0.2	$D \propto R^{0.6\pm0.5}$
$z \geq 0.3$	Qs($Q \leq 1.5$)	0.0	$D \propto Q^{-0.5\pm0.4}$	−0.8	$D \propto R^{-1.2\pm0.3}$
$z \geq 0.3$	Gs($Q > 1.5$)	−0.6	$D \propto Q^{-3.6\pm0.4}$	0.4	$D \propto R^{0.8\pm0.5}$
$z \geq 0.3$	Qs($Q > 1.5$)	−0.3	$D \propto Q^{-2.5\pm0.5}$	0.3	$D \propto R^{0.9\pm0.5}$
Median		D/Q	D/Q	D/R	D/R
z	Q	r		r	
z(All)	Gs(ALL Q)	−0.5	$D \propto Q^{-9.5\pm0.5}$	0.4	$D \propto R^{4.4\pm0.5}$
z(All)	Qs(ALL Q)	−0.8	$D \propto Q^{-10.8\pm0.3}$	−0.6	$D \propto R^{-2.2\pm0.4}$
z(All)	Gs($Q \leq 1.5$)	−0.4	$D \propto Q^{-8.4\pm0.4}$	0.2	$D \propto R^{1.8\pm0.5}$
z(All)	Qs($Q \leq 1.5$)	−0.1	$D \propto Q^{-2.5\pm0.4}$	−0.5	$D \propto R^{-1.5\pm0.4}$
z(All)	Gs($Q > 1.5$)	−0.6	$D \propto Q^{-9.7\pm0.5}$	0.2	$D \propto R^{0.7\pm0.7}$
z(All)	Qs($Q > 1.5$)	−0.3	$D \propto Q^{-3.8\pm0.4}$	−0.2	$D \propto R^{-0.4\pm0.5}$
$z \geq 0.3$	Gs(ALL Q)	−0.7	$D \propto Q^{-6.4\pm0.4}$	0.8	$D \propto R^{3.7\pm0.3}$
$z \geq 0.3$	Qs(ALL Q)	−0.9	$D \propto Q^{-10.5\pm0.2}$	−0.5	$D \propto R^{-1.9\pm0.4}$
$z \geq 0.3$	Gs($Q \leq 1.5$)	−0.5	$D \propto Q^{-7.4\pm0.4}$	0.4	$D \propto R^{1.5\pm0.4}$
$z \geq 0.3$	Qs($Q \leq 1.5$)	0.0	$D \propto Q^{0.6\pm0.4}$	−0.2	$D \propto R^{-0.5\pm0.4}$
$z \geq 0.3$	Gs($Q > 1.5$)	−0.6	$D \propto Q^{-3.6\pm0.4}$	0.4	$D \propto R^{0.7\pm0.5}$
$z \geq 0.3$	Qs($Q > 1.5$)	−0.4	$D \propto Q^{-4.4\pm0.4}$	−0.2	$D \propto R^{-0.4\pm0.4}$

*For different redshift and Q subsamples for radio-loud quasars and FR-II radio galaxies.

also brighten the side, creating an anti-correlation in Q/R relation, but a more positive correlation in the D/R relation.

The authors acknowledge the ASN (Astronomical Society of Nigeria) for providing the platform for exchanging ideas with colleagues and the contribution of the anonymous referee to improve this work.

REFERENCES

Antonucci, R. 1993, ARA&A, 31, 473
Arshakain, T. G. & Longair, M. S. 2000, MNRAS, 311, 846
Barthel, P. D. 1989, ApJ, 336, 606
Best, P. N., Bailer, M. D., Longair, M. S., & Riley, J. M. 1995, MNRAS, 275, 1171
Fanaroff, B. & Riley, J. M. 1974, MNRAS, 167, 31P
Garrington, S. T. & Conway, R. G. 1991, MNRAS, 250, 198
Gopal-Krishna & Wiita, P. J. 1996, ApJ, 467, 191
_________. 2000, A&A, 363, 507
_________. 2004, e-print arXiv:astro-ph/0409761
Ingham, W. & Morrison, P. 1975, MNRAS, 173, 569
Jeyakumar, S. & Saikia, D. J. 2000, MNRAS, 311, 397J
Jeyakumar, S., Wiita, P. J., Saikia, D. J., & Hooda, J. S. 2005, A&A, 432, 823J
Laing, R. A. 1988, Natur, 331, 149
Mackay, C. D. 1971, MNRAS, 154, 209
Macklin, J. T. 1981, MNRAS, 196, 967
McCarthy, P. J., van Breugel, W., & Kapahi, V. K. 1991, ApJ, 371, 478
Nilsson, K. 1998, A&AS, 132, 31
O'Dea, C. P. 1998, PASP, 110, 493
Onah, C. I., Ubachukwu, A. A., Odo, F. C., & Onuchukwu, C. C. 2018, RMxAA, 54, 271
Onuchukwu, C. C. 2014, Cosmological Evolution In Extended Extragalactic Radio Sources, Advances in Science and Technology, 8, 23

_________. 2017, Ap&SS, 362, 100
Onuchukwu, C. C. & Ubachukwu, A. A. 2013, Ap&SS, 344, 211, DOI 10.1007/s10509-012-1325-x
Priya, A., Saikia, D. J., Singh, M., & Chandola, H. C. 2012, MNRAS, 426, 758
Rees, M. J. 1967, MNRAS, 135, 345
Ryś, S. 1994, A&A, 281, 15
_________. 2000, A&A, 355, 79
Ryle, M. & Longair, M. S. 1967, MNRAS, 136, 123
Safouris, V., Subrahmanyan, R., Bicknell, G. V., & Saripalli, L. 2009, MNRAS, 393, 2
Saikia, D. J., Jeyakumar, S. K., Mantovani, F., et al. 2003, PASA, 20, 50
Scheuer, P. A. G. & Readhead, A. C. S. 1979, Natur, 277, 182
Smith, E. P. & Heckman, T. M. 1989, BAAS, 21Q, 777
Subrahmanyan, R., Saripalli, L., Safouris, V., & Hunstead, R. W. 2008, ApJ, 677, 63
Ubachukwu, A. A. 1996, Ap&SS, 236, 167
_________. 1998, Ap&SS, 254, 23
_________. 2002, Ap&SS, 279, 251
Ubachukwu, A. A. & Ogwo, J. N. 1998, AJP, 51, 143
Urry, C. M. & Padovani, P. 1995, PASP, 107, 803
Valtonen, M. J. 1979, ApJ, 231, 312
Wardle, J. F. C. & Aaron S. E. 1997,MNRAS286, 425
Willot, C. J., Rawlings, S., Blundell, K. M., & Lacy, M. 1998, MNRAS, 300, 625
Zensus, J. A. 1997, ARA&A, 35, 607

Onuchukwu, C. C.: Department Of Industrial Physics, Chukwuemeka Odumegwu Ojukwu University, Anambra State, Nigeria (onuchukwu71chika@yahoo.com).
Ubachukwu, A. A.: Department of Physics and Astronomy, Faculty of Physical Sciences, Carver Building, University of Nigeria Nsukka, Enugu State, Nigeria.

Revista Mexicana de Astronomía y Astrofísica, **55**, 117–123 (2019)

THE HH34 JET/COUNTERJET SYSTEM AT 1.5 AND 4.5μm

A. C. Raga[1], B. Reipurth[2], and A. Noriega-Crespo[3]

Received October 29 2018; accepted February 13 2019

ABSTRACT

We present a (previously unpublished) 1.5 μm archival HST image of the HH 34 Herbig-Haro jet, in which the northern counterjet is seen at an unprecedented angular resolution of $\approx 0.1''$ (this counterjet had only been imaged previously at lower resolution with Spitzer). The jet/counterjet structure observed in this image shows evidence of low-amplitude, point-symmetric deviations from the outflow axis, indicating the presence of a precession in the ejection direction. We use the ratios between the 1.5 and 4.5 μm intensities of the emitting knots (from the HST image and from a previously published 4.5 μm Spitzer image) to obtain an estimate of the spatial dependence of the optical extinction to the HH 34 jet/counterjet system. We find evidence for extinction from a central, dense core surrounding the outflow source and from a more extended region in the foreground of the HH 34 counterjet.

RESUMEN

Presentamos una imagen del chorro Herbig-Haro HH 34 (inédita) a 1.5 μm del archivo del HST, en la que el contrachorro norte se detecta con una resolución angular sin precedentes de $\approx 0.1''$ (las únicas imagenes previas de este contrachorro, obtenidas con el Spitzer, tienen una menor resolución). La estructura de chorro/contrachorro observada en esta imagen muestra evidencia de desviaciones de baja amplitud, con simetría de punto con respecto al eje del flujo, e indica la presencia de una precesión en la dirección de la expulsión. Usamos cocientes entre los flujos a 1.5 y 4.5 μm de los nudos emisores (obtenidos de la imagen del HST y de una imagen a 4.5 μm del Spitzer publicada previamente) para obtener una estimación de la dependencia espacial de la extinción óptica del sistema chorro/contrachorro HH 34. Encontramos evidencia de extinción debida a un núcleo denso rodeando a la fuente del flujo y a una zona más extendida situada enfrente del contrachorro de HH 34.

Key Words: Herbig-Haro objects — ISM: individual objects (HH34) — ISM: jets and outflows — ISM: kinematics and dynamics — stars: formation — stars: winds, outflows

1. INTRODUCTION

Since its discovery, the HH 34 jet has been one of the finest, brightest, and best collimated HH jets known to emanate from a young star. Early studies established the basic characteristics of the jet, showing that the jet moves out of a compact cloud core in the L1641 cloud in Orion (Reipurth et al. 1986, Bührke et al. 1988, Raga & Mateo 1988, Reipurth & Heathcote 1992).

A series of distant bow shocks have been discovered both to the south and the north, showing that HH 34 comprises a giant HH flow (Bally & Devine 1994), modeled by Cabrit & Raga (2000) and Masciadri et al. (2002). At the here adopted distance of 400 pc (Kounkel et al. 2017, Menten et al. 2007), the total projected extent of the HH complex is 2.5 pc.

The source is an embedded Class I protostar with a total luminosity of 21 $L_\odot$ (value from Reipurth et al. 1993, but converted to a distance of 400 pc); the source was detected in the radio continuum by Rodríguez & Reipurth (1996) and Rodríguez et al. (2014). The HH 34 source is surrounded by a molecular cloud core, which has been studied by Stapelfeldt & Scoville (1993), Davis & Dent (1993), and Anglada et al. (1995). As the jet moves out from the core it entrains gas and forms a small molecular outflow (Chernin & Masson 1995).

[1]Instituto de Ciencias Nucleares, UNAM, México.
[2]Institute for Astronomy, Univ. of Hawaii, USA.
[3]Space Telescope Science Institute, USA.

HH 34 moves away from the driving source with a velocity of about 300 km/s at an angle of roughly 25° to the plane of the sky (Heathcote & Reipurth 1992, Eisloeffel & Mundt 1992), values that have been confirmed and refined with subsequent HST images obtained over longer timescales (Reipurth et al. 2002, Raga et al. 2012a).

Devine et al. (1997) showed that the components of the giant HH complex slow down with distance and come to almost a stand-still at the terminal bow shocks. Physical conditions along the jet have been studied by e.g. Morse et al. (1992, 1993), Takami et al. (2006), Beck et al. (2007), García López et al. (2008), Rodríguez-González et al. (2012), and Nisini et al. (2016). The shocks within the HH 34 jet have been successfully modelled as resulting from multi-mode variable velocity flows (Raga & Noriega-Crespo 1998). Refined models have been presented by Raga et al. (2002a, b, 2011b, c, 2012b) and Raga & Noriega-Crespo (2013).

The optical images of the HH 34 complex show that the jet is one-sided, but using Spitzer data Raga et al. (2011a) concluded that this is due to extinction from the cloud core surrounding the driving source, and they found that a counterjet is detected at infrared wavelengths (see also García López et al. 2008 and Antoniucci et al. 2014). In this paper, we discuss the nature of the counterjet based on archival near-infrared HST images which reveal its fine structure.

In particular, we discuss an archival HST image taken with the F160W filter (with a dominant contribution from the [Fe II] 1.64 μm line), which shows the northern HH 34 counterjet at higher resolution than the Spitzer 4.5 μm image of Raga et al. (2011a). The counterjet emission (in the [Fe II] 1.64 μm and H_2 2.12 μm lines) has been previously seen in the long-slit spectra of García López et al. (2008), and in the [Fe II] 1.64 μm image of Antoniucci et al. (2014).

In § 2, we describe the F160W HST image, as well as the 4.5 μm Spitzer image of Raga et al. (2011a). In § 3, we present these two images and determine knot positions along the jet and the counterjet. In § 4, we discuss the lateral offsets of the knot positions from the jet axis and the 1.5 and 4.5 μm intensities as a function of position for the jet and the counterjet. The 4.5 to 1.5 μm intensity ratios are then used to estimate the visual extinction to the knots along the HH 34 jet and counterjet. Finally, the results are summarized in § 5.

2. THE OBSERVATIONS

In this paper we analyze an archival HST image of HH 34 obtained under proposal 11548 (P.I. Thomas Megeath) in October 2009. This image was taken with the F160W filter on the WFC3 camera, with a 2946 s exposure. The F160W filter has a 1.5369 μm pivot wavelength and a 0.0826 μm RMS bandwidth. For the HH 34 jet, the emission in the F160W filter bandpass is dominated by the [Fe II] 1.64 μm line, with a smaller contribution (at $\approx 10\%$) from the [Fe II] 1.60 μm line, as shown by the spectroscopic observations of García López et al. (2008). This image has an angular resolution of $\approx 0.1''$.

In order to obtain a calibrated [Fe II] 1.64 μm map, we multiply the original HST image by the "PHOTFLAM" parameter (in the header of the fits file) and by the 0.268 μm "rectangular passband width" of the F160W filter. This width is given in the WFC3 Instrument Handbook.

We compare the F160W image with the 4.5 μm Spitzer image of Raga et al. (2011a). This image is a 6×6 array (with a total integration time of 30 s per pixel) obtained with Channel 2 of the IRAC camera. This channel covers from approximately 4 to 5 μm, and includes three relatively bright, purely rotational H_2 lines. This image has an angular resolution of $\approx 2''$.

3. THE 1.5 AND 4.5μm EMISSION OF THE HH 34 OUTFLOW

The left frame of Figure 1 shows the 1.5 μm image of a region around the source of the HH 34 outflow. It is clear that the counterjet is detected. The central frame of Figure 1 shows a convolution of this image with a $\sigma = 6$ pix ($0.54''$) half-width "Mexican hat" wavelet (see Raga et al. 2017), in which the relatively smooth emission/reflection within $\approx 30''$ from the source is eliminated, so that the jet and counterjet knots are seen more clearly. The right frame of Figure 1 shows the 4.5μm image, with a vertical (7 pixel wide) strip in which the background emission has been subtracted (by carrying out linear interpolations between the intensities on the left and right edges of the strip, as described by Raga et al. 2011a).

In the central frame of Figure 1 (showing the 1.5μm image convolved with a $\sigma = 6$ pix$= 0.54''$ half-width wavelet) we have identified the knots along the jet following Reipurth et al. (2002). For the knots along the counterjet, we have used the letters

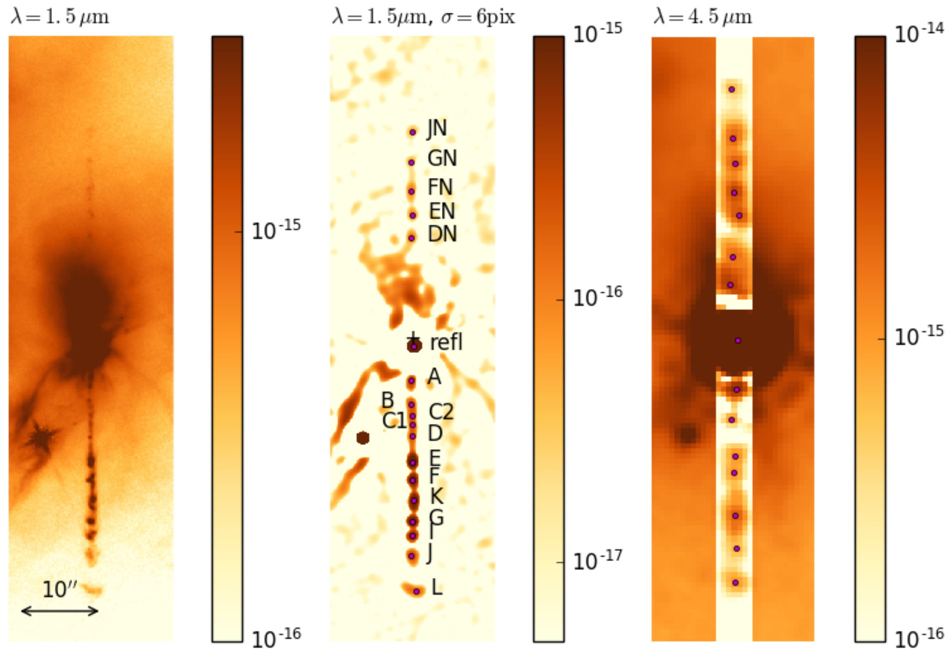

Fig. 1. The HH 34 jet/counterjet system, rotated (14°, counterclockwise) so that the outflow axis is parallel to the ordinate. Left: HST 1.5 μm image. Center: 1.5 μm image convolved with a 6 pixel ($0''.54$) half-width wavelet. Right: Spitzer 4.5 μm image, with a central band in which a linear background (tied to the fluxes at the edges of the band) has been subtracted. In the central and right frames we show the positions of the fitted intensity peaks; the identifications of the peaks are given only in the central frame. The position of the outflow source is shown with a cross in the central frame. The images are displayed with a logarithmic scale on the right of each frame (in units erg cm^{-2} s^{-1} arcsec^{-2}). The color figure can be viewed online.

of the jet knots at similar distances from the outflow source, followed by a "N" (to indicate that they belong to the N counterjet).

The knot along the outflow axis closest to the outflow source (labeled "refl" in Figure 1) corresponds to the reflection nebula at the base of the HH 34 jet. The position of the VLA source of Reipurth et al. (2000a), shown with a cross (in the central frame of Figure 1) is $\approx 1''$ to the N of the reflection nebula. This radio source most probably coincides with the position of the outflow source.

4. THE KNOT POSITIONS AND INTENSITIES

We have determined the positions and intensities of the knots along the HH 34 jet and counterjet by fitting paraboloids to the intensity peaks along the outflow axis. The resulting knot positions are shown on the central (1.5 μm) and right (4.5 μm) panels of Figure 1.

Figure 2 shows the (x, y) positions of the 1.5 μm knots, where x is the distance from the outflow source along the flow axis (with $x < 0$ for the jet and $x > 0$ for the counterjet), and y is the distance perpendicular to this axis (with positive y to the W). From this figure, we note several interesting features:

- the 4.5 μm jet and counterjet show almost coincident knots at distances $< 15''$ from the source, and somewhat larger offsets in the jet/counterjet knot positions at larger distances. This effect was described in detail by Raga et al. (2011a, c),
- for $x > 12''$ we see reasonable position coincidences between the 1.5 and 4.5 μm jet and counterjet knots. Offsets of $\approx 1''$ in the jet/counterjet directions (with the 1.5 μm knots always at larger distances from the source) probably correspond to the proper motions of the knots during the time-interval between the two frames (see § 2),
- for $x \leq 12''$ there are no clear correspondences between the 1.5 and 4.5 μm knots.

Also, the 1.5μm knots have systematic displacements, with the knots at $\approx 20''$ from the source showing $y \approx 0.1''$ for the jet and $y \approx -0.1''$ offsets for the counterjet. These (somewhat marginal)

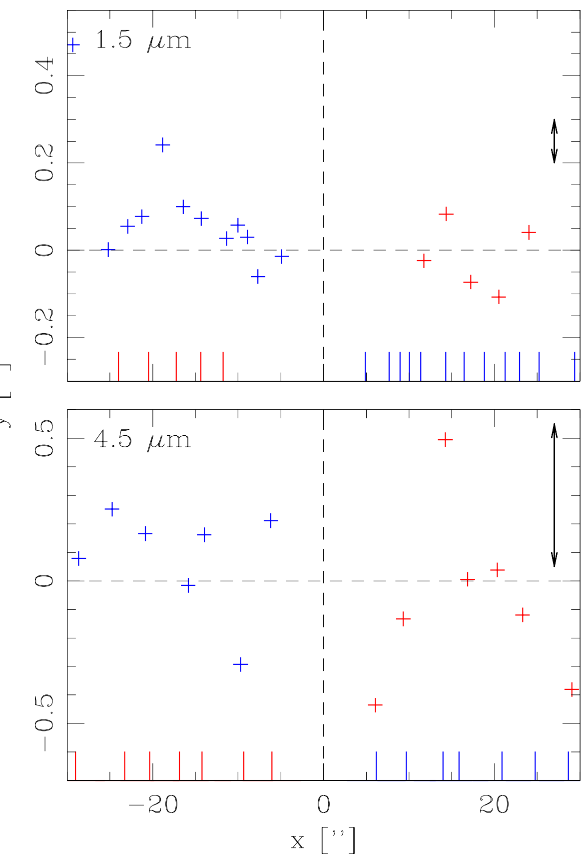

Fig. 2. Offsets perpendicular to the outflow axis as a function of distance from the source measured in the convolved 1.5 μm (top) and in the 4.5 μm frame (bottom). The blue crosses correspond to the southern jet (negative x values), and the red crosses to the northern counterjet ($x > 0$). Positive y values denote offsets to the W of the outflow axis. The blue (jet) and red ticks (counterjet) along the bottom axis show the positions of the knots along the oppositely directed outflow lobes. The double arrows on the right of the plots show the errors in the offsets. The color figure can be viewed online.

"point symmetric" offsets could indicate the presence of a precession of the outflow axis. At 4.5 μm we do not see any systematic offsets of the knots (perpendicular to the outflow axis), as a direct result of the lower angular resolution of this image.

Figure 3 shows the intensities of the jet and counterjet knots in the 1.5 μm convolved frame (top) and in the 4.5 μm frame (bottom) as a function of distance from the outflow source. The 1.5 μm emission shows that:

- the jet knots start at $x \approx 4.5''$, have low intensities with $I_{1.5} \approx 8 \times 10^{-16}$erg s^{-1}cm^{-2}arcsec^{-2} values for $x < 12''$, and high $I_{1.5} \approx 5 \times 10^{-15}$erg s^{-1}cm^{-2}arcsec^{-2} values for $12 < x < 22''$. At larger distances from the source, the knot intensities drop monotonically with increasing x,

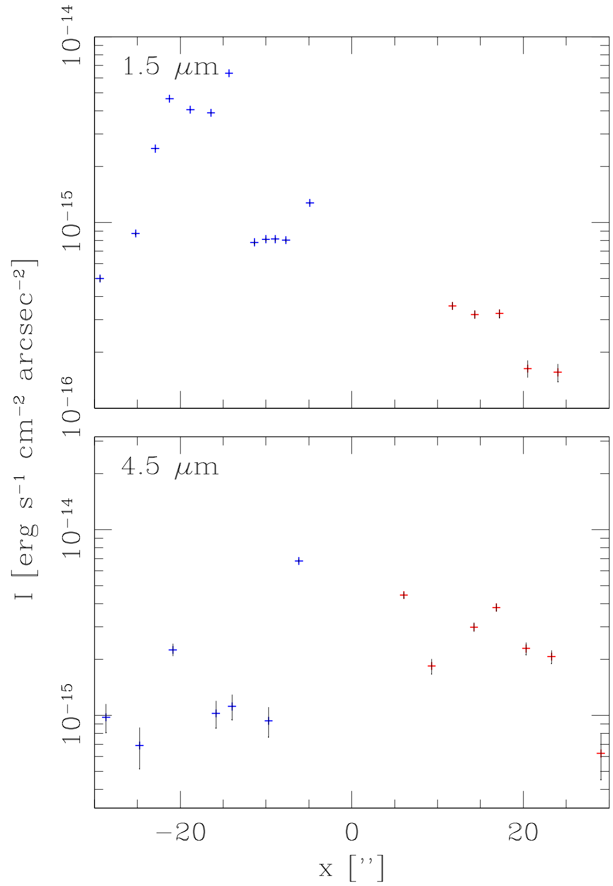

Fig. 3. Peak intensities of the knots along the jet (negative x, blue crosses) and counterjet (positive x, red crosses) in the convolved 1.5 μm (top) and in the 4.5μm frame (bottom). The color figure can be viewed online.

- the counterjet knots start at $x \approx 11''$, have $I_{1.5} \approx 3 \times 10^{-16}$erg s^{-1}cm^{-2}arcsec^{-2} values for $x < 20''$ and lower intensities at larger x.

The lack of counterjet knots and low jet knot intensities close to the source (at $x < 11''$) can be interpreted as evidence for a high extinction circumstellar region. Also, the large contrast between the jet and counterjet emission for $x > 11''$ might be due to the presence of a high extinction cloud covering the counterjet.

The 4.5 μm emission (bottom frame of Figure 3) shows that:

- the jet and counterjet knots start at a distance $x \approx 6''$ from the outflow source,

- the jet/counterjet knots at similar distances from the source have intensities that differ by factors of at most 3, with brighter knots in the jet or in the counterjet at different values of x.

We now assume that the 4.5 to 1.5 μm intrinsic intensity ratio has the same value for all of the jet/counterjet knot pairs (grouping into pairs the jet and counterjet knots with similar distances to the outflow source) at distances larger than $10''$ from the source (i.e., excluding the first two knots along the jet and the counterjet seen in the bottom frames of Figures 2 and 3). We additionally assume that the $|x| > 10''$ knots of the jet do not have a substantial extinction at 4.5 and 1.5μm, which is consistent with the relatively low $A_v \approx 1.3$ optical extinction determined (from optical line ratios) by Podio et al. (2006) for this region. We then compare the counterjet and jet 4.5/1.5 μm ratios of the knots (at similar distances from the source, assuming that the knot pairs have the same intrinsic 4.5/1.5 μm ratios) to compute the extinction towards the counterjet knots.

For the jet knots within $10''$ from the source, we assume that the intrinsic 4.5/1.5 μm ratios are constant, with values equal to the 4.5/1.5 μm ratio of knot D (at $x \approx -16''$, see Figures 1-3). With this assumption, we can then compute the extinction towards the jet knots within $10''$ from the outflow source.

In order to convert the "observed vs. intrinsic" 4.5/1.5 μm ratios to a visual extinction A_v, we use an $R = A_v/E(B-V) = 5$ extinction curve, as appropriate for star formation regions (see, e.g., Olofsson and Oloffson 2010). We take this extinction curve from Fitzpatrick (1999), who presents similar results to the ones of Cardelli et al. (1989).

The results of this exercise are given in Figure 4 (where we show the extinction obtained for the southern jet with negative x and for the northern counterjet with positive x). To derive the plotted values we have set $A_v = 0$ for the jet knots with $x < -10''$.

In Figure 4 we see the following:

- there is a region within $\approx 5''$ from the source with no detected emission. This region is likely to have very high extinction,

- as we approach the source along the jet (with $x < 0$), we see a fast growth in A_v as we get within $\approx 10''$ from the outflow source,

- as we move away from the source along the counterjet (for $x > 0$), we see a plateau with $A_v \approx 24 \to 27$ (comparable to the higher A_v value seen in the jet), and then a rapid fall in A_v for $x > 18''$.

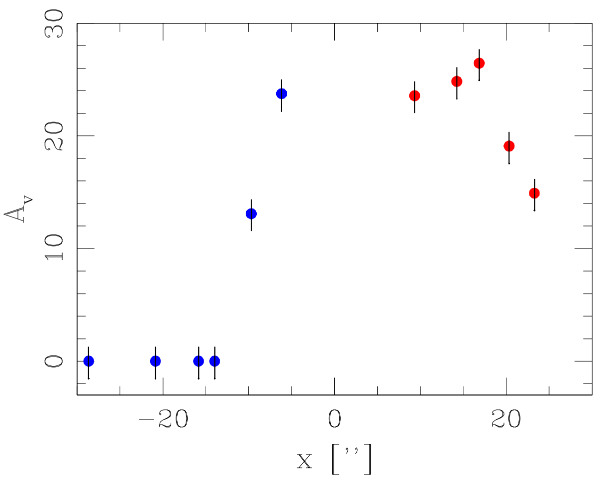

Fig. 4. Optical extinction A_v (calculated from the 1.5 and 4.5 μm intensities, as described in the text) as a function of distance x from the outflow source. The region of the southern jet is shown with negative x values, and the northern counterjet with positive x. The color figure can be viewed online.

We note that Podio et al. (2006) used optical and near-IR diagnostics to obtain an $A_v \approx 1.3$ extinction for the HH 34 jet knots at larger distances from the source, and a higher $A_v \approx 7$ value for the knots closest to the outflow source. This result is qualitatively consistent with the rise in A_v towards the source that we obtain from the 4.5 to 1.5 μm intensity ratios. Also, Reipurth et al. (2000b) determined a rapid rise of A_v when approaching within $\approx 10''$ from the outflow source for the HH 1 jet, which is again qualitatively consistent with our results for the HH 34 jet.

5. CONCLUSIONS

We present a previously unpublished HST 1.5 μm archival image that shows the HH 34 jet and counterjet. This is the first time that we can see the structure of the HH 34 counterjet at $\approx 0.1''$ resolution. We have compared this image with a 4.5 μm Spitzer image of this outflow (which has a lower, $\approx 2''$ resolution, see Raga et al. 2011a).

A comparison of the positions of the jet and counterjet knots shows that in the lower resolution 4.5 μm image we do not see significant offsets from the outflow axis. However, in the new, higher resolution 1.5 μm image we see systematic offsets which indicate (somewhat marginal) point-symmetric jet/counterjet curvatures (see Figure 2).

This result implies that we are probably seeing the effect of a small precession of the outflow axis.

We also measure the intensities of the knots along the jet and counterjet in the 1.5 and 4.5 μm images. We find that at 4.5 μm the knots at similar distances along the jet and counterjet have intensities that differ by at most a factor of ≈ 3 (with brighter counterjet knots at distances $x \approx 10 \to 18''$ from the outflow source). At 1.5 μm, the jet knots are systematically brighter than the counterjet knots (at similar distances from the source) by factors of $\approx 10 \to 20$, with the counterjet not being detected for $x < 10''$. This result is likely to be an effect of higher extinction towards the counterjet.

The fact that the jet and counterjet show highly symmetric structures at 4.5 μm (Raga et al. 2011a), while the HH 34 system shows a "one sided" jet at optical wavelengths (with an invisible counterjet that reappears at the HH 34N "head", see Bührke et al. 1988), indicates that a strong asymmetry in the extinction towards the jet and the counterjet is present.

We have then computed the relative extinction between the jet and the counterjet assuming that the intrinsic 1.5 to 4.5 μm ratios have identical values for the jet and counterjet knots at similar distances from the outflow source. With this assumption (and using an appropriate extinction curve) we have calculated the visual extinction A_v along the HH 34 jet and counterjet.

We find that, approaching the outflow source along the southern jet, A_v grows quite dramatically within $\approx 10''$ from the source (see Figure 4). This rapid increase in A_v (for decreasing distances from the source) is consistent with the result obtained by Podio et al. (2006) from optical and near-IR diagnostics of the HH 34 jet.

Moving away from the source along the northern lobe of the outflow, the counterjet emission is first detected at $\approx 5''$ from the source at 4.5 μm, and then at $\approx 10''$ from the source at 1.5 μm (see Figure 3). For larger distances from the source (where we detect the counterjet at both 1.5 and 4.5 μm), we obtain an extinction with $A_v \approx 24 \to 27$ out to $\approx 17''$, followed by a strong decrease to $A_v \approx 15$ (at $\approx 23''$ from the source, see Figure 4).

We therefore see the existence of:

- a very high extinction region within $\approx 10''$ from the source, with a steep rise in A_v along the jet towards the outflow source, and an undetected counterjet within $\approx 5''$ from the source,
- a plateau in the extinction along the counterjet from $\approx 10''$ (where the counterjet first appears in the 1.5 μm image) out to $\approx 17''$ to the N of the outflow source, followed by a sharp decrease in A_v at larger distances.

It then appears that we see evidence for the existence of two structures that produce the extinction:

- a central core with a $\approx 10''$ radius,
- a spatially more extended, dense structure in the foreground of the counterjet.

This extended structure could be related to the complex molecular emission observed in the region around the HH 34 outflow (see, e.g., Stapelfeldt & Scoville 1993 and Anglada et al. 1995).

Our determination of the extinction, however hinges on an assumed symmetry between the 4.5/1.5 μm ratios of the jet and counterjet knots with $|x| > 10''$, and an assumed constancy of this ratio for the $|x| < 10''$ jet knots. The precision of our position-dependent A_v determination is therefore quite questionable!

A more precise measurement of the extinction in the HH 34 jet and counterjet will be obtained with future James Webb Space Telescope observations of this outflow system. These observations will provide the IR diagnostic lines appropriate for carrying out a proper determination of the position-dependent extinction.

AR acknowledges support from the DGAPA-UNAM grant IG100218. We thank an anonymous referee for relevant corrections.

REFERENCES

Anglada, G., Estalella, R., Mauersberger, R., et al. 1995, ApJ, 443, 682
Antoniucci, S., La Camera, A., Nisini, B., et al. 2014, A&A, 566, A129
Bally, J. & Devine, D. 1994, ApJ, 428, L65
Beck, T. L., Riera, A., Raga, A. C., & Reipurth, B., 2007, AJ, 133, 1221
Bührke, T., Mundt, R., & Ray, T. P. 1988, A&A, 200, 99
Cabrit, S. & Raga, A. C. 2000, A&A, 354, 667
Cardelli, J. A., Clayton, G. C., & Mathis, J. S. 1989, ApJ, 345, 245
Chernin, L. M. & Masson, C. R. 1995, ApJ, 443, 181
Davis, C. J. & Dent, W. R. F. 1993, MNRAS, 261, 371
Devine, D., Bally, J., Reipurth, B., & Heathcote, S. 1997, AJ, 114, 2095
Eisloeffel, J. & Mundt, R. 1992, A&A, 263, 292
Fitzpatrick, E. L. 1999, PASP, 111, 63
García López, R., Nisini, B., Giannini, T., et al. 2008, A&A, 487, 1019
Heathcote, S. & Reipurth, B. 1992, AJ, 104, 2193

Kounkel, M., Hartmann, L., Loinard, L., et al. 2017, ApJ, 834, A142
Masciadri, E., de Gouveia Dal Pino, E. M., Raga, A. C., & Noriega-Crespo, A. 2002, ApJ, 580, 950
Menten, K. M., Reid, M. J., Forbrich, J., & Brunthaler, A. 2007, A&A, 474, 515
Morse, J. A., Hartigan, P., Cecil, G., & Raymomnd, J. C. 1992, ApJ, 399, 231
Morse, J. A., Heathcote, S., Hartigan, P., & Cecil, G. 1993, AJ, 106, 1139
Nisini, B., Giannini, T., Antoniucci, S., et al. 2016, A&A, 595, A76
Olofsson, S. & Olofsson, G. 2010, A&A, 522, A84
Podio, L., Bacciotti, F., Nisini, B., et al. 2006, A&A, 456, 189
Raga, A. C. & Mateo, M. 1988, AJ, 95, 543
Raga, A. C. & Noriega-Crespo, A. 1998, AJ, 116, 2943
__________. 2013, RMxAA, 49, 363
Raga, A. C., Velázquez, P. F., Cantó, J., & Masciadri, E. 2002a, RMxAA, 38, 251
__________. 2002b, A&A, 395, 647
Raga, A. C., Noriega-Crespo, A., Lora, V., et al. 2011a, ApJ, 730:L17
Raga, A. C., Noriega-Crespo, A., Kajdic, P., et al. 2011b, RMxAA, 47, 277
Raga, A. C., Noriega-Crespo, A., Rodríguez-Ramírez, J. C., et al. 2011c, RMxAA, 47, 289
Raga, A. C., Noriega-Crespo, A., Rodríguez-González, A., et al. 2012a, ApJ, 748, 103
Raga, A. C., Rodríguez-González, A., Noriega-Crespo, A., & Esquivel, A. 2012b, ApJ, 744, L12
Raga, A. C., Reipurth, B., Esquivel, A., et al. 2017, RMxAA, 53, 485
Reipurth, B. & Heathcote, S. 1992, A&A, 257, 693
Reipurth, B., Chini, R., Krügel, E., et al. 1993, A&A, 273, 221
Reipurth, B., Bally, J., Graham, J. A., et al. 1986, A&A, 164, 51
Reipurth, B., Yu, K. C., Heathcote, S., et al. 2000a, AJ, 120, 1449
Reipurth, B., Heathcote, S., Yu, K. C., et al. 2000b, ApJ, 534, 317
Reipurth, B., Heathcote, S., Morse, J., Hartigan, P., & Bally, J. 2002, AJ, 123, 362
Rodríguez, L. F. & Reipurth, B. 1996, RMxAA, 32, 27
Rodríguez, L. F., Reipurth, B., & Chiang, H.-F. 2014, RMxAA, 50, 285
Rodríguez-González, A., Esquivel, A., Raga, A. C., et al. 2012, AJ, 143, 60
Stapelfeldt, K. R. & Scoville, N. Z. 1993, ApJ, 408, 239
Takami, M., Chrysostomou, Ray, T. P., et al. 2006, ApJ, 641, 357

A. Noriega-Crespo: Space Telescope Science Institute, 3700 San Martin Drive, Baltimore, MD 21218, USA.
A. C. Raga: Instituto de Ciencias Nucleares, Universidad Nacional Autónoma de México, Ap. 70-543, 04510 Ciudad de México, México (raga@nucleares.unam.mx).
B. Reipurth: Institute for Astronomy, University of Hawaii at Manoa, Hilo, HI 96720, USA.

Revista Mexicana de Astronomía y Astrofísica, **55**, 125–126 (2019)

OBITUARY

Bárbara Pichardo
1969–2019

Bárbara Pichardo, a talented astrophysicist, teacher and science communicator at the Instituto de Astronomía of the Universidad Nacional Autónoma de México (IAUNAM), sadly passed away on March 12th in Mexico City. She was 49 years old.

Dr. Pichardo was an expert in astrophysical disc dynamics, ranging from stellar circumbinary discs to spiral galaxy dynamics.

Bárbara obtained the BSc in Physics from the Universidad Autónoma del Estado de México (UAEM). In 1995, she joined IAUNAM in Mexico City to pursue undergraduate studies on galaxies in radio wavelenghts, working with Jose Antonio García-Barreto. She quickly turned out to be a charismatic, optimistic and sensible student. She obtained her M.Sc. in astronomy at IAUNAM in 1997. During that time Bárbara explored tidally interacting dwarf galaxies with Elias Brinks, and interstellar matter turbulence theory with Enrique Vázquez; she later published papers on both subjects. In 2003 she obtained her PhD in astronomy at IAUNAM, supervised by Marco Martos and Edmundo Moreno. The Milky Way potential model developed in her thesis is one of the most detailed and adjustable ones, and includes non-axisymetric components. Her PERLAS spiral arms model has been widely used.

In 2003 Bárbara started a postdoctoral position at the University of Wisconsin in Madison collaborating with Linda Sparke and Luis Aguilar in the development of a model for circumbinary discs dynamics, based on invariant loops; the model aimed to constrain planetary environments. In 2004 she collaborated with Isaac Shloshman at the University of Kentucky simulating the hydrodynamics of discs of galaxies inside triaxial halos. During 2006 Bárbara was a postdoc in the Department for Theoretical Astrophysics of the University of Zurich, collaborating with George Lake in the theoretical study of the survival of circumstellar accretion discs.

In 2007 she joined IAUNAM as a researcher, and continued the Mexican tradition of galactic astronomy, extending it to orbital chaos and the nature of spiral arms in different disc galaxy morphologies. She also studied globular cluster orbits, in collaboration with Edmundo Moreno and Christine Allen. In 2007 she and a group of UNAM astronomers started a long-term collaboration with the University of Barcelona GAIA group led by Francesca Figueras. Bárbara's Milky Way potential model was used to make several predictions suitable to be tested with GAIA and other surveys. Her dynamical work extended to the stellar halo structure and kinematics, as well as to chemodynamical studies of the galactic disc and to the bar-spiral arms connection.

Because of her charisma, cheerful attitude and passion for many topics in astrophysics, students and colleagues clustered around her. It was common to find her office full of young students and collaborators arguing about astronomical problems. Predictably, such popularity soon turned into leadership, and in 2011 she was invited to be Academic Secretary of IAUNAM, a position she held until 2013, and again during 2015.

In addition to her research, Bárbara generously contributed both creativity and passion to science public outreach. She was a key figure in the "Noche de las Estrellas" yearly program, which has gathered hundreds of participants every year since its beginning. She also implemented an institutional project for science communication at IAUNAM, collaborating with Brenda Arias. This effort originated the "Pequeños Cosmonautas" project, focused on children and with the participation of several institutes at UNAM. Other results were the organization of conference cycles and exhibitions, and the design and manufacture of calendars and souvenirs seeking sustainability for the diffusion of science activities.

For the last two years Bárbara fought cancer, always with a great positive attitude and always as joyful for science and life as ever. During that time, she gave many talks, taught classes, published papers (perhaps at an even greater rate), produced videos, supervised postdocs and students, reviewed papers and participated in several academic committees. Even during her last months she submitted papers for publication, defined student projects and discussed with colleagues their ongoing research. Bárbara's loss is painful for all those who knew her and worked with her, but her sensible mind and her commitment to science and life will continue to be an inspiration for many.

Her passion for astronomy and for research was surpassed only by that for her family. She is survived by her husband and collaborator Antonio Peimbert and their child Yara.

Octavio Valenzuela

La *Revista Mexicana de Astronomía y Astrofísica*, fundada en 1974, publica trabajos originales de investigación en todas las ramas de la astronomía, astrofísica y temas vinculados a éstas. Se editan dos números por año y su distribución es gratuita a todas las instituciones relacionadas con los campos cubiertos por esta revista.

La política editorial de la *RMxAA* consiste en enviar a arbitrar los artículos recibidos a especialistas en el campo. Los interesados en publicar en nuestra revista deberán enviar por correo electrónico, a la dirección rmaa@astro.unam.mx, la versión completa de su artículo en formato PostScript o PDF y el archivo LaTeX. Estos archivos deberán ir acompañados de una carta de presentación. Todos los trabajos deben ser preparados en inglés usando la versión más reciente del macro en LaTeX de la *RMxAA* "rmaa.cls" (disponible en https://www.irya.unam.mx/rmaa/). Se requiere un "Abstract" no mayor que 12 líneas, y un "Resumen" en español (este último podrá ser provisto por los editores de ser necesario); también se incluirán de 1 a 6 palabras clave ("Keywords") de la lista de las revistas astronómicas internacionales. Se requiere que cada tabla incluida en el texto esté numerada y con título; las figuras deberán estar en formato PostScript (.ps) o PostScript encapsulado (.eps), estar numeradas y con leyenda explicativa. Se requiere que cada tabla y figura estén mencionadas en el texto. El estilo de las referencias sigue las normas astronómicas internacionales recientes. Para mayor información sobre el estilo de la *RMxAA* se puede consultar el archivo de ejemplo que viene incluido en los macros. La publicación es gratuita para los autores.

En 1995 se inició la Serie de Conferencias de la *Revista Mexicana de Astronomía y Astrofísica*, dedicada a la publicación de las memorias de reuniones astrónomicas efectuadas en México y en otros países del continente. Hasta 1994 las memorias de reuniones astronómicas de la región se publicaron como volúmenes especiales de la *RMxAA*.

Las condiciones de publicación de cada volumen de las memorias de conferencias serán el resultado de un convenio establecido entre la *RMxAC* y los organizadores de cada evento. Los detalles de la publicación, que incluyen fechas y extensión de los textos, serán anunciados por los editores de cada conferencia. Las contribuciones extensas estarán en inglés con un resumen en español (o portugués en caso de las Reuniones regionales). Los resúmenes de las reuniones que no son temáticas tendrán una extensión máxima de 300 palabras incluyendo título, autores y afiliación; serán exclusivamente en inglés. Los macros LaTeX para las memorias se encuentran en http://www.astroscu.unam.mx/~rmaa. Todas las contribuciones y resúmenes deberán estar en estos formatos.

Se concede permiso a los autores de artículos y libros científi-cos para citar trabajos publicados en la *RMxAA* y en la *RMxAC* siempre y cuando se dé la referencia completa. También se permite la reproducción de figuras y tablas bajo las mismas condiciones.

La *RMxAA* aparece indexada en Current Contents, Science Citation Index, Astronomy and Astrophysics Abstracts, Physics Briefs, Publicaciones Científicas en América Latina, Astronomy and Astrophysics Monthly Index, PERIODICA, RedALyC, Latindex y SciELO.

The *Revista Mexicana de Astronomía y Astrofísica*, founded in 1974, publishes original research papers in all branches of astronomy, astrophysics and closely related fields. Two numbers per year are issued and are distributed free of charge to all institutions engaged in the fields covered by the *RMxAA*.

All papers received by the *RMxAA* are sent to a specialist in the field for refereeing. Authors interested in publishing in the *RMxAA* should send their papers to the e-mail address rmaa@astro.unam.mx, in PostScript or PDF format, along with the LaTeX file. A submission letter should also be sent. Papers should be prepared in English, using the most recent version of the *RMxAA* LaTeX document class "rmaa.cls" (available from https://www.irya.unam.mx/rmaa/). An "Abstract" of at most 12 lines is required, as well as a "Resumen" in Spanish. The latter can be provided by the Editors, if necessary. A total of six or fewer "Keywords", taken from the lists of international astronomical journals should be included. Tables should be numbered and include a title. Figures should be submitted in PostScript (.ps) or Encapsulated PostScript (.eps) format, should be numbered, and should include a caption. Both tables and figures should be mentioned in the text. The style of the references follows recent international astronomical usage. For more information about the style norms of *RMxAA* please consult the example included in the LaTeX package. Publication in *RMxAA* is free of charge to authors.

The Conference Series of *Revista Mexicana de Astronomía y Astrofísica* was founded in 1995 to publish the proceedings of astronomical meetings held in Mexico and other countries throughout the continent. Until 1994 such proceedings had been published as special issues of *Revista Mexicana de Astronomía y Astrofísica*.

Conditions of publication of proceedings of each conference will be the result of a mutual agreement between the *RMxAC* and the organizing committee. Details of publication, including length of papers, will be announced by the editors of each event. The extensive contributions should be in English, and should include an abstract in Spanish (or Portuguese for regional meetings). The abstracts of non-thematic meetings should not exceed 300 words including title, authors, and affiliation; they should be exclusively in English. The LaTeX templates specially prepared for proceedings can be obtained at http://www.astroscu.unam.mx/~rmaa; all papers should be submitted in this format.

Authors of scientific papers and books may quote articles published both in *RMxAA* and *RMxAC* provided that a complete reference to the source is given. Reproduction of figures and tables is also permitted on the same basis.

The *RMxAA* is indexed in Current Contents, Science Citation Index, Astronomy and Astrophysics Abstracts, Physics Briefs, Publicaciones Científicas en América Latina, Astronomy and Astrophysics Monthly Index, PERIODICA, RedALyC, Latindex, and SciELO.